Vera C. Rubin Observatory
Systems Engineering

LSST Camera Electro-Optical Test Results

The LSST Camera group: Pierre Antilogus, Pierre Astier, John Banovetz, James Chiang, Seth Digel, Thibault Guillemin, Sean MacBride, Stuart Marshall, Andrew Rasmussen, Aaron Roodman, Tony Tyson, Yousuke Utsumi,

SITCOMTN-148

Latest Revision: 2025-01-20

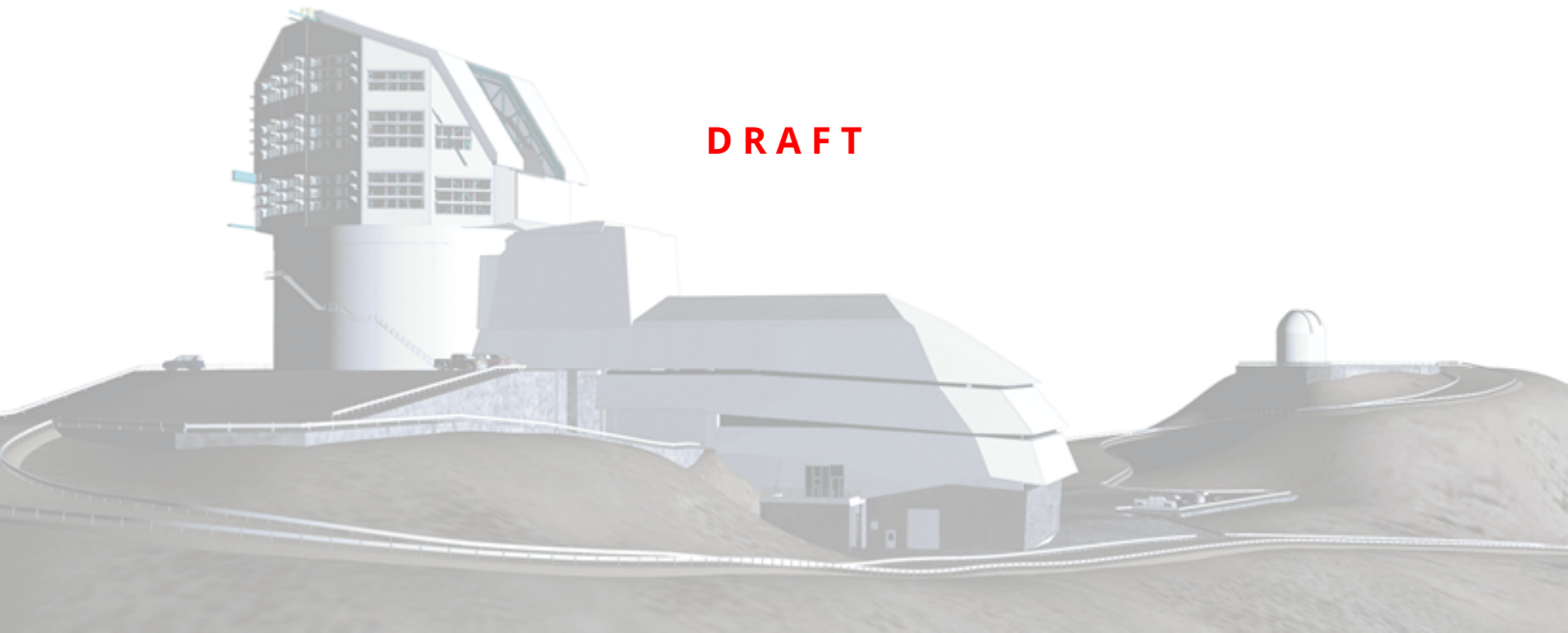

DRAFT

Abstract

This note collects results from the LSST Camera electro-optical testing prior to installation on the TMA. We describe the CCD and Focal Plane optimization and the resulting default settings. Results from eopipe are shown for standard runs such as B-protocols, Dense and SuperDense PTCs, gain stability, OpSim runs of Darks, and Darks with variable delays. We also describe features such as e2v Persistence, ITL phosphorescence in coffee stains, remnant charge near Serial register following saturated images, vampire pixels, ITL dips, and others.

Change Record

Version	Date	Description	Owner name
1	YYYY-MM-DD	Unreleased.	

Document source location: `https://github.com/lsst-sitcom/sitcomtn-148`

Contents

LSST Camera Electro-Optical Test Results

1 Introduction

The naming of the EO runs was established during initial LSSTCam integration and testing. The final SLAC IR2 run from November 2023 was named “Run 6”, while the data acquisitions from Cerro Pachon from September through December 2024 are considered “Run 7”. Additionally, individual EO acquisitions are tagged with a run identifier. This is commonly referred to as a Run ID. For all SLAC runs, the run identifier was a five digit numeric code, while the Cerro Pachon runs were “E-numbers” that started with a capital E followed by a numeric code.

2 Electro-optical setup

2.1 Run 7 Optical modifications

For Run 7 in the white room on Level 3 our electro-optical test setup had a few differences from the Run 6 setup in IR2 at SLAC. One difference was that we were not able to use the CCOB Narrow/Thin beam because we did not have the resources or expertise to configure it. As such, the majority of the testing was done with the CCOB Wide Beam projector. We did obtain an additional projector, the 4K projector, partway through Run 7 that will be discussed later. With the CCOB Wide Beam, we used a cone attached to the L1 cover as well as a shroud to create a dark environment (Fig. 1).

This allowed us to operate on Level 3 with a dark current of <0.1 ADU/sec with the shutter open. The initial setup of the CCOB Wide Beam projector was the same as for Run 6, with a minimal ND filter (10%) attached to a C-mount lens. One difference was that the f/stop of the lens was changed from 2.6 to 1.6 (fully open). This was done to try to reduce the effect of the ‘weather’ and the ‘CMB pattern’ two effects that we found in Run 6 and were found to be due to our projection setup (see [Banovetz2024]). While changing the f/stop did reduce the weather pattern, it also caused a much steeper illumination roll-off across the focal plane. We evaluated the weather pattern and illumination roll-off relative to Run 6.

To both reduce the effects of the ‘weather’ and ‘CMB’ but retain uniform illumination across the focal plane, we installed a diffuser in the cone attached to L1. Figure 2 shows the place-

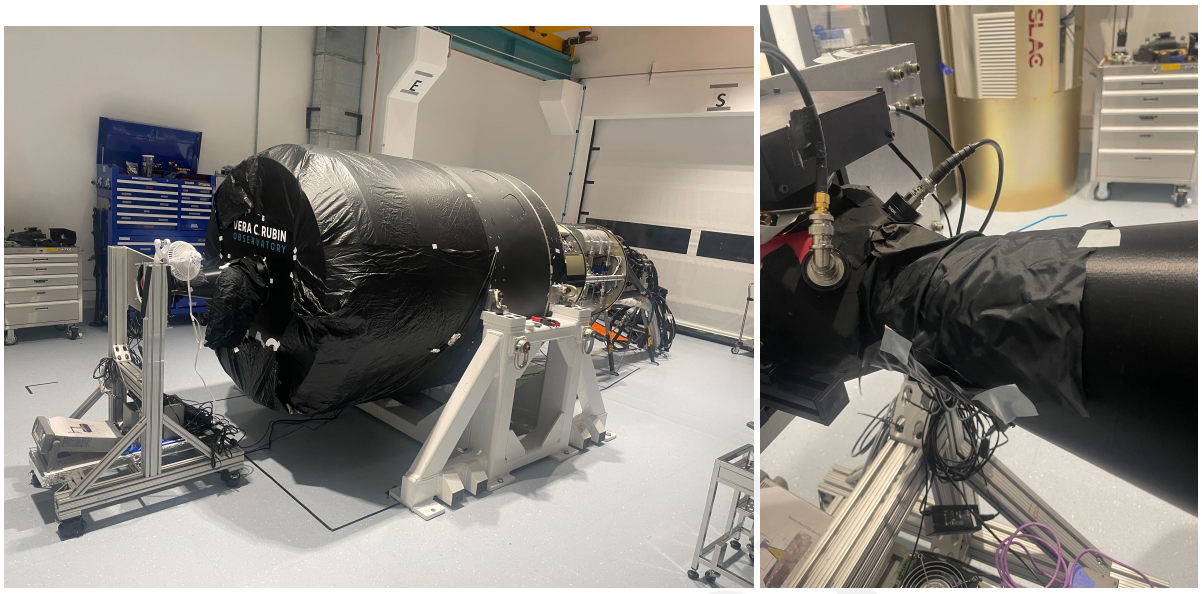

Figure 1: (left) Final shroud configuration of LSSTCam in Level 3 to reduce light leaks. (right) CCOB Wide Beam attached to the cone and shrouded.

ment of the diffuser within the cone.

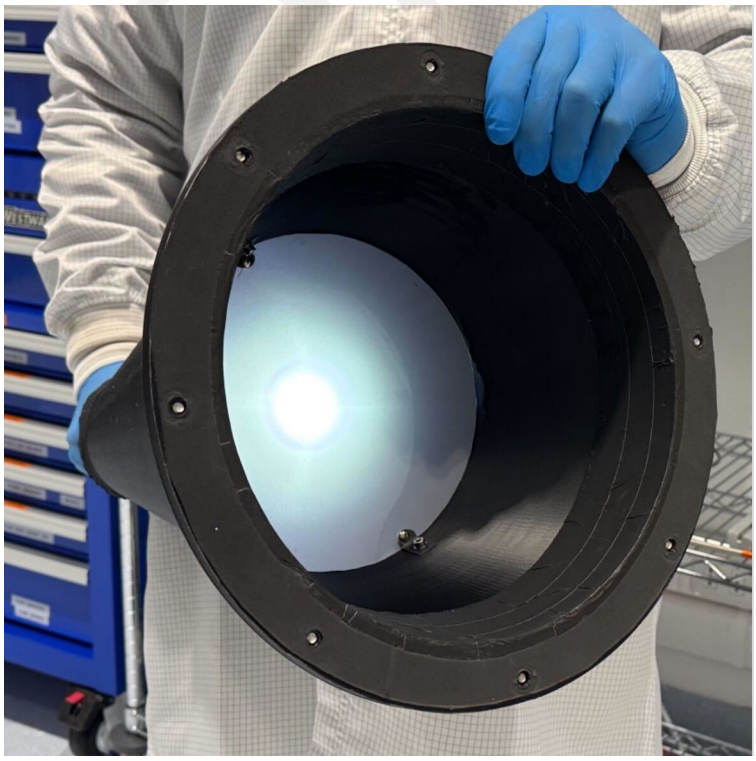

Figure 2: Diffuser installed into the light cone.

We found that the diffuser greatly reduced the 'weather' (Fig. 3) and eliminated the CMB pattern and more uniformly illuminated the focal plane (Fig. 4), with a penalty of decreasing the overall illumination by roughly 35% even though we fully opened the f-stop.

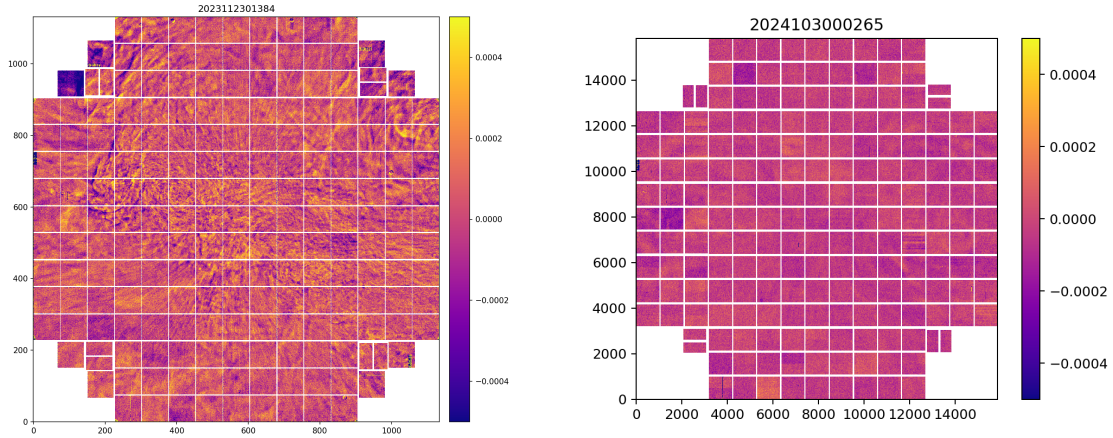

Figure 3: Full focal plane fractional difference images for Run 6 (left) and Run 7 (right).

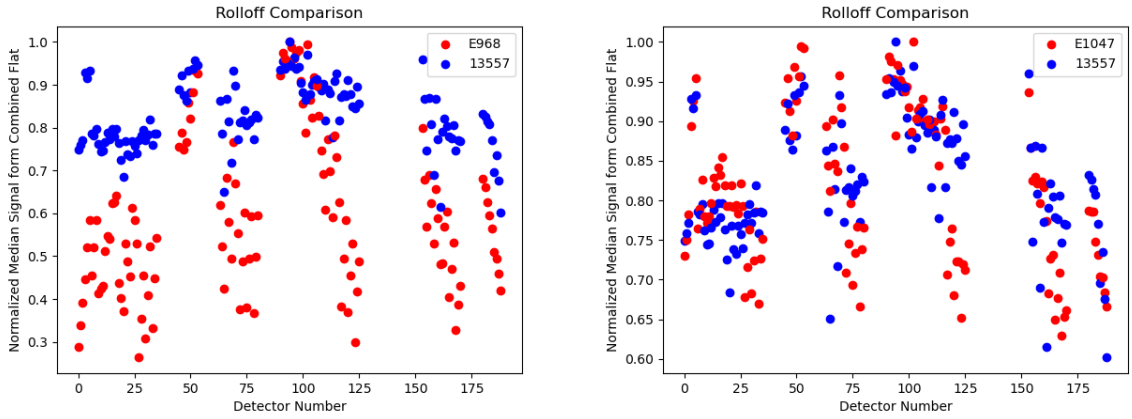

Figure 4: (left) Illumination across the focal plane from Run 7 without the diffuser (E968) as compared to Run 6. (right) Illumination across the focal plane from Run 7 with the diffuser (E1047) as compared to Run 6.

The diffuser was installed for all B protocol and PTC runs (see Section 3) moving forward, being taken out only for pinhole projection runs and when using the 4K projector.

2.2 Projector spots

The addition to the projectors used for EO testing was a 4K projector, similar to those used in conference rooms. This projector was first tested at SLAC and arrived at the observatory about halfway through Run 7. It was used primarily as a spot projector, as the pinhole filter was not available at that time because of the Filter Exchange System was temporarily inoperable. The projector has an advantage, instead, as it could illuminate all 3206 amplifiers instead of just the 21 illuminated by the pinhole projector. Figure 5 shows both the setup of the projector on Level 3 and an example of a spot image and the spots across the focal plane. Since the projector does not have fast illumination control, we primarily used the LSST camera main shutter instead of any flashing of the light source (e.g., as we did with the LEDs of the CCOB Wide Beam). One downside that was found was that the projector illuminated the entire focal plane at some background level, not just the spot regions. The background illumination also had structure that changed with time and could not be easily subtracted. Figure 6 shows an example of a spot image of just one detector as well as a zoomed in image of a single spot which highlights the background structure. The resulting contrast between the spot and the background was only about a factor of 6. Changing the spot shape to large rectangles for crosstalk measurements increased the contrast ratio to 30. Examples of the rectangles can be seen in Figure 7. Though the contrast was much improved, there was still a background structure as can be seen in the saturated image of the figure.

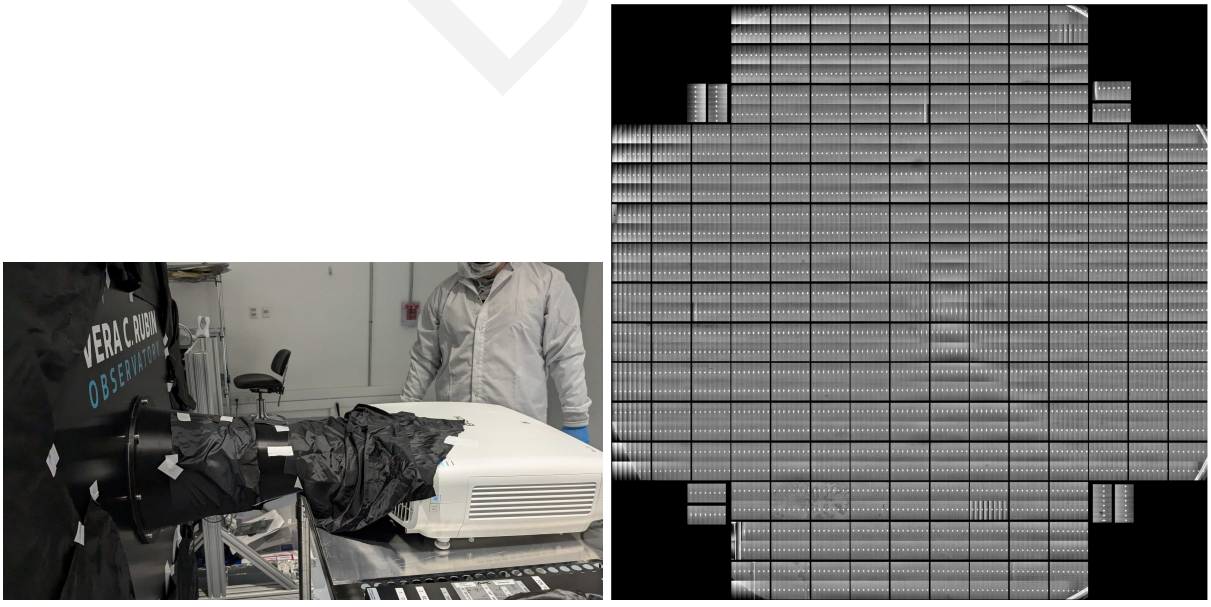

Figure 5: (left) The spot projector set up on Level 3. (right) An example of an image taken with the spot projector with all the amplifiers containing a spot.

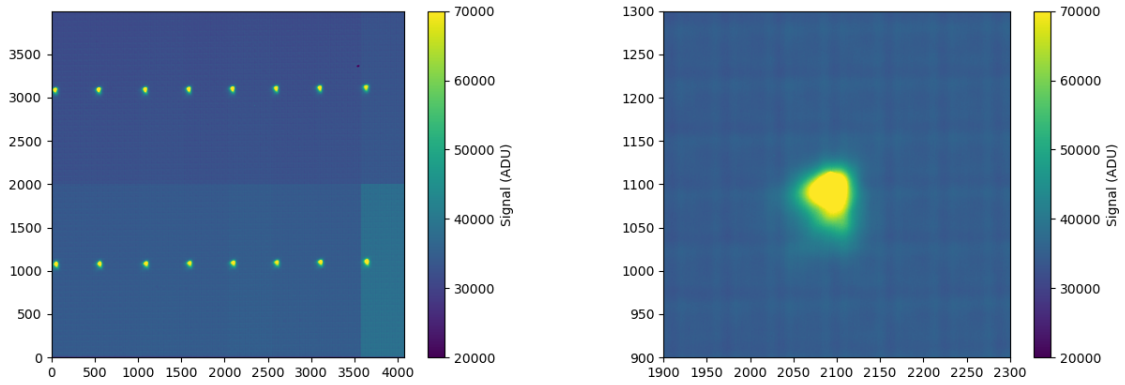

Figure 6: (left) Example of a spot image zooming into a single detector. (right) Example of a spot image zooming further into a single spot. In both the images, there is a clear background structure caused by the projector.

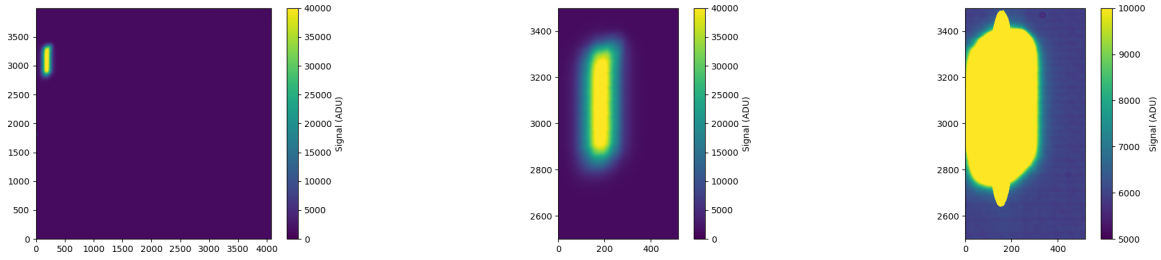

Figure 7: (left) Example of a spot image that utilized the rectangle shape, zoomed into a single detector (left), zoomed into the spot (middle) and zoomed into the spot with a saturated image to highlight the background pattern caused by the projector (right).

This section describes the spots and rectangle patterns used for tests with the 4K projector.

- Projector background
- Spots on many amps
- Spots on one amp
- Optical setup

2.3 Dark current and light leaks

This section describes dark current and light leaks in Run 7 testing.

2.3.1 Light leak mitigation with shrouding the camera body

One of the first tests we attempted with LSSTCam was measuring dark current and sources of light leaks in the camera body. Before beginning we covered gaps between the L1 cover and the gaskets with tape, in accessible locations . Below shows the gaps that we could see between L1 and its cover.

Once these were sealed, we took some initial measurements and then started to cover the LSSTCam body with a blackout fabric shroud. Figure 1 shows the final configuration of the shroud covering the camera. We also found light leaks where the light cone attached to L1 was housed, and from the Utility Trunk.

Table 1 includes the observations, the corresponding measured dark currents, and comments on what changed during the leak chasing.

Table 1: Summary of the 15 s dark exposures, the different conditions, and the resulting dark current. Exposure ID is preceded by "MC_C202409". The shroud was in place for each of these measurements. ("Initial Covering" was just the CCOB cone and around the L1 cover.)

Exposure	Dark Current	Room Lights	Shutter	Comments
09_000012	0.16	Off	Closed	
09_000018	0.16	On	Closed	
09_000038	2.94	On	Open	Initial Covering
09_000054	1.34	On	Open	+ Blanket over the FCS
09_000072	0.41	On	Open	+ Blanket over AND under the FCS

09_000078	0.18	Off	Open	+ Blanket over AND under the FCS
10_000031	0.03	On	Open	+ Blanket over AND under the FCS + UT

2.3.2 Filter Exchange System Autochanger light leak masking

A dedicated light leak study of the Filter Exchange System (FES) Autochanger (AC) was performed during Run 6 at SLAC in summer 2023 and a localized faint light source of up to ~0.04 e^-/s/pix was found to be associated with the 24 V Clean of the AC.

In the AC this voltage is used to power some probes and all controllers. In February 2024, as AC-1 was extracted from LSSTCam for global maintenance, a direct investigation to localize the light source was performed unsuccessfully. A light source in the AC was not expected, as in the AC all controllers' LEDs have been removed, and most electronics are in "black boxes". Still, two small probes, which had LEDs that could not be removed, were initially masked by a black epoxy. As we had doubts about the quality of this masking at IR wavelengths, we applied extra masking (aluminum black tape) on them during the Feb 2024 maintenance (on AC 1 and 2).

At the start of Run 7 a new study of the light leak based on 900 s dark exposures with the shutter open and the empty frame filter in place, showed that the AC light leaks were still present (see left hand image of Fig. 8). Following this finding, a full review of all the AC hardware powered by the 24 V dirty was performed, and a candidate was found: the encoders of the five main motors of the AC had only partial documentation from the vendor that did not mention the presence of LEDs. After interaction with the vendor, the encoders were understood to contain ~700 nm LEDs. The hypothesis of ~700 nm LED sources has been found compatible with the observation as no AC light leaks were detected using various filters (g, r, and y) in LSSTCam at the start of Run 7 (g, r, and y filters). A dedicated test in Paris using an AC spare encoder and a precision photometric set-up allowed identification of the leak in the masking of those LEDs in the vendor packaging. A complementary masking method based on a 3D printed part + tape + cable tie was qualified in Paris. It was found to mask the light leak and to be safe (all parts correctly secured).

In November 2024, we masked all the lights in the back of the Level 3 white room (not the part containing LSSTCam) to set up a high-quality dark room allowing a direct observation with a

CMOS camera of the light leak on the AC2 motor encoders. The level of darkness reached allowed us to validate the quality of the light masking of the AC encoders. Notice that the FES-prototype in Paris does not have encoders on the Online Clamps, so we had to tune/qualify the masking of those encoders directly on the AC 2 at the summit.

For both AC 1 and 2, the encoders of the five motors with the vendor issue on their LED masking have been successfully enveloped in a light-tight mask.

We note that the AC was turned off starting on 27 September 2024 at 21:15 UTC in the first part of Run 7. For the second part of Run 7 (i.e., after mid-November) the AC was back on: as the AC 1 was back in LSSTCam with the new light masks in place on the motor encorders, we were able to take a new series of 900 s darks with the AC turned on and off, confirming that the light leak associated with the FES was eliminated (see right hand image of Fig. 8).

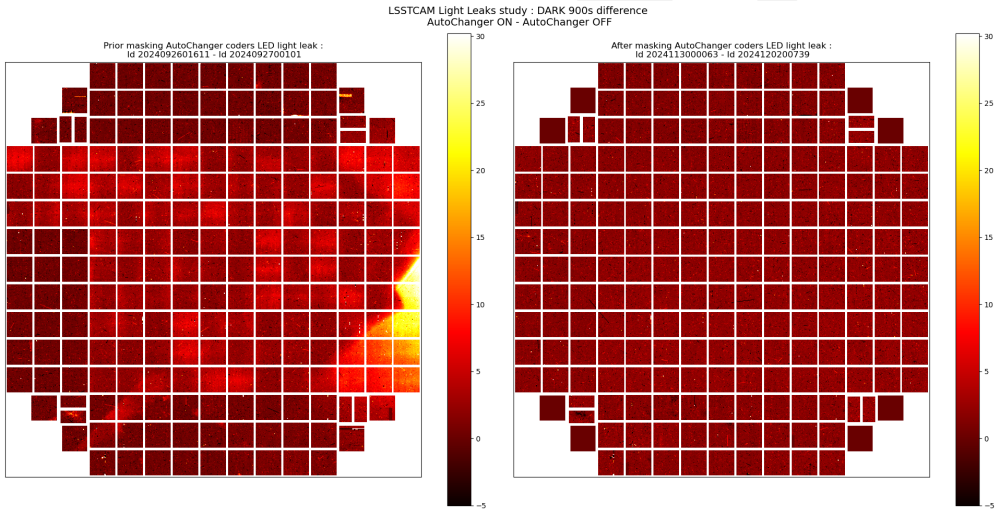

Figure 8: (left) The original impact of the AC light leak on a 900 s dark difference image (AC on minus AC off). (right) The result after masking the LEDsc of the motor encoders in the AC. No light associated with the FES is present in 900 s dark difference image.

2.3.2.1 Shutter condition impact on darks

2.3.2.2 Filter condition impact on darks To investigate how the filter affects the dark current, we took 900 second darks with the available filters in the filter wheel: E1114 (empty filter), E1115 (g), E1116 (y), and E1117 (r). The heat maps of the dark currents from EO pipe

can be found in Figure 9. The major effect of including the filters was reducing the glow the AC (see Figure 8). The global average of the median amplifier dark currents drop from 0.026 e-/sec with the empty filter to 0.0035 e-/sec for r, 0.0011 e-/sec for y, and 0.00063 e-/sec for g. The discrepancy between the filters could be the AC light shines more brightly in the redder wavelengths and even the IR. Unfortunately, we were not able to obtain data with the other 3 filters to confirm this.

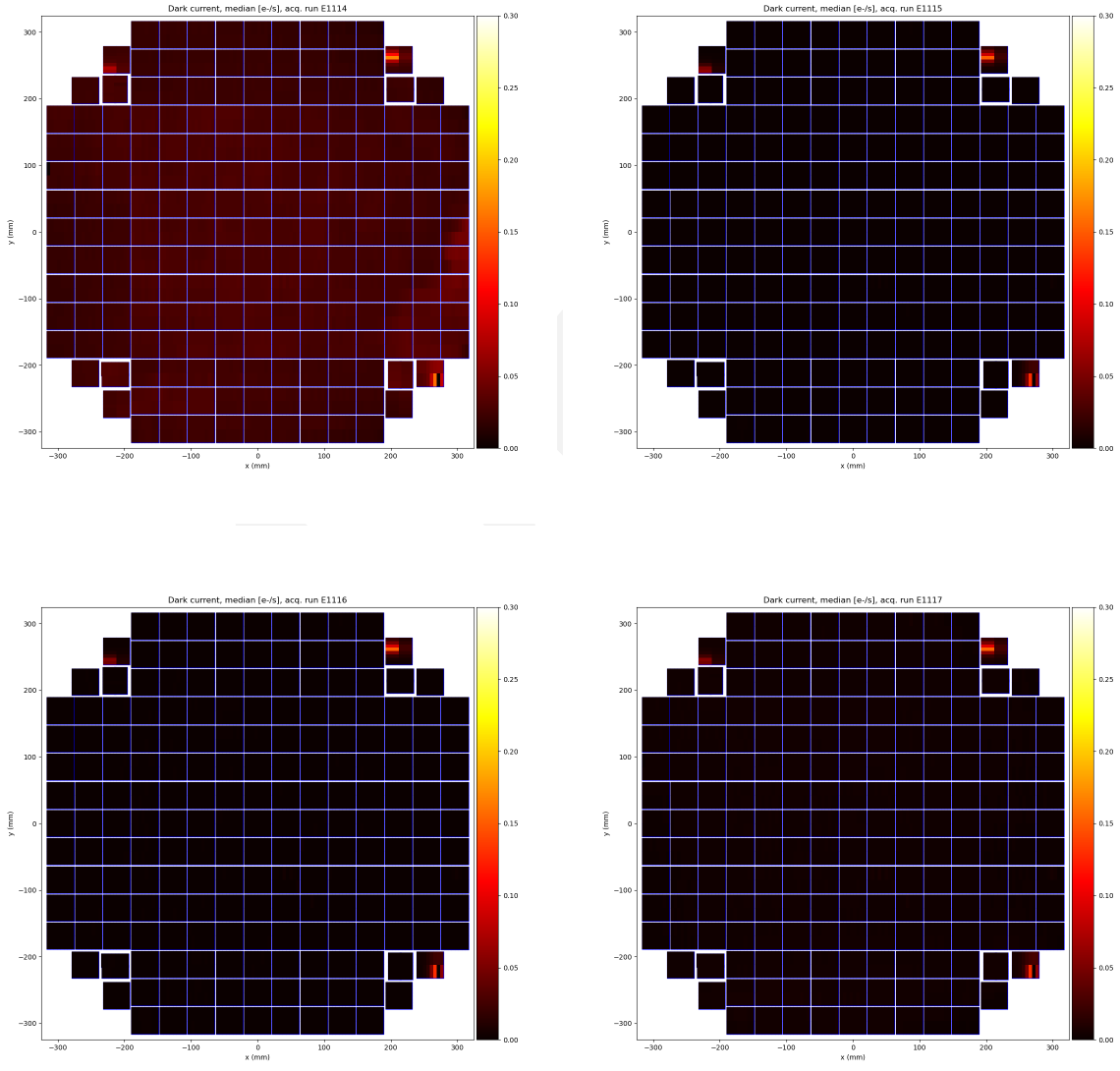

Figure 9: The heat map of the dark current with the empty filter installed (E1114; top left), the g filter installed (E1115; top right), the y filter installed (E1116; bottom left), and the r filter installed (E1117; bottom right)

2.3.3 Final measurements of dark current

3 Reverification

All electro-optical (EO) camera test data is processed through the calibration products and electro-optical pipelines to extract key metrics from the data run. The key camera metrics from Run 7, and their comparison to previous runs are discussed below.

Among the motivations for these measurements, the primary concern is whether LSSTCam has maintained its performance characteristics between Run 6 and Run 7, since LSSTCam was transported from SLAC to Cerro Pachon. The testing condition is supposed to be identical; however as described in Section 3.4.3, two Rafts have slightly different voltages between two runs.

3.1 Background

Initial characterization studies performed on LSSTCam during Run 7 primarily used two image acquisition sequences.

- B protocols: this acquisition sequence consists of the minimal set of camera acquisitions for electro-optical testing, including
  - Bias images
  - Dark images
  - Flat pairs - flat illumination images (flats) taken at varying flux levels
  - Stability flats - flats taken at constant flux levels
  - Wavelength flats - flats taken with different LEDs
  - A persistence dataset - a saturated flat, followed by several darks
- PTCs (photon transfer curves): this acquisition sequence consists of a sequence of flat pairs taken at different flux levels. The flat acquisition sequence samples different flux levels at a higher density than the B protocol flat sequence, enabling more precise estimates of flat pair metrics including pixel covariances (see Fig. 10).

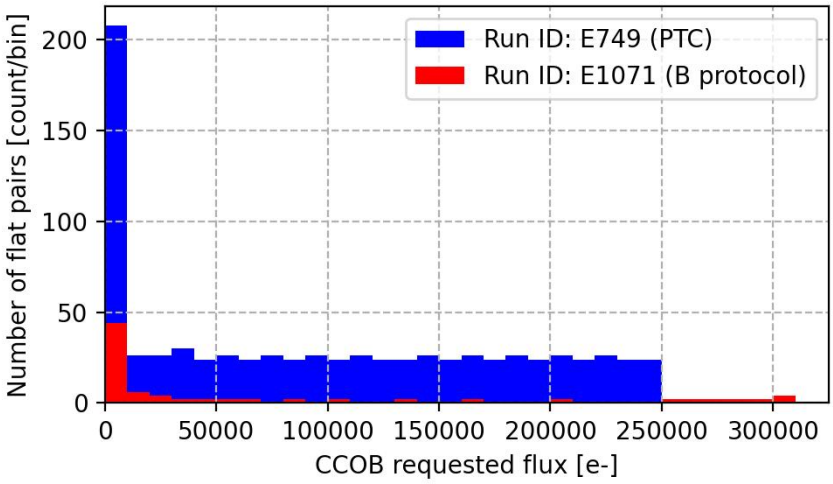

Figure 10: Flat-pair comparison between PTC and B protocol

For comparisons between Cerro Pachon EO runs and the final SLAC IR2 equivalents, the following runs are used (see Table 2).

Table 2: Reference runs for Run 6 and Run 7 comparisons

Run Type	Run 6	Run 7
B Protocol	13550	E1071
PTC	13591	E749

3.2 Stability flat metrics

3.2.1 Charge transfer inefficiency

CTI, or charge transfer inefficiency, measures the fraction of charge that fails to transfer from row to row during readout, and appears as trailing charge in the image area. Consequences of high CTI include loss of charge, distorted signals in the direction of parallel transfer, and reduced sensitivity in low light imaging. CTI measurements are made using the EPER method (Snyder et al., 2021), for which the ratio of the residual charge in the overscan pixels to the total signal charge in the imaging region is evaluated. In the context of LSSTCam, we measure CTI along both the serial and parallel directions.

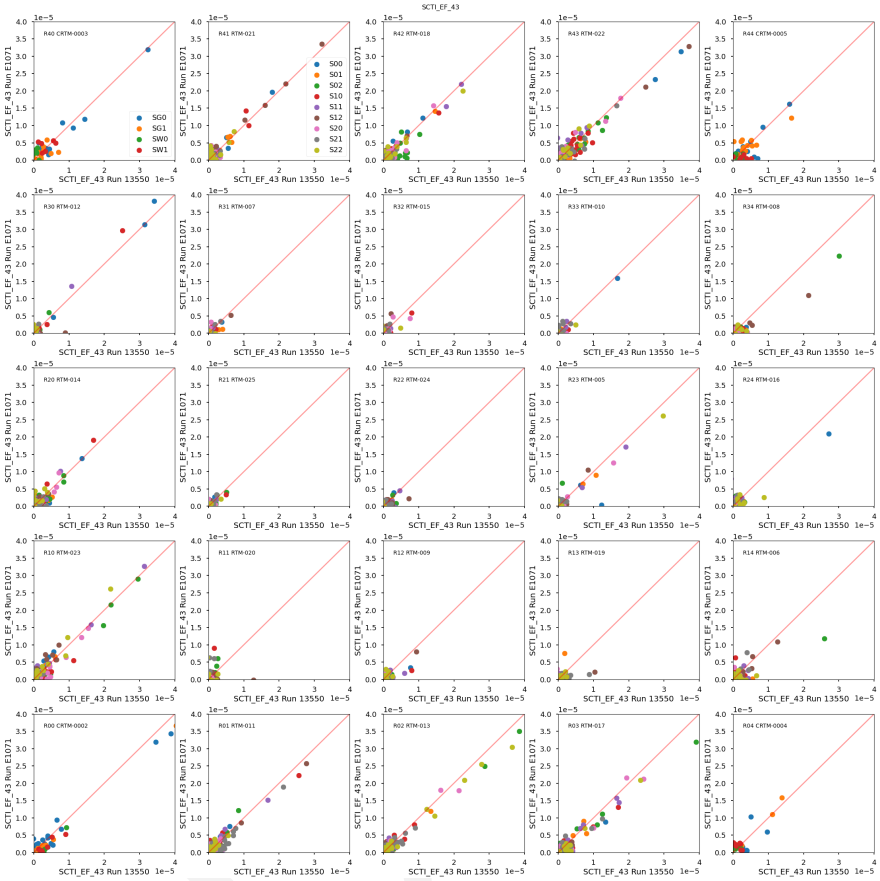

Figure 11: Serial CTI amplifier measurements separated by raft for Run 7 (E1071) and Run 6 (13550)

3.2.1.1 Serial CTI The CTI along the serial registers of the amplifier segments of the LSSTCam CCDs is consistent between Run 6 and Run 7 (Fig. 11). Both sensor types show low CTI, span a range of ~2×10^{-5} % for e2v sensors, and by ~4×10^{-6} % for ITL sensors (Fig. 12).

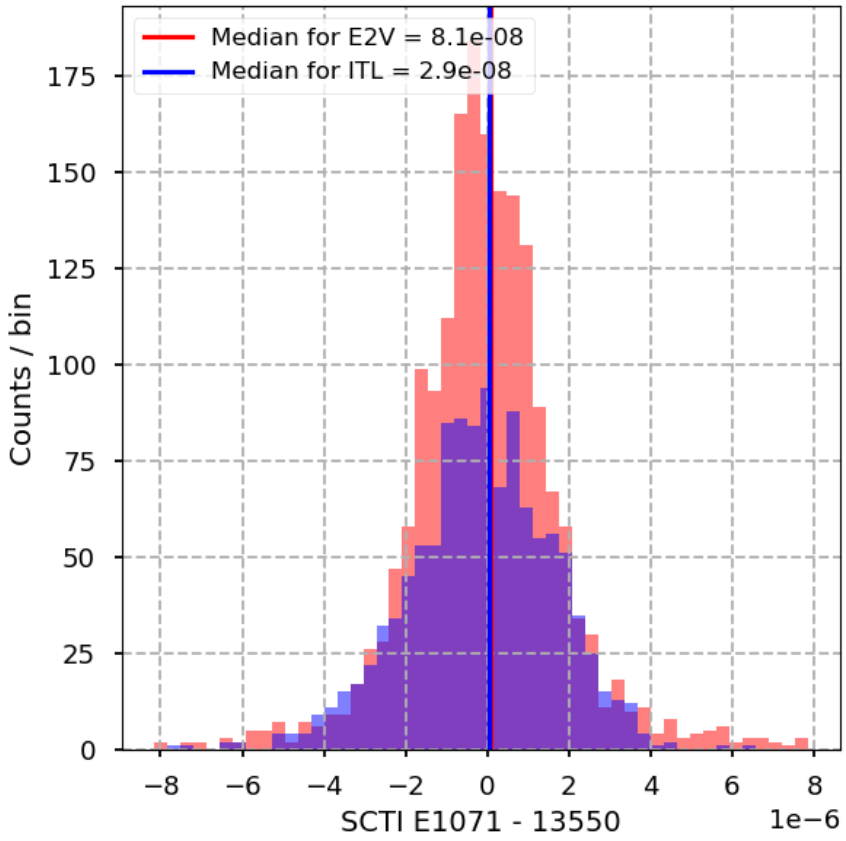

Figure 12: Distributions of differences in serial charge transfer inefficiencies between Run 7 (E1071) and Run 6 (13550), grouped by CCD type.

3.2.1.2 Parallel CTI The CTI along the parallel direction is consistent between Run 6 and Run 7 (Fig. 13). Both sensor types are found to have extremely low CTI on the order of 10^{-5} %, and span a range of ~1×10^{-5} % for e2v sensors, and by ~7×10^{-4} % for ITL sensors (Fig. 14).

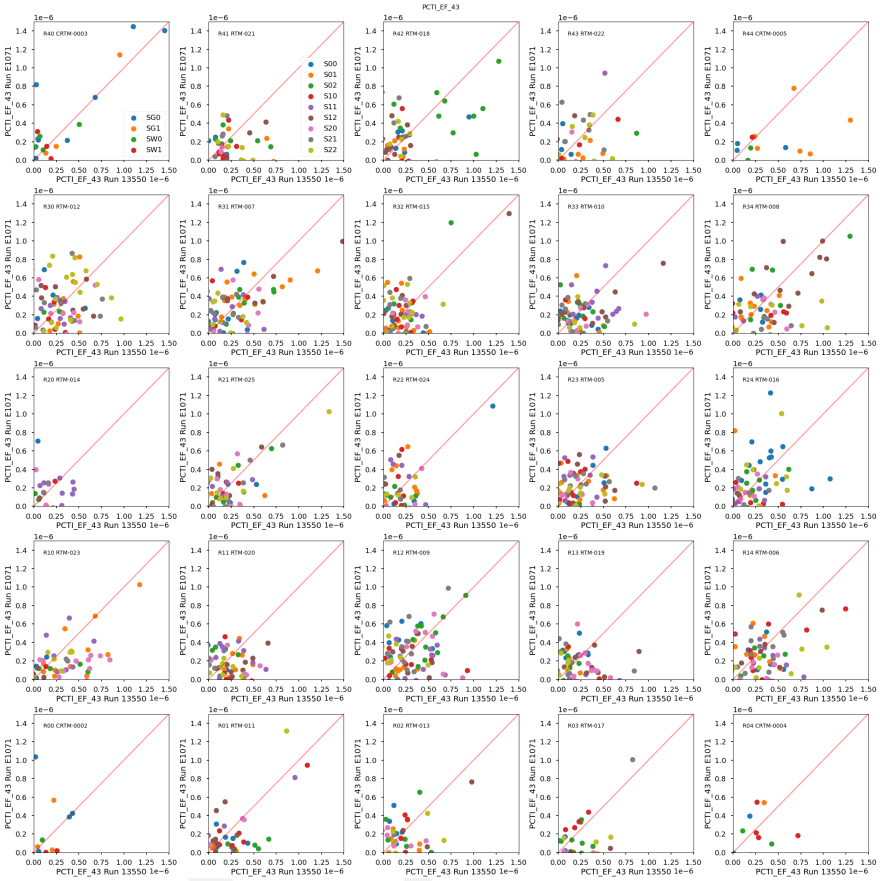

Figure 13: Parallel CTI comparison by raft for Run 7 (E1017) and Run 6 (13550).

R00 observations

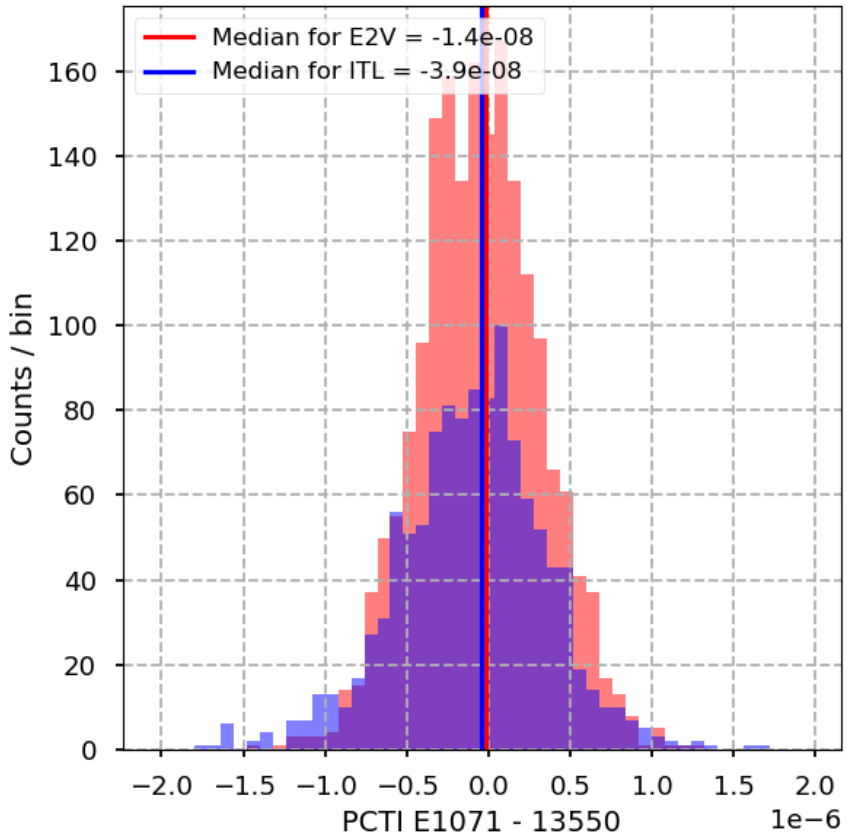

Figure 14: Distributions of differences in parallel charge transfer inefficiencies between Run 7 (E1071) and Run 6 (13550), grouped by CCD type.

3.3 Dark metrics

3.3.1 Dark current

Dark current is the small amount of electrical charge generated in the absence of light due to thermal activity within the semiconductor material of a CCD. This effect occurs when electron/hole pairs are thermally released into the conduction band in the CCD, mimicking the signal that light would produce. Dark current increases with temperature, so cooling the CCD is a common method to reduce it in sensitive imaging applications. Dark current introduces noise into an image, particularly in low-sky background conditions in long exposures. The measurement of dark includes the dark current and stray light, making them impossible to distinguish each other since they both linearly evolve with time. In the context of LSSTCam,

we measure dark current from the combined dark images across all amplifiers as the upper limit.

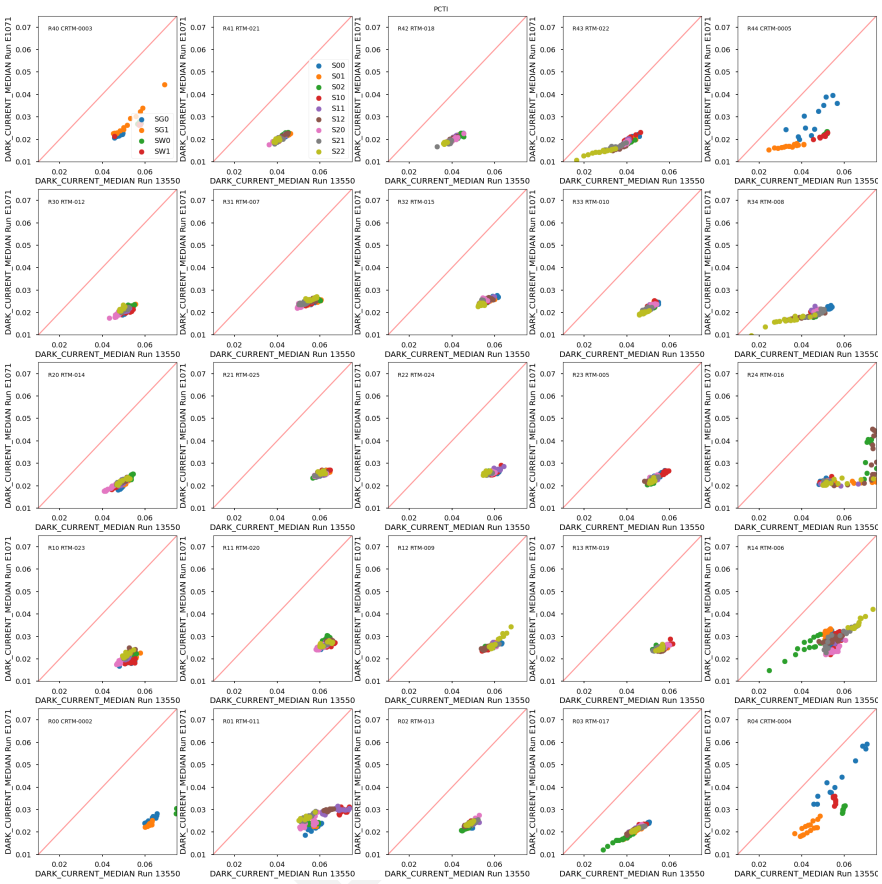

Figure 15: Dark current comparison by raft for Run 7 (E1071) and Run 6 (13550).

Unexpectedly, the dark current was significantly less in Run 7 than Run 6 (Fig. 15). We do not attach particular significance to the finding because this could be the result of improved shrouding on the camera in the Level 3 white room relative to the IR2 clean room SLAC.

3.3.2 Bright defects

Bright defects are localized regions or individual pixels that produce abnormally high signal levels, even in the absence of light. These defects are typically caused by imperfections in the semiconductor material or manufacturing process of the CCD. Bright defects can manifest as “hot pixels” with consistently high dark current, small clusters of pixels with elevated dark current, or as “hot columns” (pixels along the same column that have high dark current).

In the context of LSSTCam, we identify and exclude bright pixels from the dark current measurement, with the threshold for a bright defect set at 5 e^-/pix/s, above which the pixel/cluster/column is registered as a bright defect. In addition to the bright pixel metric, eo-pipe also computes a bright column metric, which is any region of bright pixels that is contiguous over 50 pixels or more.

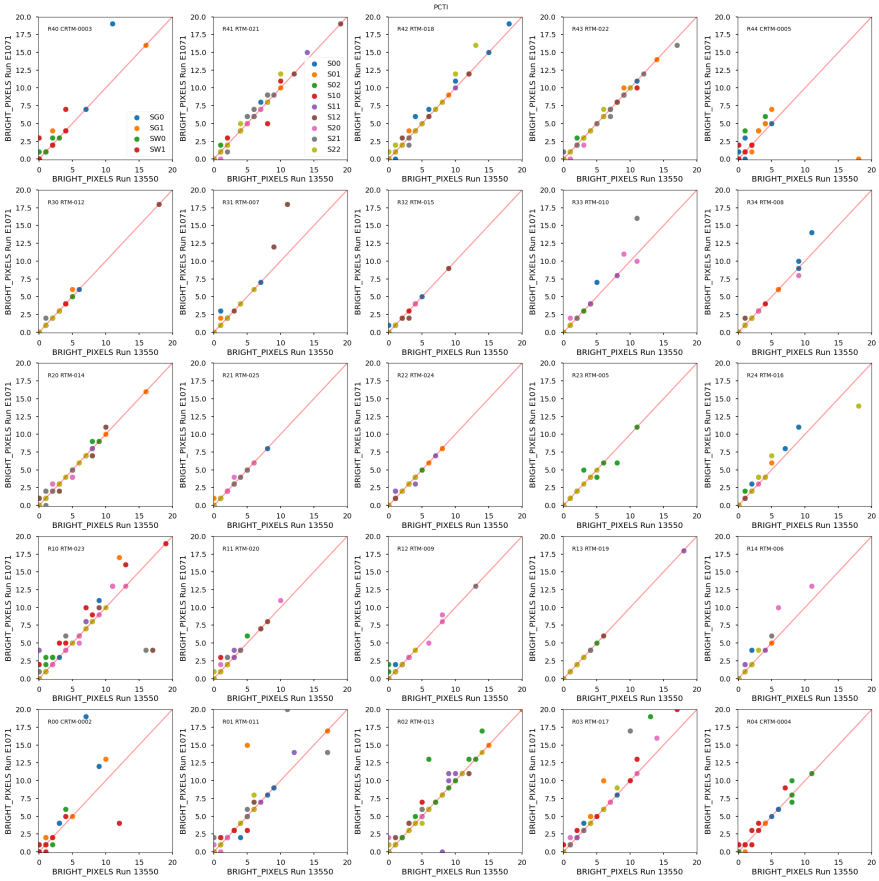

Figure 16: Bright pixel comparison by raft for Run 7 (E1071) and Run 6 (13550)

Evaluating the change in defect counts on each amplifier segment between Run 6 and Run 7, and aggregating the amplifiers by the detector manufacturer shows a small increase of bright defects in Run 7 (Fig. 16). Figure 17) displays differences of the measurements. The median values agree well, while there are signs of the positive tail. For ITL sensors, we find that 12% of the amplifiers have more bright pixels than in Run 6. For e2v sensors, we find 4% of the amplifiers that have more bright pixels. Despite this, the number of bright defects between runs does not increase for most sensors.

The reason is not totally clear, but the difference in the illumination pattern as described in Section 2.1 might play a role, which implies that a small number of defects could be involved by optical path.

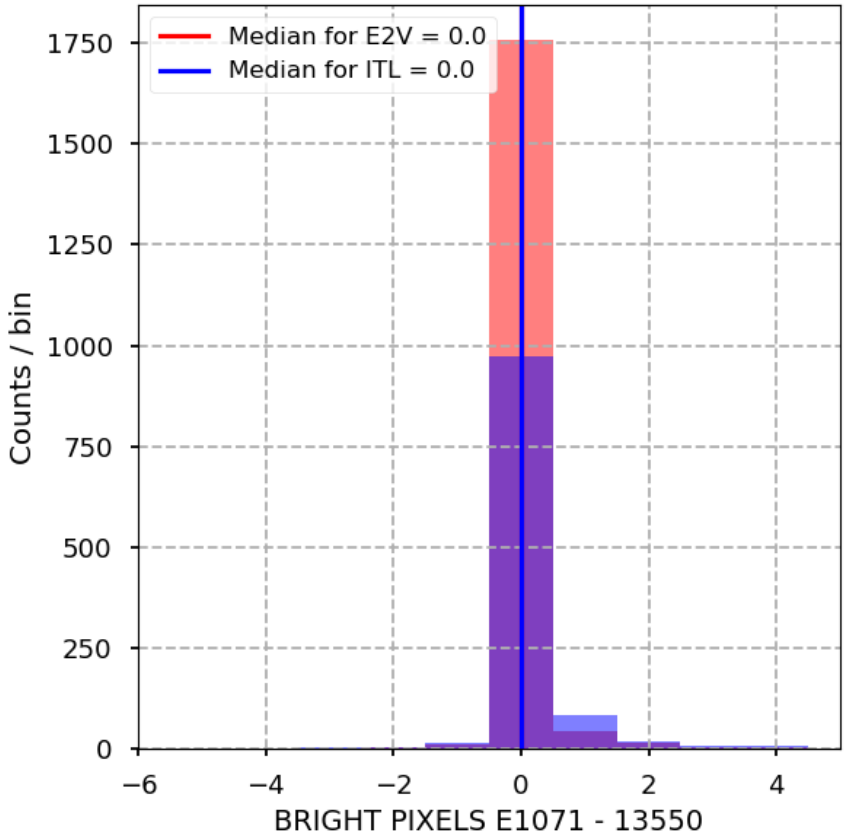

Figure 17: Distributions of differences in bright pixel count per amplifier between Run 7 (E1071) and Run 6 (13550), grouped by CCD type.

3.4 Flat pair metrics

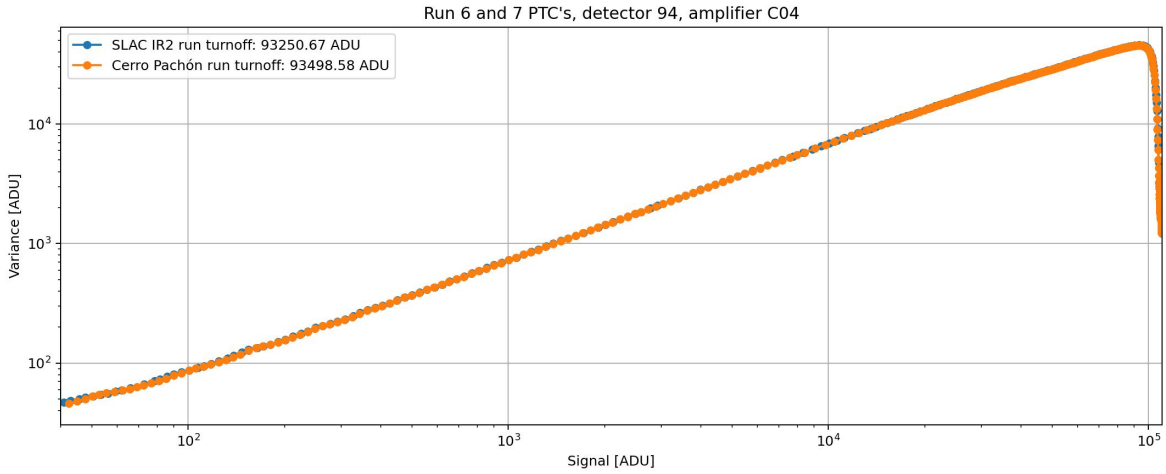

Figure 18: A comparison of Run 6 and Run 7 PTCs for a central amplifier.

3.4.1 Linearity and PTC turnoff

Linearity turnoff and PTC turnoff are two closely related metrics used to characterize the upper limit of the usable signal range for accurate shape measurements and photometry. Linearity turnoff is the signal level above which the PTC curve deviates from linearity and is measured for each amplifier segment of each CCD. We have defined the deviation threshold as 2%. PTC turnoff refers to the high-signal region of the PTC above which the PTC variance decreases with increasing signal. This is due to saturation within the pixel wells of the CCDs. While slightly different, both metrics provide important information about the upper limits of the dynamic range in our sensors. Linearity turnoff is measured in units of e^-, while PTC turnoff is measured in ADU.

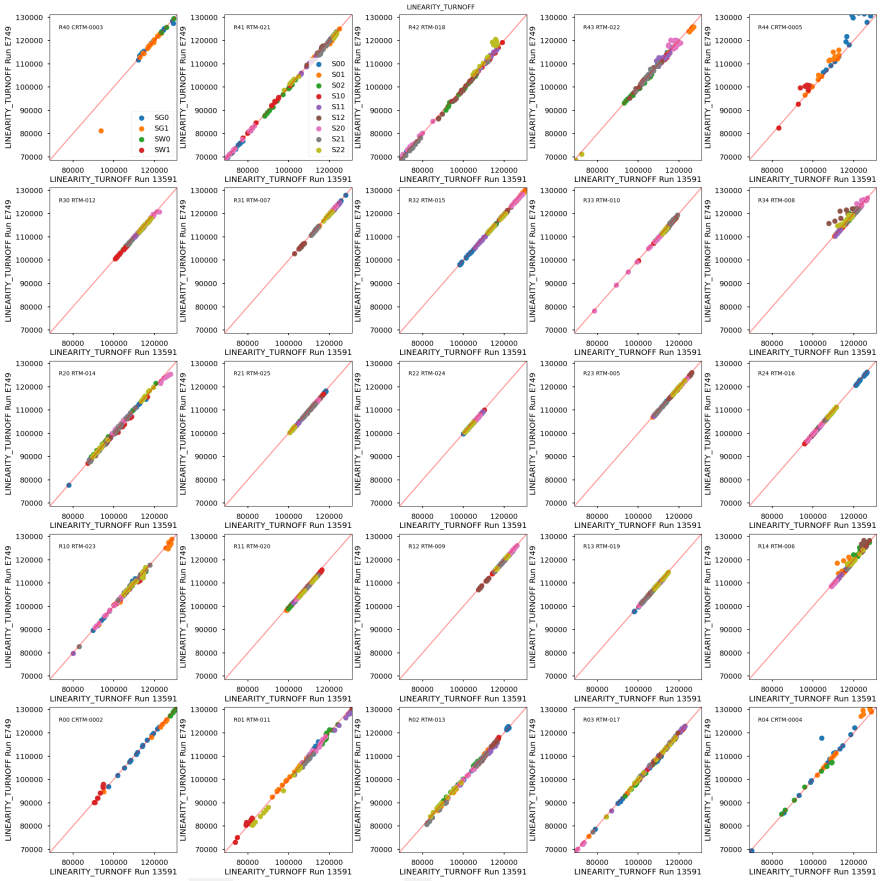

Figure 19: A comparison of Run 7 amplifier measurements of linearity turnoff, separated by sensor type. For both sensor types, measurements agree across both runs.

In our linearity turnoff measurements, we find close agreement between our Run 7 and Run 6 measurements for both ITL and e2v sensors.

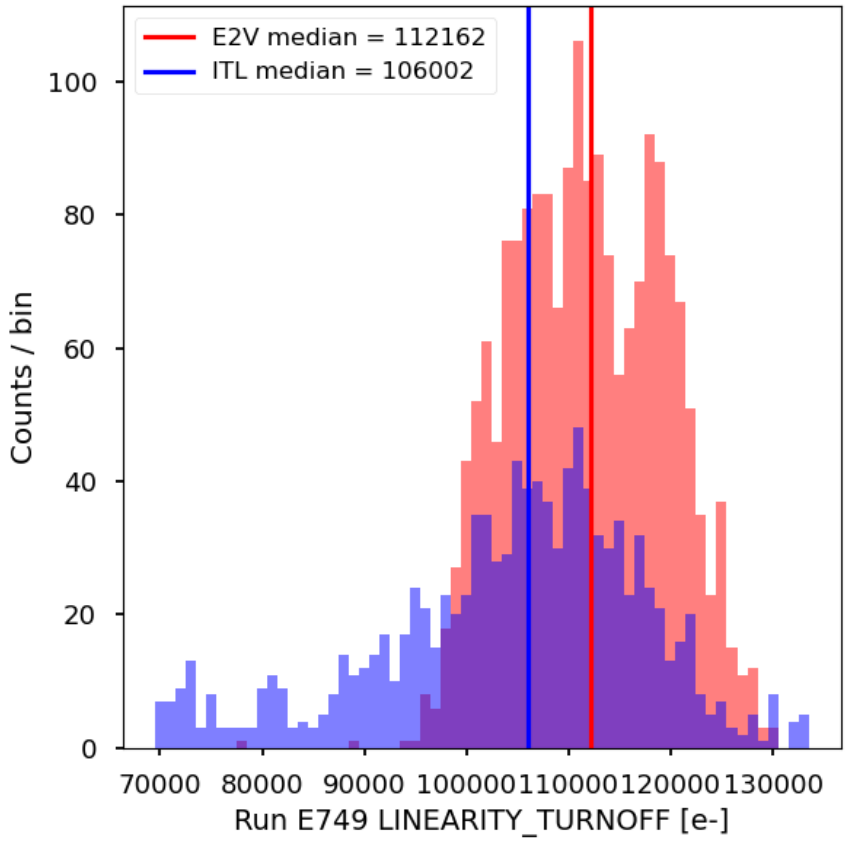

Figure 20: A comparison of Run 7 amplifier measurements of linearity turnoff, separated by sensor type. For both sensor types, linearity turnoff is above the 90k e- specification for a majority of amplifiers. A subset of ITL amplifiers are below the 90k e- threshold, while two e2v amplifiers are below that specification.

Run 7 PTC turnoff measurements agree closely between Run 6 and Run 7, differing by ≤ 200 e^- for both ITL and e2v sensors. Notably, they are lower on average for both detector types.

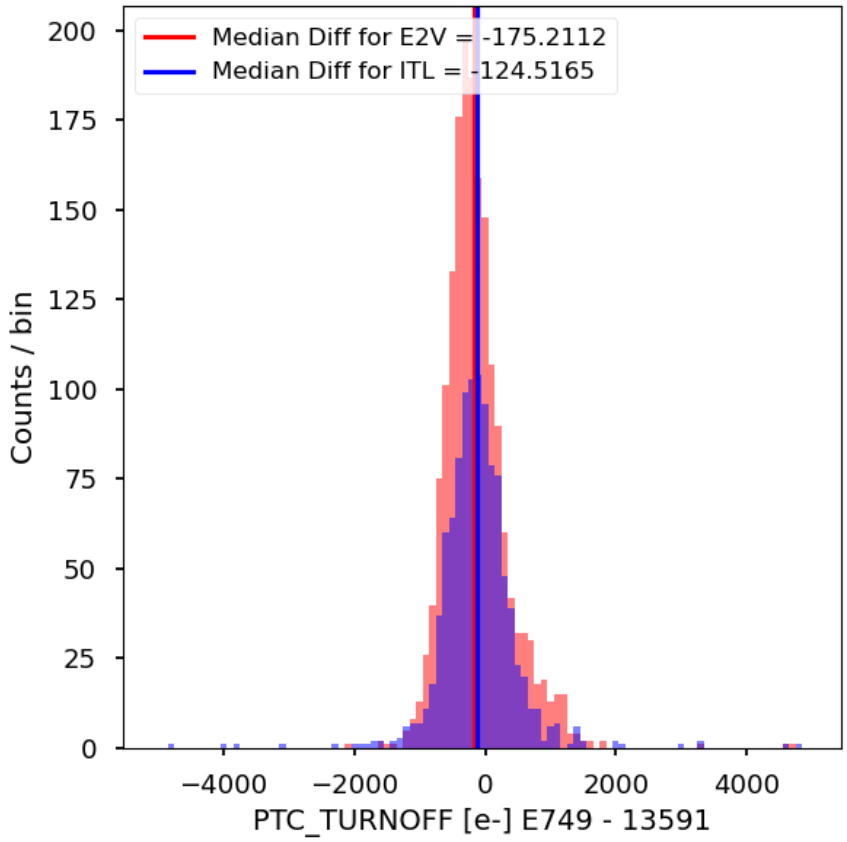

Figure 21: A comparison of Run 6 and Run 7 amplifier differences in PTC turnoff, separated by sensor type. For both sensor types, PTC turnoff is very consistent.

3.4.2 PTC Gain

PTC gain is the conversion factor between digital output signal and the the number of electrons generated in the pixels of the CCD. It is one of the key parameters derived from the Photon Transfer Curve, as it is the slope above the flux range at which the variance is dominated by shot noise, and below the PTC turnoff. Gain is expressed in e^-/ADU, and scales the digitized analog signals from the ASPICs to units of e^{-1}.

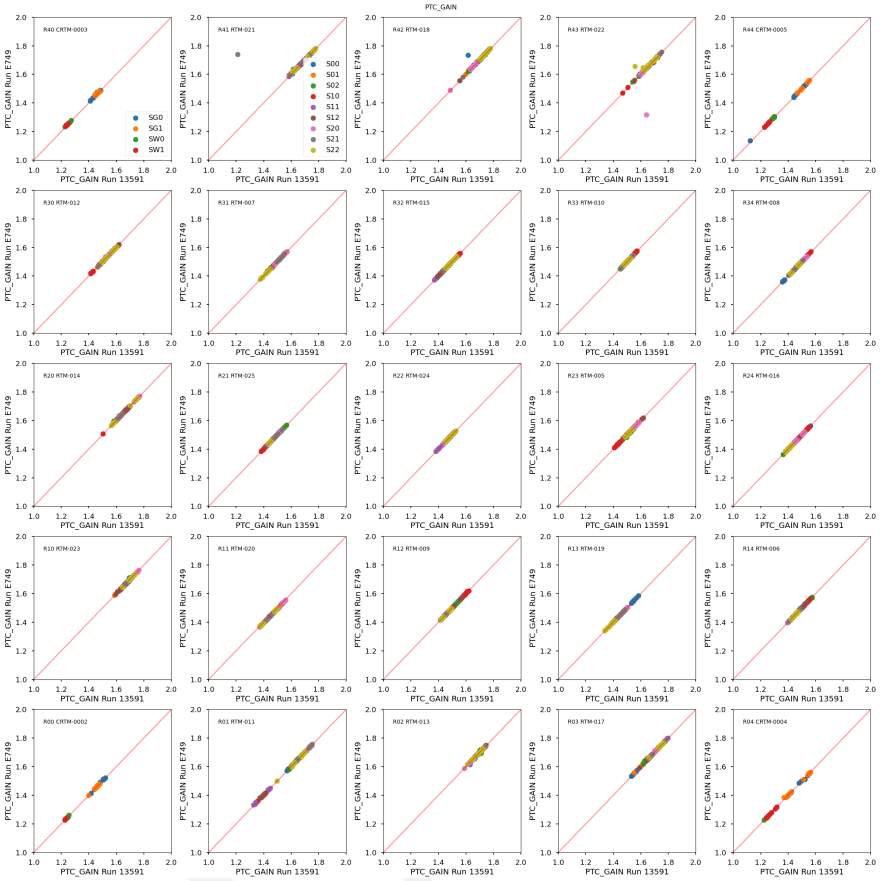

Figure 22: A comparison of Run 6 and Run 7 amplifier measurements in gain, separated by sensor type. For both sensor types, gain is very consistent.

PTC gain measurements agree extremely closely across all sensors in the focal plane.

3.4.3 Brighter fatter coefficients

The brighter-fatter effect in CCDs refers to the phenomenon where brighter sources appear larger (or ”fatter” than dimmer ones). This occurs due to electrostatic interactions within the pixel wells of the CCDs, when a pixel accumulates a high charge from incoming photons and creates an electric field that slightly repels incoming charge carriers into neighboring pixels. The brighter fatter effect can be modeled as the most dominant source of pixel-pixel correlations. Following the PTC model from [Astier] Astier et al. (2019), a_{00} describes the change of a pixel area due to its own charge content, or the relative strength of the brighter-fatter effect. Since same-charge carriers repel each other, the pixel area decreases as charge accumulates

inside the pixel well, which implies $a_{00} < 0$. Similarly a_{10} describes the area change cause by a pixel to its nearest serial neighbor, and a_{01} to the parallel nearest neighbor. Fig. 23 compares the measurement of these coefficients carried out at SLAC and at the summit. We see that the variations are modest (and could be explained by noise) except for two rafts: R10 and R11. The Run 6 data used for this comparison was acquired with a high voltage of 45V applied to these two rafts, rather than the usual 50V. The sensitivity of our measurements of the brighter-fatter coefficients is sufficient to detect the change of electrostatic conditions due to this change of drift field in the sensors. In `eo_pipe`, an absolute value is taken of the a_{00} parameter, so the tabulated quantities are positive.

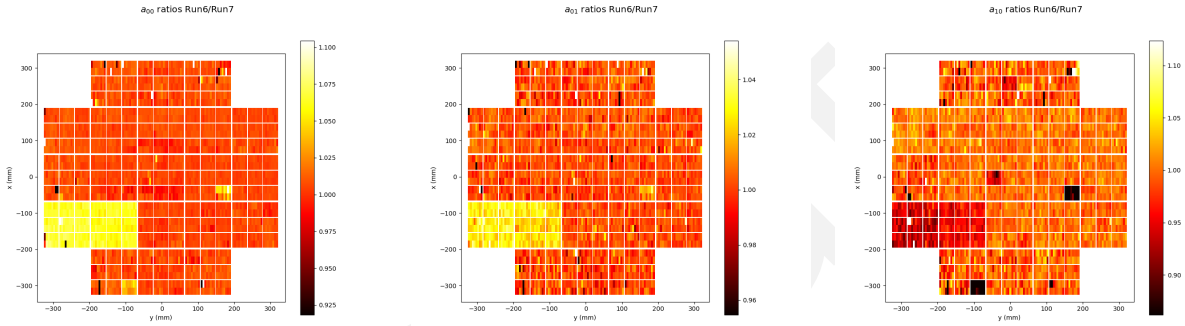

Figure 23: Ratio of amplifier measurements of a_{00}, a_{01} and a_{10} coefficients at Run 6 and Run 7. They are very consistent, except for two rafts (R10 and R11) where the high voltage was changed between the two runs. the sense

The distribution of difference of a_{00} measurements is displayed in Figure 24, and shows a tight agreement for both sensor types.

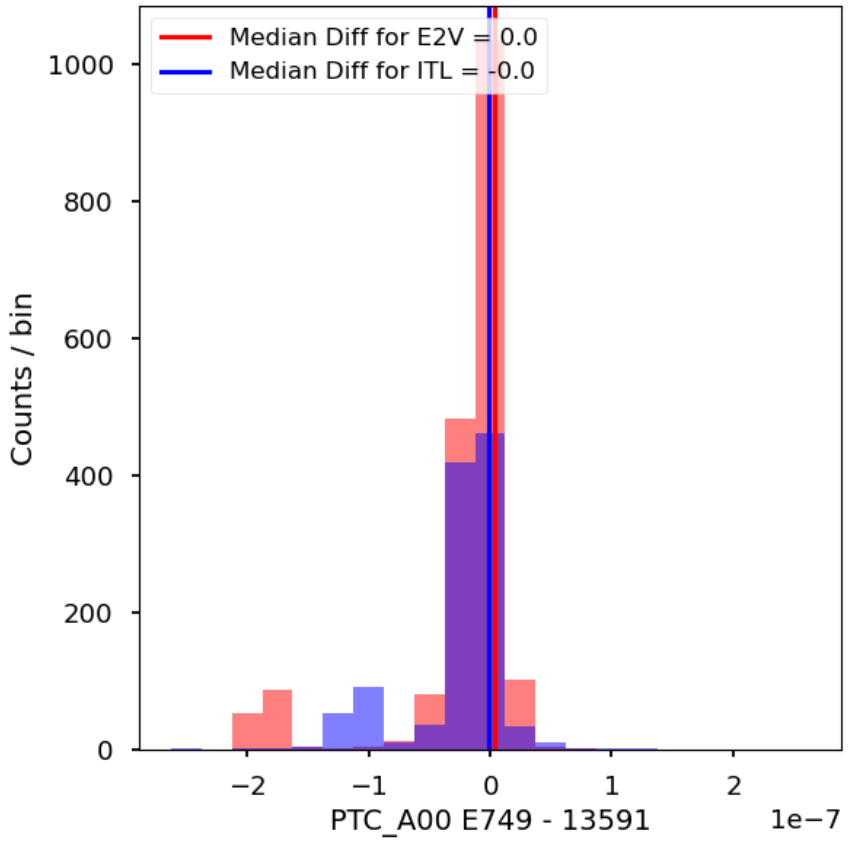

Figure 24: A comparison of Run 6 and Run 7 amplifier differences in the a_{00} coefficient, separated by sensor type. For both sensor types, the a_{00} coefficient is very consistent. The two peaks on the left represent the two outlier rafts visible on Figure 23. The a_{00} values are of the order of 2 to 3 10^{-6} e^{-1}.

However, the differences in the brighter-fatter a_{00} coefficient between Run 6 and Run 7 show that the magnitude of a_{00} decreased for most of the outliers, which implies an improvement in imaging for those pixels.

3.4.4 Row-means variance

Row-means variance is a metric that measures the mean row-to-row variance of differences between a pair of flats. By computing variance of means of differenced rows at each flux level, we can measure any changes in gain row-by-row and also changes in correlated noise along with row.

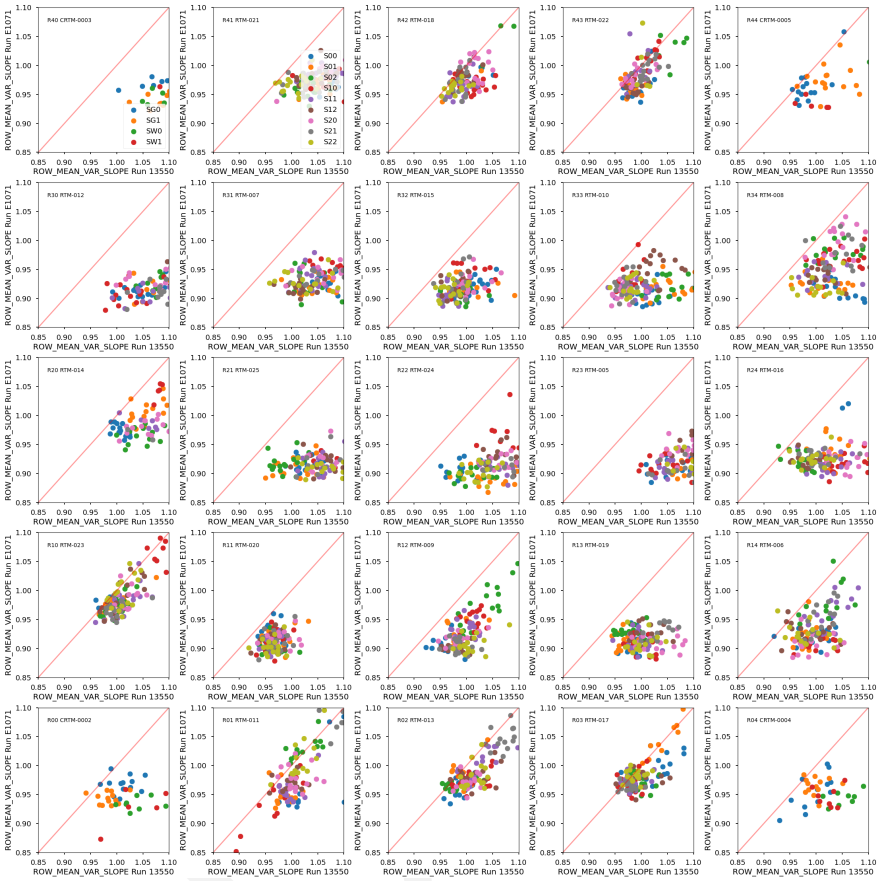

Figure 25: A comparison of Run 6 and Run 7 amplifier differences in row-mean-variance slope. For both sensor types, row-means-variance slope is weaker in Run 7. This is more pronounced for e2v sensors.

Differences in row-means variance between runs are evident, and are distinctly different for different detector types. The difference between runs is more significant for ITL sensors, ~9% smaller on average in Run 7. For e2v sensors, the effect is ~3% smaller in Run 7. This indicates that either row-by-row correlated noise or row-by-row gain change is less in Run 7b. Since we did not change the sequencer file, the most natural explanation is the row-by-row correlated noise. But further investigation is needed.

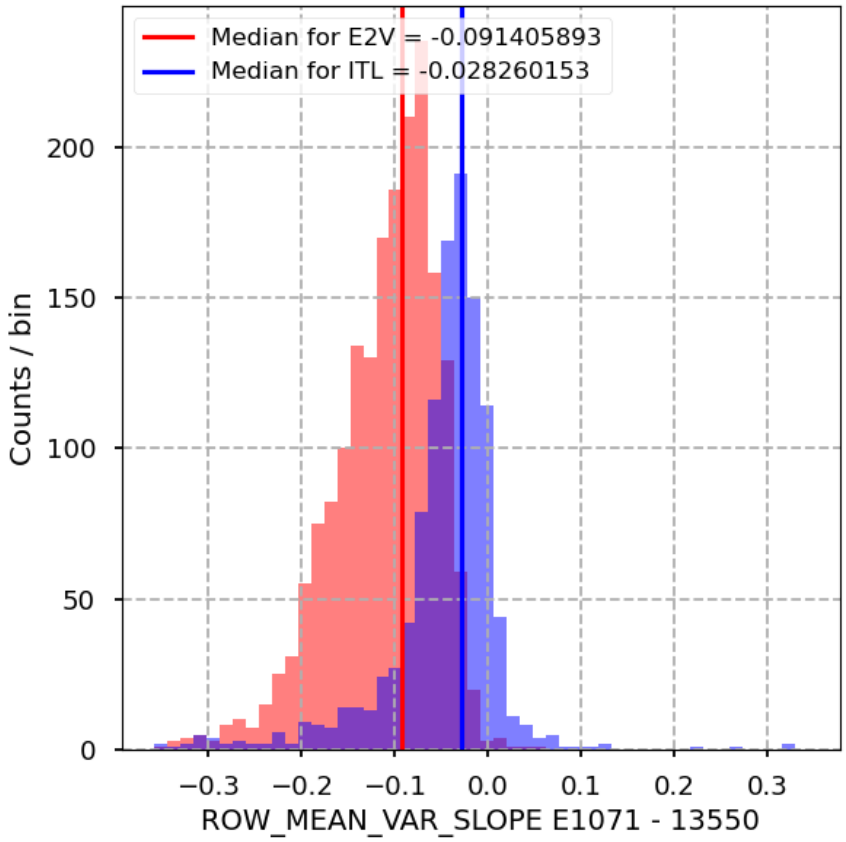

Figure 26: A comparison of Run 6 and Run 7 amplifier differences in row-mean-variance slope, separated by sensor type. For both sensor types, row-means-variance slope is weaker in Run 7. This is more pronounced for e2v sensors.

3.4.5 Divisadero Tearing

Divisadero tearing (or Rabbit ears) is manifested as signal variations near amplifier boundaries, connected features that are often jagged Juramy et al. (2020); Utsumi et al. (2024). These variations are on the order of ~1% relative to the flat field signal. To quantify divisadero tearing in a given column, we measure the column signal, and compare it to the mean column signal from flat fields.

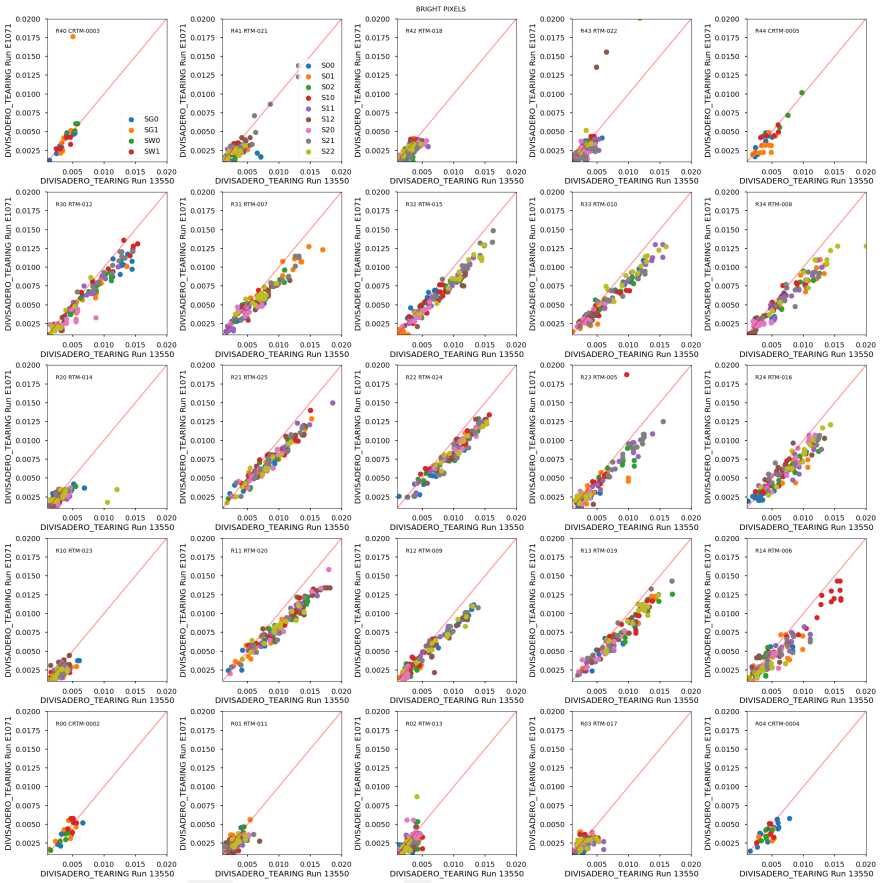

Figure 27: A comparison of Run 6 and Run 7 amplifier differences in Divisadero tearing, separated by sensor type. For both sensor types, Divisadero tearing is weaker in Run 7. The difference is more pronounced for e2v sensors, which have larger Divisadero tearing in general.

Divisadero tearing is broadly consistent between Run 6 and Run 7, with both sensor types demonstrating lower Divisadero tearing in Run 7. Taking amplifier differences, e2v sensors show a weaker Divisadero signal in Run 7 by 0.1%, while ITL sensors demonstrate a weaker Divisadero signal in Run 7 by 0.05% (see Fig. 28).

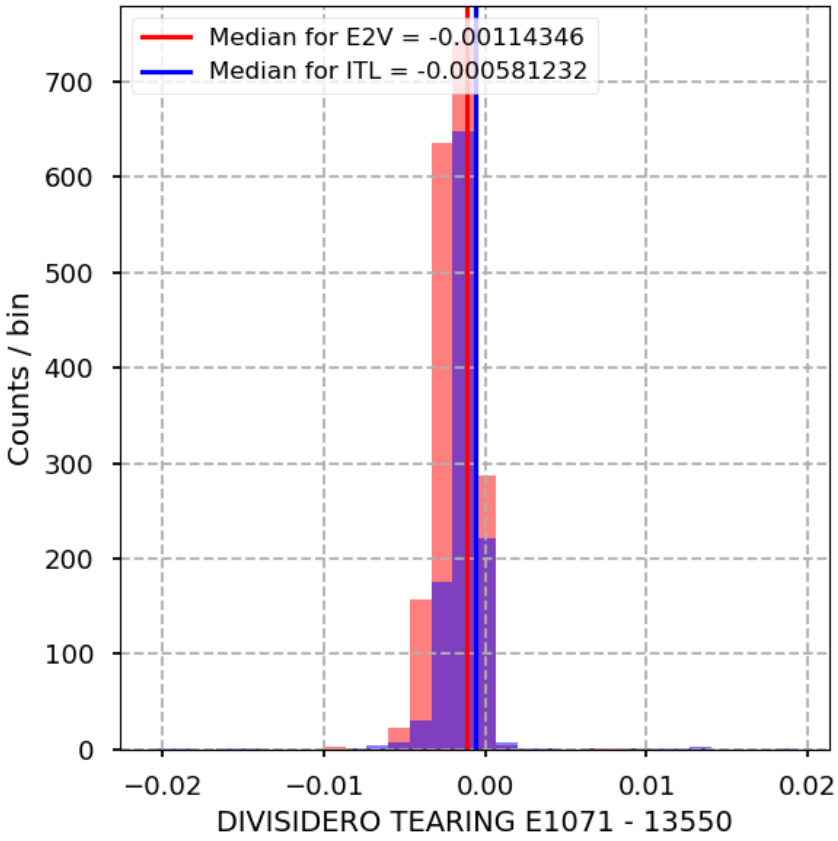

Figure 28: A comparison of Run 6 and Run 7 amplifier differences in Divisadero tearing, separated by sensor type. For both sensor types, Divisadero tearing is weaker in Run 7.

3.4.6 Dark defects

Dark defects are localized regions or individual pixels that produce abnormally low signal levels, even in the presence of light. Similar to bright pixels, dark pixels are also quantified in dark columns over 50 pixel contiguous regions. These defects are caused by imperfections in the semiconductor material, imperfections during the manufacturing process of a CCD. For our evaluation, we extract dark pixels from combined flats, with the threshold for a dark defect defined as a −20% deficit from the average flat field flux measured in the image segment.

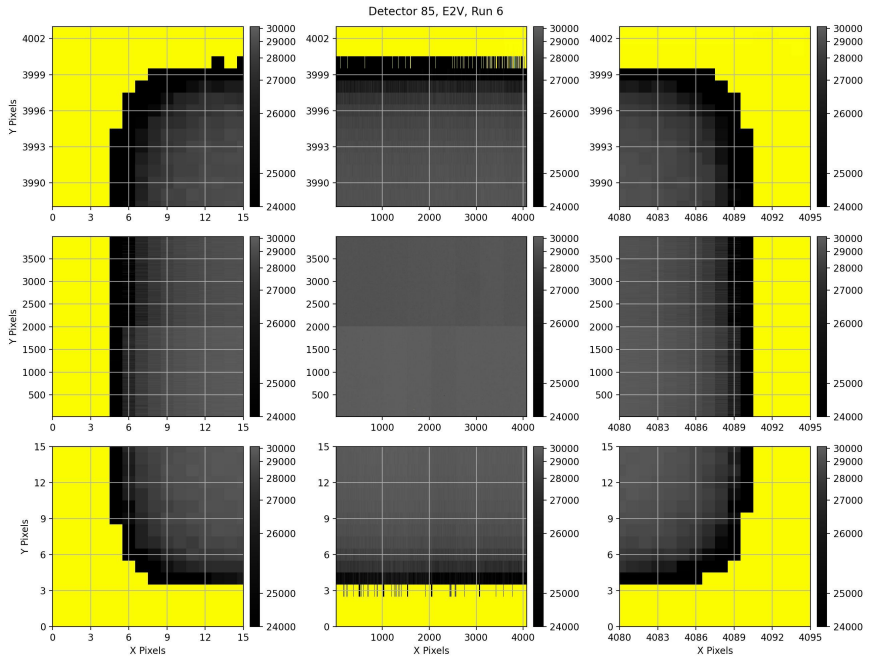

Figure 29: Illustration of masked border pixels (yellow) for detector 85 (R21_S11). The average defect mask size is 4 pixels along the serial (x-pixel) direction, and 5 pixels along the parallel direction. Additional dark defects exist in the sensor, but are difficult to quantify due to the overwhelming contribution from the picture frame response.

The eo-pipe configuration for evaluating dark defects considers a border pixel region that is masked differently from the dark pixels. The default size for this edge is zero pixels. With a zero pixel border mask, the average dark defect count is 1800 per amplifier, with ≥95% of the contribution coming from the picture frame. The 'picture-frame response' (also called 'edge roll-off') near the edges of the sensors is due to a decrease in the pixel active area. It is difficult to extract useful information about the dark defects in the focal plane without excluding the picture frame. The effects of the picture frame signal on dark defect masking is shown in figure 29.

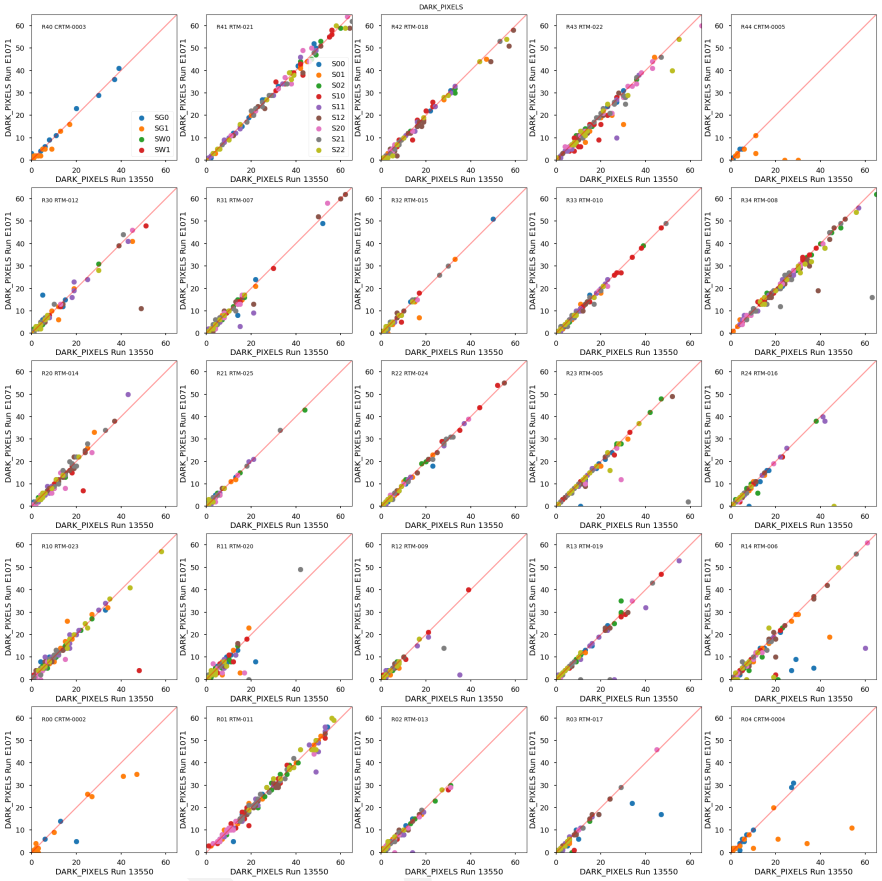

Figure 30: Comparison of dark pixel counts in Run 7 (E1071) and Run 6 (13550), with separate plots for each raft. Within each plot the color coding for all amplifier segments in a given CCD is the same.

The default eo-pipe configuration has no border masking. The largest region permitted for the picture frame region is 9 pixels, determined by LCA-19363. Using a 9 pixel mask, the picture frame signal is removed, leaving true dark defects to be measured without contamination.

In both instances, the contamination of dark pixels across the focal plane is ≤10 pixels per amplifier on average. There is a measurable improvement in the dark pixel counts, decreasing by one pixel per amplifier between Run 6 and Run 7.

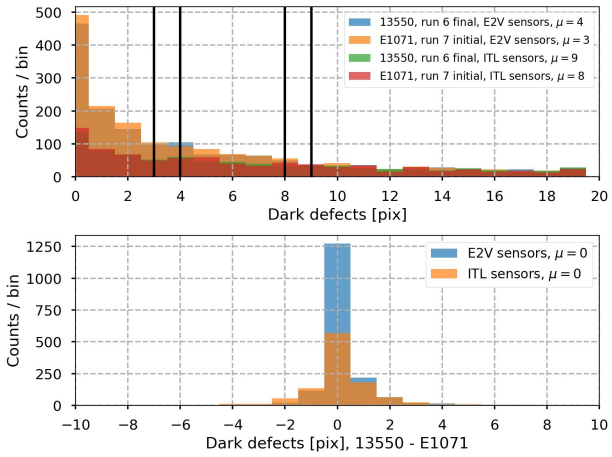

Figure 31: Comparison of dark pixel counts in Run 7 (E1071) and Run 6 (13550). Top: A histogram of amplifier measurements, separated by run number and sensor type. Bottom: A histogram of the amplifier dark pixel count differences, the difference is taken as the measurement from Run 6 and the measurement from Run 7.

3.5 Persistence

Persistence is a feature of CCDs and how they are operated involving charge trapped in the surface layer after high-flux exposures (Banovetz et al., DMTN-276; Utsumi et al., 2024). Persistence is described in detail in Section 4.1. Here we consider the measurements taken as part of a persistence measurement task in the typical B protocol. For measuring persistence, a high-flux acquisition is taken, followed by a sequence of dark images. The persistence signal has been observed to decrease in subsequent dark images as the trapped charge is released (see Figure 32 for an example). As a metric for persistence, we evaluate the difference between the residual ADU in the first dark image and the average of the residual ADU in the final dark images. This residual signal is found to be ~10 ADU.

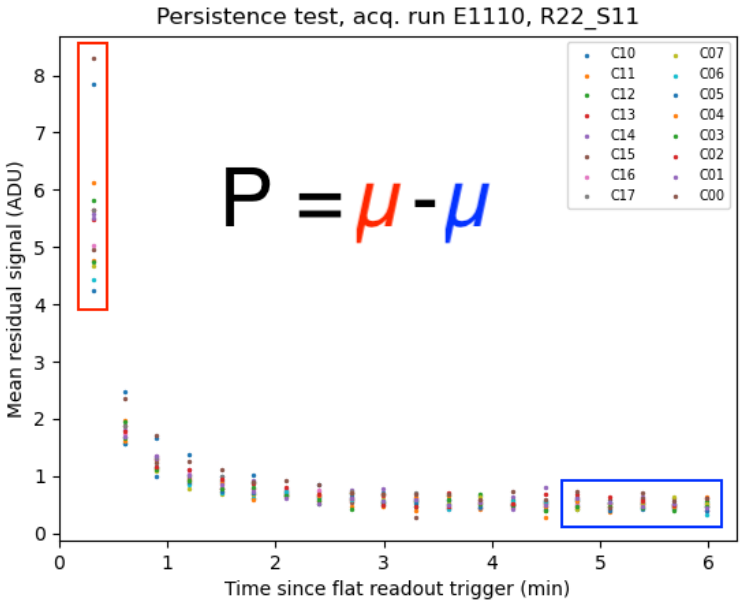

Figure 32: Persistence signal observed in R22_S11 in Run 7 (E1110) as a function of time after the high-flux flat image. The color coding indicates the individual amplifier segments. The persistence metric is defined as the residual signal in the first dark image after the flat acquisition (red box). Note that over time the signal does not decay entirely to zero.

In the initial Run 7 measurements, we had not changed any operating parameters of LSSTCam, so we would expect persistence to still be present images at the same level as in Run 6.

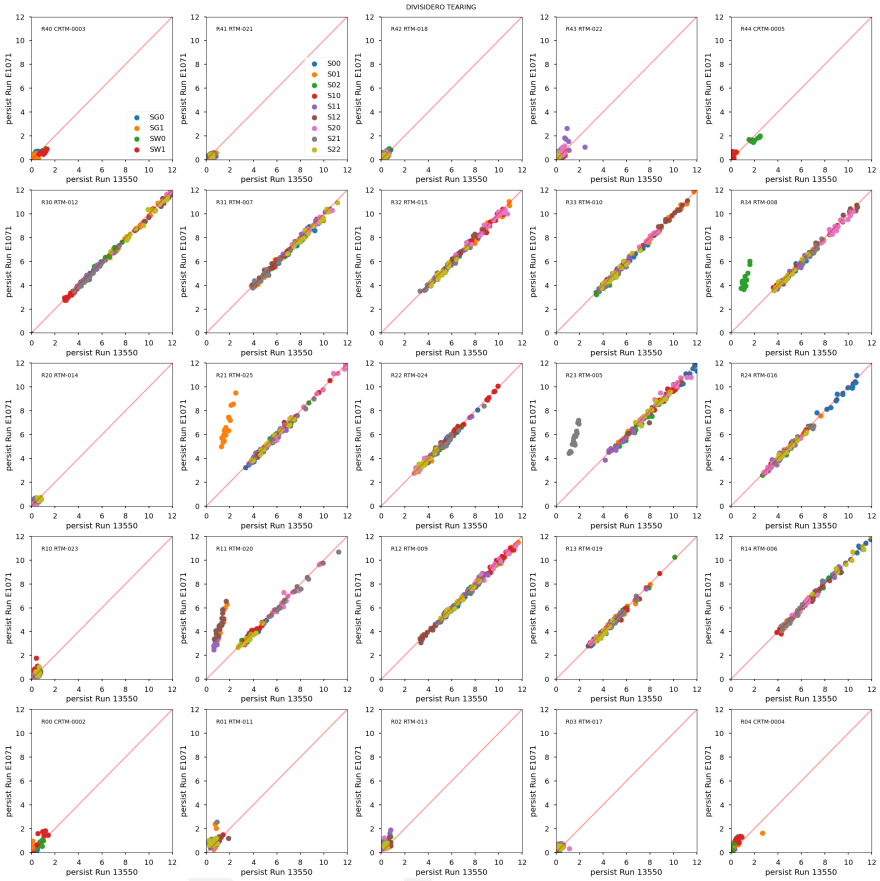

Figure 33: Comparison of persistence metric between Run 7 (E1071) and Run 6 (13350), organized by raft. The color coding indicates individual CCDs. Several e2v CCDs have markedly greater persistence in Run 7.

The persistence signal is generally consistent in e2v sensors between Run 6 and Run 7. Several e2v CCDs have greater persistence metric value in Run 7 (Fig. 33). The outliers in these persistence measurements are due to higher initial residual ADU, resulting in an excess of ~5 ADU when comparing Run 6 with Run 7 (see Fig. 34).

3.6 Differences between Run 6 and Run 7

All camera performance metrics from the summit show close agreement with SLAC IR2 tests. PTC/full-well metrics were consistent, and no significant bright cosmetic defects developed. Dark cosmetic defects are difficult to quantify due to the edge sensor effects, though the consistency in CTI measurements would indicate that dark defects did not change from previous

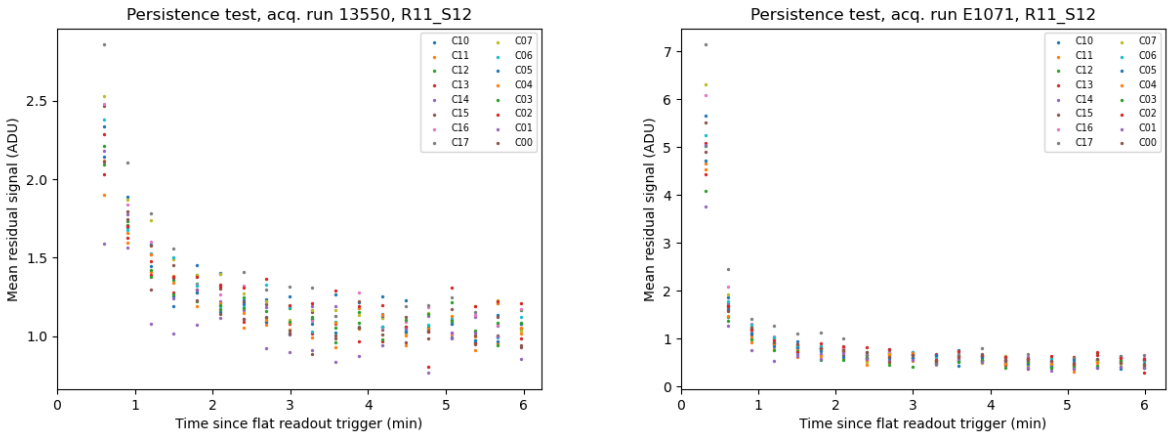

Figure 34: Comparison of persistence profiles for R12_S21 between (left) Run 6 (13550) and (right) Run 7 (E1071). The decay time constants are similar but the initial persistence level is greater in Run 7. The asymptotic levels are also slightly different.

runs. Dark current and Divisadero tearing show improved performance compared to Run 6, while the Persistence feature is still prominent in e2v sensors.

Parameter [unit]	Specification	e2v		ITL	
		Run 6	Run 7	Run 6	Run 7
Serial CTI [%]	Val	3.7068E-5	1.1357E-5	1.1488E-4	1.6478E-4
Parallel CTI [%]	Val	1.2162E-5	1.1534E-5	3.4067E-7	-4.7849E-6
Dark current [e-/pix/s]	Val	5.5439E-2	2.4783E-2	4.6424E-2	2.1217E-2
Bright defects [count]	Val	0	0	0	0
Linearity turnoff [e-]	Val	156,339	167,797	172,580	178,154
PTC turnoff [e-]	Val	126,002	132,963	117,019	128,595
PTC Gain [e- / ADU]	Val	1.4785	1.4811	1.6717	1.6760
PTC a_{00} [$\frac{1}{pix^2}$]	Val	3.0854E-6	3.0863E-6	1.7119E-6	1.7031E-6
BF x-correlation	Val	0.5236	0.5169	0.7155	0.7521
BF y-correlation	Val	0.1785	0.1707	0.2859	0.2869
Row-means variance	Val	0.9927	0.8836	0.9924	0.9466
Dark defects [count]	Val	4	3	9	8
Divisadero tearing maximum [%]	None	0.32709	0.27348	0.75191	0.62622
Persistence [ADU]	None	5.6673	5.6435	0.48018	0.42051

Table 3: Comparison of the median values of different parameters between Run 6 and Run 7, separated by detector type. For this comparison, only science detectors are considered.

4 Camera Optimization

4.1 Persistence optimization

Leftover signal ("persistence") in the first dark image acquired after intense illumination has been observed **??**. Persistence has been observed in an early prototype e2v sensor as early as 2014 (Doherty et al., 2014). It was confirmed that the amplitude of the persistence decreased as the parallel swing voltage was decreased. This is consistent with the persistence being a Residual Surface Image (RSI) effect as described in (Janesick, 2001), i.e., the excess charges are being trapped at the surface layer. The level of persistence is about 10–20 ADU, and the decay time constant is about 30 s (Banovetz et al., DMTN-276).

During the EO testing in 2021 (Run 13177, for example) Run 5, we also found the persistence made a streak toward the readout direction from the place where a bright spot illumination occurred in a previous image. We call this "trailing persistence".

As noted in Section (ref. tearing section above), depending on operating conditions e2v sensors have another major non-ideality, so-called "tearing", which is considered a consequence of the non-uniform distribution of holes. Over the past few years, our primary focus in the optimization of the operating parameters was mitigation of the tearing, and we successfully eliminated the tearing by changing the e2v voltages from unipolar (both parallel rails high and low are positive) to bipolar (the parallel high is positive, and the low is negative) following the Bipolar voltage formula [1]. However, the persistence issue remained unchanged.

For the persistence issue, if this is a residual surface image, two approaches could be taken as discussed in (Utsumi et al., 2024): either 1) establishing the pinning condition where the holes make a thin layer at the front surface so that the excess charges recombine with the holes, or 2) narrowing the parallel swing so that the accumulated charges in the silicon do not get close to the surface state.

The pinning condition could be established by decreasing the parallel low voltage to as low as -7 V or lower. The transition voltage needs to be empirically determined. However, Teledyne e2v advised that the measured current flow increases as the parallel low voltage is decreased, which increases the risk of damaging the sensor by inducing a breakdown[2]. Also, the excess charges could be recombined by the thin layer of the holes, which could affect linearity at high

[1] https://github.com/lsst-camera-dh/mkconfigs/blob/master/newformula.py

[2] We note that ITL operates at a parallel low voltage of −8.0 V. We have observed the increased current flow. But we have software protection so that the current does not increase too much.

flux levels when charges start to interact with the holes.

The parallel swing determines the full-well. Depending on whether the accumulated charges spread over the columns or interact with the surface layer, there are blooming full-well regimes and the surface full-well regime. A full-well level between these two regimes is considered to be optimal (Janesick, 2001), with no persistence and dynamic range as great as possible. Because we observe the persistence effect, we likely operate the sensor in the surface full-well condition and we need to decrease the parallel swing to get the blooming full-well or the optimal full-well. The obvious downside decreasing the full-well capacity.

The sensor control voltages are defined relative to each other. Changing, e.g., the parallel swing also requires changes to all other voltages to operate the sensor properly, e.g., to properly reset the amplifier. The initial voltages were given in the original Bipolar formula but to decrease the parallel swing we had to switch to the new persistence mitigation formula in order to satisfy the constraints[3]

Snyder et al. (2024), set up a single sensor test-stand at UC Davis. They attempted multiple different approaches mentioned above and reported the results[4]. The summary is as follows:

- The new voltages following the persistence mitigation voltage rule produces reasonable bias, dark, flat images visually.
- Narrowing the parallel swing eliminates the persistence.
- Lowering the parallel low voltage did not work as we expected; going to a more negative voltage is probably needed.

Note that the e2v sensor in the UCD setup did not exhibit persistence. This might be due to the characteristics of the sensor, or perhaps the differences in the electronics (e.g., the long cable between CCD and REB). They need to move the both parallel high and low up to reproduce persistence as the similar as the main Camera.

[3]Persitence mitigation voltage: https://github.com/lsst-camera-dh/e2v_voltages/blob/main/setup_e2v_v4.py

[4]Davis report: https://docs.google.com/document/d/1V4o9tzKBLnI1nlOlMFImPko8pDkD6qE7jzzk-duE-Qo/edit?tab=t.0#heading=h.frkqtvvyydkr

4.1.1 Persistence optimization

Based on this test result, we decided to test the new voltages with the narrower parallel swing on the LSSTCam focal plane. Keeping the parallel low voltage at -6 V in order to operate the sensor safely (very conservative limit), we changed the parallel swing voltage from 9.3 V to 8.0 V as well as all the other voltages using the new formula. We overexposed the CCDs and took 20 darks afterward. Figure 35 compares the mean and median of pixel-by-pixel differences between the first and the last dark exposures, as a function of the parallel swing (We note that this is not the persistence metric defined in Sec. 2.5. but almost identical). As the parallel swing is decreased, the residual signal decreases, reaching roughly 10× less than the original level at 9.3 V. Although we sampled at 8.0 (E1363), 8.4 (E1430), 8.65 (E1411), 8.8 (E1424)and 9.3 V (E1110), 8.0 V appears to work the best and could be lower with the penalty of decreasing the full-well capacity.

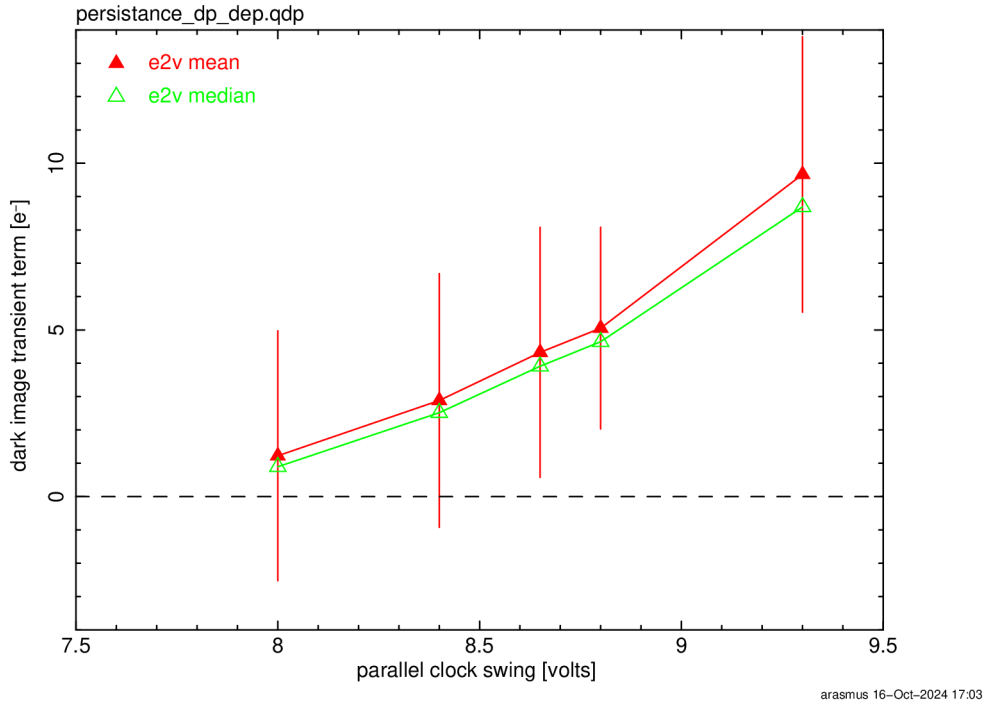

Figure 35: The remaining charges measured in every amplifier but aggregated by mean and median as a function of the parallel clock swing are shown.

Figure 36 displays how the persistence is reduced by the parallel swing decrease. The images were processed with the standard instrumental signature removal and assembled in the full

focal-plane view. The dark exposure was taken right after a 400 ke-equivalent flat exposure. The figure shows the distinct pattern of elevated signal associated with the e2v sensors, which fill the inner part of the focal plane.

The right-hand figure shows the same dark exposure but taken with the narrow parallel swing voltage of 8.0 V. The distinct pattern goes away. This demonstrates the persistence in e2v sensors becomes the (low) level of the ITL sensors.

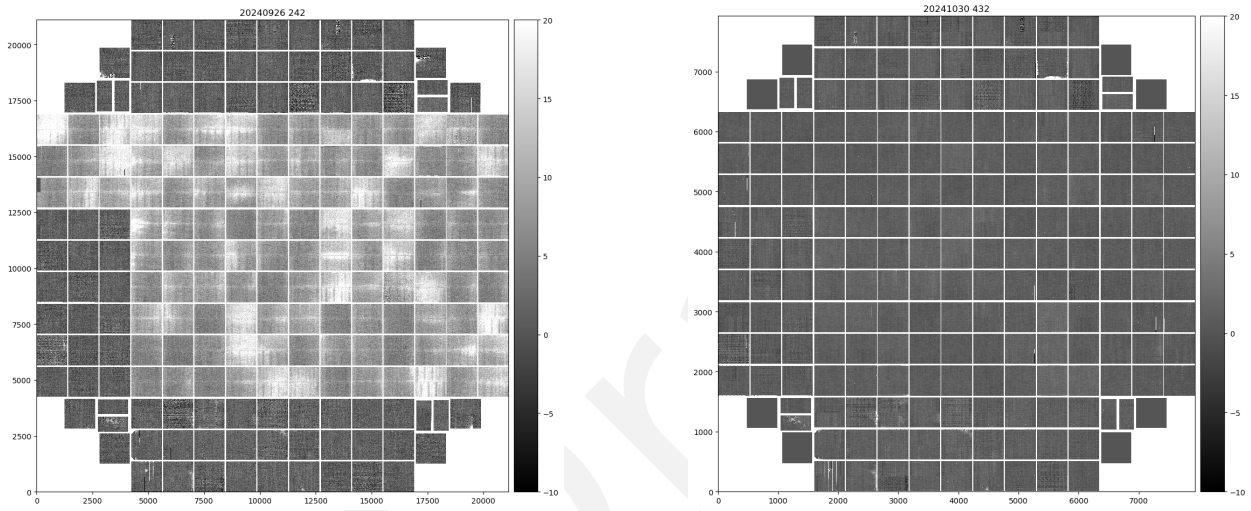

Figure 36: Comparison of dark exposures under different parallel swings. (left) The first dark exposure after a 400 ke$^-$ flat image under the parallel swing of 9.3 V (Run E1110); (right) The first dark exposure after a 400 ke$^-$ flat image under the parallel swing of 8.0 V (Run E1880). The figure shows no distinct patterns from persistence in e2v sensors. Note that the guide sensors were not displayed here because they were being operated in guider mode. Also some of the residuals in ITL caused by defects disappeared here because of the employment of the new sequencer file (v30).

4.1.2 Impact on full-well

Reduction of the full well is expected from narrowing the parallel swing voltage. This subsection explores how much reduction in the PTC turnoff is observed in the dense PTC runs. Two runs were acquired with identical setting except for the CCD operating voltage (E1113 for 9.3 V and E1335 for 8.0 V). As the PTC turnoff is defined in ADU, it needs to be multiplied by PTC_GAIN to compare the turnoff values in electrons. Figure 37 compares the PTC turnoffs in electrons and also shows their fractional difference. The median of each peak are 133065e-, 102728e-, and the median reduction was 22%.

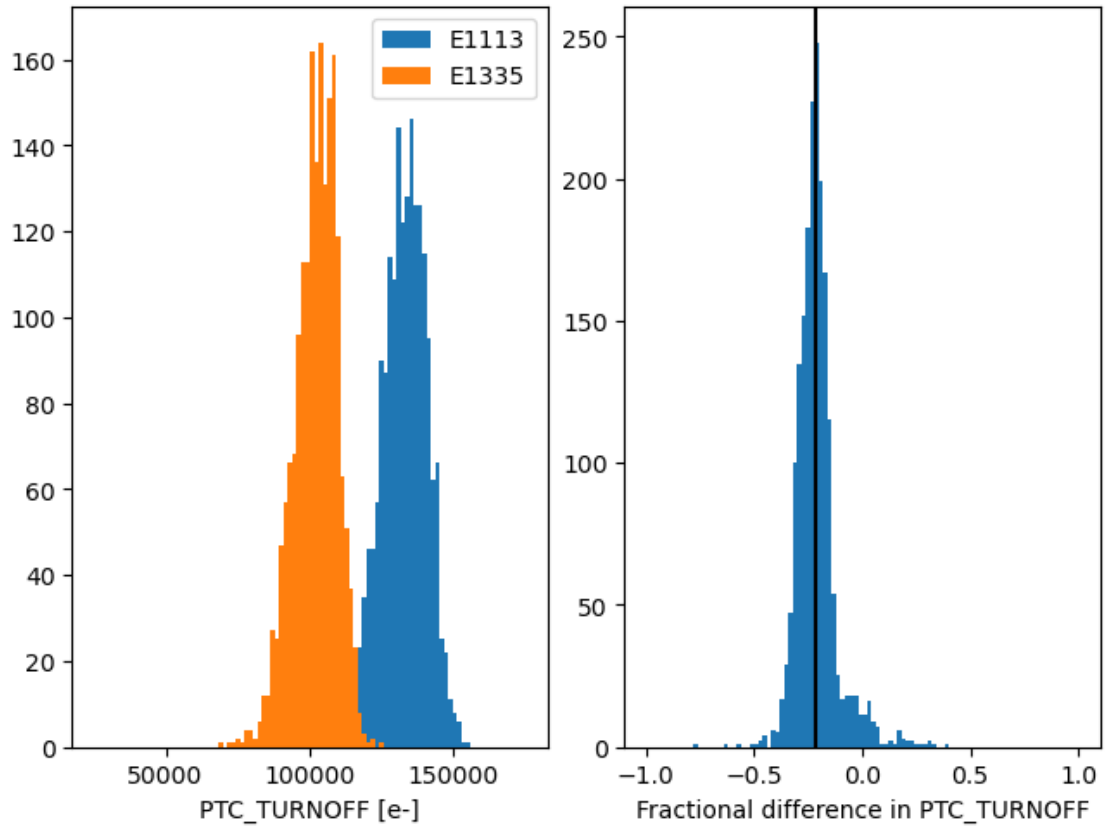

Figure 37: Histograms of the PTC turnoff values scaled to electron units (left) and the ratios of differences (right) between E1113 (9.3 V) vs E1335 (8.0 V). The median of the reduction is 22%.

4.1.3 Impact on brighter-fatter effect

Reducing the parallel swing is expected to enhance the brighter-fatter effect (BFE), possibly in an anisotropic way. The BFE can be characterized via the evolution of the variance and covariances of flat field exposures as a function of flux, i.e., via a PTC analysis. To evaluate the impact of reducing the parallel voltage swing on e2v sensors, we acquired two series of flat field exposures with the respective voltage setups and extracted the "area" coefficients a_{ij} (Equation (1) in Astier & Regnault (2023)). The area coefficients describe by how much a unit charge stored in a pixel will alter the area of some other pixel (or itself). We find that reducing the parallel swing from 9.3 V to 8.0 V typically increases the area coefficients by 10% (between 5 and 19% depending on distance indexed by i, j), and the increase is almost isotropic (i.e., very similar along serial and parallel directions; see Fig. 38). From these measurements, we anticipate that the increase of star sizes with flux in LSST data will not become more anisotropic at 8.0 V than it was at 9.3 V, and hence this reduction of parallel swing does not risk increasing systematic uncertainty of the PSF ellipticity.

4.2 Sequencer Optimization

Several efforts were undertaken to optimize the sequencer configurations during Run 7. The following points summarize the key investigations:

- **Clear**: Addressing the leftover charges at the image/serial register. The discussion is provided in Section 4.3:
- **Whether toggling the RG output during the parallel transfer for the e2v sensors is needed or not.**: Given the fact that there was some impact on making the bias structure in ITL better. The same question was raised for e2v sensors. The detail is described in Section 4.4
- **Whether keeping the IDLE_FLUSH running or not**: Addressing the worsening of the Divisadero tearing. The detail is described in Section 4.5
- **Phase overlap during parallel transfer for e2v**: e2v sensors feature four parallel phases. To improve the uniformity of the full well across a sensor, overlapping two phases during each time slice of the parallel transfer was introduced.
  - Sequencer files that are based on the regular v29 but have changes in the parallel

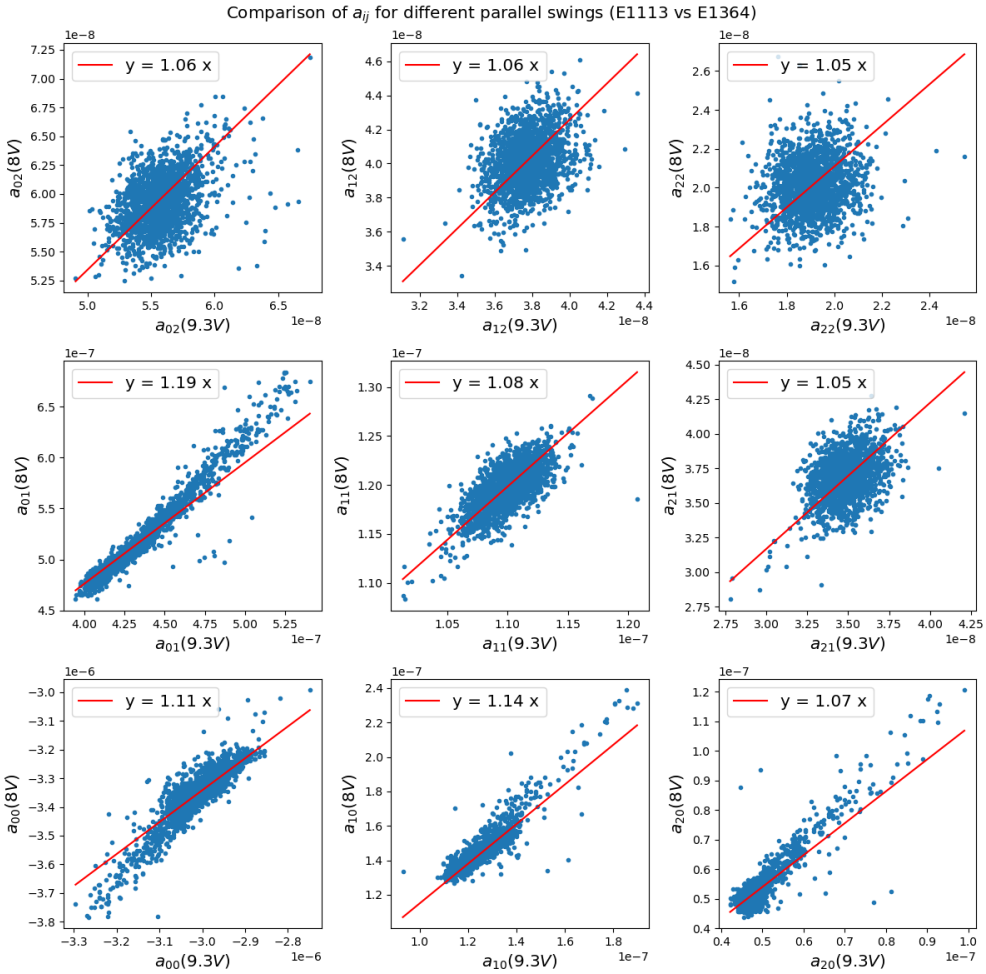

Figure 38: Scatter plots of area coefficients a_{ij} (one entry per amplifier) measured at 8.0 V and 9.3 V. The sub-figures correspond to separations in rows (j) and columns (i) between the source of the area distortion and its victim, with the self interaction coefficient a_{00} at the bottom left. The first neighbors increase respectively by 19% in the parallel direction by 14% in the serial direction. So the BFE is slightly larger at 8.0 V but not dramatically more anisotropic: the ratio of parallel to serial nearest neighbor correlations increases only from 3.43 to 3.54 with the reduction of the parallel swing.

transfer by having a half overlap of what it was in the original (_halfoverlapping.seq), a small amount of overlap compared to what it was in the original (_overlap113.seq), ero overlapping at all (_nonoverlapping.seq) are created.

- This overlap is known to cause trailing persistence, as reported in the Davis Report. We conducted several runs using both half overlapping (E1245) and non-overlapping (E1396) sequencers but we have not studied these because the trailing persistence is no longer a concern by optimizing the operating voltages to avoid charge trapping.

4.3 Improved Clear

4.3.1 Overview

In this section, we describe the work done during Run 7 to improve the image clear prior to collecting a new exposure.

The problem we wanted to address is the presence of residual charges in the first rows read for an image taken just after the clear of a saturated image. These "hard to clear" charges are associated with highly saturated flats or columns (or stars as observed in AuxTel or ComCam), which leave signal in the first row of the subsequent exposure. The effect has a sensor-specific signature:

- In all ITL CCDs (except in R01_S10 for which the effect is much more significant and which will be addressed later in this section): After a very bright exposure that saturates the overscan, the first row of the subseqeunt image has residual charges which are close to saturation. In most cases a small leftover signal in the second row is also present.
- In e2v CCDs: the first row read after an exposure that follows an exposure with saturated overscan, has residual charges which are close to saturation, and a significant signal is visible in the subsequent 20–50 rows (see left-hand plot in Figure 39). The effect is slightly amplifier dependent.

These leftover electrons are not associated with what we usually call residual image or persistence. They are suspected to be associated with pockets, induced by the electric field configuration in the sensor and the field associated with saturated pixels. Investigation has revealed

that only the first exposure taken after an image with saturated overscan is impacted. Our standard clear is not able to flush away those charges, while a standard readout of $\gtrsim 2000$ rows does remove them. There is a chance that a change of the electric field (e.g., a change in the clocking scheme defined in sequencer files) can remove the pockets, and free the charges, allowing them to be cleared.

The location of these uncleared electrons in the first row of the CCDs indicates that the interface between the image area and the serial register is the location of the pockets. For this reason we investigated changes in the electric field configuration of the serial register during the clear, to avoid generating pockets at the image-serial register interface.

To address this clear issue, we focused on updating the serial register field as the rows are moved into it. The constraint is that the changes introduced should not significantly increase the clear execution time. It should be noted that in 2021 we tried a sequencer called "Deep Clear" [sequencerV23_DC] as a first attempt to address the clear issue; it added one full row flush on top of the existing one at the end of the clear. This sequencer did improve the clear, but did not fully fix the clear issue (see Table 4).

Table 4: Clear methods used so far.

Clear Type	Duration (ms)	e2v after Saturated Flat	ITL after Saturated Flat	R01_S10 ITL "unique"
Default Clear 1 clear (seq. V29)	65.5	First row saturated signal up to row 50	1st row saturated signal up to 2nd row	First 500 rows saturated for 4 amp, 13 amp with signals
Multi Clear 3 clears (seq. V29)	196.5	No residual electrons	No residual electrons	First 150 rows saturated for 2 amp, 5 amp with signals
Multi Clear 5 clears (seq. V29)	327.4	No residual electrons	No residual electrons	First 100 rows saturated for 2 amp, 2 amp impacted
Deep Clear 1 clear (Seq. V23 DC)	64.69	1st row saturated signal up to row <20	Tiny signal left in the first row	not measured
No Pocket (Nop) 1 clear (seq. V29)	65.8	signal up to row 20	No residual electrons	First 1000 rows saturated for 16 amp, 16 amp with signals
No Pocket Serial Flush (NopSf) 1 clear (seq. V29, V30)	67.0	No residual electrons	No residual electrons	first 750 rows saturated for 16 amp, 16 amp with signals

4.3.2 New sequencers

In Run 7, we considered two new configurations on top of the default clear. The changes are in the ParallelFlush function, which moves the charges from the image area to the serial register:

- The default clear (V29): In the default clear, all serial clock voltages are kept up as the parallel clocks move charges from the image area to the serial register ([sequencerV29]).

The charges once on the serial register are expected to flow to the ground; the serial register clocks being all up, without pixel boundaries, and with its amplifier in clear state. At the end of the clear, a full flush of the serial register is done (~ the serial clocks changes to read a single row).

- The No-pocket Clear (Nop): a clear where the serial register has the same configuration (S1 & S2 up, S3 low) when the parallel clock P1 moves the charges to the serial register than in a standard image read. Still we kept all phases up for the rest of the time for a fast clear of the charges along the serial register ([sequencerV29_Nop]). The idea is that the S3 phase is not designed to be up when charges are transferred to the serial register, and is probably playing a major role in the creation of pockets.
- The No-Pocket with Serial Flush Clear (NopSf): this sequencer is close to the Nop solution, except that during the transfer of one row to the serial register, the serial phases are also manipulated to transfer two pixels along the serial register. The changes in electric field at the image-serial register interface are then even more representative of what a standard read produces, and should further prevent the creation of pockets. ([sequencerV29_NopSf]).

sequencerV23_DC `https://github.com/lsst-camera-dh/sequencer-files/blob/master/run5/FP_E2V_2s_ir2_v23_DC.seq`

sequencerV29 `https://github.com/lsst-camera-dh/sequencer-files/blob/master/run7/FP_E2V_2s_l3cp_v29.seq`

sequencerV29_Nop `https://github.com/lsst-camera-dh/sequencer-files/blob/master/run7/FP_E2V_2s_l3cp_v29_Nop.seq`

sequencerV29_NopSf `https://github.com/lsst-camera-dh/sequencer-files/blob/master/run7/FP_E2V_2s_l3cp_v29_NopSf.seq`

4.3.3 Results on standard e2v and ITL CCDs

In Figures 40 and 39, we present for three types of sequencer (from left to right: V29, Nop, and NopSf), a zoom on the first rows of an ITL or e2v amplifier (for ITL R03_S11_C14 and for e2v R12_S20_C10 shown as a 2D row-columns image (top plots) or as the mean signal per rows for the first row read of an amplifier (bottom plots).

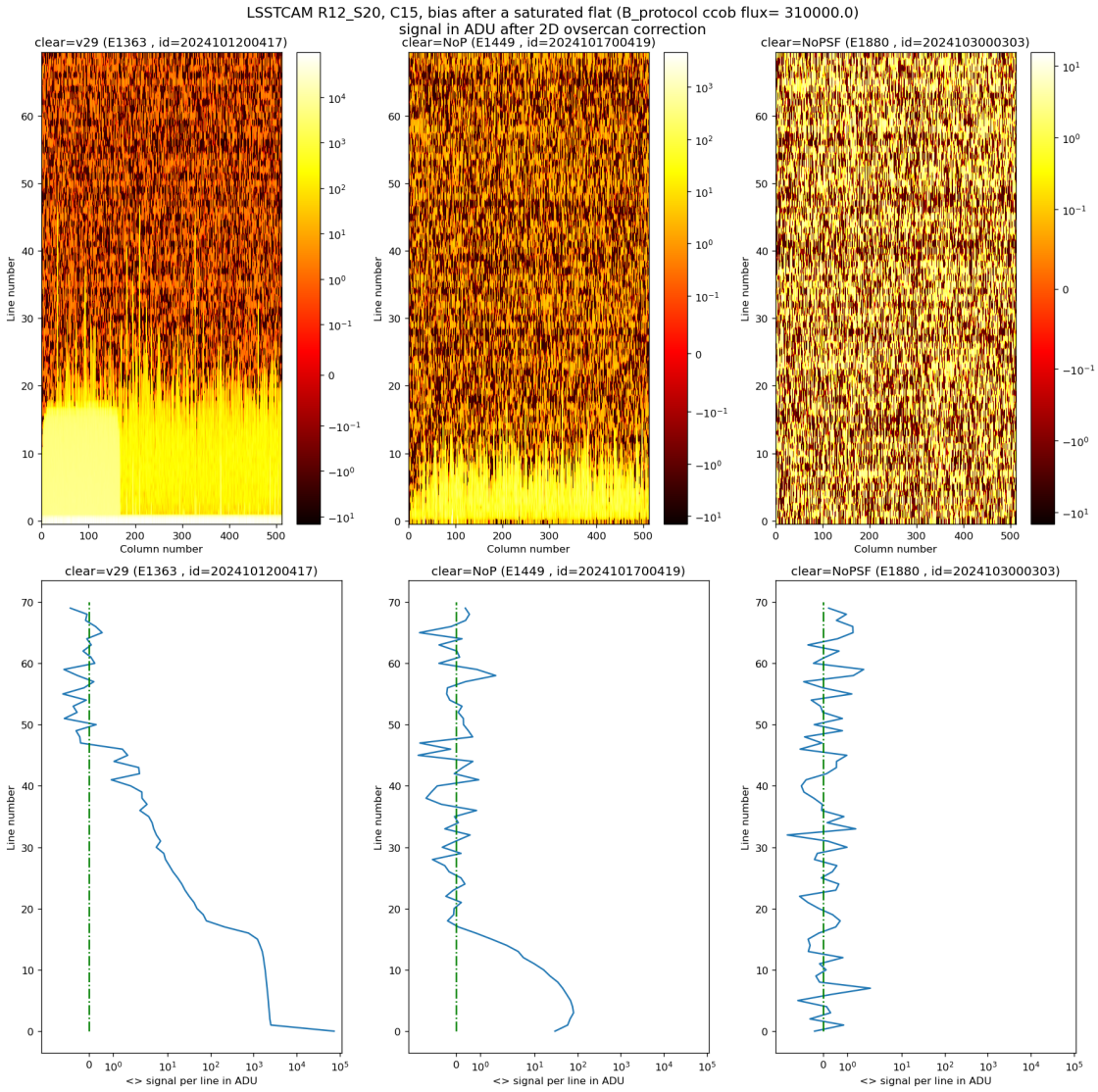

Figure 39: Impact of the three types of clear on a bias taken after a saturated flat for an e2v sensor (R12_S20). The three panels on top show the interface region between the imaging section and the serial register. The aspect ratio is not 1 for presentation purpose; the bottom three plots are the averaged column profiles.

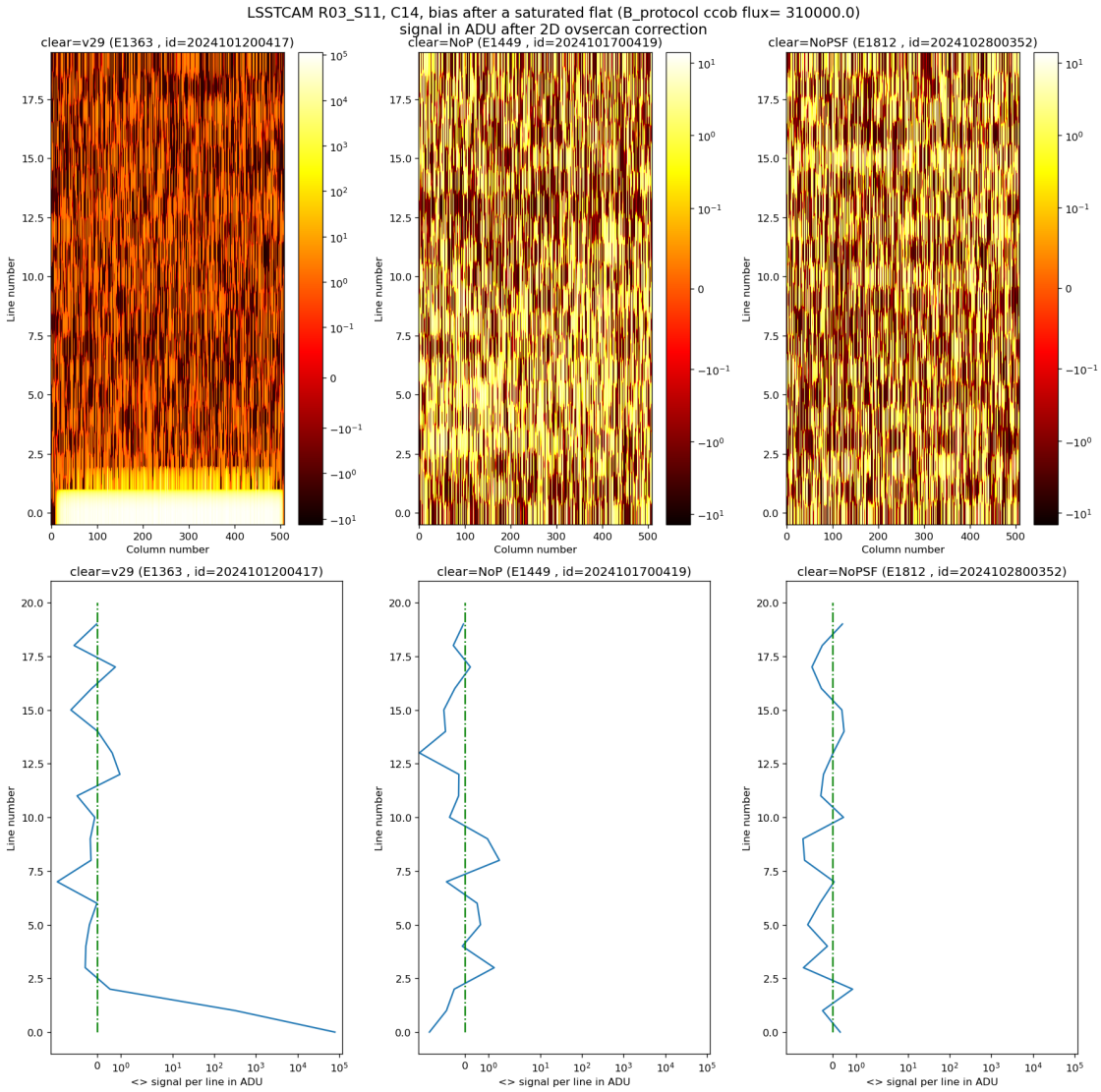

Figure 40: Same as Figure 39 but for an ITL sensor (R03_S11).

As seen in the left-hand panel of Figure 39 for an e2v CCD, a bias taken just after a saturated flat will show a residual signal in the first lines read when using the default clear (left images, clear= V29): the first row has an almost saturated signal (~100 kADU here), and a significant signal is seen up to row ~50. In practice, depending on the amplifier, signal can be seen up to row 20–50. When using the Nop clear (central plots), we can already see a strong reduction of the uncleared charges in the first acquired bias after a saturated flat. Still a small residual signal is visible in the first ~ 20 rows. The NopSf clear (right plots) fully clears the saturated flat, and no uncleared charges are observed in the following bias.

As seen in the left-hand panel of Figure 40 for an ITL CCD, a bias taken just after a saturated flat will show a residual signal in the first rows read when using the default clear (left images, clear=v29): the first row has an almost saturated signal (~ 100 kADU here), and a significant signal is seen in the following row. Both Nop clear (central plots) and NopSf clear (right plots) fully clear the saturated flat, and no uncleared charges are observed in the following bias.

4.3.4 An exceptional case: ITL R01_S10

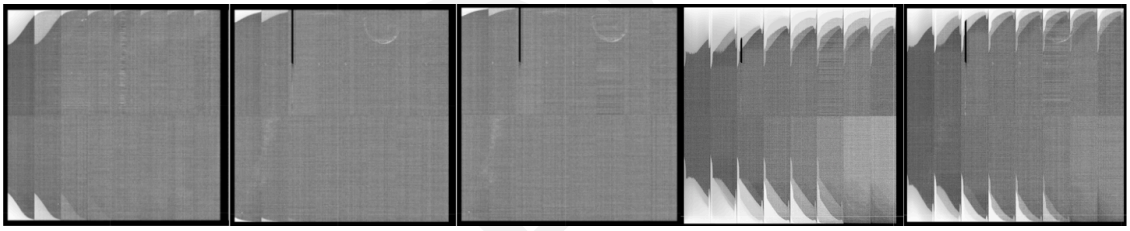

Figure 41: Impact of the various types of clear on ITL R01_S10 after a saturated flat (bias after a saturated flat), from left to right: 1 standard clear, 3 standard clears, 5 standard clears, 1 Nop clear, 1 NopSf clear.

One ITL sensor, R01_S10, presents a specific behavior that is not understood:

- It has a quite low full well (2/3 of nominal).
- The 3 CCDs of this REB (REB1) have a gain 20% lower than all other ITL CCDs.
- The images taken after a large saturation, as seen in Figure 41, show a large amount of uncleared charged (with the standard clear: 4 amplifiers retain ~500 rows of saturated signal!).

It appears that putting S3 low during the clear as done in Nop and NopSf, is even worse than a standard clear. This is strange, as a full frame read, which does this too, manages to clear

a saturated image. We notice that NopSf is ~50% better than Nop, but still worse than the standard clear, in particular for the 12 amplifiers that are almost correct with the standard clear.

At this time we do not have a correct way to clear this sensor once the CCD heavily saturates by uniform illumination, but it is not clear yet if a saturated star in this sensor, leaving signal in the parallel overscan, will present the same clear issue.

4.3.5 Conclusion on clears

For e2v sensors, Run 7 finds the NopSf clear fully clear the leftover electrons at the image and the serial register interface. The NopSf clear grants that the first 50 rows of e2v CCDs that had leftover electrons from the previous exposure are now free of such contamination. NopSf will be the default clear method.

For the ITL sensors, the improvement is still needed even if Nop or NopSf overcome the clear issue because there is the exception of R01_S10 prevented the usage of those sequencers for ITL devices for Run 7. Note that aside from R01_S10 the numbers of lines potentially "not cleared" in ITL devices after saturated images are small (2 first rows), and they correspond to a CCD area that is difficult to use anyway (sensor edges with low efficiency). So at this stage the default clear is still our default for ITL, and further studies to overcome the problem with R01_S10 are forseen (e.g., investigate using a continuous serial flush during exposure at low rate, 10^6 pixel flushes in 15 s). The original clear (serial phase 3 always), slightly extended in time to match the NopSf e2v clear execution time, will stay the default method.

4.4 Toggling the RG Bit During Parallel Transfer for e2v sensors

This investigation comes from an analogy drawn with the ITL sequencer file. Although the vendor recommended toggling the RG bit at the end of the parallel transfer, it was unclear whether this step was truly necessary. Given the improvements observed in ITL devices, applying this approach to e2v devices also became an area of interest.

4.5 Disable IDLE FLUSH

IDLE_FLUSH is one of the main settings in the sequencer file that enables the sequencer output to run while in the IDLE state (the period between one exposure and the next). The specific implementation of IDLE_FLUSH can be selected from various functions in the sequencer file. In Run 5, we chose the `ReadPixel` function, which reads out a pixel. This choice was initially made to mitigate the so-called yellow corner issue, a 2D structure of elevated signal near an amplifier corner observed in bias and dark exposures for certain amplifiers on e2v CCDs (see details in Utsumi et al. (2024)).

However, it was reported that running IDLE_FLUSH exacerbates the Divisidero tearing issue. Divisidero tearing appears as a signal deficiency at amplifier boundaries in e2v sensors, accompanied by increased signal in adjacent columns. Additionally, using `ReadPixel` as the IDLE_FLUSH function has the highest thermal impact because it continuously operates the Analog-to-Digital Converter at its maximum rate. This results in a significant difference in power consumption, more than 50 W over all rafts, between the exposure state and the IDLE state. Consequently, the focal plane experiences a temperature variation of approximately 2 deg C between periods of image acquisition and idle periods (Figure 42).

Figure 42: Impact of enabling and disabling IDLE_FLUSH on focal-plane temperature and power consumption.

This temperature variation in the focal plane can lead to changes in the REB temperature,

potentially causing gain variations or instability in the bias. Based on these considerations, we decided to disable IDLE_FLUSH. The impact of this change on bias stability is discussed in Sections 5.9 and 5.10.

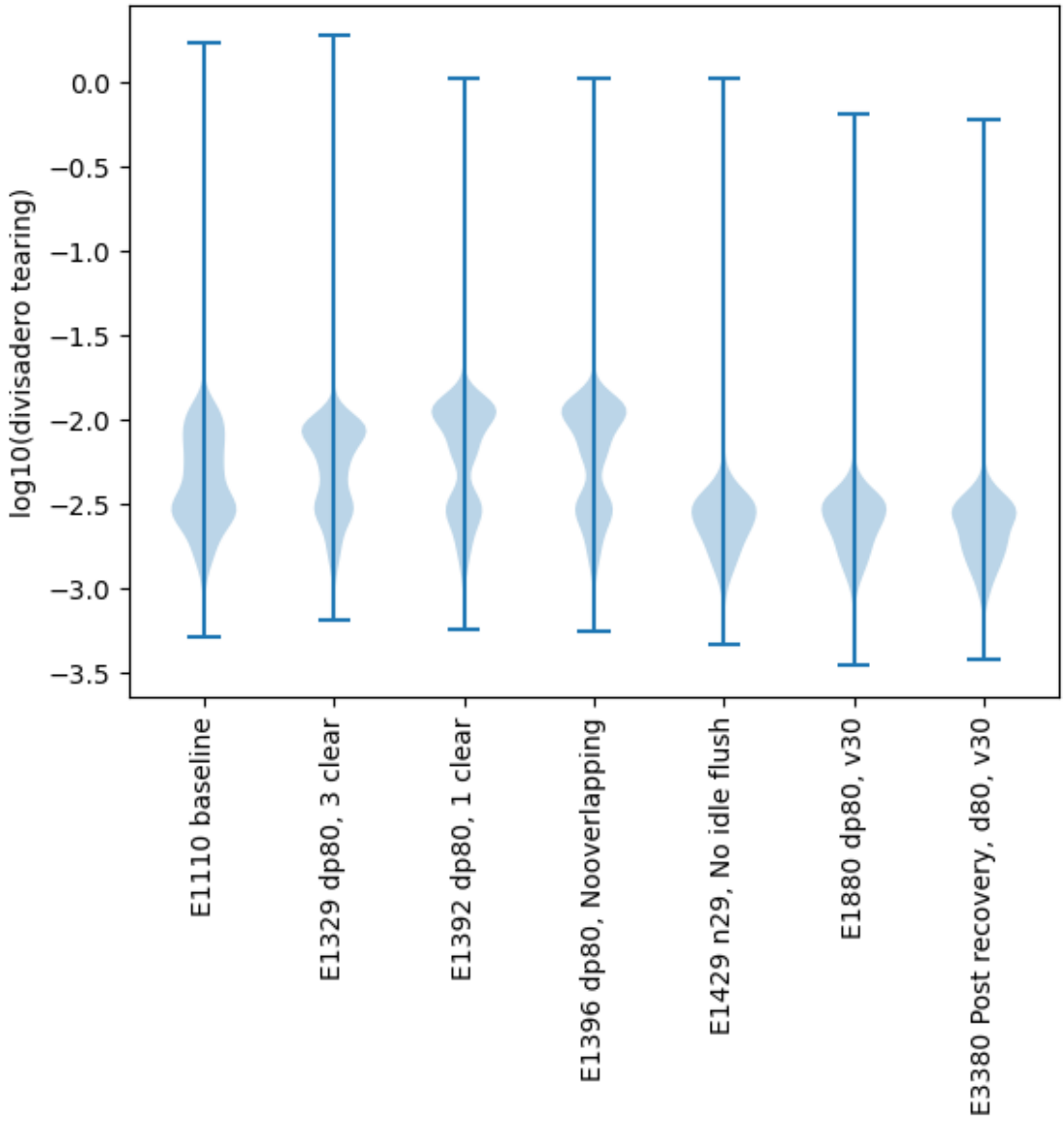

Figure 43: Impact of disabling IDLE_FLUSH on Divisadero tearing

Figure 43 shows the impact on the Divisadero tearing. The runs shown here are selected B protocol runs with different settings in the time order. There were few changes: (1) switching to narrower parallel swing voltage, (2) changing the number of clears before the exposure, (3) disabling IDLE_FLUSH. Some minor changes in each changes are also included such as

changing the number of clears, or changing the sequencer file (the change from v29 to v30 is primarily incorporation of the change in the clear). The figure includes both ITL and e2v results. The two distinct distributions in earlier runs correspond to the differences between the two types of CCD (the higher one is e2v and the lower one is ITL). The greatest change can be seen when we switched to not running IDLE_FLUSH at E1429, which brought the overall distribution down. The two distributions became indistinguishable, which indicates the majority of the Divisadero tearing for e2v is mitigated.

E3380 was the run taken after the recovery from the shutdown due to poor performance of the Pumped Coolant System. This fact confirms that the metric is consistent over power cycling of LSSTCam.

4.6 Summary

e2v sensors had persistence. We confirmed that narrowing the parallel swing voltage of the e2v CCD operation greatly reduced persistence. As penalties, we observed a full well reduction of 22% and a ~10% increase of the brighter-fatter effect, essentially in an isotropic way.

Sequencer files have undergone evolution for both ITL and e2v versions. The final sequencer file from Run 6 was the v26noRG version for ITL and the regular v26 for e2v. The suffix noRG indicates that the RG bit is not toggled during parallel transfer. This modification appears to enhance the stability of the bias structure for most ITL amplifiers.

During Run 7, several changes were implemented, as described below:

- v27 incorporated guider functionalities, including ParallelFlushG and ReadGFrame. However, the noRG change was inadvertently included. Consequently, we abandoned this version and switched to v28.
- v28 sequencer files merged v26noRG and v27. `https://rubinobs.atlassian.net/browse/LSSTCAM-5`
- v29 introduced changes to speed up the guider. `https://rubinobs.atlassian.net/browse/LSSTCAM-34`
- v30 primarily focused on e2v. We introduced a new approach to NopSf for e2v CCDs `https://github.com/lsst-camera-dh/sequencer-files/pull/17`. To align timing with the ITL version, a change was made. `https://github.com/lsst-camera-dh/sequencer-files/`

pull/18

We also disabled IDLE_FLUSH to improve the thermal situation and the Divisadero tearing.

5 Characterization & Camera stability

5.1 Illumination corrected flat

5.2 Glow search

5.3 Final characterization

5.3.1 Background

For a description of each quantity within this section and its acquisition process, refer to Section 3. To compare initial and final camera metrics on Cerro Pachón, we used standard B protocols and dense red PTCs.

Table 5: Reference runs for initial and final Run 7 comparisons

Run Type	Cerro Pachón Initial Run	Cerro Pachón Final Run
B Protocol	E1071	E1880
PTC	E749	E1881

For the final operating parameters of LSSTCam for Run 7, see Section 7.1.

5.3.2 Stability flat metrics

5.3.2.1 Serial CTI Serial CTI is extracted from the B protocols, and show high consistency between initial and final operating parameters.

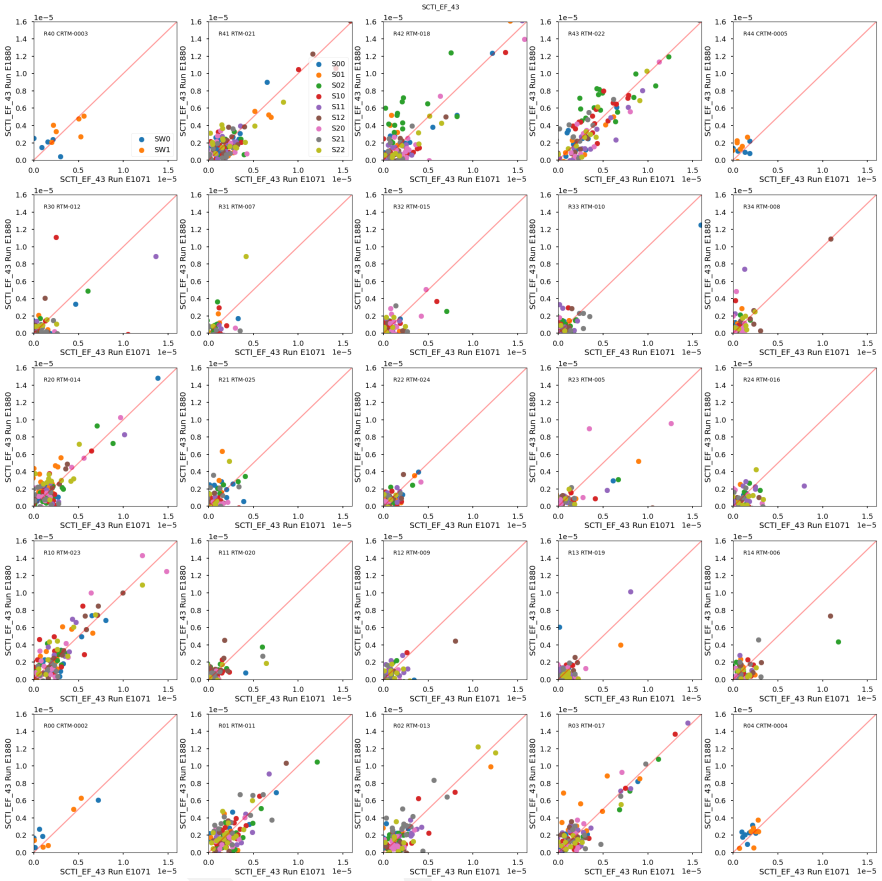

Figure 44: Comparison of serial CTI measurements for initial and final Run 7 configurations.

The serial CTI for both sensor types is a noisy measurement, but serial CTI is not impacted by the changes to the camera operating configuration.

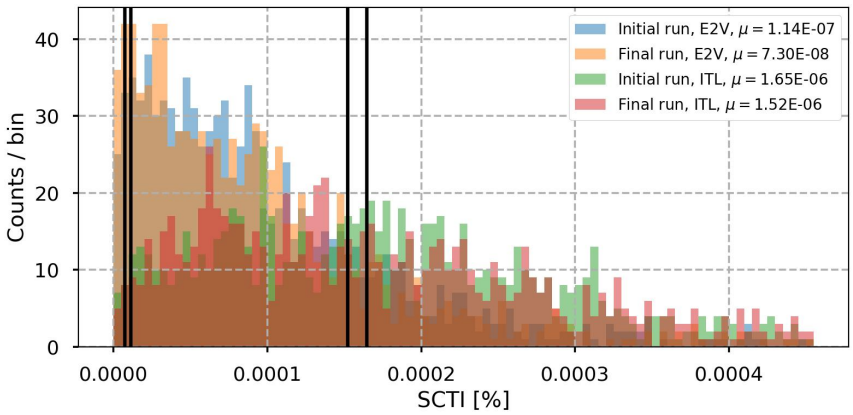

Figure 45: Histogram of serial CTI measurements for initial and final Run 7 configurations, separated by detector type.

5.3.2.2 Parallel CTI Parallel CTI is extracted from the B protocols, and show high consistency between initial and final operating parameters.

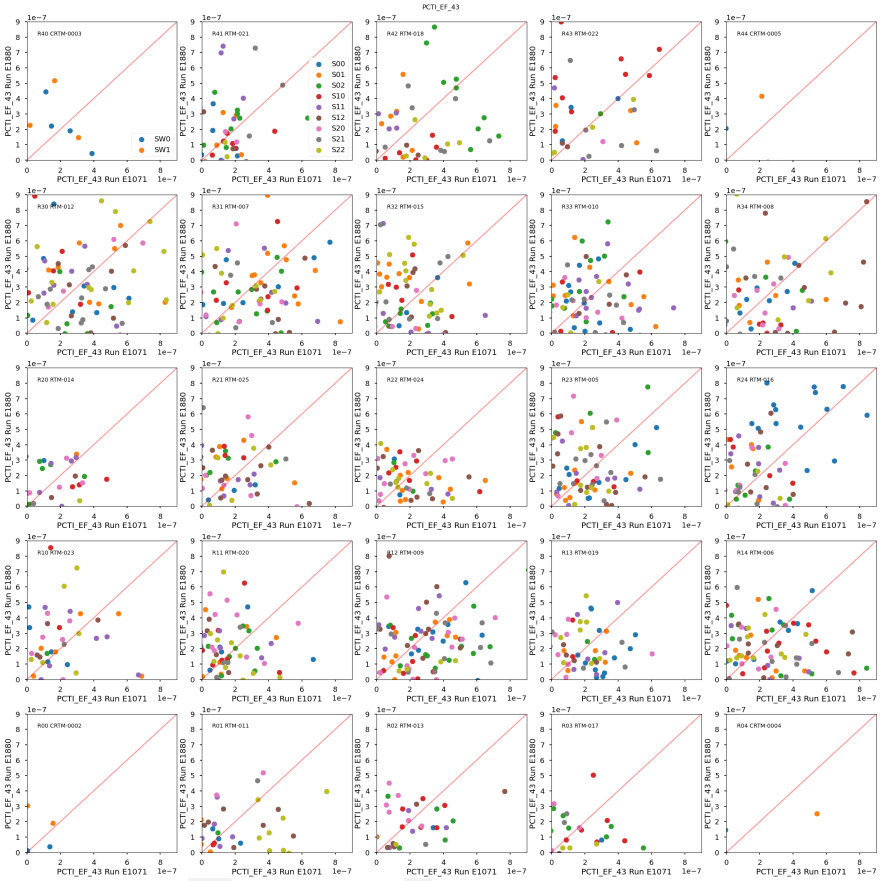

Figure 46: Comparison of parallel CTI measurements for initial and final Run 7 configurations.

Similar to serial CTI, the parallel CTI for both sensor types is a noisy measurement, but is not impacted by the changes to the camera operating configuration.

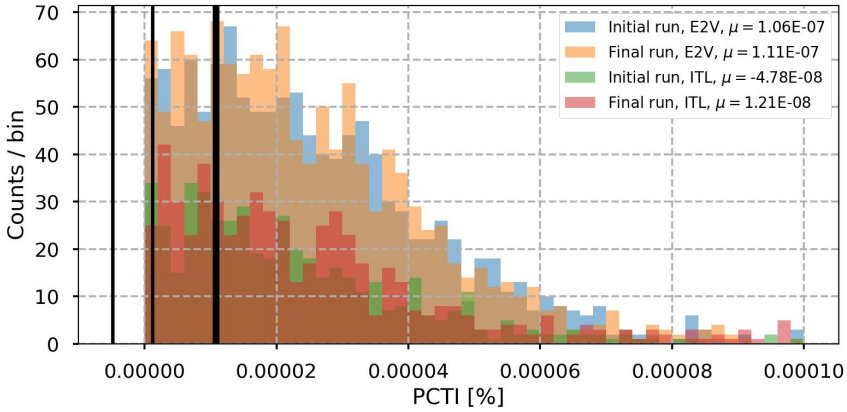

Figure 47: Histogram of parallel CTI measurements for initial and final Run 7 configurations, separated by detector type.

5.3.3 Dark metrics

5.3.3.1 Dark current Dark current measurements were extracted from the B-protocol runs. Across the focal plane, dark current measurements are consistent with initial and final Run 7 runs. In a subset of rafts, a notable decrease in dark current is observed. These rafts are local to the autochanger light leak, which was mitigated as part of optimization efforts (see Sec. 2.3.2).

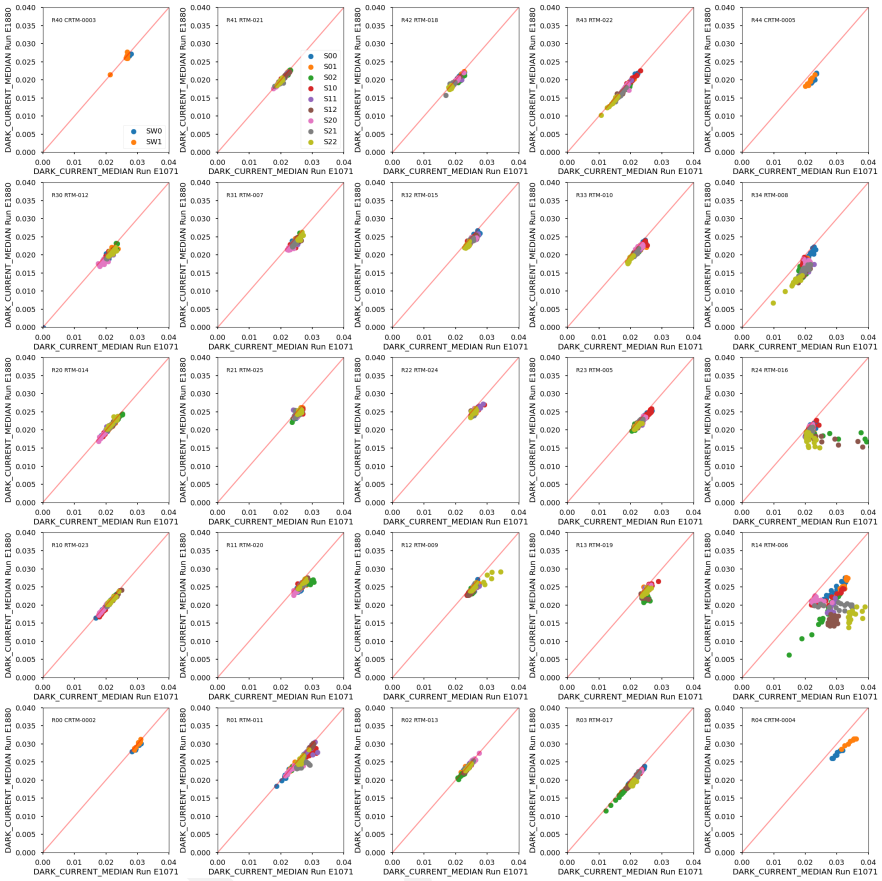

Figure 48: Comparison of dark current measurements for initial and final Run 7 measurements. A marked decrease in dark current is present in rafts local to the autochanger light leak (see Sec. 2.3.2)

The reduction in dark current in the subset of rafts is indicative of successful light leak mitigation, and lowers the dark current on local rafts to levels similar to the rest of the focal plane.

5.3.3.2 Bright defects Bright defects are extracted using the B protocol runs, and show an extremely close agreement between runs. No significant bright defects developed as a result of the different voltage, sequencer, and idle flush conditions.

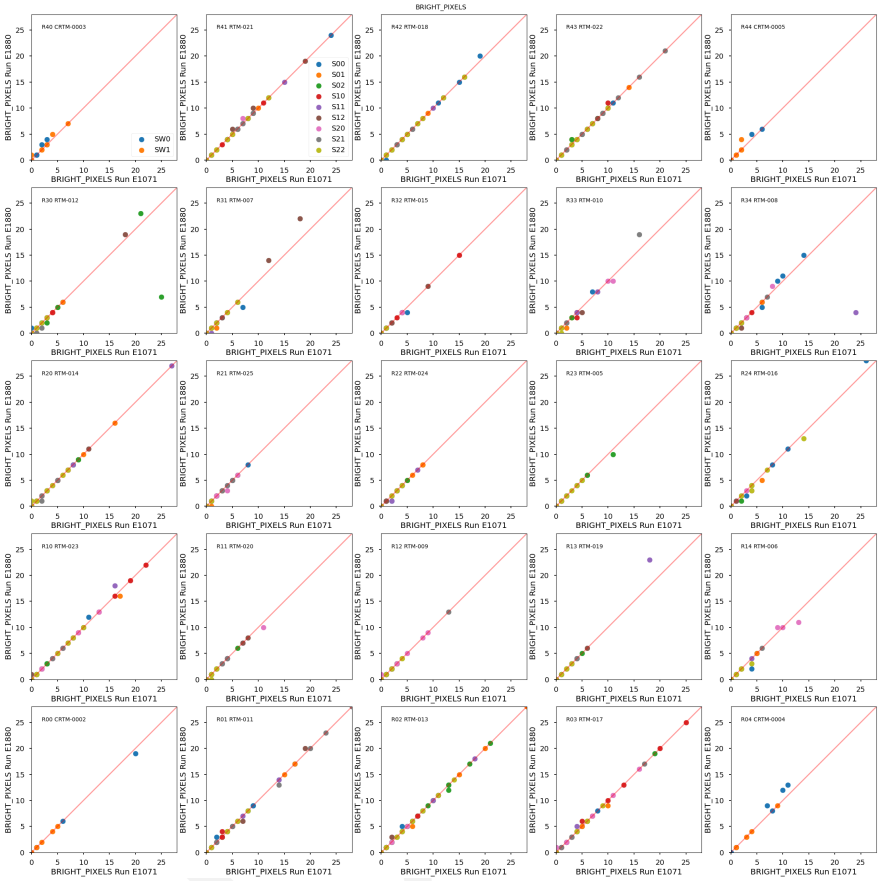

Figure 49: Comparison of bright pixel measurements for initial and final Run 7 measurements.)

For additional discussion about defect stability, see Section 5.8.

5.3.4 Flat pair metrics

5.3.4.1 Linearity and PTC turnoff Both linearity and PTC turnoff were extracted from the PTC runs. Due to the lower parallel swing for e2v sensors, we anticipate a lower full-well capacity (see Janesick (2001)). As described in Section 4.1.1, we observe a decrease in full well capacity for e2v sensors. ITL sensors exhibit stable full-well measures, despite the changes to the v30 sequencer and disabling idle flush.

For e2v sensors we find the reduction in full-well to be significant, ~20 - 25% depending on the full-well metric used (see Fig. 53).

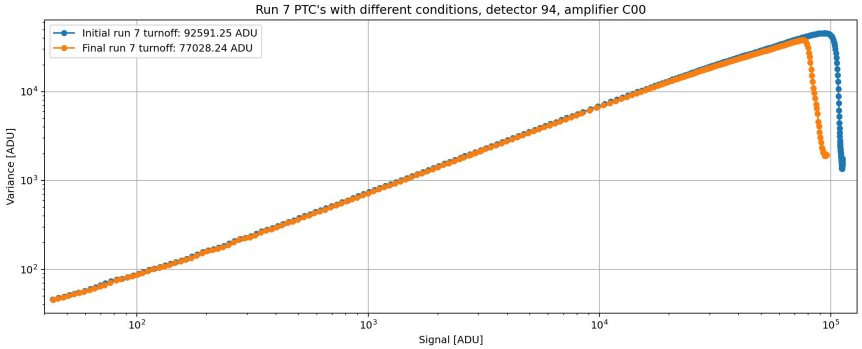

Figure 50: Comparison of PTCs from initial and final Run 7 conditions, evaluated on a central detector and amplifier.

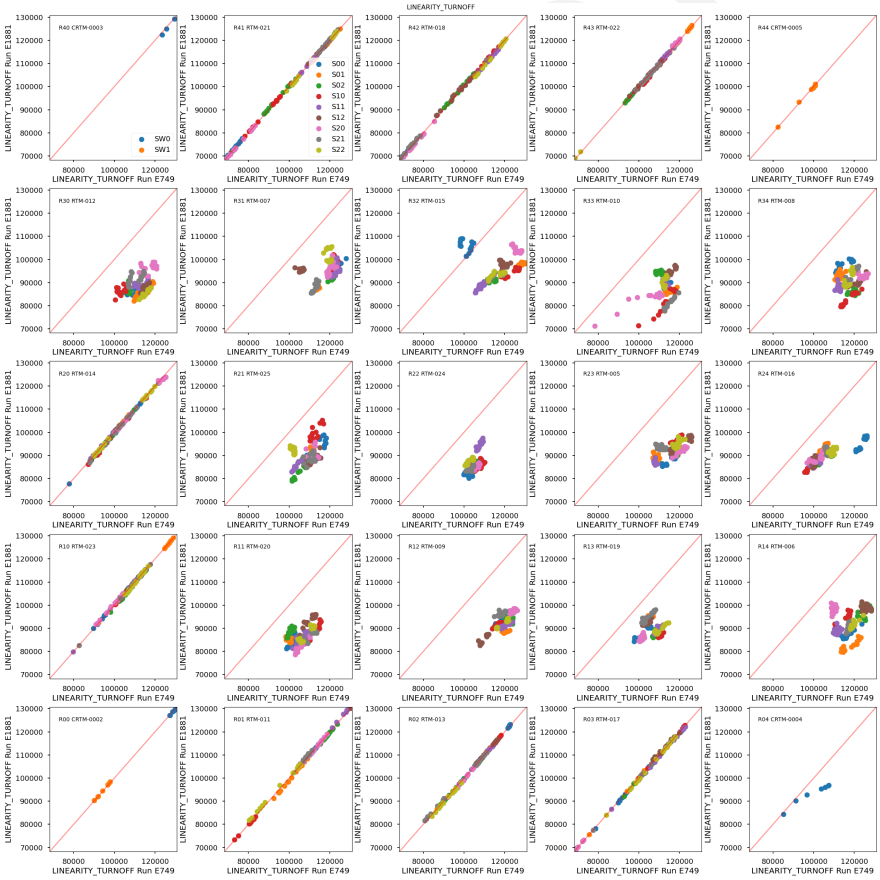

Figure 51: Comparison of linearity turnoff measurements from the initial and final Run 7 measurements. The e2v sensors show a notable decrease in linearity turnoff, while ITL sensors stay the same. The values reported here are in ADU, and not gain corrected.

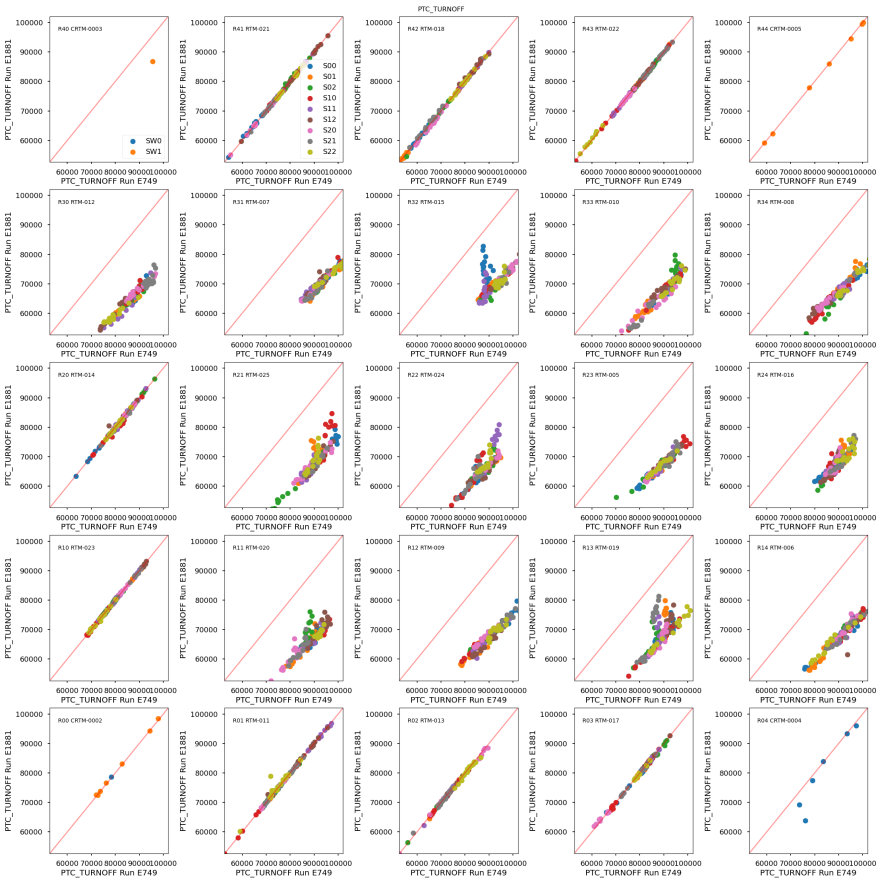

Figure 52: Comparison of PTC turnoff measurements from the initial and final Run 7 measurements. The e2v sensors show a notable decrease in PTC turnoff, while ITL sensors stay the same. The values reported here are in ADU, and not gain corrected.

Early in LSST's design, a 90,000 e- full-well capacity was established as a requirement for an 8 magnitude dynamic range across all bands. If linearity turnoff is the metric used to quantify full-well, all e2v amplifiers pass this system requirement. If PTC turnoff is the metric used to quantify full-well, 6.41% e2v amplifiers do not pass this system requirement (120/1872 total amplifiers).

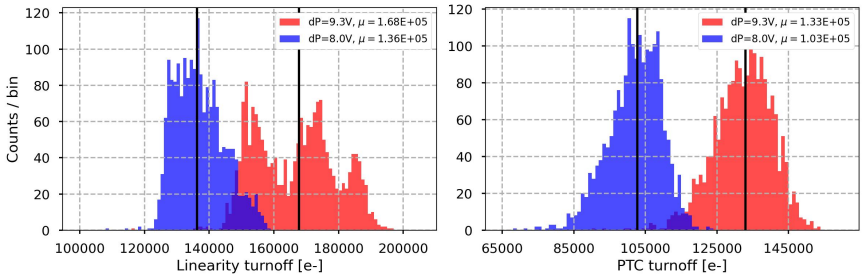

Figure 53: Comparisons of PTC turnoff and linearity turnoff for e2v science sensors. The runs analyzed here are the PTC runs noted in table 5. Note that both metrics have been gain corrected.

5.3.4.2 PTC Gain PTC Gain was extracted from the PTC runs. PTC gain is extremely comparable between initial and final Run 7 conditions, with a minor increase in gain observed in e2v sensors.

The magnitude of the gain increase for e2v sensors in final Run 7 conditions is ~0.03 e-/ADU on average.

5.3.4.3 Brighter fatter a_{00} coefficient The relative strength of the brighter-fatter effect, quantified by a_{00} following the model from Astier et al. (2019), is modified in the final Run 7 operating conditions by the lower parallel swing for e2v sensors. We observe an extremely high consistency for ITL sensors.

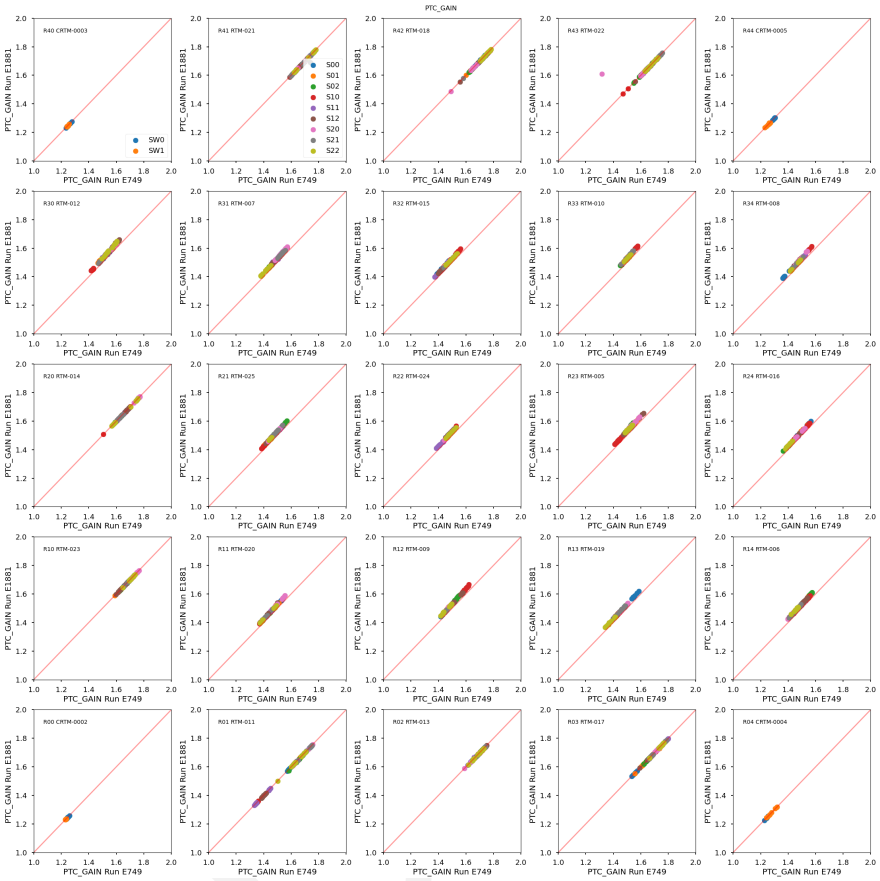

Figure 54: Comparison of PTC gain amplifier measurements, showing high consistency from initial and final Run 7 conditions.

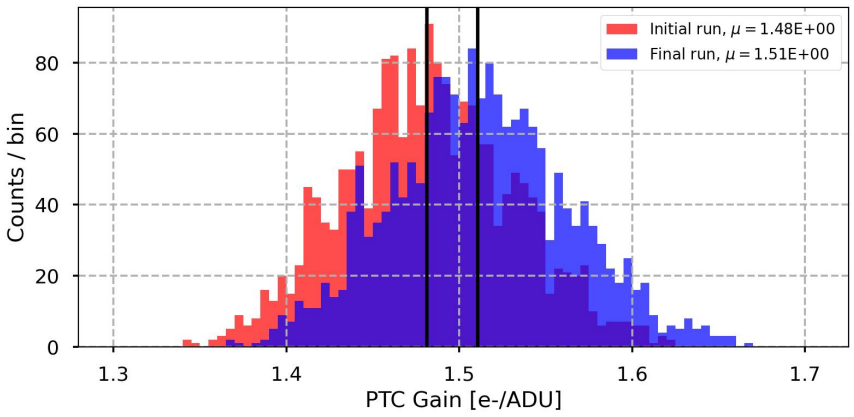

Figure 55: Comparison of PTC gains in e2v science sensors, with a moderate increase in the final run condition.

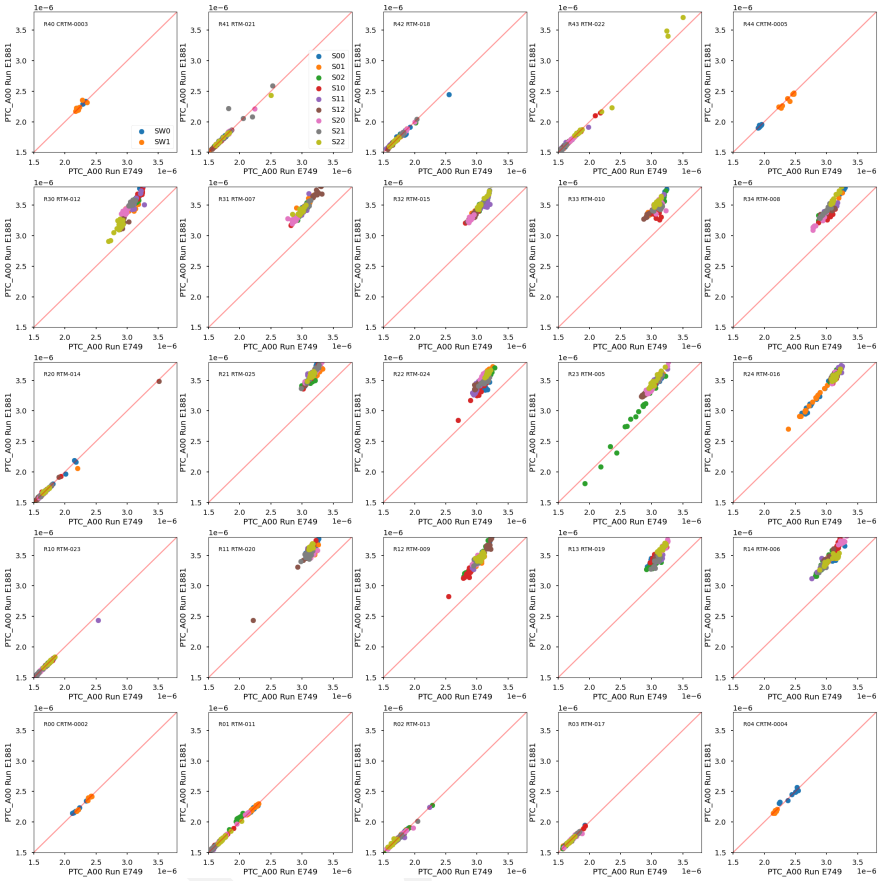

Figure 56: Comparison of amplifier measurements of the a_{00} parameter for initial and final Run 7 conditions.

The change in the a_{00} value for e2v sensors is illustrated in Figure 57, showing a ~12% increase in the strength of the brighter fatter effect for e2v sensors due to the lower parallel swing. For additional discussion on the brighter fatter coefficient, see Section 4.1.3.

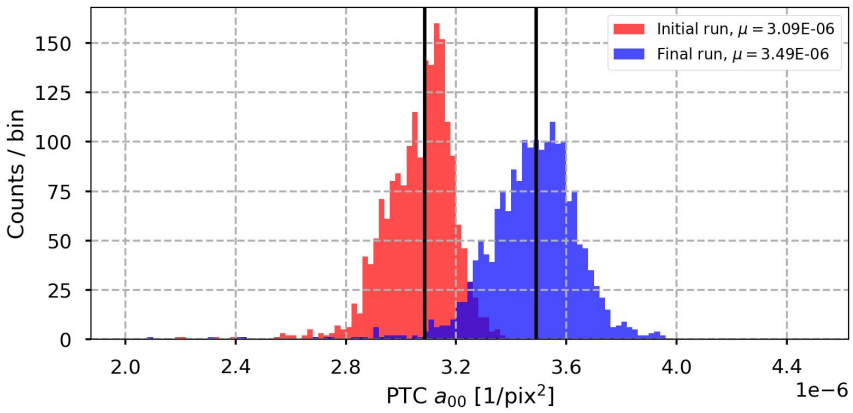

Figure 57: Comparison of the a_{00} values in e2v sensors, showing a notable increase from the final operating conditions.

5.3.4.4 Brighter-Fatter Correlation The strength of the brighter fatter correlation was extracted from the PTC runs. In both instances, the correlation is extremely consistent across initial and final Run 7 operating conditions.

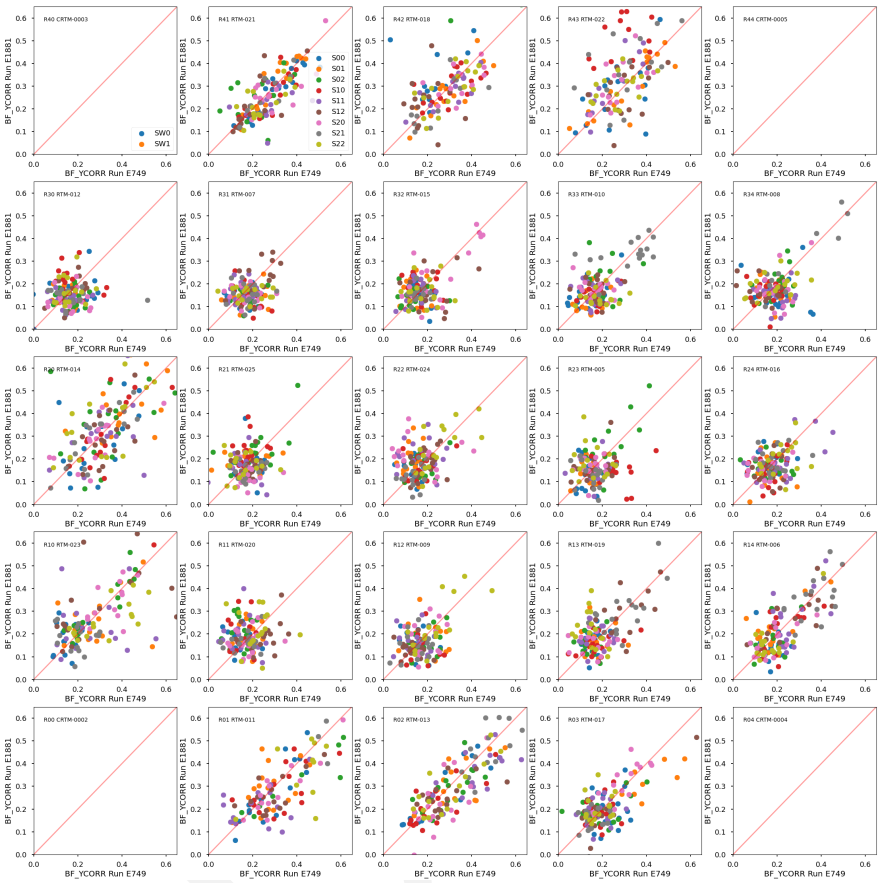

Figure 58: Comparison of amplifier measurements of the brighter-fatter y-correlation for initial and final Run 7 conditions.

Both correlations vary by 2.2% on average, decreasing in both instances (see table 6). The measurement is noisy, with all rafts showing unbiased scatter around the correlation measurement on the raft level, evident in figures 59 and 58.

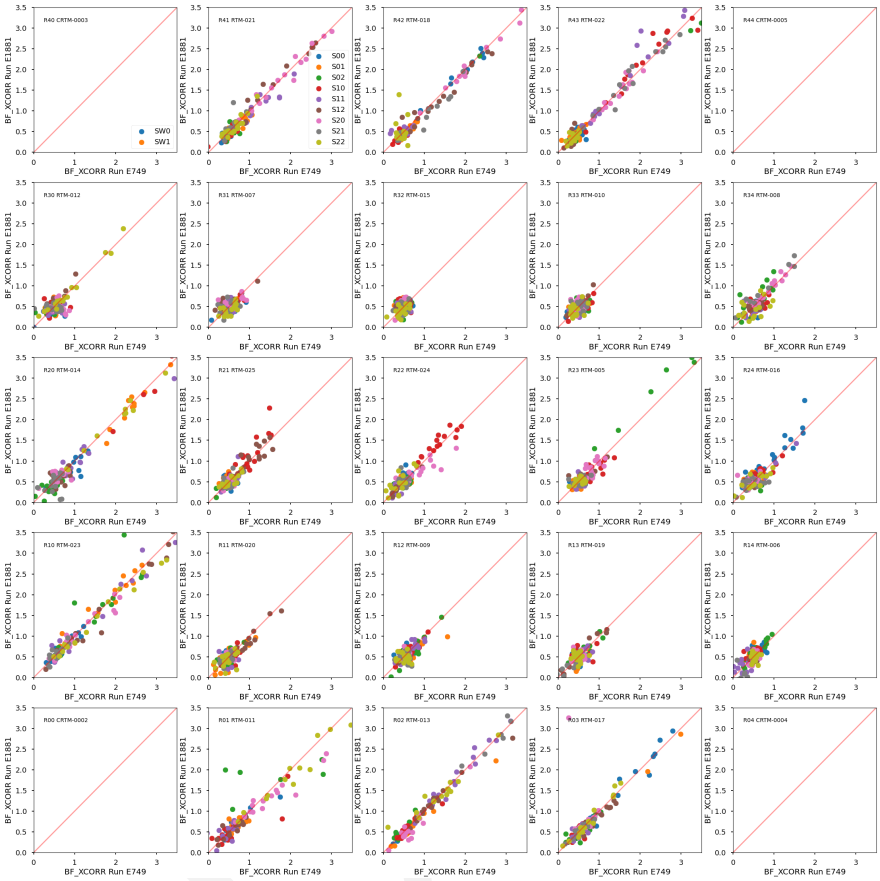

Figure 59: Comparison of amplifier measurements of the brighter-fatter x-correlation for initial and final Run 7 conditions.

5.3.4.5 Row-means variance Row means variance is extracted from the PTC runs, and shows an extremely tight correlation when comparing the initial and final operating conditions of Run 7. ITL sensors show an extremely tight agreement, while e2v sensors show a lower row-means variance by ~1.8% in the final operating conditions.

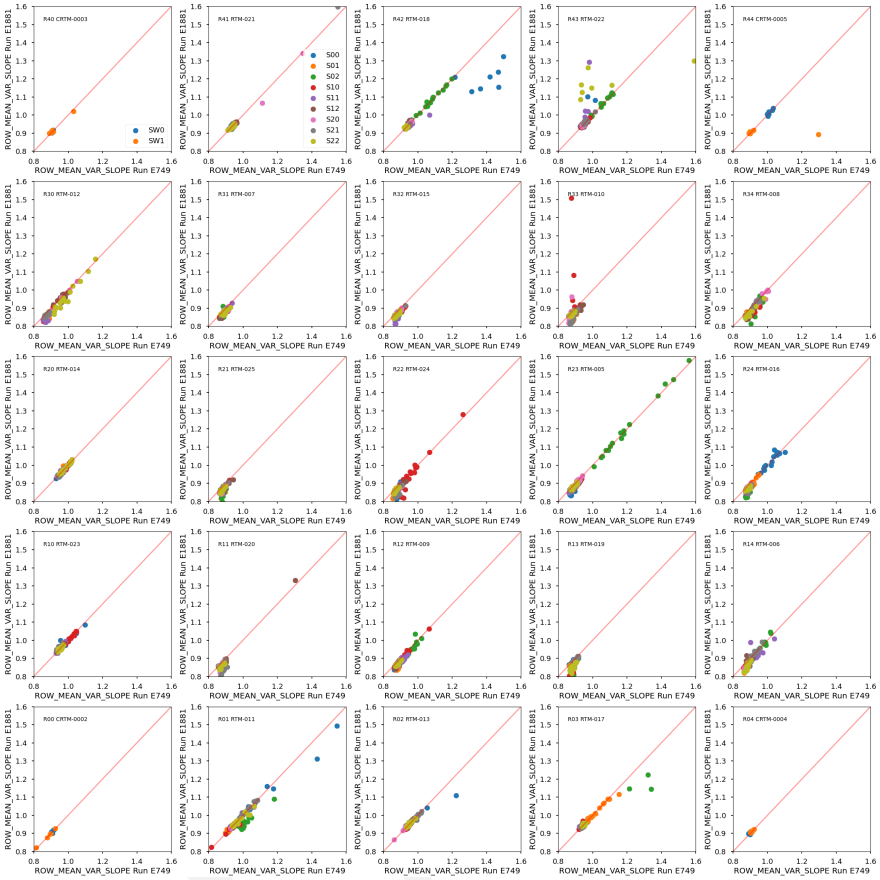

Figure 60: Comparison of amplifier measurements of the row-means variance slope for initial and final Run 7 conditions.

5.3.4.6 Divisadero Tearing Divisadero tearing measurements were extracted from the B protocols, and are significantly different for e2v sensors in the final operating condition. The change in Divisadero strength is driven by idle flush, which is described in detail in Section 4.5. The e2v sensors show a 60.7% decrease in the original Divisadero signal under the final operating conditions. ITL sensors show a 0.2% increase in the original Divisadero signal under the final operating conditions.

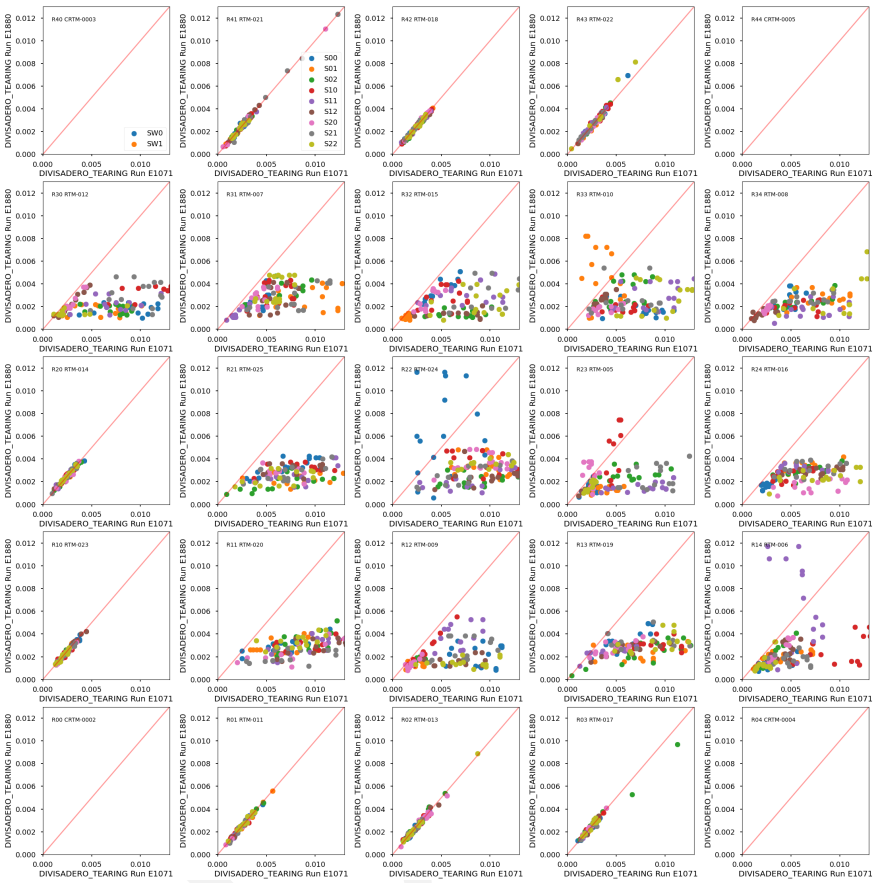

Figure 61: Comparison of amplifier measurements of Divisadero tearing for initial and final Run 7 conditions.

In Figure 61, several e2v sensors do not follow the global trend of decreased Divisadero signal.

5.3.4.7 Dark defects Dark defects in LSSTCam were extracted using the B protocols, and are contaminated by the picture frame effect regardless of operating conditions (see Sec. 3.4.6 for additional discussion). When applying a 9 pixel mask to the edges of each sensor, the picture frame signal is removed, leaving true dark defects acquired by the analysis pipeline.

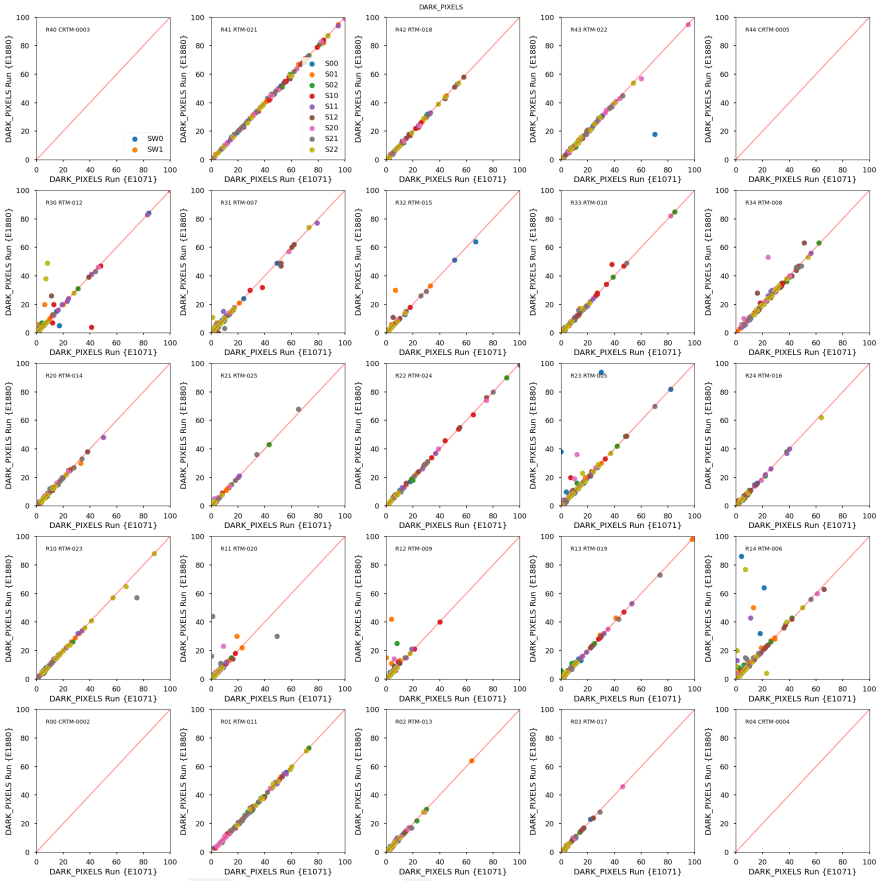

Figure 62: Comparison of amplifier measurements of the dark pixel for initial and final Run 7 conditions.

Dark defects are consistent between initial and final Run 7 data. Dark defects are a minimal contribution to the focal-plane, with an average contribution of 3 pixels per e2v amp and 8 pixels per ITL amp. There is no global change in dark defect counts per amp, with measurements of the difference of dark pixel counts per detector centered on zero for both detector types (see Fig. 63).

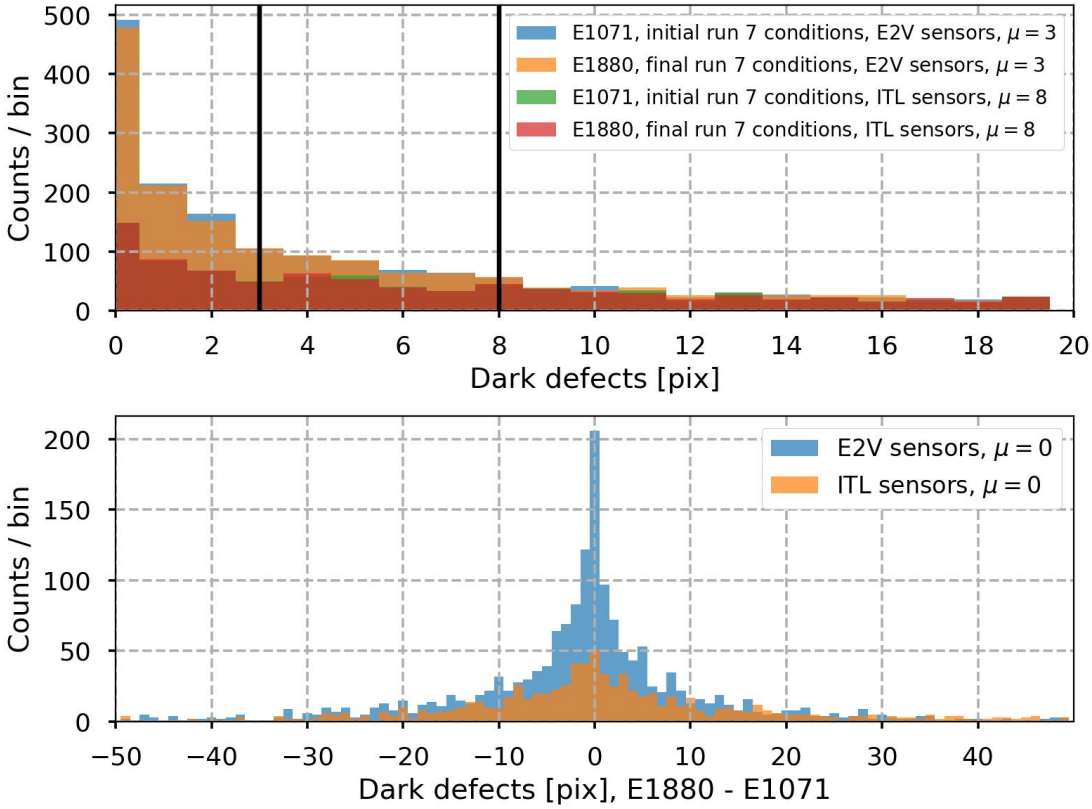

Figure 63: The amplifier measurements of dark pixel defects, with a 9 pixel mask applied to each sensor. Top: A histogram of the dark pixel measurements, with each count representing one amplifier. Histogram groups are separated by sensor type, and also by initial (E1071) and final (E1880) runs. Bottom: The difference in amplifier dark pixel measurements, separated by detector type. For both detector types, there is no significant evolution in the defect counts.

5.3.5 Persistence

The primary optimization target of Run 7 was to mitigate persistence, described in Section 4.1.1. The major change in the final camera operating conditions to combat persistence is decreased parallel swing. This change is applied to the e2v sensors only, as they are the subset of sensors that exhibit ≥1 ADU persistence when using the Run 7 initial operating parameters.

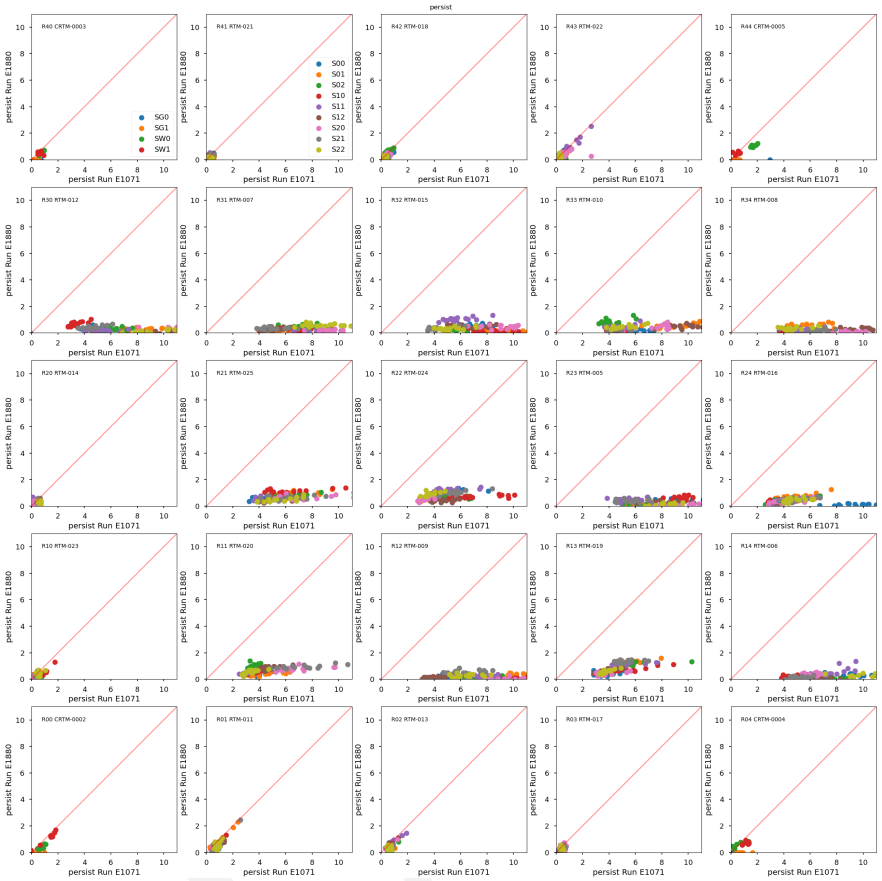

Figure 64: Comparison of amplifier measurements of persistence for initial and final Run 7 conditions.

The amplifier measurements of persistence using the metric described in Section 3.5 show a significant decrease in persistence signal in e2v sensors due to the lower parallel swing, from 5.66 ADU 0.40 ADU on average when measured using the red LED (corresponding to the LSST r band filter).

The B protocol uses a persistence dataset that uses the red LED, and flashes at 400k e- only (description of B protocol persistence dataset in Section 3.1). Additional persistence datasets were acquired using other LEDs and other exposure levels with the CCOB wide beam projector. This was to verify that persistence was mitigated for the complete LSST photometric range. The runs used for this analysis are listed in table 25.

We find that ≥95% of e2v sensors exhibit a persistence signal ≤ 0.55 ADU at all flux levels below full-well capacity. The CCOB requested flux varied by ∼ 10% across the focal plane, and

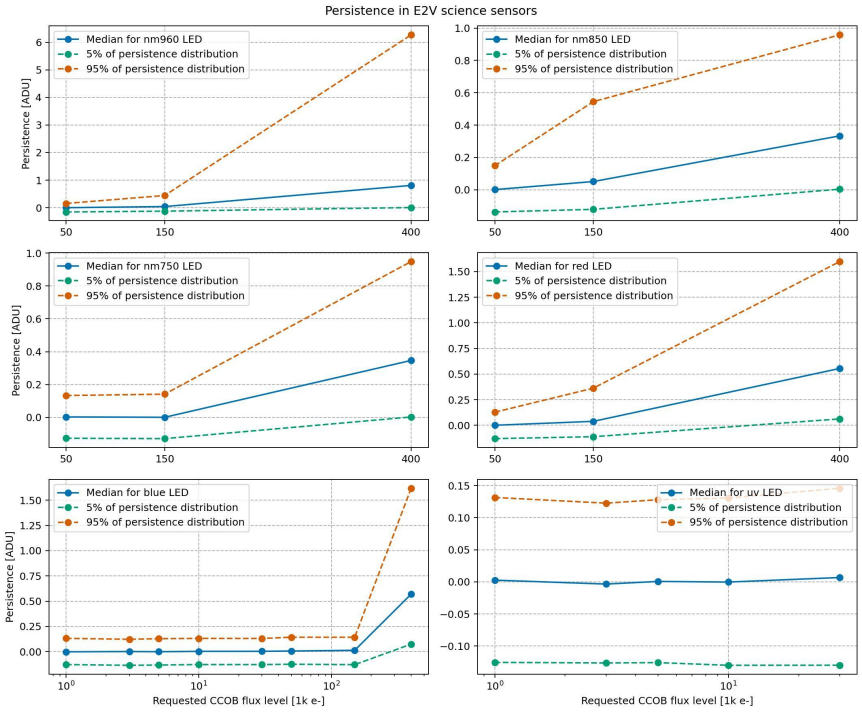

Figure 65: Demonstration of persistence mitigation in e2v sensors.

the maximum PTC turnoff for e2v amplifiers under the final operating conditions was 123,243 e- (see Fig. 53), within the flux levels probed in Fig. 65.

5.3.6 Differences between Run 7 initial and Run 7 final measurements

Comparing the initial and final Run 7 measurements, there are four metrics that are impacted by the optimization efforts described in Section 4.

- **Persistence:** We minimized persistence in e2v sensors, the main optimization target of Run 7, decreasing it from 5.66 ADU to 0.40 ADU on average with the red LED (LSST-r band), and maintaining sub-ADU levels across the entire LSST bandpass. Due to no change in ITL voltages and lack of an initial persistence feature, ITL sensors do not show a significant change in persistence, and remain at a sub-ADU level (0.48 ADU 0.32 ADU).
- **Full well capacity:** As a direct consequence of lower parallel swing in e2v sensors, the full-well capacity of e2v sensors decreased significantly with the final operating parameters. For linearity turnoff, e2v sensors decrease from 167,796 e- 136,302 e-. PTC turnoff

measurements decrease from 132,963 e- 102,713 e-. ITL sensors do not show a significant change, and remain consistent between initial and final runs.

- **Brighter-fatter strength (PTC a_{00}):** The strength of the brighter fatter effect is also significantly impacted by the change in parallel swing for e2v sensors. The a_{00} parameter increases from $3.08 \times 10^{-6} \rightarrow 3.49 \times 10^{-6}$ for e2v sensors, a 13% increase. ITL sensors are not significantly impacted.

- **Divisadero:** The strength of Divisadero tearing is impacted by idle flush. For e2v sensors, we measure a reduction in maximum Divisadero signal from 0.62% 0.25%, a 60% reduction in signal. ITL sensors did not exhibit a strong divisadero signal under the initial conditions, and therefore did not measure a reduction in maximum Divisadero signal (0.273% 0.274%). The initial strength of Divisadero tearing in ITL sensors is taken as a reference size, and is therefore not minimized by the change in idle flush.

Parameter [unit]	Specification	e2v		ITL	
		R7 initial	R7 final	R7 initial	R7 final
Serial CTI [%]		1.1357E-5	7.3015E-6	1.6478E-4	1.5221E-4
Parallel CTI [%]		1.0555E-5	1.1111E-5	-4.7850E-6	1.2103E-6
Dark current [e-/pix/s]		0.024783	0.023188	0.021217	0.020734
Bright defects [count]		0	0	0	0
Linearity turnoff [e-]		167,796	136,302	178,153	178,177
PTC turnoff [e-]		132,963	102,713	128,594	128,487
PTC Gain [e- / ADU]		1.4812	1.5107	1.6761	1.6752
PTC a_{00} [$\frac{1}{pix^2}$]		3.0863E-6	3.4899E-6	1.7031E-6	1.7009E-6
BF x-correlation		0.51693	0.51022	0.75212	0.73648
BF y-correlation		0.17077	0.16740	0.28695	0.28439
Row-means variance		0.88367	0.86809	0.94664	0.94633
Dark defects [count]		3	3	7	7
Divisadero tearing maximum [%]	None	0.62622	0.24599	0.27348	0.27414
Persistence [ADU]	None	5.6673	0.40181	0.48018	0.32639

Table 6: Comparison of median parameter values on each amplifier between Run 7 initial and final measurements, separated by detector type.

All other metrics were not significantly impacted by the final operating conditions. For a complete list of the final operating conditions of LSSTCam as a result of Run 7 testing, see Section 7.1.

5.4 List of Non-Functional Amplifiers

We classify amplifier sections as non-functional if they produce effectively no signal (*dead*) for incident light, or if the read noise level is above $18e^-$ (*hi-noise*). Dead amplifiers are found with either read noise levels below $4e^-$ which indicates no signal is reaching the ADC, or from anomalous PTC gain values, outside the range 1.2–2.0 (or 0.8–1.8 for BOT data).

A list of nonfunctional amplifiers on Science Rafts was produced from both single-raft testing as well as a selection of runs from the BOT data taking period. A summary of those amplifiers is shown in Table 7. As the table indicates, two amplifiers (R01_S01_C00 and R10_S00_C00) transitioned from dead to working during the course of the BOT testing, and another channel (R03_S11_C00) was dead in single-raft testing, then began working during BOT testing but was dead at the end of BOT testing. At the end of the BOT testing, only (R03_S11_C00 and R30_S00_C10) were classified as dead. Furthermore, of the six channels that were flagged as hi-noise during single raft or BOT testing, only one (R41_S21_C02) remained as hi-noise at the end of BOT testing.

Channel	Problem	Single Raft testing	Run 12433 Oct 19	Run 12610 Oct 20	Run 12795 Nov 20	Run 12845 Jan 21	Run 13016 Nov 21	Run 13101 Nov 21	Run 13137 Dec 21
R01_S01_C00	Dead Amp	Dead	Dead	OK	OK	OK	OK	OK	OK
R01_S02_C07	Hi Noise	OK	27e	22e	20e	21e	15e	14e	14e
R01_S11_C00	Hi Noise	OK	24e	OK	OK	12e	OK	OK	OK
R03_S11_C00	Dead Amp	OK	NA	OK	OK	Dead	Dead	Dead	Dead
R10_S00_C00	Dead Amp	Dead	NA	OK	OK	OK	OK	OK	OK
R30_S00_C10	Dead Amp	Dead	Dead	Dead	Dead	Dead	Dead	Dead	Dead
R41_S11_C14	Hi Noise	OK	NA	36e	OK	OK	OK	OK	OK
R41_S21_C02	Hi Noise	OK	NA	OK	108e	96e	85e	110e	115e
R43_S02_C03	Hi Noise	18e	NA	18e	18e	18e	17e	18e	17e
R43_S20_C14	Hi Noise	OK	NA	OK	OK	69e	145e	OK	OK

Table 7: Table of non-functioning Science Raft amplifiers. For hi-noise amplifiers the measured read noise is listed for levels above $12e^-$.

Next, we list non-functional amplifiers detected in full Camera EO testing during Runs 6a, 6b and 7. We filter for potentially non-functional amplifiers with the same cuts as above a) read noise less than $4e^-$, b) read noise greater than $18e^-$, or c) PTC gain outside the range from $1.2 - 2.0e^-/ADU$ in a number of B sequence runs (13391,13557,E1110,E1363,E1880,E2233,E3380) and PTC runs (13412,13591,E1113,E1364,E1881,E2237,E3577). Note that one amplifier flagged in the BOT EO period (R10_S00_C00) is not flagged here, while there is one new amplifier (R03_S01_C05) which had never previously been flagged as non-functional. To study these further, the PTC and linearity plots for these eight amplifiers are shown in PTC runs in Figure 66 and Figure 67. The eight amplifiers flagged by this selection are listed in Table **??**, with comments. Note that the amplifiers listed as *Dead* come in two flavors: no signal whatsoever (R30_S00_C10) or a tiny signal roughly linear with input but reduced by 10^3 (R01_S01_C00,

R03_S11_C00).

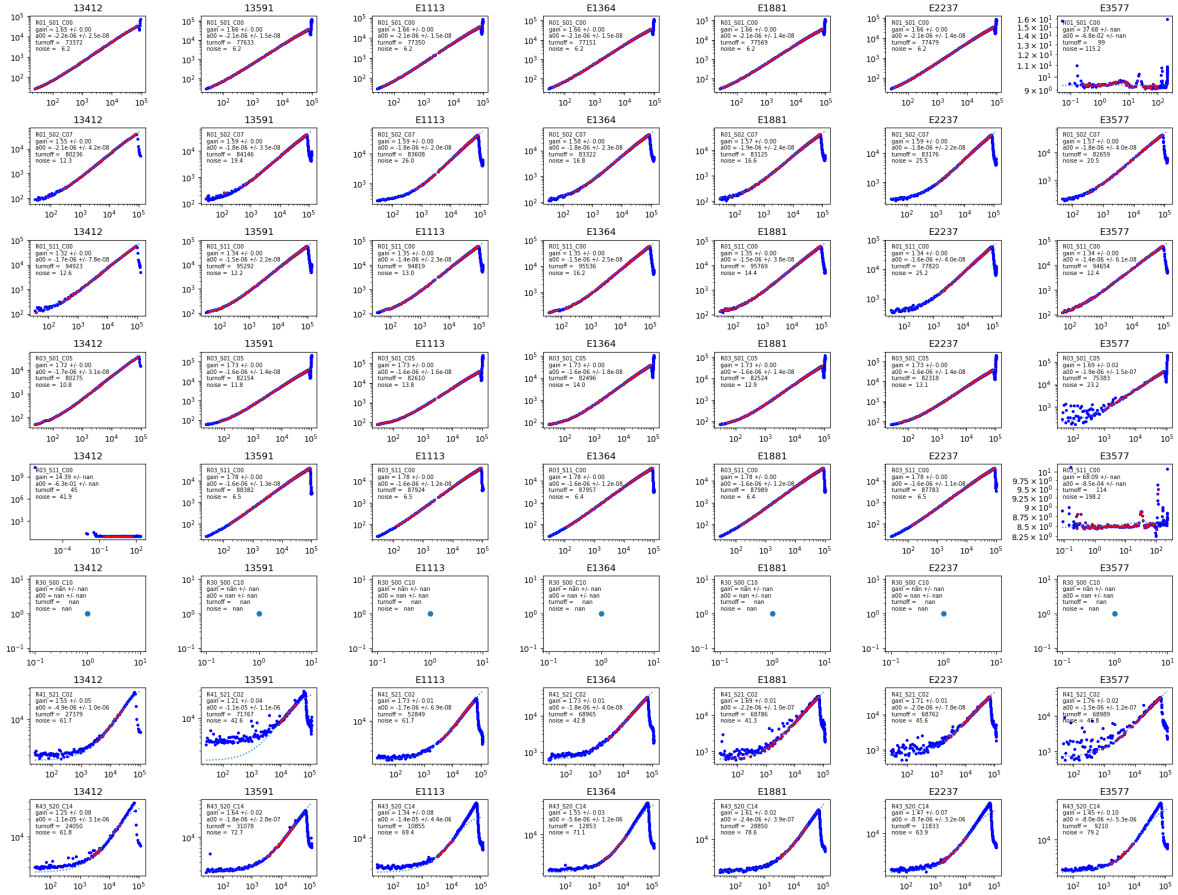

Figure 66: PTC plots for amplifiers flagged as potentially non-functional, from Dense PTC runs

Channel	Summary	Comments
R01_S01_C00	SometimesDead	Usually OK, turns Dead in E3577, previously seen as Dead
R01_S02_C07	OK	noise fluctuates sometimes over $18e^-$ consistent with previous behavior
R01_S11_C00	OK	noise fluctuates sometimes over $18e^-$ consistent with previous behavior
R03_S01_C05	SometimesHiNoise	previously OK, High Noise in E3577 for first time, NEW bad amp
R03_S11_C00	SometimesDead	Usually OK, turns Dead in E3577, previously seen as Dead
R30_S00_C10	Dead	always Dead
R41_S21_C02	HiNoise	always Hi Noise
R43_S20_C14	HiNoise	always Hi Noise

Table 8: Table of potentially non-functioning Science Raft amplifiers, from Runs 6a, 6b, and 7. Categories are OK, SometimesHiNoise, SometimesDead, HiNoise, Dead.

Finally, we list non-functional Corner raft amplifiers, selected with the same filter. There are three such amplifiers all in Guide sensors, that have been non-functional since single CCD testing. These CCDs were selected for the Guiders due to the single non-functional amplifier, rather than use a fully working Science grade device. PTC and linearity curves for these channels, for three dense PTC runs, are shown in Figure 68, to classify these channels as either Dead or HiNoise. These three channels are listed in Table 9

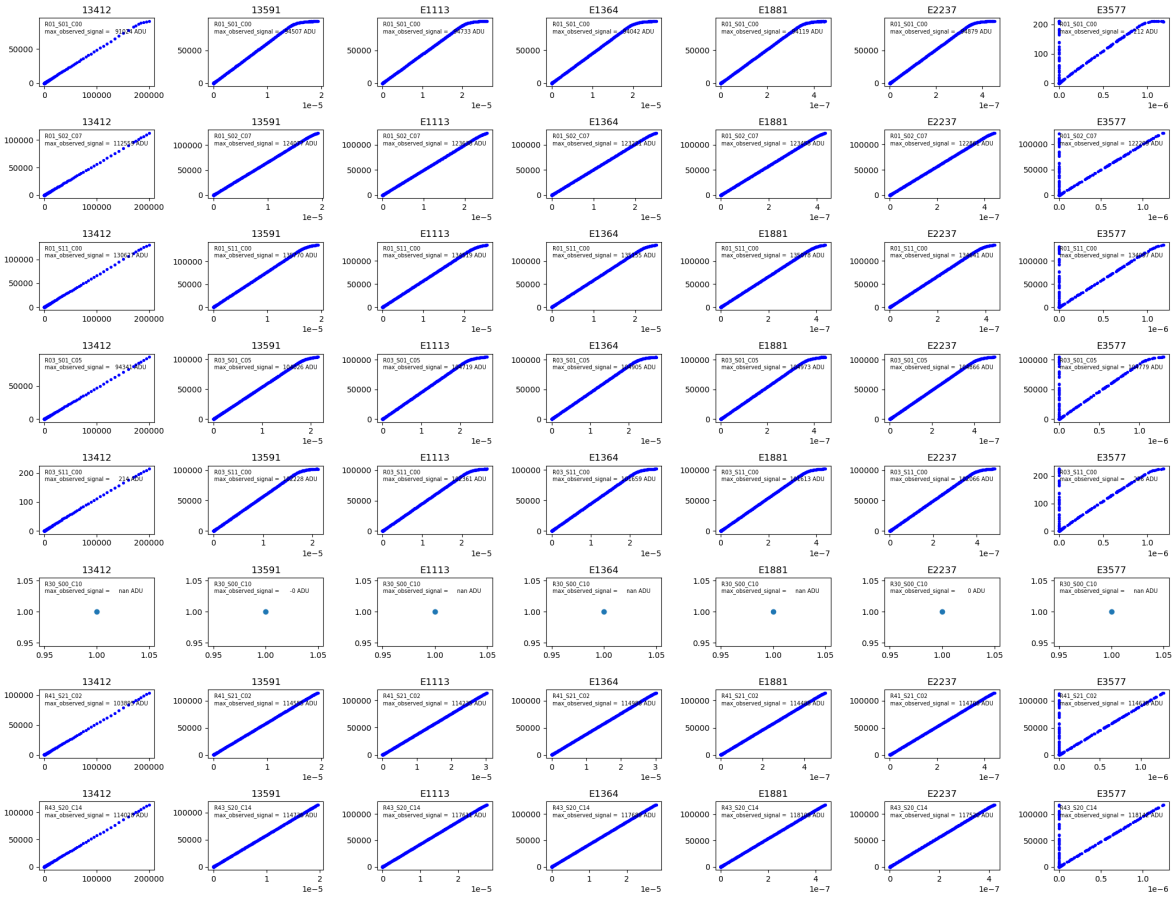

Figure 67: Linearity plots for amplifiers flagged as potentially non-functional, from Dense PTC runs

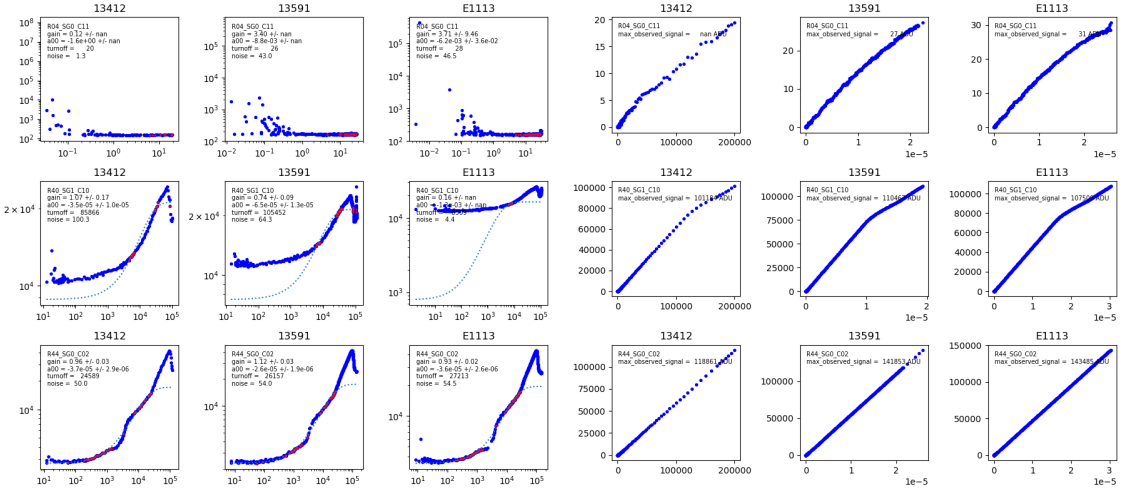

Figure 68: PTC and Linearity plots for Corner Raft amplifiers flagged as potentially non-functional, from Dense PTC runs

Channel	Summary	Comments
R04_SG0_C11	Dead	always Dead
R40_SG1_C10	HiNoise	always Hi Noise
R44_SG0_C02	HiNoise	always Hi Noise

Table 9: Table of non-functioning Corner Raft amplifiers, from Runs 6a, 6b, and 7. Categories are OK, SometimesHiNoise, SometimesDead, HiNoise, Dead.

5.5 Full well measurements

5.6 Non-linearity studies

PTC runs are meant primarily to measure variance and co-variance curves. We collect pairs of flat images, obtained using the CCOB wide-beam described in 2. To cover the entire dynamic range of the CCDs, we vary the length of the LED flash, the number of flashes, and the current of the LED. These data sets can be used to measure nonlinearity by comparing the CCD response to the integrated signal measured from a photodiode installed on a port of the integrating sphere that feeds a picoammeter. To avoid any shortcomings from picoammeter nonlinearity, we only compare photodiode signals of the same amplitude (illumination intensity) but different durations. We do not assume that integrated charges measured at different LED currents (and hence different photodiode currents) are on the same scale, although this turns out to be essentially true, as discussed later.

For the nonlinearity study, we use the average signal measured on each CCD channel separately, using 2D overscan subtraction and masking outlier pixels. The photodiode signal is simply bias-subtracted and time-integrated.

Technically, we model the nonlinearity using a spline function that we fit to the CCD/photodiode data pairs by minimizing:

$$Q = \sum_{ij} w_{ij}^2 \left(\frac{S(\mu_{ij}) + \mu_{ij}}{D_{ij} f_i} - 1 \right)^2 \tag{1}$$

where Q_{ij} is the CCD signal measured in exposure j at LED current i, D_{ij} is the corresponding photodiode signal, f_i is the "photodiode factor" for current i, S is the spline nonlinearity correction, and w_{ij} is some weight. We add two constraints: the average of the spline over the fitting range is zero $< S(\mu) = 0 >$, and $S(0) = 0$. If we choose equal fitting weights $w_{ij} = 1$, the residuals exhibit a scatter that varies a lot with signal level, and hence forbid meaningful outlier detection. We model the fitting weights w_{ij} using an expression determined empiri-

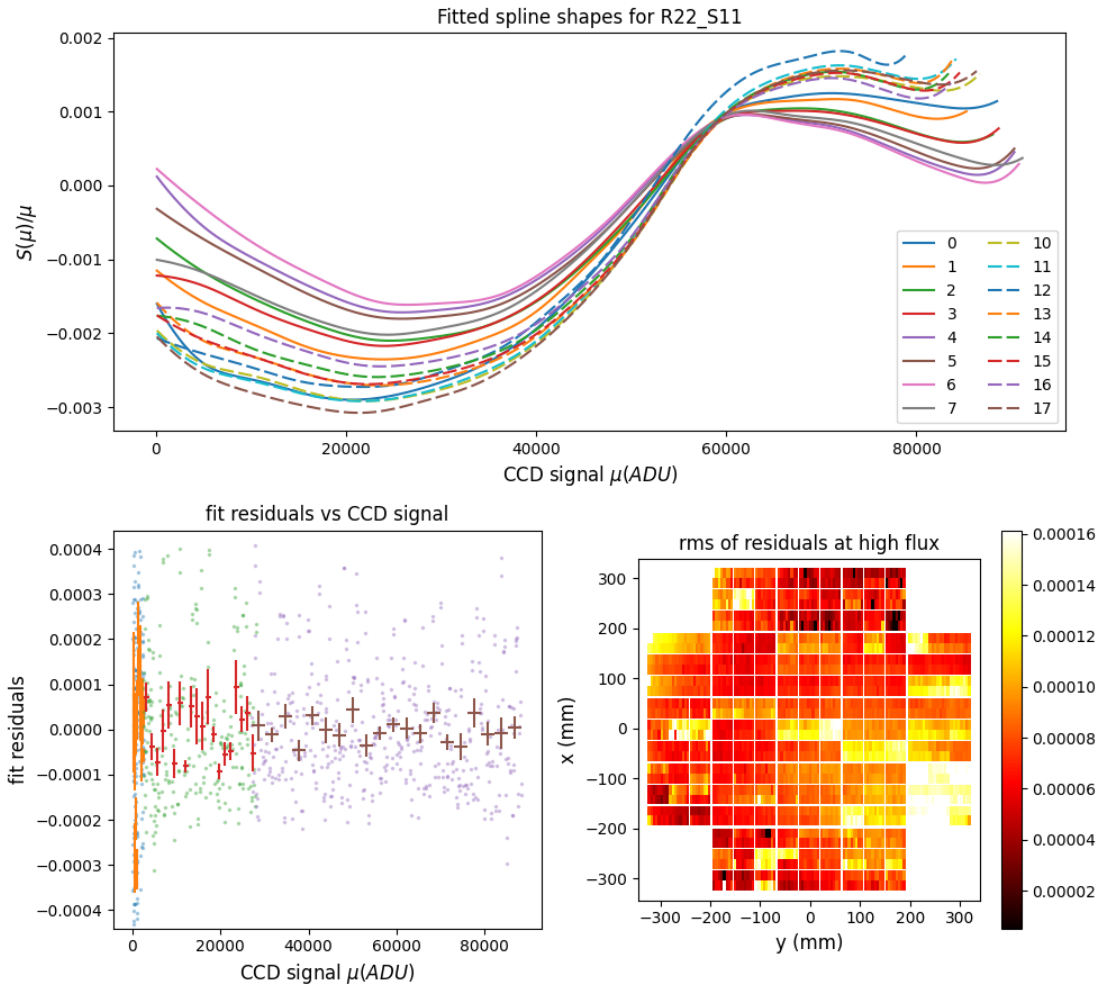

Figure 69: top: fitted nonlinearity spline (divided by the signal level) for the 16 channels of the central CCD. The main feature is due to the distortion introduced by the preamplifier. Left bottom: The fit residuals for channel 0 of the same CCD. Different colors refer to different LED current settings. Bottom right : r.m.s of high-flux fit residuals (the c parameter of the fitted dispersion model) for all camera channels. Those are about 10^{-4} on average, and some are correlated within REBs, for an unknown reason. The quality of the obtained correction is well within goals.

cally, $w_{ij} = 1/\sqrt{c^2 + v^2/\mu_{ij}}$, and the two extra parameters, c and v are also fitted by turning the least-squares expression 1 into a maximum likelihood one:

$$Q = \sum_{ij} w_{ij}^2 \left(\frac{S(\mu_{ij}) + \mu_{ij}}{D_{ij} f_i} - 1 \right)^2 - 2 \sum_{ij} \log w_{ij} \tag{2}$$

We fit the spline coefficients, the f_i factors (there are typically 3 of them), and the weight

parameters c and v, for every image segment separately. We perform an iterative 5σ outlier rejection which rejects on average ~0.5 % of the data points (this small rates validates the modeling of weights). Figure 69 displays some results of the fits. The quality of the measured non-linearity is sufficient for our needs.

5.7 Guider operation

This section describes guider operation.

- Initial guider operation
- Power cycling the guiders to get to proper mode
- Synchronization
- Guider ROI characterization

Table 10: Summary of results for the different Guider configurations.

ROI Size	Integration Time (ms)	Number of Sensors	Number of Rafts	ROI Alignment	Rate (Hz)	Noise (ADU)
Noise Study Configurations						
50x50	50	1	1	n/a	9.28	5.60
50x50	50	2	1	aligned	9.27	4.57
50x50	50	2	1	unaligned	9.26	6.98
50x50	50	4	4	aligned	9.26	4.70
50x50	50	4	4	unaligned	9.26	4.71
50x50	50	8	4	aligned	9.23	4.61
50x50	50	8	4	unaligned	9.23	4.62
Nominal Configurations						
50x50	50	8	4	aligned	9.22	4.61
50x50	50	8	4	unaligned	9.23	6.50
ROI Study Configurations						
400x400	200	1	1	n/a	1.67	4.03
400x400	50	1	1	n/a	2.23	3.95
400x400	5	1	1	n/a	2.48	3.91
10x10	50	1	1	n/a	11.80	13.56
400x400	50	1	1	SplitROI	2.23	105.30

5.7.1 Noise Investigation (take 20 images for each, 15 seconds each)

We measure the noise level of ROIs acquired under various configurations, shown in Table 10. We take 20 images in each configuration, where each image undergoes a 15-second exposure time. Due to different ROI sizes (and thus different read-out frequencies), the number of frames within each image varies. The noise is calculated as the standard deviation of an entire ROI, and averaged over all frames from all of the 20 images. In cases where multiple sensors are running at the same time, the noise is also averaged over all sensors. The images were taken on 30 Nov. 2024 and 01 Dec. 2024. We note that all images taken on 30 Nov. 2024 suffer from an abnormal high-gain sensor state, where the counts level in each image is about one-tenth of expected values. This affects most of the rows in Table 10 except the last two rows. The cause of such an abnormal state is under active investigation.

Guider configurations for Table 10 are listed below:

Start with a single GREB

- Acquire nominal ROI on a single sensor

```
gds_noise_01.cfg
{ "common": { "rows": 50,"cols": 50, "integrationTimeMillis": 50  },
  "R00SG0": { "segment": 3, "startRow":  975, "startCol": 254} }
```

- Acquire nominal aligned ROIs on two sensors on the same GREB

```
gds_noise_02.cfg
{ "common": { "rows": 50,"cols": 50, "integrationTimeMillis": 50 },
  "R00SG0": { "segment": 3, "startRow":  975, "startCol": 254},
  "R00SG1": { "segment": 3, "startRow":  975, "startCol": 254} }
```

- Acquire nominal misaligned ROIs on two sensors on the same GREB

```
gds_noise_03.cfg
{ "common": { "rows": 50,"cols": 50, "integrationTimeMillis": 50 },
```

```
  "R00SG0": { "segment": 3, "startRow":  975, "startCol": 254},
  "R00SG1": { "segment": 3, "startRow": 1075, "startCol": 254} }
```

Four GREBs

- Acquire nominal aligned ROIs on single sensors on all GREBs

```
gds_noise_04.cfg
{ "common": { "rows": 50,"cols": 50, "integrationTimeMillis": 50 },
  "R00SG0": { "segment": 3, "startRow": 975, "startCol": 254},
  "R04SG0": { "segment": 3, "startRow": 975, "startCol": 254},
  "R40SG0": { "segment": 3, "startRow": 975, "startCol": 254},
  "R44SG0": { "segment": 3, "startRow": 975, "startCol": 254} }
```

- Acquire nominal misaligned ROIs on one sensor on all GREBs

```
gds_noise_05.cfg
{ "common": { "rows": 50,"cols": 50, "integrationTimeMillis": 50 },
  "R00SG0": { "segment": 3, "startRow":  775, "startCol": 254},
  "R04SG0": { "segment": 3, "startRow":  875, "startCol": 254},
  "R40SG0": { "segment": 3, "startRow":  975, "startCol": 254},
  "R44SG0": { "segment": 3, "startRow": 1075, "startCol": 254} }
```

ROI reconstruction (take 20 images for each, 15 seconds each)

Unsplit ROI different exposures and sizes

- 200 ms

```
gds_roi_01.cfg
{ "common":{ "rows": 400,"cols": 400, "integrationTimeMillis": [200] },
  "R00SG0": { "segment": 2, "startRow":  800, "startCol": 54} }
```

- 50 ms

```
gds_roi_02.cfg
{ "common":{ "rows": 400,"cols": 400, "integrationTimeMillis": 50 },
  "R00SG0": { "segment": 2, "startRow":  800, "startCol": 54} }
```

Impact on science sensors

5.8 Defect stability

5.8.1 Bright defects

5.8.2 Dark defects

5.9 Bias stability

We have found bias instabilities, typically above the 1 ADU level, for a number of CCDs in the focal plane, both ITL and e2v. Two main kinds of instability are observed:

1. ITL bias jumps : large variations of the column-wise structure from exposure to exposure.
2. e2v yellow corners : a residual 2D shape of the bias even after 2D-overscan correction. These residuals depend on the acquisition sequence and the exposure time, and the enhancement is greatest near the readout nodes (hence 'yelllow corner').

Both issues were observed and deeply studied in Run 6 EO data. The ITL issue is believed to be phase shifts in clocks between Readout Electronics Boards (REBs) because REBs rely on the frequency converted from their natural frequency. We tried to mitigate the e2v issue by optimizing the acquisition configuration in Run 7.

For the baseline acquisition configuration (see conclusion), three relevant stability runs were recorded:

1. Run E2136: 15 s darks with some very long delays throughout the run
2. Run E2236: 50 15 s darks, 50 biases recorded with 30 s delays between exposures
3. Run E2330: 15 s and 30 s darks with variable delays between exposures

To analyze these runs for bias instability, the `eo_pipe` bias stability task is used. For the ISR part, a serial ('meanper_row') overscan correction and a bias subtraction (computed from the corresponding B-protocol run) are applied. The final data product of the task is the mean of the per-amplifier science image over the full set of exposures of the run. Two typical examples from Run E2136 are shown in Figure 70. In the stable case, the variations are typically at the 0.1 ADU level; in the unstable case, the variations range up to 4 ADUs.

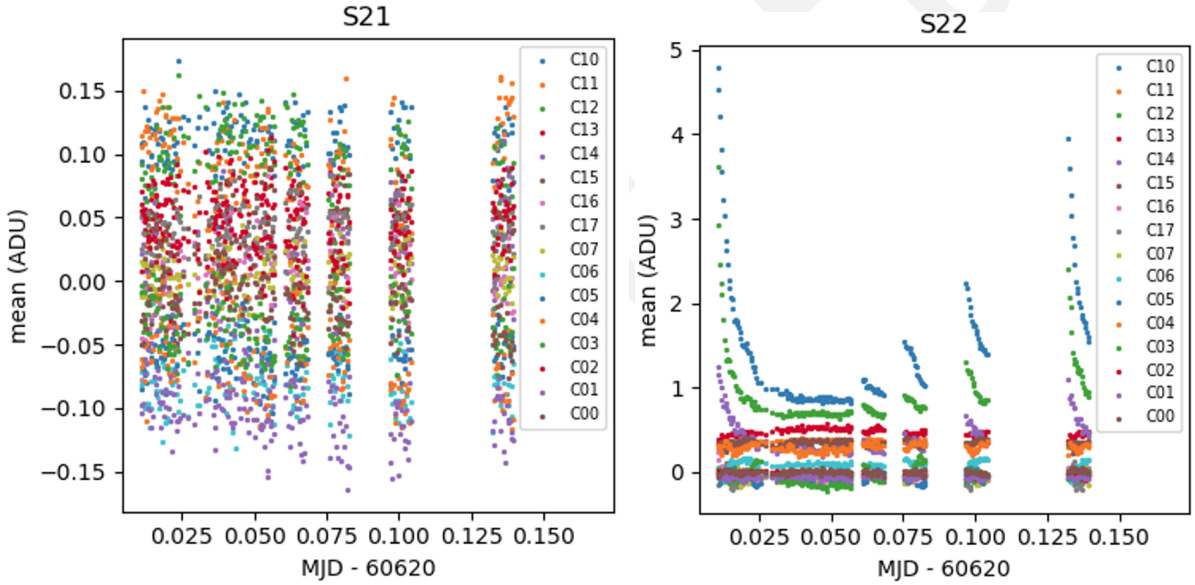

Figure 70: (left) Stable case for bias (R21_S21); (right) Unstable case (R23_S22)

A comparison of the results for an unstable e2v CCD (R33_S02) is shown in Figure 71 for the three runs.

To highlight the 2D shape differences in e2v bias instability, a 2D-overscan correction is applied. A few exposures illustrating the variations of the 2D shape for the same unstable CCD R33_S02 are shown in Figures 72-74. The 2D shape of the image in amplifier C01 is different in the 3 cases.

In order to quantify the number of unstable e2v amplifiers, a stability metric *d* is defined from the `eo_pipe` stability task data products. More precisely, *d* is defined, for a given amplifier in a

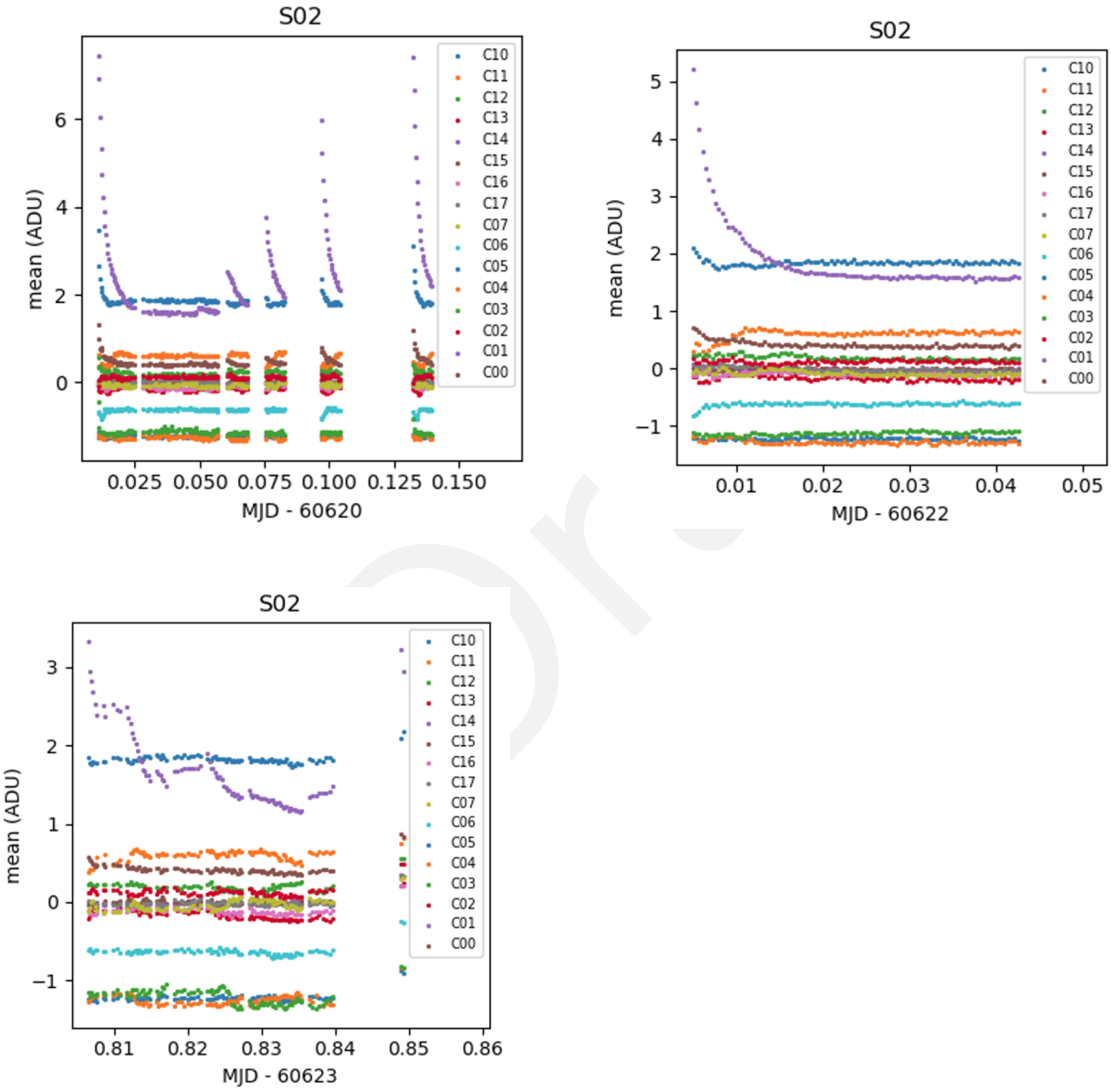

Figure 71: Bias level variations for R33_S02, an unstable e2v CCD for three runs: (upper left) E2136, (upper right) E2236, (lower left) E2330. The segments CXX and CYY are most strongly variable in each run. Note that the range of the time axes is different in each plot.

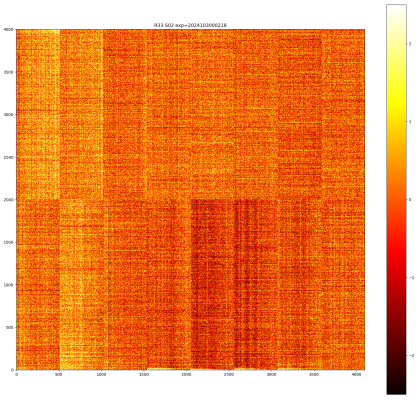

Figure 72: Bias exposure, run 1880, R33_S02

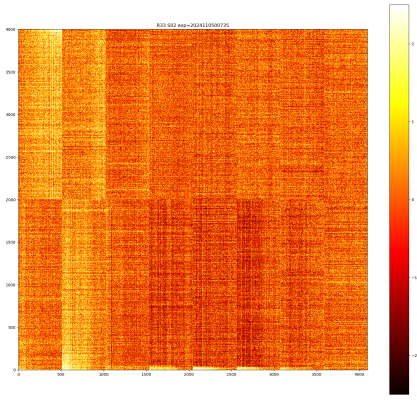

Figure 73: 15-s dark exposure, run E2136 in 'stable' conditions, R33_S02

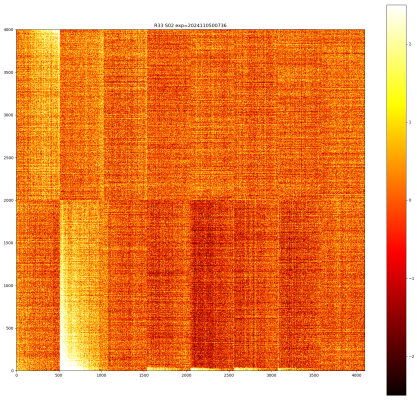

Figure 74: 15 s dark exposure, run E2136 after a 3 min delay, R33_S02

given run, as the difference between the 5th and 95th percentiles of the image mean over all the bias image acquisitions. The distribution of d for run E2136 is shown in Figure 75. Applying a threshold at 0.3 ADU, 51 amplifiers are identified as unstable (see the corresponding mosaic in Fig. 76). This corresponds to ~3% of the e2v amplifiers.

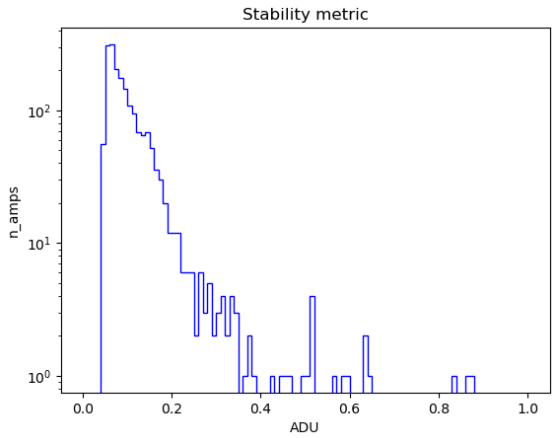

Figure 75: Distribution of the stability metric for the e2v amplifiers in run E2136

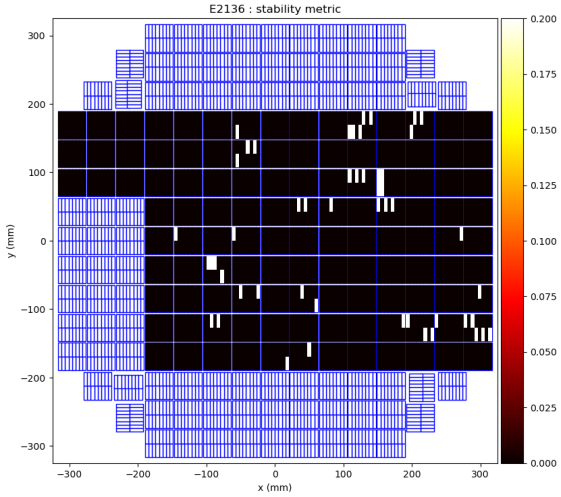

Figure 76: Mosaic of e2v amplifiers identified as unstable (white color) in run E2136

Further studies are required in order to converge on the best mitigation strategy for the start of the LSST survey.

5.10 Gain stability

We use “relative gain” in this section to study gain stability over time. The relative gain is defined as the ratio of the signal observed in a CCD image segment divided by the integration of the photodiode current with respect to an arbitrary normalization. With a fixed flat illumination, the variation of the relative gain over successive exposures can be utilized to investigate the gain stability. In the past run (Utsumi et al., 2024), we used the run that was obtained at the constant temperature, which reflects the real observing condition. We repeated this test during Run 7 and we acquired flat images at the two representative flux level with two distinct temperature conditions: either intentionally altered or maintained constant.

- E1496 (dp80, 6 hours, constant temp, v29_Nop, nm750, 10k e-)
- E1367 (dp80, 6 hours, temp swing, v29, nm750, 50k e-)

- E756 (dp80, 6 hours, gain stability @ 50k e-), unprocessed
- E1362 (dp80, 6 hours, 10k e-), unprocessed

Here we focus on E1496 and E1367 which have a difference in the temperature condition whether the temp was kept constant (E1496) or altered (E1367).

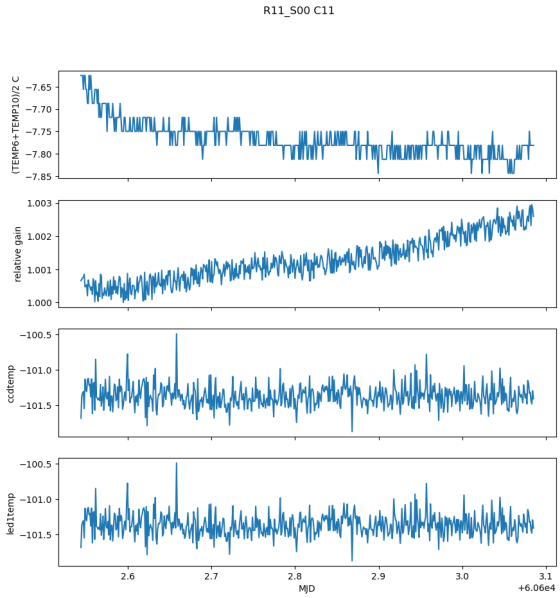

Figure 77: relative gain changes with other parameters for one amplifier R01/S00/C11 in run E1496

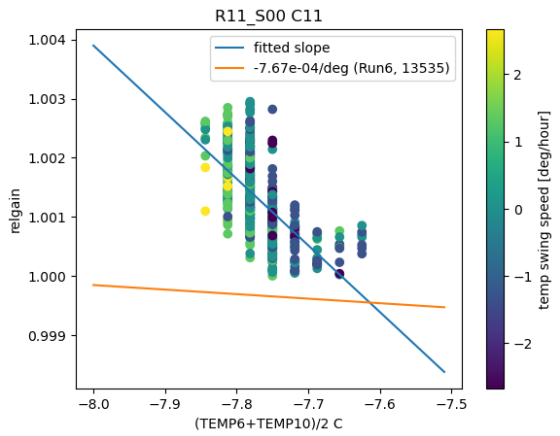

Figure 78: Relative gain as a function of REB temp (TEMP6 and TEMP10), with color based on temperature swing run E1496

Figure 77 shows the derived relative gain change for one amplifier (R11/S00/C11) over time alogn with other representative parameters such as an aggregated REB temperature (TEMP6+TEMP10)/2, CCD temp, and led1temp (the temperatue measured at the LED board on the CCOB projector). The REB temp was determined as a good proxy for the relative gain change in the past run. As the intention of the acquisition condition, the REB temperature was almost maintained at the same level within 0.2 deg, with a slight decreasing slope probably due to the change in the thermal load and stabilization process of the entire thermal system. At the same time the gain slowly increase over time, while other CCD, LED temperatures are kept at the same.

Figure 78 shows the relationship between the relative gain and the REB temperature, with color coding by the speed of temperature change, along with its fit. A reference line from the past result is overlaid with an arbitrary vertical offset. Clearly, the gain-temp relationship is steeper than the previous result. The distribution of the data points has a more complicated

structure than the linear relationship, while there is no obvious change in either CCD nor LED temperatures.

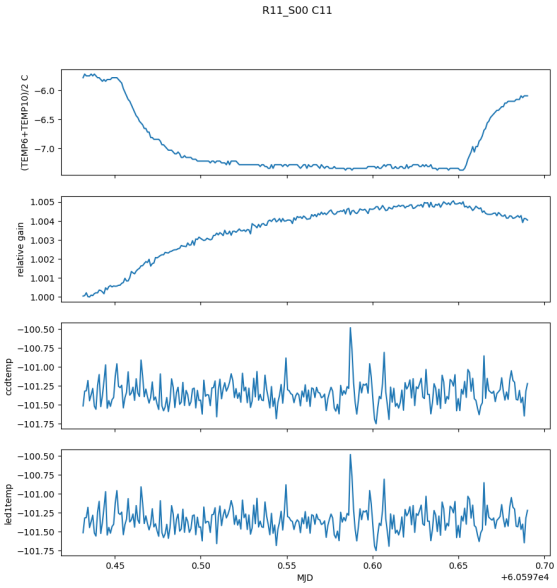

Figure 79: relative gain changes with other parameters for one amplifier R01/S00/C11 in run E1367

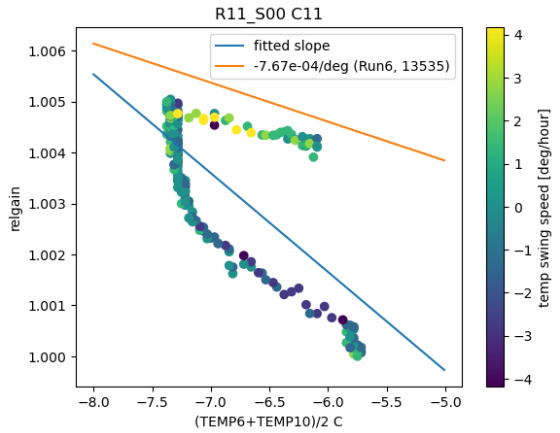

Figure 80: Relative gain as a function of REB temp (TEMP6 and TEMP10), with color based on temperature swing run in run E1367

Figures 79 and 80 show the same set of figures but for the Run that has a temperature change in the cold plate by 2 degrees. The temperature was kept the same in the beginning, but the set point was changed later, and then it was brought back to the original temperature. Clearly, Figure 80 shows not only temperature dependency but also hysteresis in the gain-temp relationship, which does not match the slope originally derived from the past run, although there are no obvious changes in the system other than the REB temperature.

The reason why the relationship becomes much more complicated is not clear. It is understandable that hysteresis was not observed in Run 6 because there was no intentional temperature change in the cold plate, which means the cold plate/REB temperature swing was minimal. However, looking at the result from E1496 where we took images at the same temperature, the relationship is much more complicated than what it looked like before. A number of possibilities can be considered to explain this: 1) there is a hidden variable that changes the gain other than the REB temp, 2) illumination from the LED is somehow changing overtime, which is not correlated with the LED temp, 3) air turbulence in the lens volume contributes to this, or 4) condensation on the lens might come into play. As the hysteresis is observed, the possibility 1 is definitely present but it cannot explain the gain temp change in the constant

temperature. For the possibility 2, it is unlikely given the fact that Run 6 observed the complicated relationship. The option 3 could play some role since Banovetz et al. (2024) discovered illumination changes due to the turbulence in the lens volume. However, it is not clear if any kind of long-term trending over 6 hours can be explained by this. For the possibility 4, we did visual check in a different period and we did not find anything obvious.

The gain change issue can be split into 2 categories: global or local in an amplifier. The global coherent change can be, in principle, correctable as it degenerates with the atmospheric transparency, which will be corrected by the calibration process. The local amp-by-amp change is a more serious issue in respect because the number of stars might not be sufficient for making the precise photometric calibration statistically. In order to study the local amp-by-amp gain change, Figures 81 for the constant temperature condition and 81 for the temperature swing condition show the differential gain changes with respect to the medianed relative gain for the entire focal plane.

The differential gain change with respect to global change for the constant temperature appears mostly stable within the level of 10^{-4}. Some of the measurements deviated from zero because of the normalization of the first measurement. R11/S12, R12/S10, R12/S22, R24/S11, R34/S20 have one amplifier that have a higher relative gain than up to 5×10^{-4} but others behave stable. This could be contaminated by the yellow corner in e2v sensors but this could be mitigated by throwing away the first few exposures, which probably required for other aspect such as bias instability. Further investigation is needed. Another interesting behavior is seen in R11/S2x. There were a spike in three sensors at the same time. We have not figured out what happened at that time.

The case for the temperature swing is complicated. Some of the amplifiers behave as well as the ones for the constant temperature case, but some of the amplifiers show correlation with the temp change in the Cold plate temp. This indicates that the relative gain change among amplifiers with respect to REB/Cold plate temperature exists. Note that E1367 has a 5 times higher flux than E1496, which reduces shot noises in the measurement. However, the conclusion still holds.

To further study, we step back to the raw measurements. Figure 83 shows the constant temperature case. The change in the relative gain is a level of 2×10^{-4}, which appears to be driven by the photodiode integration. Figure 84 shows the temp swing case with a change of 5×10^{-4}, which appears to be dominated by a change in image counts. The changes in the PD integra-

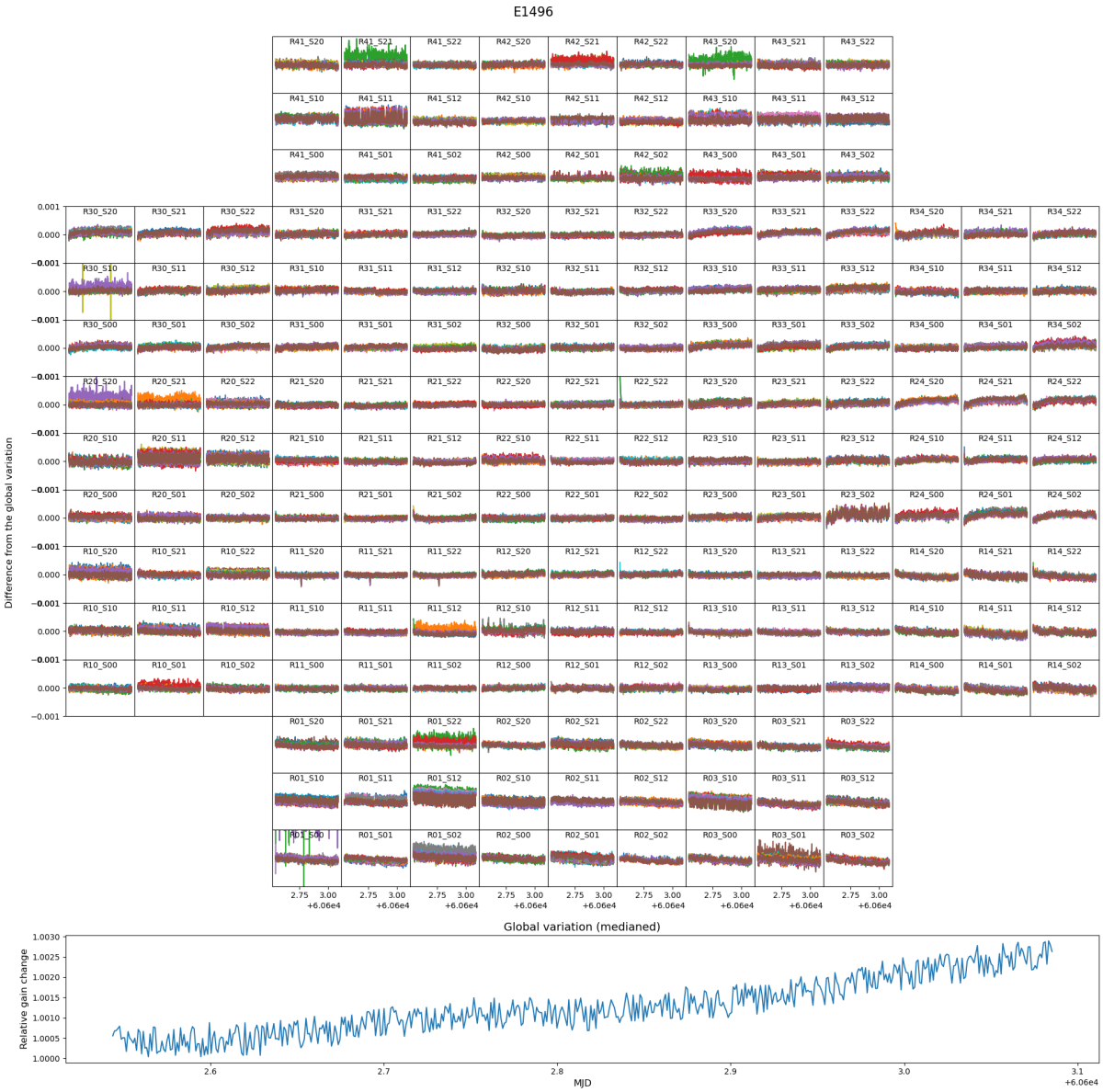

Figure 81: Differential gain change with respect to the median of relative gain change for the whole focal plane, for E1496

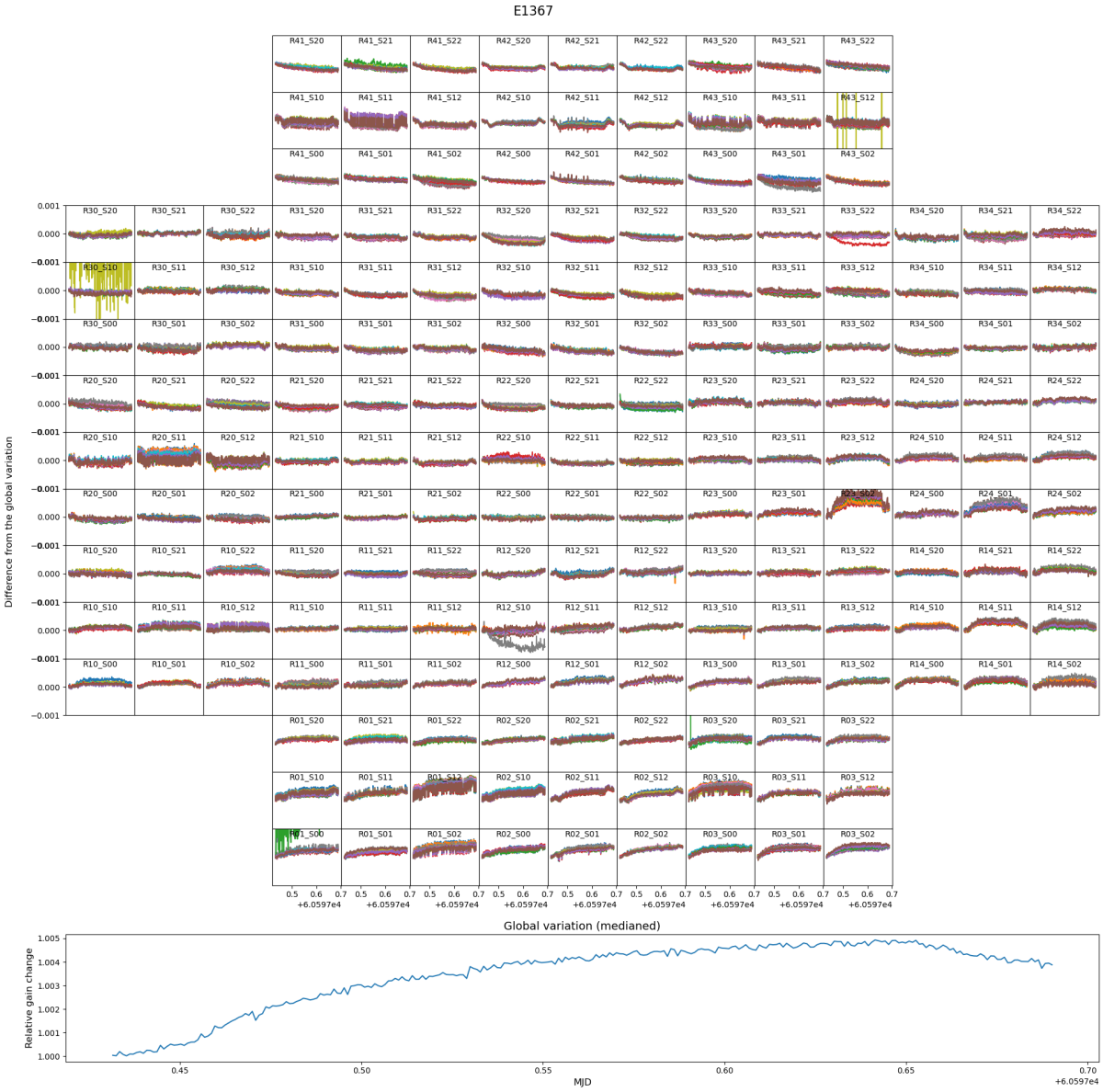

Figure 82: Same as Figure 81 but for E1367

tion are about the same in both plots. So from these facts, both of the gain change in the Camera due to the temperature change and some illumination difference of the CCOB projector play role here.

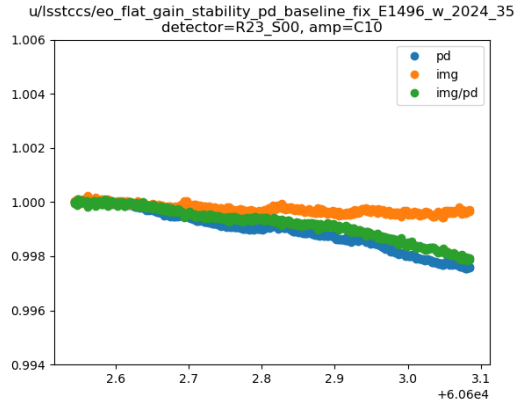

Figure 83: Raw measurements of image count and photodiode integration, as well as the ratio of those – the relative gain for E1496

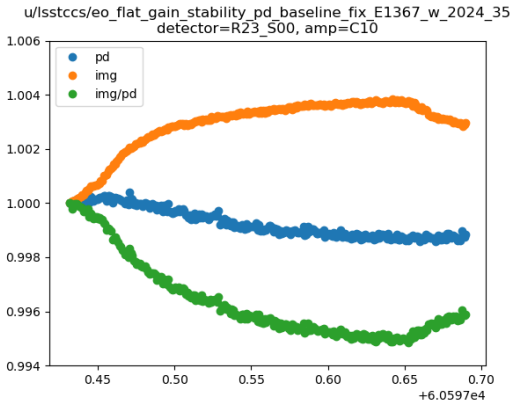

Figure 84: Same as Figure 83 but for E1367

In summary, we find

- The gain-REB temperature relationship is not as simple as Run 6.
- Global gain change could be due to the artifacts/setup, or potentially, the Camera could have a complicated behavior with respect to the REB temperature. No conclusive statement can be drawn.
- Local amp-by-amp gain change is minimal 10^{-4} over 6 hours if the REB or the focal plane temperature is maintained at the same.
- Further analysis is needed in understanding the gain change in the beginning of Run and some random spikes is needed.

6 Sensor features

6.1 Tree rings

Tree rings is circular variations in silicon doping concentration which can be observed in flat images. Both LSST The impact of the tree rings is assessed in (Esteves et al., 2023). In this section we describe an attempt to measure tree rings for each sensor from the laboratory data taken in Run 7.

6.1.1 Center of the Tree Ring

From the past study, the center of tree rings is known to have 4 distinct positions with respect to each sensor. This is because four (4) CCD is cut from one wafer. So far we have been using the four average position for the center of the Tree ring, according to the pattern direction, because it was difficult to make measurement of the treering for all the sensors due to their low amplitude. However we have new data with 0 V of back bias voltage, which increases the amplitude of the treering, allowing us to revisit the measurement of each individual center.

Figure 85 shows the positions of the Tree ring centers measured for the 189 sensors. All the measurements are concentrated around each averaged position, however, as now we have better individual measurements, we decided to use center of each sensor instead of the average value.

6.1.2 Radial study

Radial study for Tree rings pattern has been done to see if the rings are perfectly circular in shape.

Figure 86 illustrates the transformation of a flat image into a radial profile plot as the y axis to be the distance from the center of the rings.

6.1.3 Effect of diffuser

We expect that with the diffuser installed, there will be less contribution from effects such as CMB and weather patterns discussed in § XX. Comparing R22_S12 of Run 6 run 13379 (without diffuser) with Run 7 E937 (with diffuser), we verified the significant improvement from use of the diffuser.

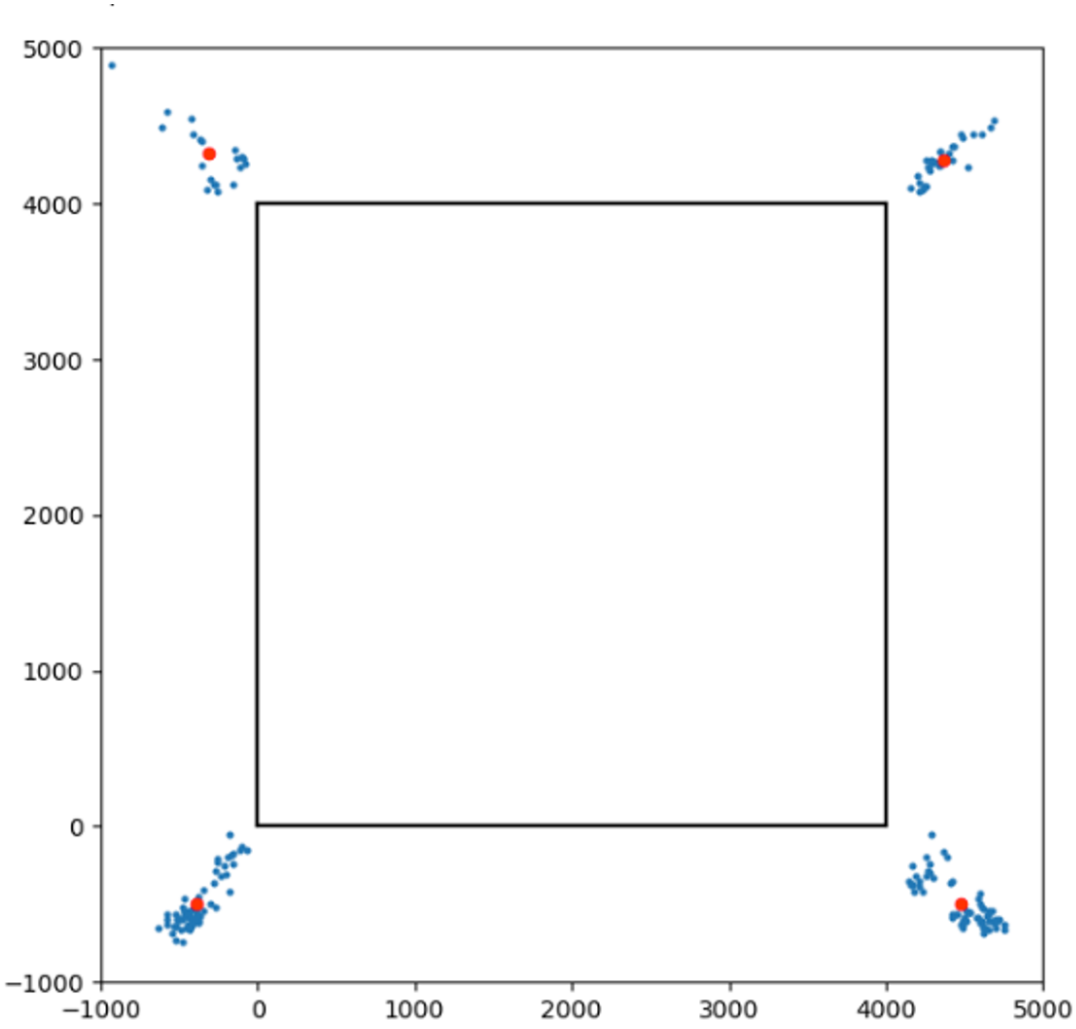

Figure 85: The center of the Tree Rings were measured for all 189 LSST sensors. Red point indicates the average center on each direction.

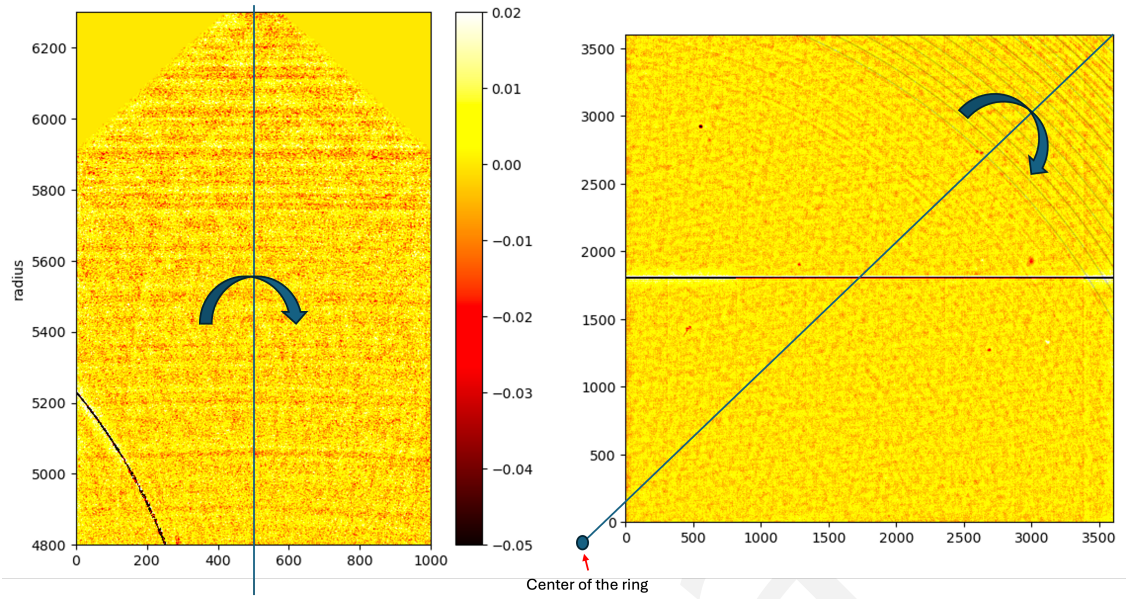

Figure 86: Folding image on diagonal line from the center of the ring, and subtracting from each other.

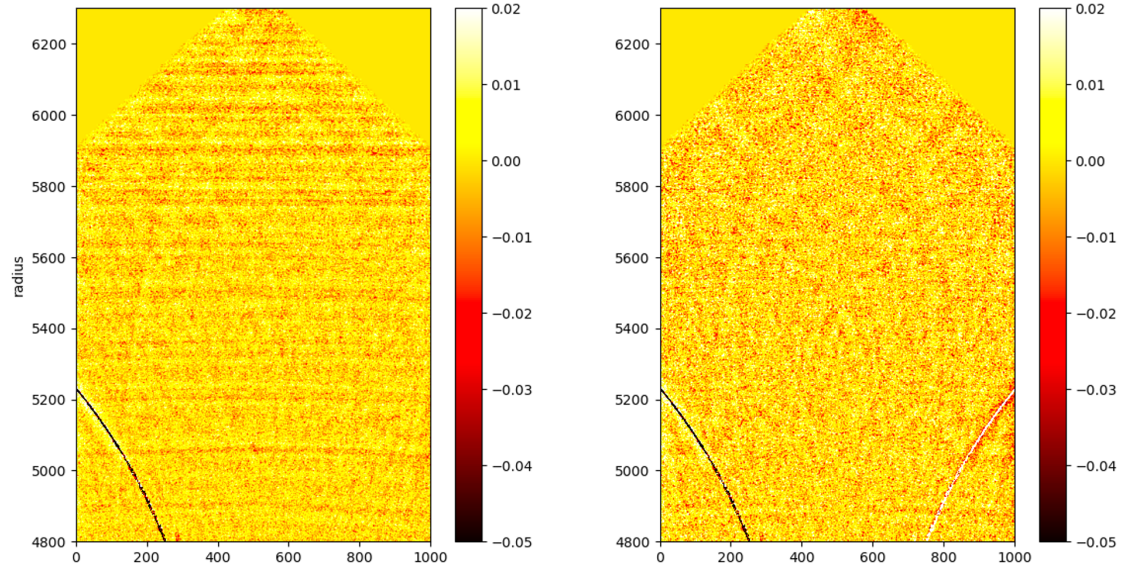

Figure 87: Radial study of the Tree Rings. Right: image subtracting left to right, right to left.

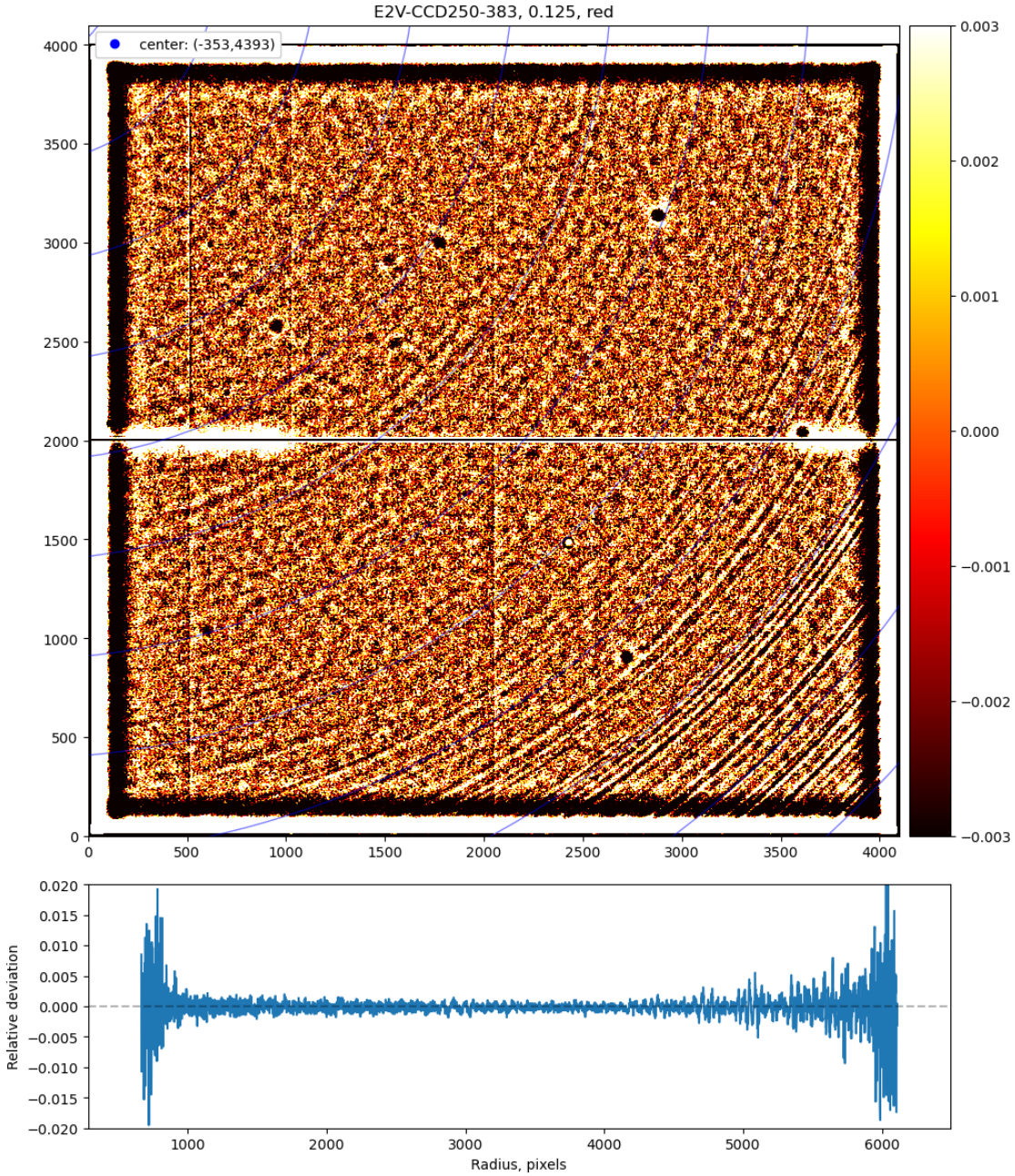

Figure 88: Tree ring without diffuser

6.1.3.1 Tree rings without diffuser

6.1.3.2 Tree rings with diffuser

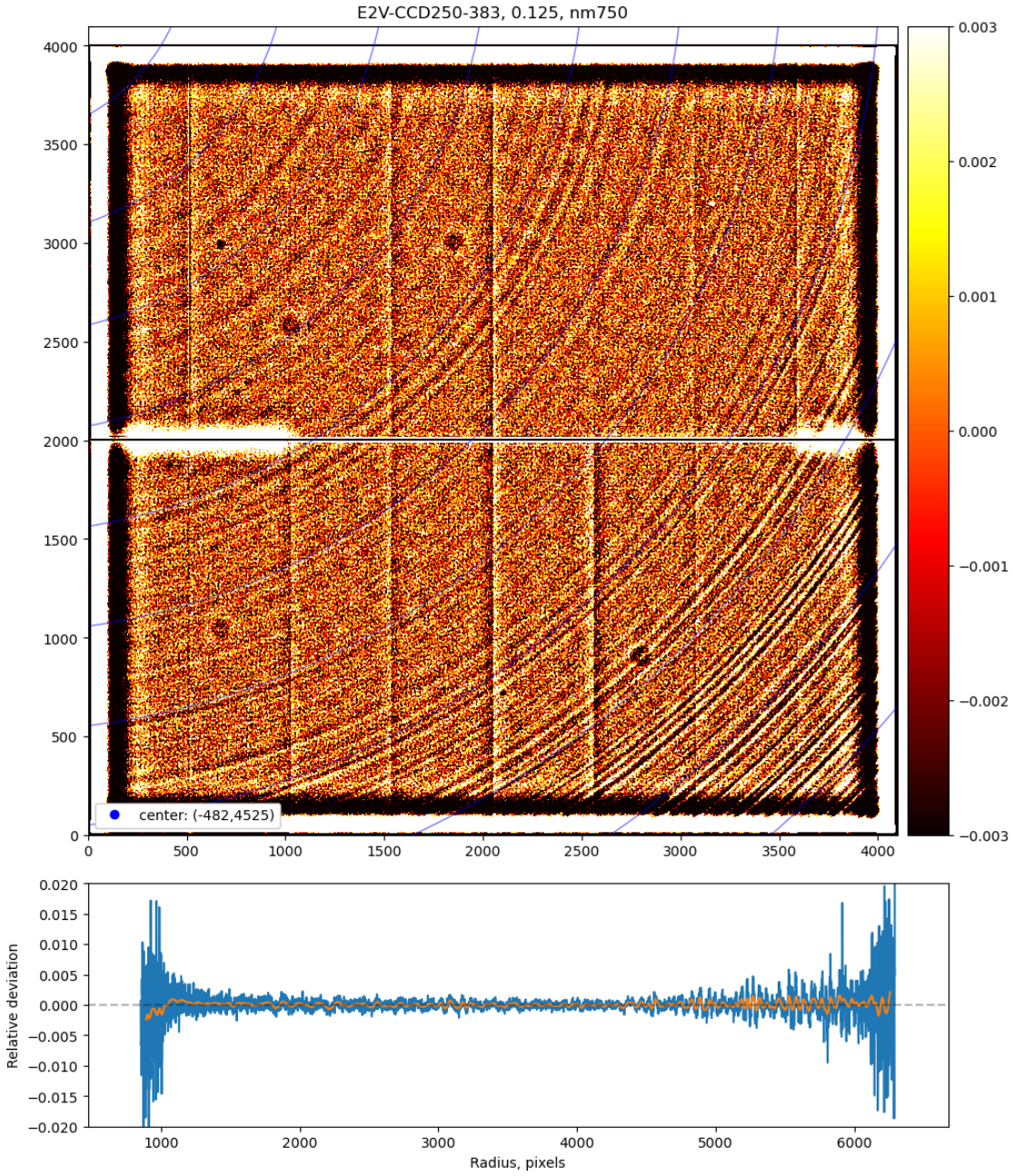

Figure 89: Tree ring with diffuser

6.1.4 Voltage dependency

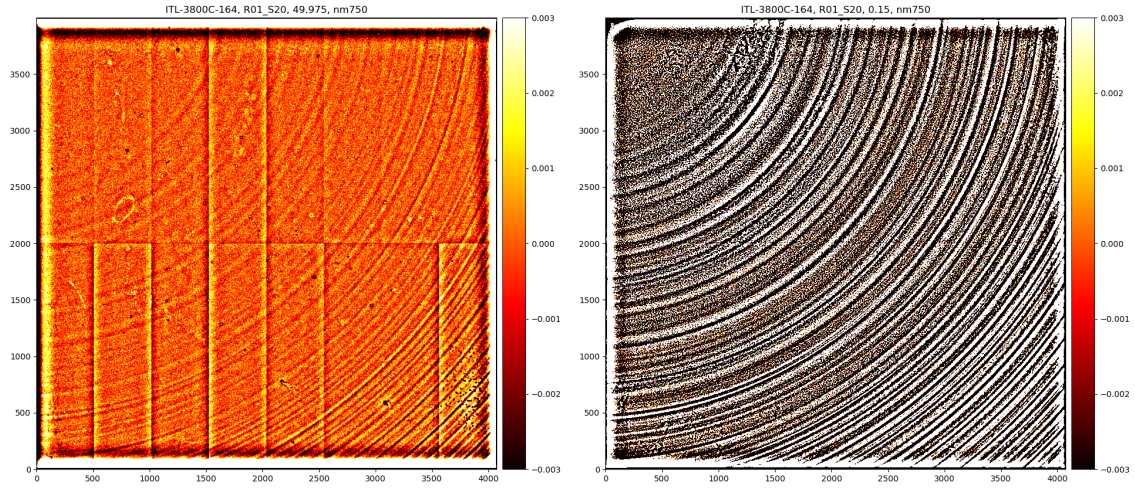

Figure 90: Comparing Tree Rings pattern on the sensor R01 S20 with (left) and without (right) back bias voltage (50 V), we can clearly see that back bias voltage reduces the impact of the tree ring effect.

6.1.5 Wavelength dependency

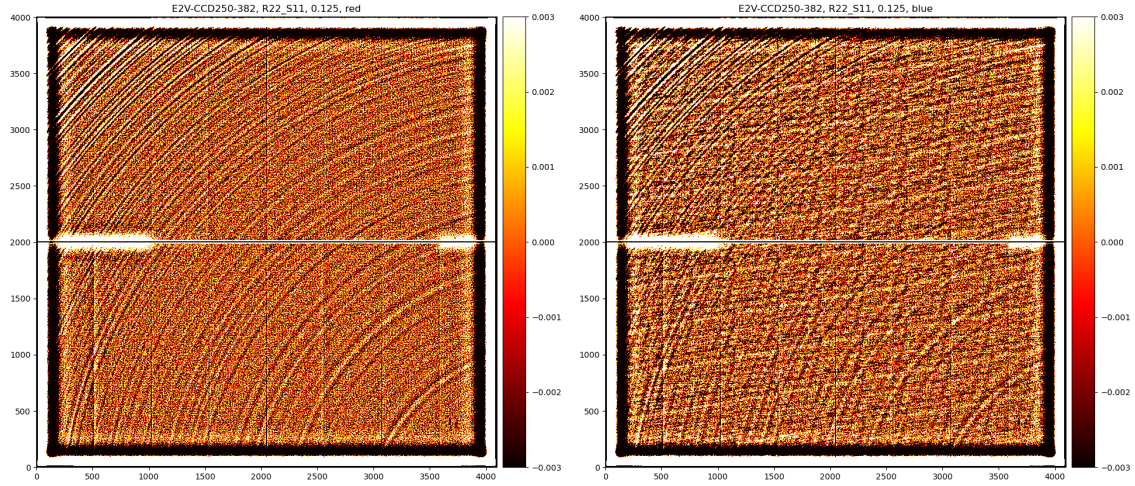

Figure 91: Comparing Tree Rings pattern on the sensor R01_S20 for red (run E1050, left image) and blue (run E1052, right image) wavelength, without back bias voltage.

6.2 ITL Dips

One of the phenomena that was studied in the later part of Run 7 was so-called 'ITL dips'. These were discovered in LSST ComCam on-sky data as bleed trails from bright stars that

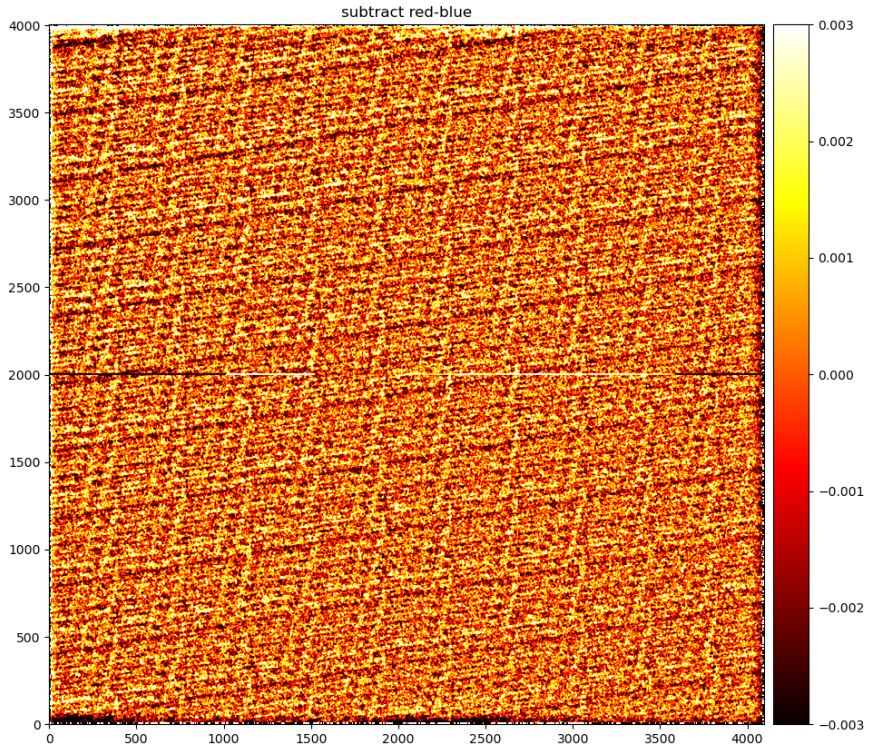

Figure 92: Subtracting blue image from red image

traversed the entire detector, crossing the amplifier boundaries. These bleed trails are unique though in that the core of the bleed trail is actually 'dark' compared to the wings of the trail, with a flux ~2% less relative to the rest of the bleed trail.

We investigated whether ITL dips could also be observed in the CCDs of LSSTCam. For this study, we used spots and rectangles projected onto the focal plane by the 4K projector. The spots were approximately 30 pixels across and were projected onto every amplifier segment of each detector. The rectangles were only in the top right amplifier (C10). One consideration with this spot projection was that the projector also provided background illumination. This led to the spots having a peak signal only 6 times greater than the background and the rectangles having a peak signal 30 times greater than the background.

We were unable to find any evidence of ITL dips in the images. Below are the images themselves along with binned horizontal cutouts of the the amplifier below the source. These show the background pattern of the projector, but no 2% dip.

While we were not able to find evidence of the ITL dip in Run 7 data, it is still not clear whether the effect will be visible in LSSTCam on-sky data. The photon rate of the in-lab data was roughly XXX per second for the 15 s exposures. The stars that were seen in ComCam with the ITL dip have a magnitude of XXX corresponding to a photon rate of XXX. This is combined with a sky background of XXX as compared with the lab sensor background of XXX.

6.3 Vampire pixels

A category of sensor feature found on some ITL sensors, that has recently benefited from fresh attention, now has a new name. They are called *vampire pixels* because of their curious flat field response: a group of pixels with photo-response exceeding the flat-field mean, surrounded by a concentric distribution of pixels with photo-response below the same flat-field mean. The *vampire pixel* name sticks because the over-responsive pixels have apparently "sucked" signal from the rightful owners, a sort of *reverse brighter-fatter* effect excited simply with flat-field illumination.

The sizes of these *vampire pixel* complexes can typically extend to tens of pixels in radius, which place strong constraints on their origin. Also, it turns out that all prominent *vampire pixel* complexes are also seen in their (ITL) phosphorescence response which is indicative of the backside surface layer (*cf.* §6.4). This means that *vampire pixels* are likely to appear also

in dark images, but only if trigger illumination is delivered a few tens of seconds prior to the dark acquisition (*cf.* vampire transients, Tab. 13).

All known cases appear to round or with circular symmetry. There are plenty of cases with similar pixel complexes that lack the central group of pixels with *high-amplitude* photo-response excess, but that the photo-response excess is simply divided into a larger number of pixels. We suggest that the underlying origin of these is common with the easier-to-detect *bright pixels* (*cf.*§6.3.1) but appear with different response properties simply because of mundane geometric details. Different detection algorithms may therefore be required finding those *vampire pixel* complexes that do *not* show central bright pixels as opposed those that *do*. Moving forward, we choose not to invent a new name for the former type, but call them both *vampire pixel* complexes.

6.3.1 First observations

Initial identification of these on ComCam may have been in a study that called them *bright pixels* by A. Roodman (20240827) and quantified in more depth by A. Ferté in a ComCam defects study (20241112). First electrostatic simulations performed to help understand them were made by C. Lage (20241119) who inferred that a circumferential surface charge variations[5] on the backside electrode could reproduce the sort of charge redistribution observed (while conserving photo-conversion charge) – and so these may be effectively described as pixel boundary distortions throughout, mediated simply by lateral (non-axial) contributions to the drift field. Any such lateral fields would mean a localized loss in pixel fidelity, not limited to the sensor's thickness scale (10 pix) as are apparently in effect in other known pixel distortion mechanisms (brighter-fatter effect, tree rings, edge rolloff, tearing, pixel boundary distortions due to midline implant & hot columns).

Since ComCam on-sky data has been available, more attention has been paid to these features and how they may impact source detection and photometric determination of field sources next to them. Luckily, *vampire pixels* are less common on average in the 88 ITL sensors of the Main Camera than they are in the 9 sensors of ComCam.

[5]We suggest that any such variations would necessarily require that the backside electrode ceases to act as an electrostatic equipotential as it does elsewhere on the sensor, with total surface charge density governed only by the normal component of the electric field strength within the silicon, responding to the HV Bias potential, and so on.

6.3.2 LSSTCam vampire pixel features

One prominent example of such a feature is located in the Main Camera on R01_S00_C13-4. This feature is often overshadowed by the bright, dark current "scratch" in close proximity to it (when HV Bias is on). In Figure 93 and Table 11 we include this example along with two other prominent *vampire pixel* complexes (and others) located on ITL sensors in the Main Camera's focal plane to describe their individual properties. Inspection reveals a broad parameter space that describe these pixel complexes that can cause distortion in one way or another as soon as they are used to record cosmic sources: astrometric and shape transfer errors inferred from flat response, and background estimation or source confusion errors from the pixel complexes' phosphorescence properties!

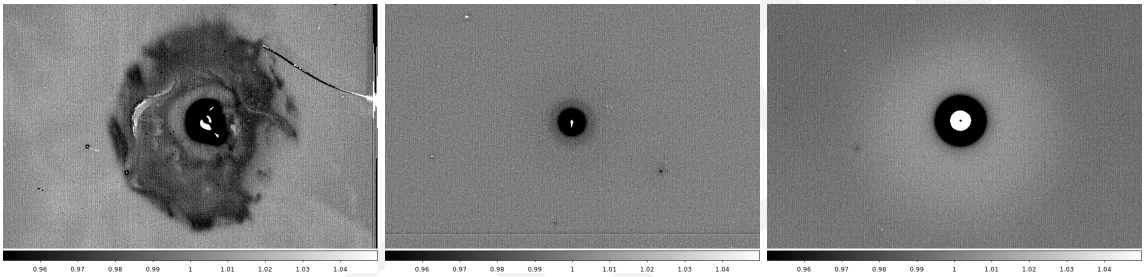

(a) R01_S00_C13-4. (b) R03_S10_C15 (c) R20_S20_C13

Figure 93: Three prototypical *vampire pixel* complexes occurring in the Main Camera. Each of these have counterparts that appear in phosphorescence (transient dark). These are each described in Table XX. In R01_S00, Two "baby" vampires appear in the 8:00 and 8:30 positions that each posess 300-400% nominal flat response. The recorded phosphorescent counterparts for R03_S10 and R20_S20 are dependent on HV Bias (cf. Figs. 97a through 97d) and should provide some constraints as to the pixel astrometric shifts at play near these *vampire pixel* complexes.

The pixel complexes evaluated in Table 11 were chosen based on their proximity to the prominent *vampire pixel* appearing at the center of the corresponding image given in Figure 93, and include (on average) 3 other, nearby complexes that may be more representative of these artifacts found on ITL sensors in the Main Camera focal-plane. In the Table they are indicated by their name ("babyX") followed by the clocking angle where they can be identified relative to the prominent pixel complex located at the center. From this list, it appears that the *vampire pixel* complexes may be reliably identified by applying a OR combination of thresholds: under-response less than 90%, or an over-response exceeding 120% and some consideration of the presence of phosphorescence. The phosphorescence, more than anything, may help to distinguish the dark pixel complexes *without* central bright pixels from dust spots (which

Table 11: Sample vampire pixel complex parameters. The last column indicates whether a concentric phosphorescence center is present.

vampire pixel complex	radius at 99% flat response	minimum under-response	maximum over-response	peak at center?	P?
R01_S00_C13-4	200 pix	1.4%	1660%	distributed (10 pix offset)	yes
baby1 (8:00)	6 pix	83%	375%	yes	yes
baby2 (8:30)	4 pix	84%	290%	yes	yes
R03_S10_C15	36 pix	21%	1570%	yes	yes
baby3 (8:30)	4 pix?	97%	152%	yes	no
baby4 (10:30)	4 pix?	98%	120%	yes	no
baby5 (4:00)	4 pix?	89%	NA	no peak	yes
R20_S20_C13	52 pix	40%	829%	no (ring-like)	yes
baby6 (10:00)	NA	NA	108%	yes	no
baby7 (3:00)	NA	NA	119%	yes	no
baby8 (7:00)	NA	NA	207%	yes	no

presumably would not preserve flux).

There are a handful of dust spots seen in these images that were not included in 11. They would presumably be detected as dark pixels provided the lower threshold is raised to levels that would be sensitive to their detection.

An imperfect listing of ITL sensors in the Main Camera focal-plane showing such *vampire pixel* complexes, is given in a table in a later section (§6.4, Tab. 13). This list shows that 83 of the 88 Main Camera ITL sensors contain finite numbers of *vampire pixel* complexes, with typical numbers less than 30, revealed by spot-like phosphorescence counts. There would be significant overlaps with pixel complex lists generated using only stacks of flat-field response, which would also be sensitive to dust spots (in *dark pixels*), which are likely to have greater numbers (and may be partially salvageable depending on host surface and dust opacity). Meanwhile, *bright pixels* will also pinpoint the larger particulates that reflect light while also casting shadows (we've seen such cases, but their discussion is outside scope of this section).

Based on this listing, there are a total of 17 (of 88) ITL sensors in the Main Camera that appear to host more than 30 *vampire pixel* complexes. These identifications may be used to study in depth more fully the science impact of their transverse electric fields as well as their phosphorescent properties (when recording is preceded directly by illumination by a star in the previous image).

As a proof of concept, a task was added to `eo_pipe` to search for bright defect pixels in combined flats. Figure 94 displays the resulting distribution, which efficiently identifies or picks up the ITL set of sensors. Without looking more closely at the specific regions flagged, it would not be possible to separate out the *vampire pixel* complexes from *reflecting particulates*. Conversely, repeating this task to identify dark pixels with a threshold of 0.90 (90% of flat level), we expect to see a combination of (flux conserving) *vampire pixel* complexes and garden variety (flux attenuating) dust to appear. (Currently, we do not know whether dust particulates prefer to stick to e2v sensors or to their ITL counterparts.)

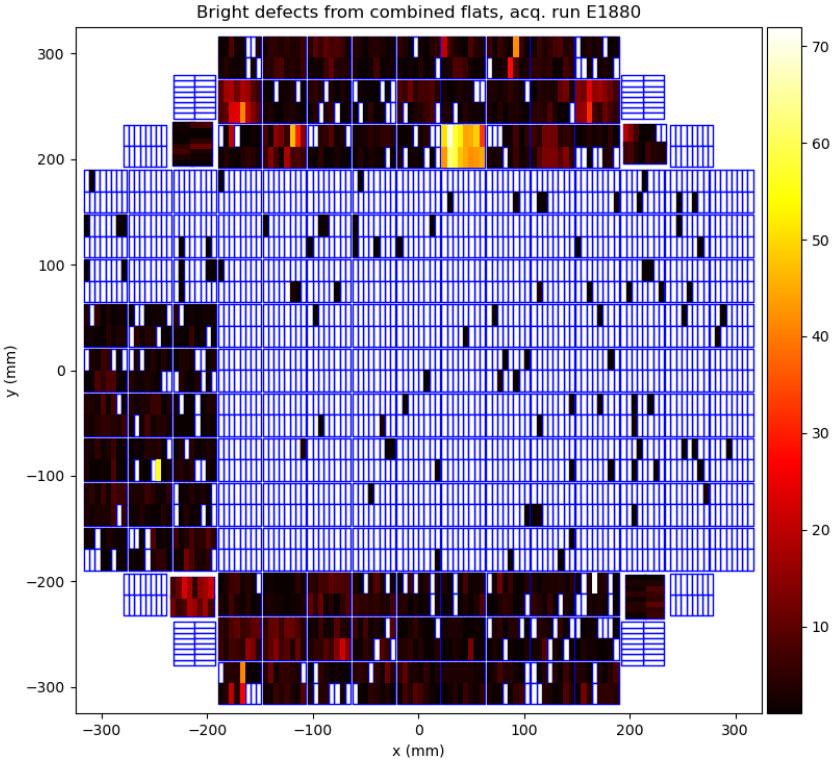

Figure 94: Results of the `eo_pipe` task written to search for bright defects in combined flats. Using a threshold of 1.2 (120% of flat level), the result highlights the 8 RTMs that operate ITL sensors (as well as those CRTMs with sensors operating in science mode).

6.4 Phosphorescence

The Run 7 persistence optimization process (cf. §4.1.1) used a short EO image acquisition sequence and analysis script, which rapidly provided persistence performance metrics as feedback for each configuration tested. Thus, as soon as the e2v sensors were shown to be nearly free of *their* undesirable effects by reducing their clock swing voltages from 9.3 V down to 8.0 V, a similar persistence (or memory effect) was immediately noticed, affecting a subset of the ITL sensors. This discovery gained immediate interest for at least two reasons: (1) that it had not been detected in prior EO campaigns, and (2) that the new memory effect on certain ITL sensors was morphologically distinct from what had just been cured on the e2vs.

The ITL sensors with the largest memory effect were evaluated, and the following observations were made:

1. The morphology of the expressed memory effect in the first dark image acquired after the trigger (the saturation flat) was reminiscent of the *"coffee stains"* seen on the same sensors in flat field response, but with the opposite polarity. The "coffee stains" are commonly assumed to be associated with minor, localized variations in the sensors' antireflective coatings or perhaps a very thin, dead layer associated with the backside surface: they tend to be larger in amplitude when shorter wavelengths are used to expose the sensors with flat field illumination.

2. The attenuation timescale of the memory effect is curiously comparable to the timescales that were seen in the persistence suffered by the e2v sensors (which are believed due to exposure of surface states by the collected conversions, on the semiconductor-insulator interface on the front side): exponential time constants of between 20 and 40 s, which unfortunately are in turn very close to the nominal exposure cadence for the LSST survey.

3. The similarity in memory effect time constants (de-trapping charges from surface states near the channel on the front side – the e2v case – vs. either de-trapping of charges located near the backside window surface or relaxation by photon emission by some excited states there – the ITL case) can be thought to favor the electron de-trapping mechanism, just from the other surface. Otherwise, the nearly matched time constants would have to be seen as an improbable coincidence.

4. A list of 12 ITL sensor serial numbers corresponding to those showing the memory ef-

fect was communicated to Mike Lesser at ITL. The list of parts shared certain properties according to his notes, and led him to develop a placeholder theory that would partially explain the mechanism. If true, it could explain what might be responsible for both the coffee stains and the memory effect with similar spatial distribution. He wrote that he tried, but was unsuccessful in diagnosing, using optical characterization tools (e.g., ellipsometer), any changes in optical constants on the affected regions of the "stained" sensors. The origin of the "stains", according to this theory, is as a consequence of there being "raised spots" on the sensors' backside surfaces that survive the final silicon acid etch. The raised silicon areas could potentially be trapping the resist used during the cleaning process that directly follows the etching step. Lesser wrote that the resist is wax-based and *does* fluoresce. If the theory is correct, he suggests that the medium would definitely be located *under* the AR coating and related neither to the coating nor the oxidation processes.

5. Discussions among the Rubin team led to the following distinction of terminology that served to name the ITL memory effect in question. The main difference between "fluorescence" and "phosphorescence" is in that the former is considered prompt re-emission and the later could be re-emission following a finite characteristic time constant. Characteristic time constants are in the nanosecond scale for fluorescence, while for phosphorescence it would be in the milliseconds to seconds range. For the purpose of this discussion, we adopt the word "phosphorescence" to refer to the memory effect present in some ITL sensors.

6. Lesser mentioned that the wax-based resist fluoresces (that would be the prompt mechanism with very short relaxation time). If there is any such residual material between the coating and the passivated silicon, it would be natural to expect a halo that would accompany any sharp (PSF-scale features) illumination that passes through these "stains" on the sensor surface: a scatter term with low integrated amplitude, whose scale should depend upon the re-emission wavelength. This has not yet been seen in lab data but may appear once the Camera goes on-sky.

6.4.1 Measurement techniques for detecting and quantifying phosphorescence

We mentioned above that certain phosphorescent morphologies strongly resemble the "coffee stains" seen on the same (ITL) sensors. It should be noted that measurement of the *shadow* caused by excess absorption (usually a couple percent) is a great deal simpler than collecting any deferred charge with adequate sensitivity and confidence. This section describes the

methods used to identify the transient term we consider phosphorescence in the ITL sensors, and list the regions where it was detected. Following that, we describe in some detail the kinematics of its expression (cherry-picking specific easy-to-measure cases), together with the wavelength- and its excitation flux-level dependence.

We parasitically used a series of B-protocol and BOT-persistence EO testing runs that were executed for the purpose of tuning the operation of e2v sensors. The reason for this was that the ITL operating parameters were left unchanged from run to run, and thereby provided multiple instances of the same EO measurement conditions, although the acquisitions were captured over a span of a few weeks. The relevant EO runs acquired a series of dark images (with the nominal 15 s integration time, or 'EXPTIME') that followed a deliberate overexposure and readout of a FLAT (CCOB LED 'red', target signal 400 ke^{-}/pix). The dark images acquired in succession following the FLAT image recorded the re-emitted or deferred signal collected within each 15 s period, and there were 20 such dark images acquired within each EO run. In all, we identified and analyzed a total of 22 runs containing this data, where the excitation flat had the properties described above. The first and the twentieth dark images were stacked and medianed following a nominal instrumental signal removal (ISR) step. The twentieth median dark images were then subtracted from the first median darks. This further suppressed any remaining ISR residuals from the pixel data, which nominally now contain the *transient term* of the ITL phosphorescence, because as far as we could tell, the 15 s expression of the deferred signal 300 s after overexposure had almost completely attenuated.

6.4.2 Results of phosphorescence detection in ITL sensors

Table 12 provides the EO run IDs analyzed according to the process outlined above. Figures 98 through 109 display the transient term in 8×8 blocked images of the 12 rafts containing ITL sensors. These serve primarily to help identify which ITL sensors exhibit regions where we suspect presence of the phosphorescence effect. It should be noted that we retained the full 1×1 pixel resolution images for follow-up inspection, because there is no guarantee that high spatial frequencies in the phosphorescence expression will not be washed out by the rebinning routinely performed for display purposes.

A subset of the 88 sensors, specifically those that either show high-signal diffuse, or morphologically unique structure in the transient term of the phosphorescence detected, are singled out to compare side-by-side with *blue* CCOB LED flat illumination, in Figures 110 through 115 in the Appendix. It is apparent from viewing these side-by-side comparisons that generally, ex-

pression of phosphorescence has a complex relationship with the *much-easier-to-detect* coffee stains (or other diffuse variations in quantum efficiency) seen on the same sensors: Presence of a coffee stain seen in flat field response may be suggestive of phosphorescence on the sensor, but predicting where it might be (or its transient amplitude) is another matter entirely. In some cases (as in Fig. 95 noted above), the phosphorescence appears to be correlated with the darker absorbed features of the coffee stain. In others (e.g., Fig. 111), the opposite correlation is seen. In still other cases (e.g., Fig. 112), there are regions of strong detail in the phosphorescence without very much coffee stain action at all. Our conclusions are that presence of coffee stains do not provide a useful proxy for the phosphorescent properties of the sensor.

Table 12: Zephyr Scale E-numbers and corresponding SeqIDs analyzed to estimate phosphorescence in the 88 ITL sensors.

Run numbers and SeqIDs of first dark following trigger		
B-protocol runs, HVBias *off*, HVBias *on* for Corners		
E1003:20240920_000056	E1009:20240921_000222	E1003:20240920_000056
B-protocol runs, HVBias *on*		
E1071:20240924_000300	E1110:20240926_000242	E1144:20240927_000369
E1146:20240928_001525	E1195:20241002_000235	E1245:20241003_000245
E1290:20241008_000286	E1329:20241011_001555	E1363:20241012_000546
E1392:20241014_000444	E1396:20241014_000701	E1411:20241015_000322
E1419:20241016_000397	E1429:20241016_000742	E1449:20241017_000548
E1497:20241020_000225	E1812:20241028_000481	E1880:20241030_000432
E2233:20241108_001468	E3380:20241130_000355	

While characterizing the phosphorescence expressed by ITL sensors using the data products described above, we have also identified correlations that concerns the localized, phosphorescence centers that tend to appear as circular disks. While we typically see a dozen or so (on average) per sensor, those with larger amplitude are strongly associated with *vampire pixels* (which are easily identified by their localized flat field response). The correlation is not per-

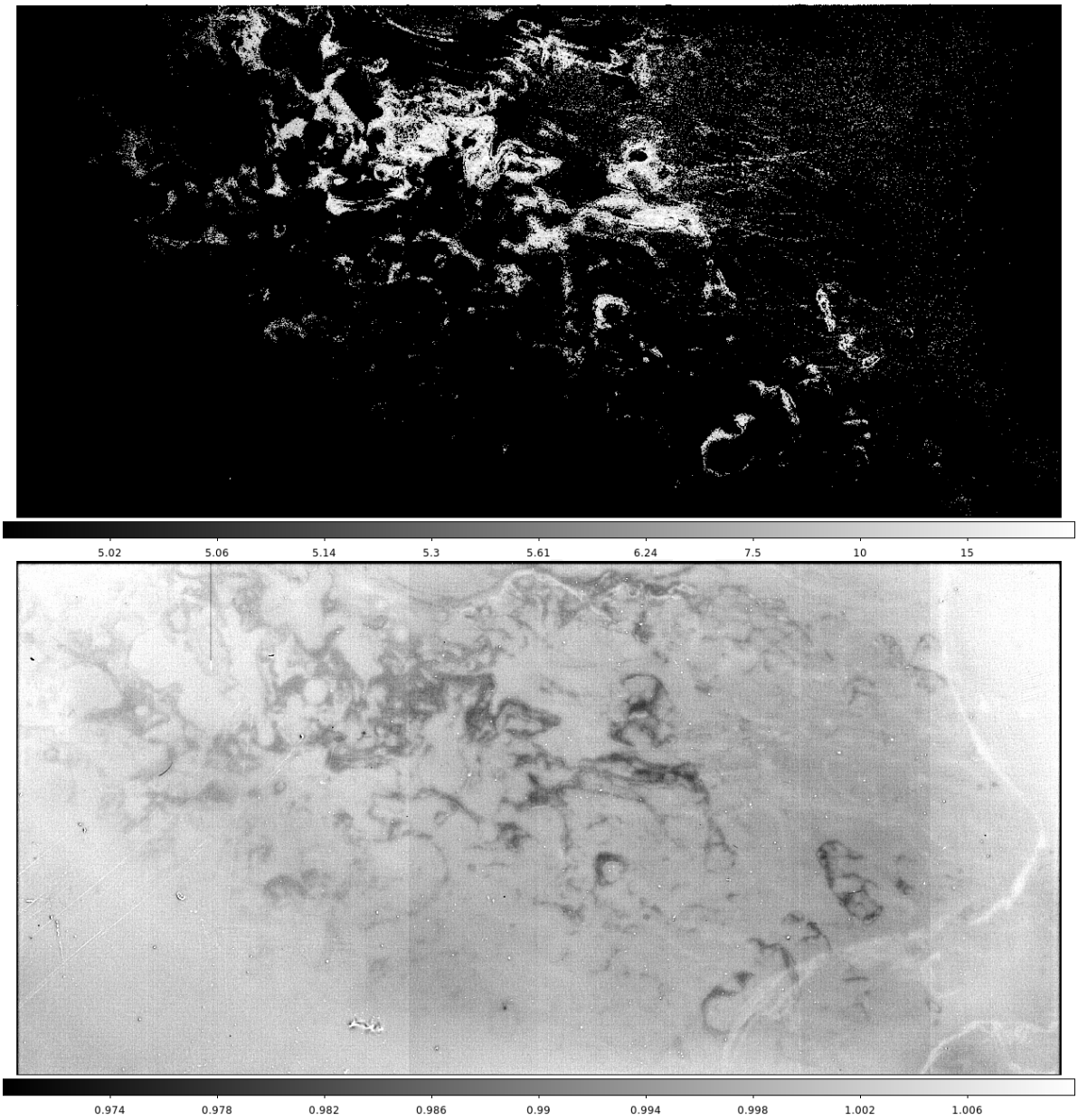

Figure 95: R00_SW1 image showing phosphorescence (top) with morphology similar to the "coffee stains" (bottom) observed with *blue* CCOB LED illumination. The phosphorescence acquired in dark exposures within the first 15 s following trigger (top) uses a logarithmic stretch with limits 5–25 e^-/pixel. The *blue* flat field (bottom) is displayed normalized, with 4% stretch limits (0.97 to 1.01), for a target signal level of 10^4 e^-/pixel. Note that the phosphorescence pattern resembles the dark wisps in the flat (with opposite polarity) but that there are apparently no significant phosphorescence features corresponding to the bright wisps.

fect, meaning that not all localized (circular) phosphorescence centers can be associated with *vampire pixels* but that nearly all *vampire pixels* express localized phosphorescence with some amplitude.

When data products of the 88 ITL sensors are inspected for transient phosphorescent response, very few, perhaps only a single sensor, show insignificant phosphorescence. Although ~24% of the ITL sensors show diffuse phosphorescence, a majority of sensors (~83%) show spot-like phosphorescence centers. Presence of diffuse phosphorescence probably can frustrate spot-like phosphorescence detection by eye, and the estimated frequency of the latter may consequently serve as a lower limit to the true frequency. The identification of the sensor groups is given in Table 13.

Table 13: Qualitative grouping of the 88 ITL sensors based on inspection of full resolution representations of Figures 98 through 109. In cases of spot-like phosphorescence, the number of features counted are given within ellipses. Transient features appearing similar to *hot columns* or as other connected pixel groups are additionally signified with a double-plus (++).

Sensor Grouping		
Sensors exhibiting insignificant phosphorescence		
R44_SW1		
Spot-like phosphorescence (vampire transients)		
R00_SG0(>36)	R00_SG1(>36)	R00_SW0(>10)
R01_S00(>33)	R01_S01(>4)	R01_S02(>6)
R01_S10(>25)	R01_S11(18)	R01_S12(14)
R01_S20(>23)	R01_S21(>30)	R01_S22(>30)
R02_S00(>32++)	R02_S01(>36)	R02_S02(>28)
R02_S10(6)	R02_S11(>30)	R02_S12(>25)
R02_S20(>14)	R02_S21(>9)	R02_S22(>6++)
R03_S00(13)	R03_S01(12)	R03_S02(>19)
R03_S10(9)	R03_S11(3)	R03_S12(10)
R03_S20(9)	R03_S21(18++)	R03_S22(16)
R04_SG0(>12)	R04_SG1(>30++)	R04_SW0(25)
R04_SW1(>30)	R10_S00(>30)	R10_S01(9)
R10_S02(32)	R10_S11(16)	R10_S12(>26)

Continued on next page

Table 13 – continued from previous page

Sensor Grouping		
R10_S20(21)	R10_S21(>11++)	R10_S22(>10++)
R20_S00(2)	R20_S01(8)	R20_S02(7)
R20_S10(>35)	R20_S11(7)	R20_S12(5)
R20_S20(10)	R20_S21(5)	R20_S22(5)
R40_SG0(>50++)	R40_SG1(6++)	R40_SW0(6)
R40_SW1(8)	R41_S00(9++)	R41_S01(16)
R41_S02(10)	R41_S10(12)	R41_S11(3)
R41_S12(10++)	R41_S20(5++)	R41_S21(~30)
R41_S22(3)	R42_S00(24)	R42_S01(6)
R42_S02(>10)	R42_S10(4)	R42_S11(11)
R42_S12(33)	R42_S20(7)	R42_S21(5)
R42_S22(4)	R43_S00(22++)	R43_S01(30)
R43_S02(19)	R43_S10(26)	R43_S12(8++)
R43_S21(14)	R43_S22(4)	R44_SG0(>12)
R44_SG1(>10)	R44_SW0(18)	
Segments exhibiting diffuse transient phosphorescence		
R00_SG1_C10-12,C03-05 (++)	R00_SW0_C17	R00_SW1_C** (++)
R01_S00_C13-14 (++)	R01_S01_C07,C16-17	R01_S10_C00-01,C14-16
R01_S20_C04-07	R01_S21_C06-07,C17	R01_S22_C00-01,C15-17
R02_S02_C03-04	R02_S11_C13-17,C07 (++)	R02_S12_C04-07,C10-12
R02_S20_C06-07	R04_SG1_C01,C11 (++)	R10_S10_C10,C16-17,C07
R40_SG0 (++)	R41_S21_C00,C10	R42_S00_C01,C07,C17
R43_S11 (++)	R43_S20_C00-01 (++)	R44_SG1_C07

The correspondence between *vampire pixels* and spot-like phosphorescence is laid out in Figure 96, for two prominent cases. These two *vampire pixels* may appear intrinsically different in that their flat-field responses **do** (or do **not**) exhibit a central bright pixel, which could aid in their identification. Details of the underlying distribution of trapped surface charges near the back-side electrode - or variations in the conductive properties of the same - apparently

drive these details of the flat field response. However, it remains intriguing that these surface electrostatic properties are accompanied by an unmistakable transient phosphorescence signature.

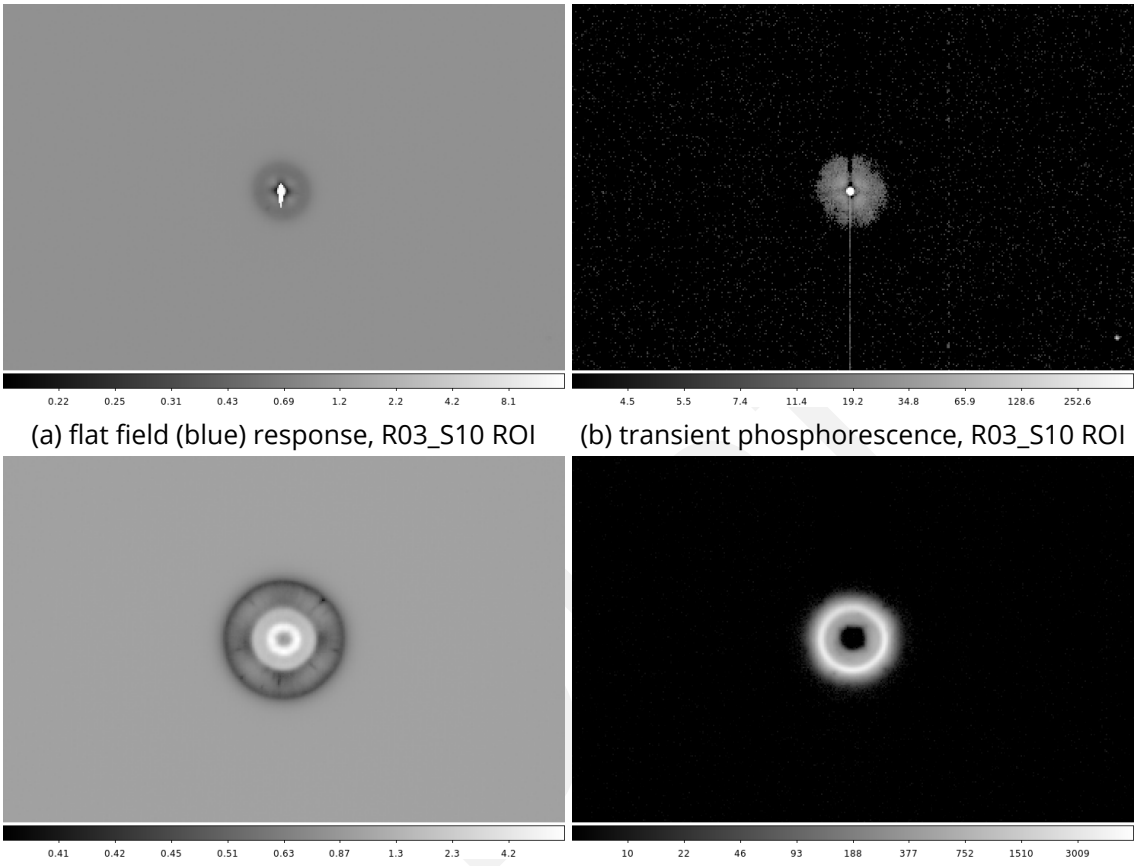

(a) flat field (blue) response, R03_S10 ROI

(b) transient phosphorescence, R03_S10 ROI

(c) flat field (blue) response, R20_S20 ROI

(d) transient phosphorescence, R20_S20 ROI

Figure 96: Vampire pixel comparisons between their flat field response and their transient phosphorescence. Signal levels are given (relative for flat field response, absolute electrons per 15s following overexposure for transient phosphorescence). The relative flat field response amplitudes swing between 0.2 & 16 (reaching full well) for R03_S10, and between 0.4 & 8 for R20_S20. The transient phosphorescence response also reaches nominal full well (135ke$^-$/pix/15s for the central pixel) for R03_S10, and a lower amplitude (3-4Ke$^-$/pix/15s for several hundred pixels) is reached for R20_S20.

A curious aspect of the phosphorescence seen in ITL sensors lies in its voltage (HV Bias) dependence. The HV Bias, when turned on, reduces lateral diffusion of the photo-conversions and thereby maintains PSF image quality. In Figure 97 we compare side-by-side several phosphorescent regions with both HVBias states (off and on). There appears to be no trend that lends to predictability in these cases. In the cases of vampire pixels (R03_S10 & R20_S20), the geometry of the phosphorescence is indeed very sensitive to the HV Bias states (cf. Figs

97a vs. 97b; 97c vs. 97d). These might be understood qualitatively However, for the diffuse phosphorescence examples, the expression appears to vanish entirely (R43_S11, Fig. 97e) or become significantly stronger, together with morphological changes (R43_S20, Fig. 97g) when the HV Bias is switched off.

6.4.3 Other properties of phosphorescence

- Dependence on HVBiasOn vs. HVBiasOff
- Dependence on wavelength of the triggering exposure
- Kinetics of the phosphorescence (based on *blue* CCOB LED)
- Phosphorescence response: triggering exposure dependence of the expressed phosphorescence, the wavelength- and signal level-dependence.

- phosphorescence background
- phosphorescence on flat fields
- phosphorescence on spot projections

7 Conclusions

7.1 Run 7 final operating parameters

This section describes the conclusions of Run 7 optimization and the operating conditions of the camera. Decisions regarding these parameters were based upon the results of the voltage optimization, sequencer optimization, and thermal optimization.

7.1.1 Voltage conditions

Table 14: Voltage Conditions with Updated Run 5 for ITL Values

Parameter	Run 5 (ITL)	Run 5 (dp93; e2v)	Run 7 (dp80; new voltage for e2v)
pclkHigh	2.0	3.3	2.0
pclkLow	−8.0	−6.0	−6.0
dpclk	10.0	9.3	8.0
sclkHigh	5.0	3.9	3.55

Parameter	Run 5 (ITL)	Run 5 (dp93; e2v)	Run 7 (dp80; new voltage for e2v)
sclkLow	−5.0	−5.4	−5.75
rgHigh	8.0	6.1	5.01
rgLow	−2.0	−4.0	−4.99
rd	13.0	11.6	10.5
od	26.9	23.4	22.3
og	−2.0	−3.4	−3.75
gd	20.0	26.0	26.0

7.1.2 Sequencer conditions

Table 15: Sequencer conditions

Detector type	File name
e2v	FP_E2V_2s_l3cp_v30.seq
ITL	FP_ITL_2s_l3cp_v30.seq

- v30 sequencers are identical to the FP_ITL_2s_l3cp_v29_Noppp.seq and FP_E2V_2s_l3cp_v29_NopSf.seq All sequencer files can be found in the GitHub repository.

7.1.3 Other camera conditions

- Idle flush disabled

7.2 Record runs

This section describes Run 7 record runs. All runs use our camera operating configuration, unless otherwise noted.

Run Type	Run ID	Links	Notes
B-protocol	E1880	Web report Test Execution	Initial B_protocol taken with the new v30 definition.
	E2233		dp80, first run after full CCS system reboot

Run Type	Run ID	Links	Notes
	E3380		First B protocol post-chiller recovery
PTC	E3630		Low flux red LED PTC, ND1 filter installed. Final operating conditions of camera.
	E3577		Dense nm960 PTC. Final operating conditions of camera.
	E2237		Final operating conditions of camera. Red LED dense. Acquired after CCS subsystem reboot.
	E748		Final operating conditions of camera. nm960 dense
	E2016		Final operating conditions of camera. Super dense red LED. HV Bias off for R13/Reb2. jGroups meltdown interrupted acquisitions, restarted
	E1886		Final operating conditions of camera. Red LED dense. Dark interleaving between flat pairs
	E1881		Final operating conditions of camera. Red LED dense. No dark interleaving between flat pairs
Gain Stability	E1955		6h Stability run 10k 750 nm V30, dp80, idle flush disabled
	E2008		6h Stability run 10k 750 nm V30, dp80, idle flush disabled, after zeroing CCOB
Long dark acquisitions	E3540		900s dark. Shutter closed.
	E3539		900s dark. Shutter closed.
	E3538		900s dark. Shutter opened.
Projector acquisitions	E2184		10 30 s dark images to capture background pattern. E2V:v29Nop, ITL:v29Nopp

Run Type	Run ID	Links	Notes
	E2181		Flat pairs from 2–60 s in 2 s intervals. Two 15 s darks interleaved after flat acquisition. Rectangle on C10 amplifier. E2V:v29Nop, ITL:v29Nopp
OpSim runs	E2330		Short dark sequence, filter changes in headers through OCS
	E2328		Flats with shutter-controlled exposure
Phosphorescence datasets	E2015		10 flats at 10 ke$^-$ followed by 10×15 s darks
	E2014		1 flat at 10 ke$^-$ followed by 10×15 s darks
	E2013		10 flats at 10 ke$^-$ followed by 10×15 s darks. Interleaved biases with the darks
	E2012		10 flats at 1 ke$^-$ followed by 10×15 s darks
	E2011		20 flats at 10 ke$^-$ followed by 10×15 s darks

7.3 Other runs of relevance

Runs that use the Run 7 final camera operating configuration (Sec. 7.1) are denoted with **bold run ID**.

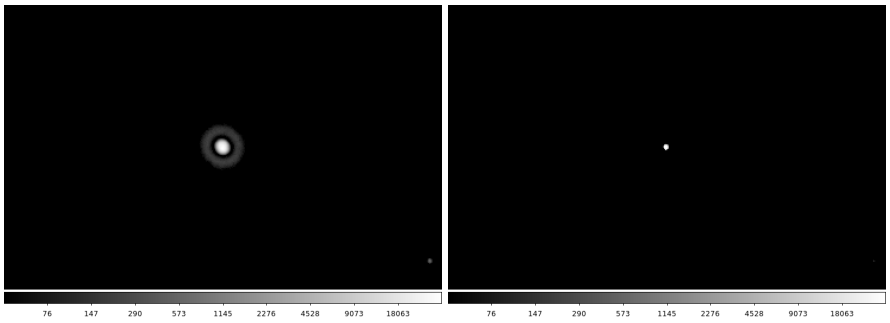

(a) HVBias off, R03_S10 ROI (b) HVBias on, R03_S10 ROI

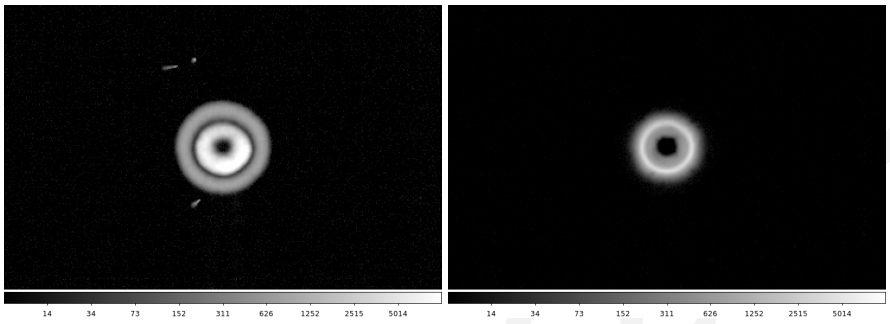

(c) HVBias off, R20_S20 ROI (d) HVBias on, R20_S20 ROI

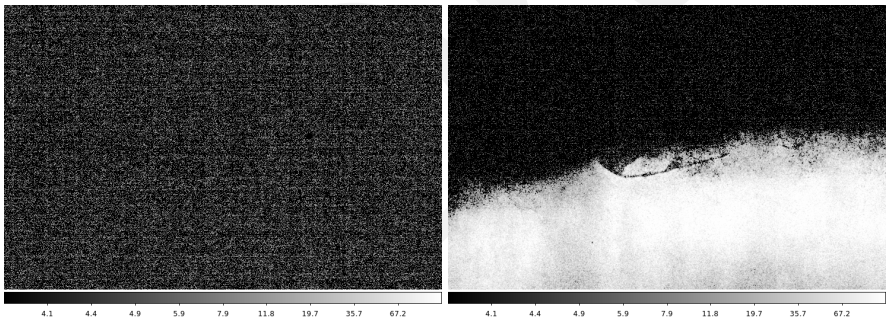

(e) HVBias off, R43_S11 ROI (f) HVBias on, R43_S11 ROI

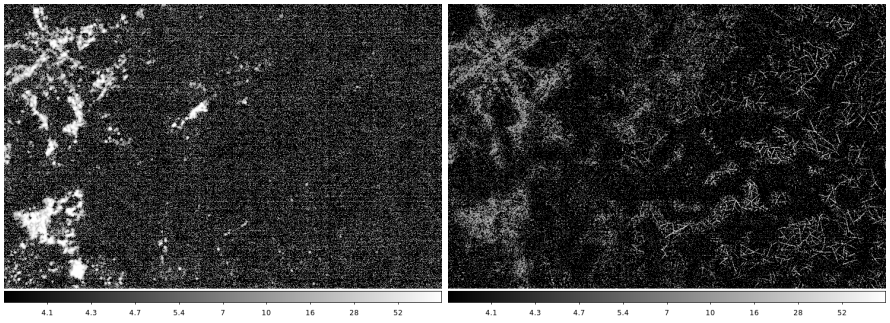

(g) HVBias off, R43_S20 ROI (h) HVBias on, R43_S20 ROI

Figure 97: Comparisons of transient phosphorescence between conditions where HV Bias is off (left) vs. on (right). Four different ROIs are shown, but with image scales set to match across HV Bias conditions.

Table 17: B Protocol Runs

Run ID	Links	Notes
E3380		First B protocol post-chiller recovery. v30, dp80, idle flush disabled.
E2233		Identical to E1880. Acquired after CCS subsystem reboot. dp80, idle flush disabled.
E1880	Web report Test Execution	Camera operating configuration
E1812		v29 NopSf (no pocket serial flush running for both e2v and ITL clear sequencers). dp80 voltages, idle flush ?? [likely disabled but verification needed]
E1497		v29 Nop sequencer, dp80, idle flush ?? [likely disabled but verification needed]
E1429		First dp84 run. v29, idle flush disabled
E1419		First dp88 run. v29, idle flush disabled
E1411		First dp865 run. v29, idle flush disabled
E1396		First dp80 run. v29 nonoverlapping sequencer, idle flush enabled
E1392		First dp80 run. v29 sequencer, idle flush enabled
E1290		using Guide sensors as guiders. v29, dp93, idle flush enabled
E1245		Refrigeration system software update mid-run. v29 halfoverlapping sequencer. dp93, idle flush enabled
E1195		v29 overlap113 sequencer (5% overlap). dp93, idle flush enabled
E1146		First run with v29 nonoverlapping. dp93, idle flush enabled
E1144		First run with v29 Nop. dp93, idle flush enabled
E1110		v29 run. dp93, idle flush enabled
E1071		SOURCE = 63 in calib3.cfg. First run with HV on. dp93, v26 sequencer, idle flush enabled

Table 18: PTC Runs

Run ID	Links	Notes
E3630		Low flux red LED PTC, ND1 filter installed. Final operating conditions of camera.
E3577		Dense nm960 PTC. Final operating conditions of camera.
E2237		Final operating conditions of camera. Red LED dense. Acquired after CCS subsystem reboot.
E748		Final operating conditions of camera. nm960 dense
E2016		Final operating conditions of camera. Super dense red LED. HV Bias off for R13/Reb2. jGroups meltdown interrupted acquisitions, restarted
E1886		Final operating conditions of camera. Red LED dense. Dark interleaving between flat pairs
E1881		Final operating conditions of camera. Red LED dense. No dark interleaving between flat pairs
E1765		Dense PTC, red, thresholded dark interleaves, overlaps in signal level for adjacent LED currents. v29 Nop sequencer, idle flush ??
E1495		dp80, nopp config. Idle flush ??
E1364		v29, dp80, idle flush ??. Possible incomplete data transfer
E1335		dp80 configuration, v29, idle flush ??.
E1275		Ordered flats. Failed dark interleaving, incomplete data transfer. v29 sequencer.
E1259		Randomized flats. v29 sequencer.
E1258		Randomized flux levels. Starting with 3 preimages, then 100 15s darks, then PTC set. No dark interleaving. v29 sequencer.
E1247		Re-do of E1188 (which lacked PD data). v29HalfOverlapping., Added pre-image acquisition to PTC-Red cfg file.
E1212		5% overlapping sequencer
E1145		No pocket sequencer
E1113		v29 sequencer
E749		v26, dp93, idle flush enabled. First PTC of run.

Table 19: Long Dark Acquisitions

Run ID	Links	Notes
E3540		900s dark. Shutter closed.
E3539		900s dark. Shutter closed.
E3538		900s dark. Shutter opened.
E1140		Empty frame filter, shutter open, 24V clean and dirty FES changer powered off, one 900s dark image only.
E1117		900s dark. r filter, shutter open.
E1116		900s dark. y filter, shutter open.
E1115		900s dark. g filter, shutter open.
E1114		900s dark. EF filter, shutter open.
E1076		PH filter in place. Shutter open. v26 no RG
E1075		PH filter in place. v26 no RG

Table 20: Projector Acquisitions

Run ID	Links	Notes
E2184		10 30 s dark images to capture background pattern
E2181		Flat pairs from 2–60 s in 2 s intervals. Two 15 s darks interleaved after flat acquisition. Rectangle on C10 amplifier. e2v:v29Nop, ITL:v29Nopp
E1586		One 100 s flat exposure, spots moved to selected phosphorescent regions. e2v:v29Nop, ITL:v29Nopp
E1558		Flat pairs, fine scan in flux from 1–100 s in 1 s intervals. e2v:v29Nop, ITL:v29Nopp
E1553		Flat pairs, coarse scan in flux from 5–120 s in 5 s intervals. e2v:v29Nop, ITL:v29Nopp

Table 21: OpSim Runs

Run ID	Links	Notes
E3629		Mock OCS calibrations, failed
E3576		Mock OCS calibrations, failed
E3570		Mock OCS calibrations, failed
E2330		Short dark sequence, filter changes in headers through OCS
E2329		Mock OCS calibrations, failed
E2328		Flats with shutter-controlled exposure
E2283		Full night of OpSim flats, failed
E2280		Mock OCS calibrations, failed
E2279		Mock OCS calibrations, failed
E1717		Long dark sequence, no filter changes
E1657		10 hour OpSim dark run, ~50% of darks were acquired properly
E1414		30 minutes OpSim run with shutter control, filter change, and realistic survey cadence
E1403		30 minutes OpSim run with shutter control, filter change, and realistic survey cadence
E1255		30 minutes OpSim run with shutter control, filter change, and realistic survey cadence
E1254		30 minutes OpSim run with shutter control, filter change, and realistic survey cadence
E1092		30 minutes OpSim run with shutter control, filter change, and realistic survey cadence

Table 22: Phosphorescence Datasets

Run ID	Links	Notes
E2015		10 flats at 10 ke^- followed by 10×15 s darks
E2014		1 flat at 10 ke^- followed by 10×15 s darks
E2013		10 flats at 10 ke^- followed by 10×15 s darks. Interleaved biases with the darks
E2012		10 flats at 1 ke^- followed by 10×15 s darks
E2011		20 flats at 10 ke^- followed by 10×15 s darks

Table 23: Tree Ring Flats

Run ID	Links	Notes
E1050		Red LED. HV off. Diffuser installed.
E1052		Blue LED. HV off. Diffuser installed.
E1053		Nm750 LED. HV off. Diffuser installed.
E1055		Nm850 LED. HV off. Diffuser installed.
E1056		Nm960 LED. HV off. Diffuser installed.
E1021		Red LED. HV off. Diffuser removed.
E1023		Blue LED. HV off. Diffuser removed.
E1024		Nm750 LED. HV off. Diffuser removed.
E1025		Nm850 LED. HV off. Diffuser removed.
E1026		Nm960 LED. HV off. Diffuser removed.

Table 24: Gain Stability Runs

Run ID	Links	Notes
E1955		6h Stability run 10k 750 nm V30, dp80, idle flush disabled
E2008		6h Stability run 10k 750 nm V30, dp80, idle flush disabled, after zero-ing CCOB
E1968		6h Stability run 2k 750 nm V30, dp80, idle flush disabled
E1367		Changing PCS setpoint mid run., PCS changed from -45 deg C to -47 deg C at 10:40:06 AM UTC. 6h, 50k at 750nm, v29 seq, dp80 config.
E1362		dp80, partial data ingestion. v29 sequencer. 6h 10k at 750nm.
E756		dp 80, v29 sequencer. 6h 10k at 750nm. Partial data ingestion.
E1496		dp80, nopp config, 6h 750nm at 10k

Table 25: Persistence Datasets

Run ID	Links	Notes
E2286		30k uv flash with increased hilim
E1507		dp80, uv led @ 30k
E1506		dp80, uv led @ 10k
E1505		dp80, uv led @ 5k
E1504		dp80, uv led @ 3k
E1503		dp80, uv led @ 1k
E1502		dp80, blue led @ 1k
E1501		dp80, blue led @ 3k
E1500		dp80, blue led @ 5k
E1499		dp80, blue led @ 10k
E1498		dp80, blue led @ 30k
E1494		dp80, nm960 led @ 50k
E1493		dp80, nm850 led @ 50k
E1492		dp80, nm750 led @ 50k
E1491		dp80, blue led @ 50k
E1490		dp80, red led @ 50k
E1489		dp80, nm960 led @ 150k
E1488		dp80, nm850 led @ 150k
E1487		dp80, nm750 led @ 150k
E1486		dp80, red led @ 150k
E1485		dp80, blue led @ 150k
E1484		dp80, blue led @ 400k
E1483		dp80, red led @ 400k
E1479		dp80, nm750 led @ 400k
E1478		dp80, nm960 led @ 400k
E1477		dp80, nm850 led @ 400k

Table 26: Guider ROI Acquisitions

Run ID	Links	Notes
E1509		ROI reference dataset
E1510		ROI crossing amplifier segments
E1518		200ms integration time
E1519		100ms integration time
E1508		50ms integration time
E1520		400x400 pixel ROIs
E1511		200x200 pixel ROIs
E1521		100x100 pixel ROIs
E1512		New row from reference dataset
E1513		New column from reference dataset
E1514		New column and row from reference dataset
E1517		Different row for sensors on the same REB

8 References

A FCS work

B Reference figures

C CCS work

C.1 JGroups issue

D OCS integration

E Phosphorescence identification on ITL set of sensors

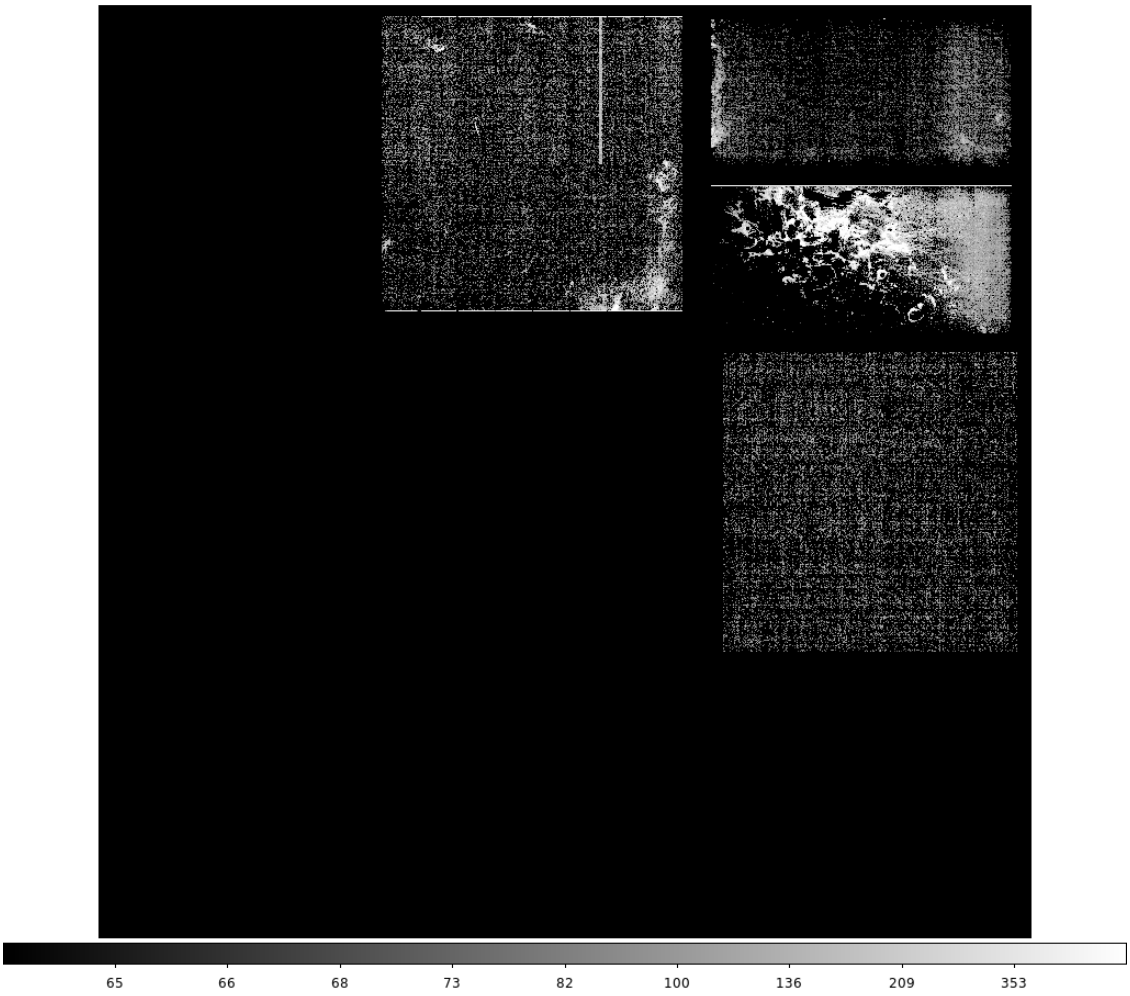

Figure 98: Phosphorescence transients for the R00 CRTM captured in the first 15 s following *red* CCOB LED at 400 ke$^-$/pix. With 8×8 blocking, the upper end of the color scale (640) corresponds to 10 e$^-$/pixel when averaged over 64 pixels contributing.

Figure 99: Phosphorescence transients for the R01 RTM captured in the first 15 s following *red* CCOB LED at 400 ke$^-$/pix. With 8×8 blocking, the upper end of the color scale (640) corresponds to 10 e$^-$/pixel when averaged over 64 pixels contributing.

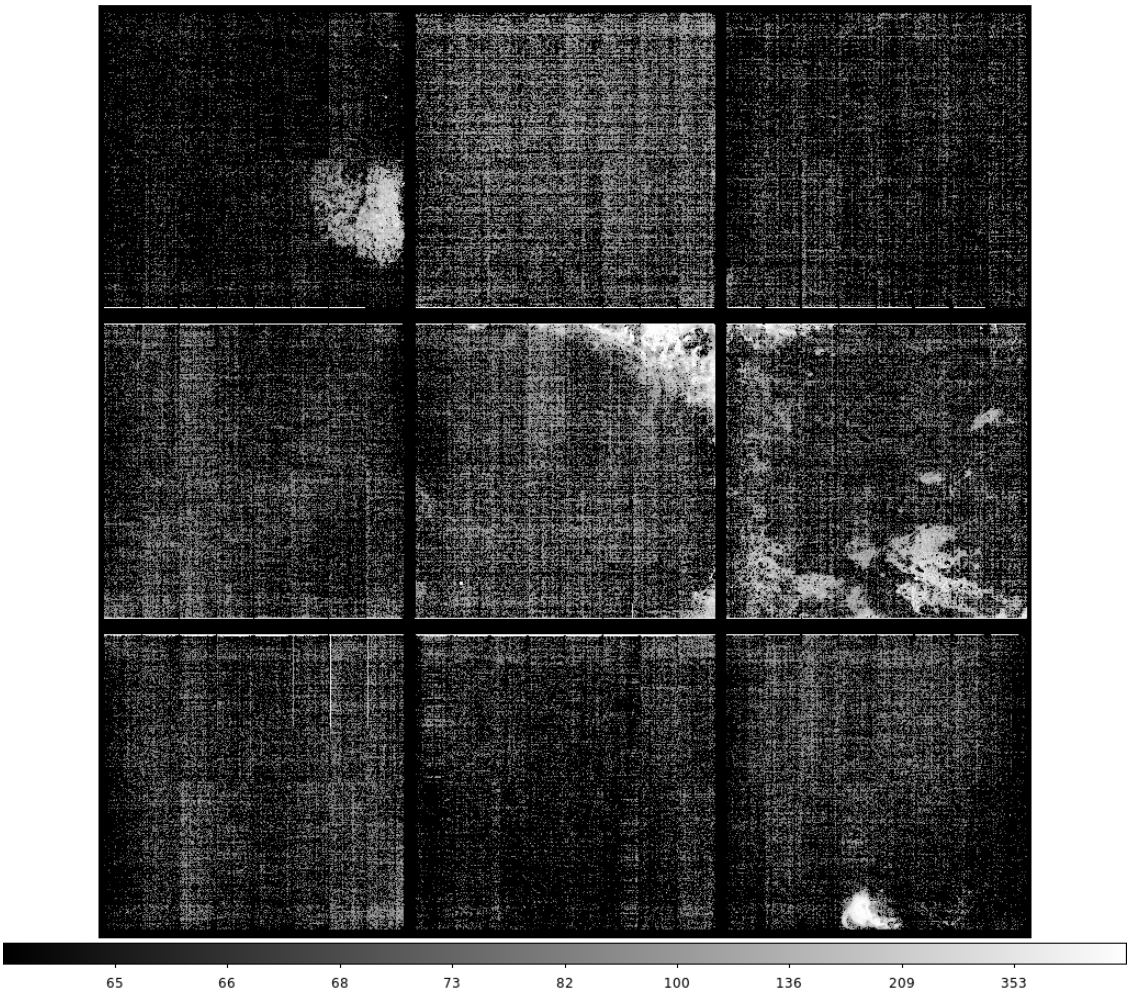

Figure 100: Phosphorescence transients for the R02 RTM captured in the first 15 s following *red* CCOB LED at 400 ke$^-$/pix. With 8×8 blocking, the upper end of the color scale (640) corresponds to 10 e$^-$/pixel when averaged over 64 pixels contributing.

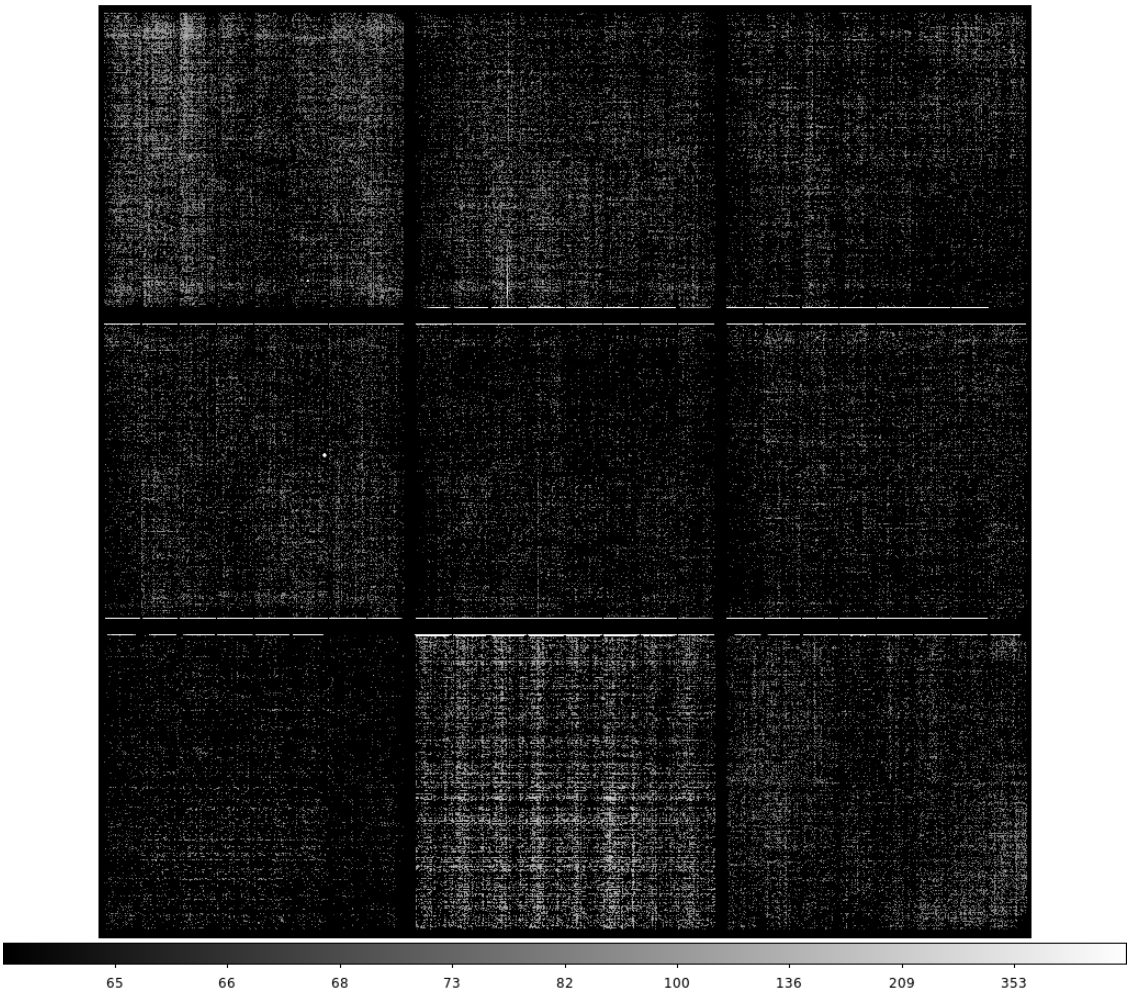

Figure 101: Phosphorescence transients for the R03 RTM captured in the first 15 s following *red* CCOB LED at 400 ke$^-$/pix. With 8×8 blocking, the upper end of the color scale (640) corresponds to 10 e$^-$/pixel when averaged over 64 pixels contributing.

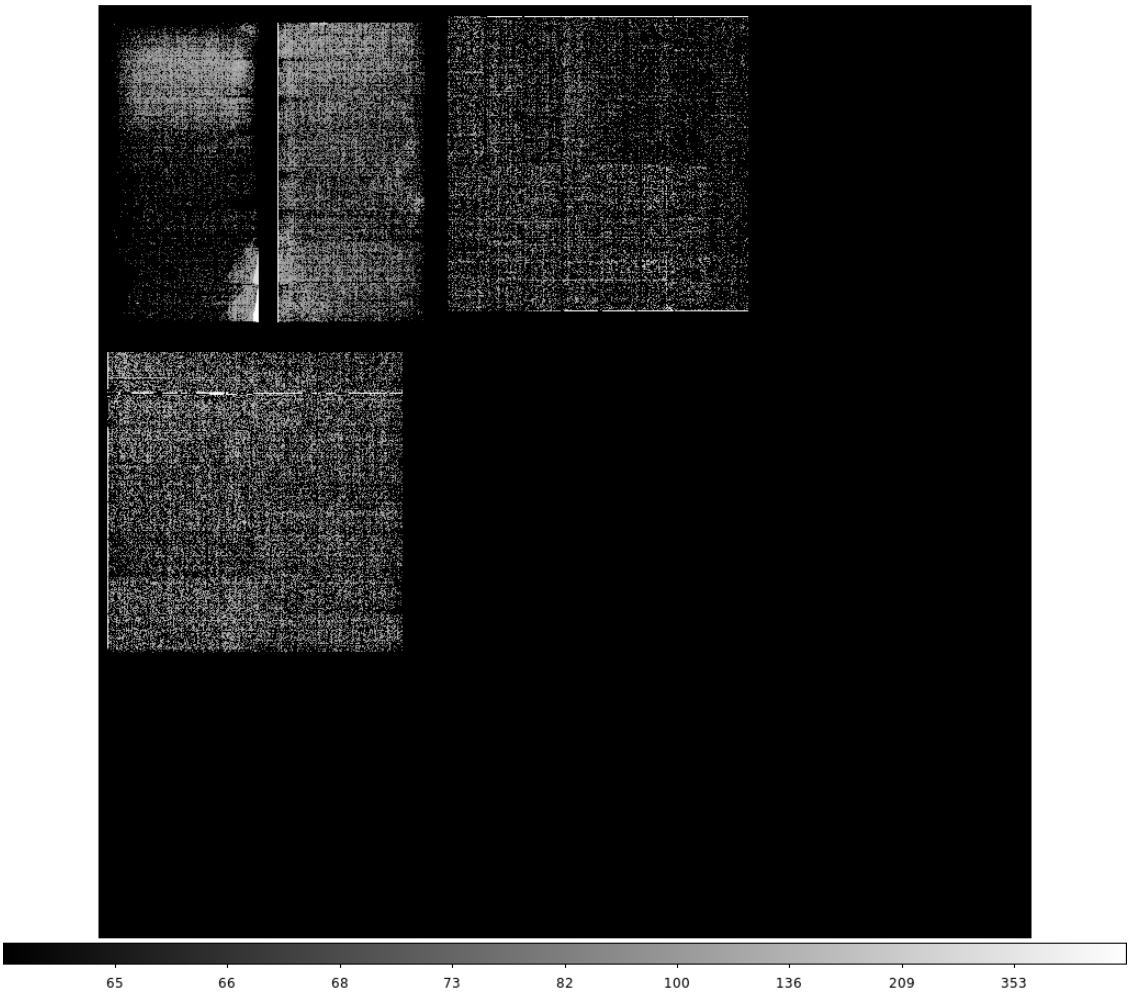

Figure 102: Phosphorescence transients for the R04 CRTM captured in the first 15 s following *red* CCOB LED at 400 ke$^-$/pix. With 8×8 blocking, the upper end of the color scale (640) corresponds to 10 e$^-$/pixel when averaged over 64 pixels contributing.

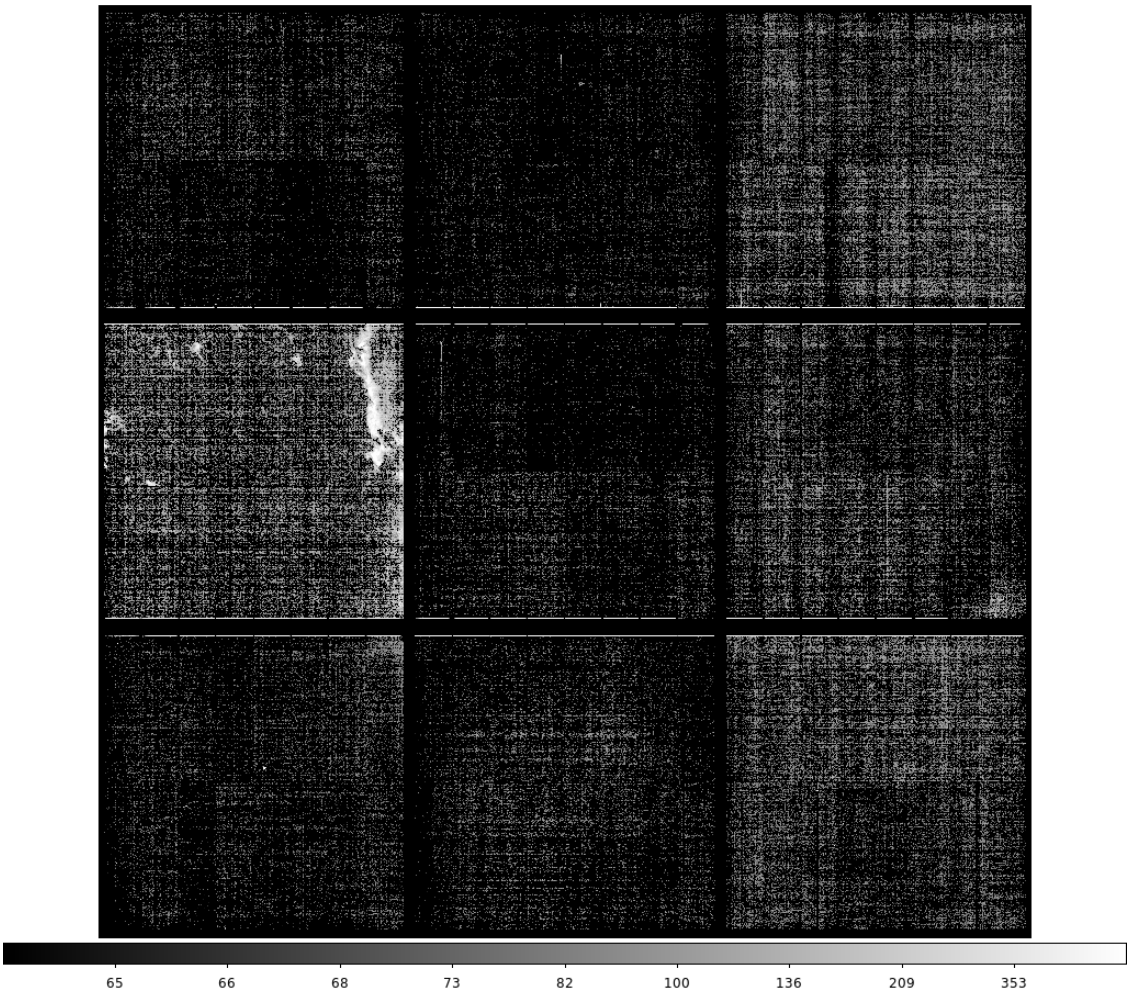

Figure 103: Phosphorescence transients for the R10 RTM captured in the first 15 s following *red* CCOB LED at 400 ke$^-$. With 8×8 blocking, the upper end of the color scale (640) corresponds to 10 e$^-$/pixel when averaged over 64 pixels contributing.

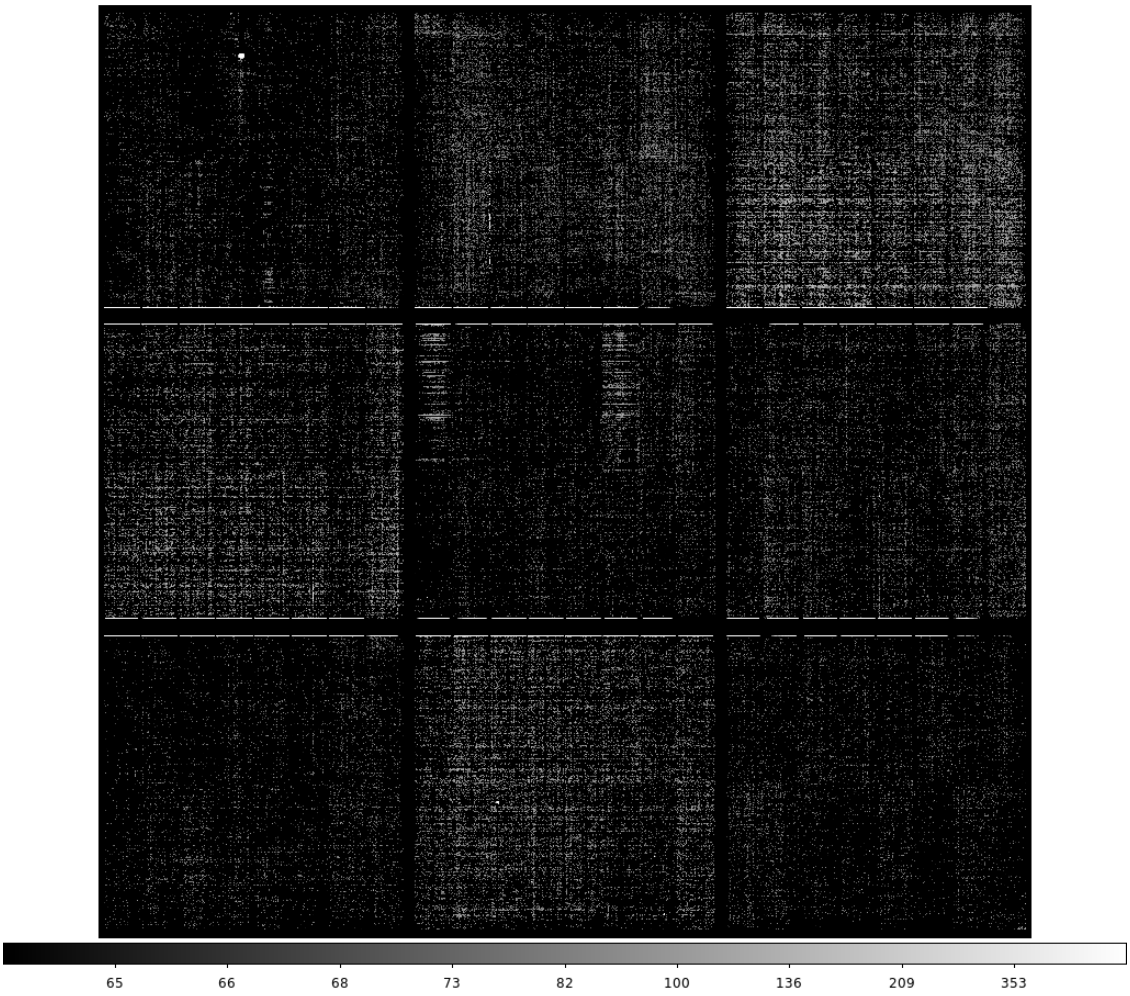

Figure 104: Phosphorescence transients for the R20 RTM captured in the first 15 s following *red* CCOB LED at 400 ke$^-$/pix. With 8×8 blocking, the upper end of the color scale (640) corresponds to 10 e$^-$/pixel when averaged over 64 pixels contributing.

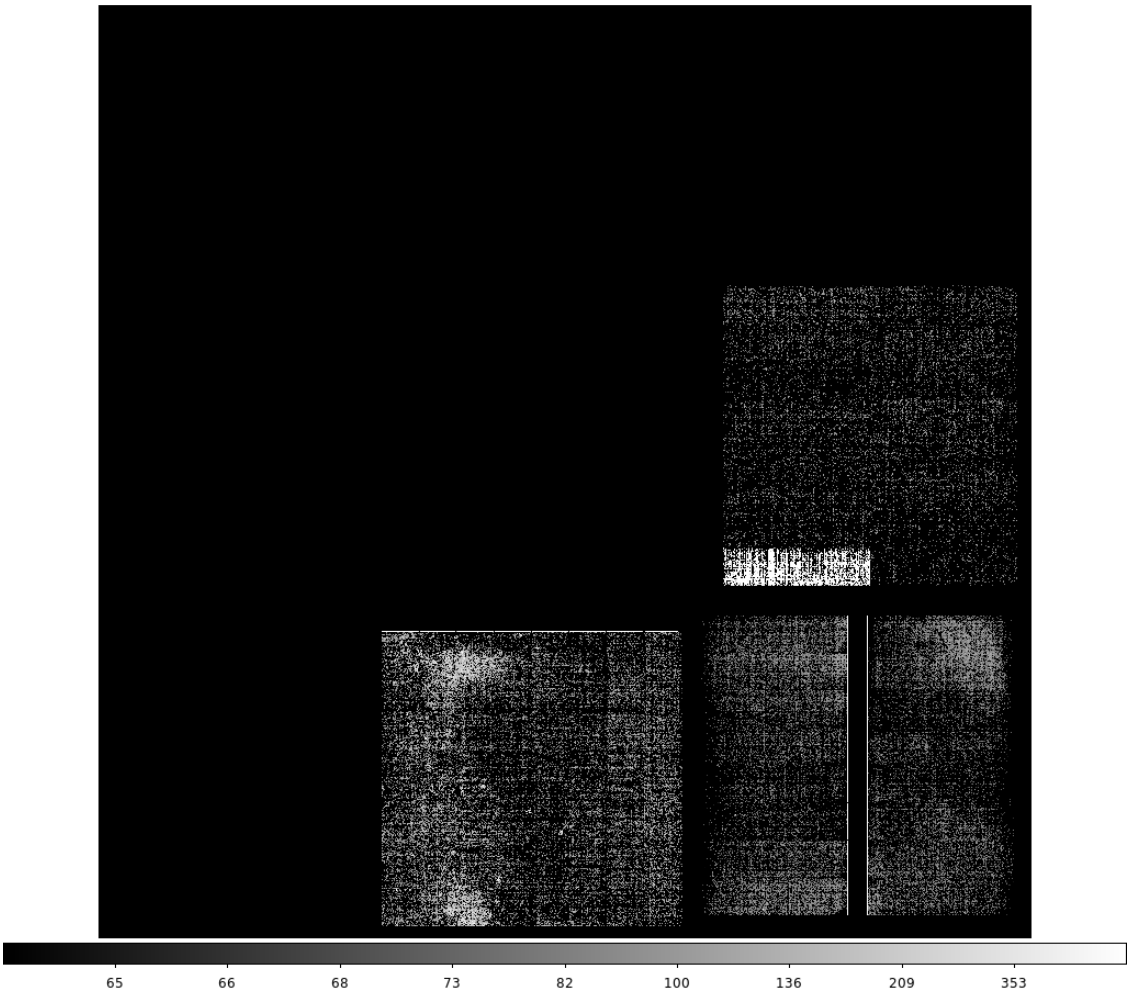

Figure 105: Phosphorescence transients for the R40 CRTM captured in the first 15 s following *red* CCOB LED at 400 ke$^-$/pix. With 8×8 blocking, the upper end of the color scale (640) corresponds to 10 e$^-$/pixel when averaged over 64 pixels contributing.

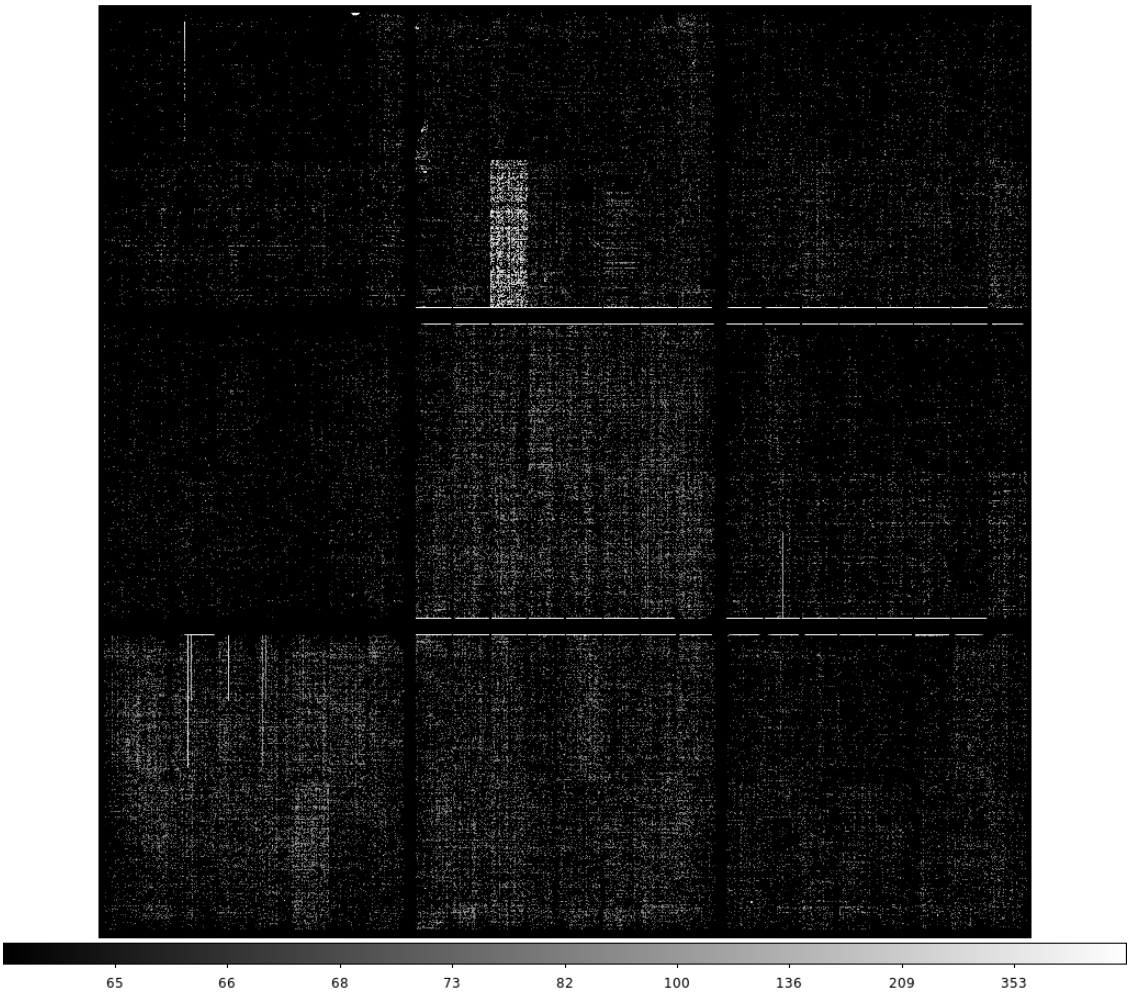

Figure 106: Phosphorescence transients for the R41 RTM captured in the first 15 s following *red* CCOB LED at 400 ke$^-$/pix. With 8×8 blocking, the upper end of the color scale (640) corresponds to 10 e$^-$/pixel when averaged over 64 pixels contributing.

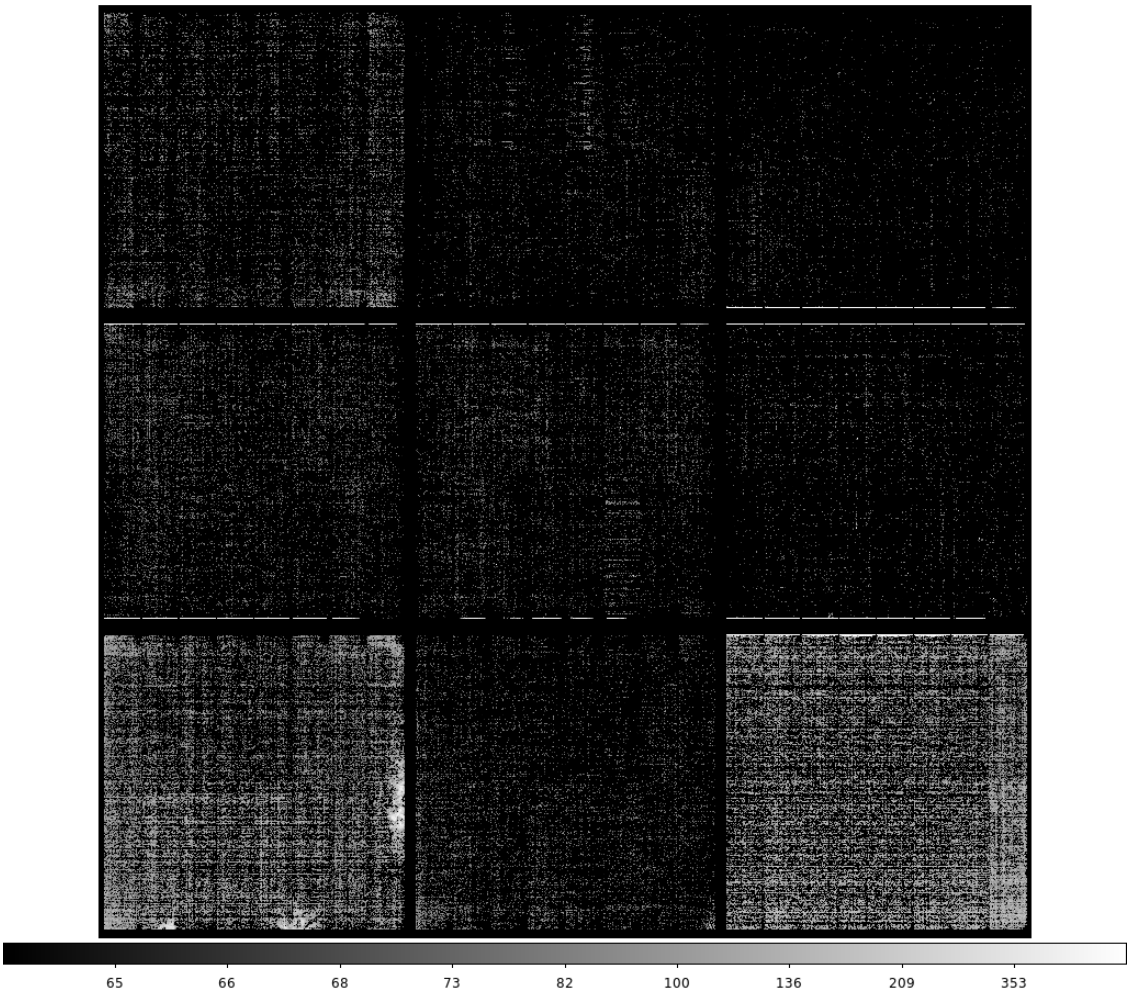

Figure 107: Phosphorescence transients for the R42 RTM captured in the first 15 s following *red* CCOB LED at 400 ke$^-$/pix. With 8×8 blocking, the upper end of the color scale (640) corresponds to 10 e$^-$/pixel when averaged over 64 pixels contributing.

Figure 108: Phosphorescence transients for the R43 RTM captured in the first 15 s following *red* CCOB LED at 400 ke$^-$/pix. With 8×8 blocking, the upper end of the color scale (640) corresponds to 10 e$^-$/pixel when averaged over 64 pixels contributing.

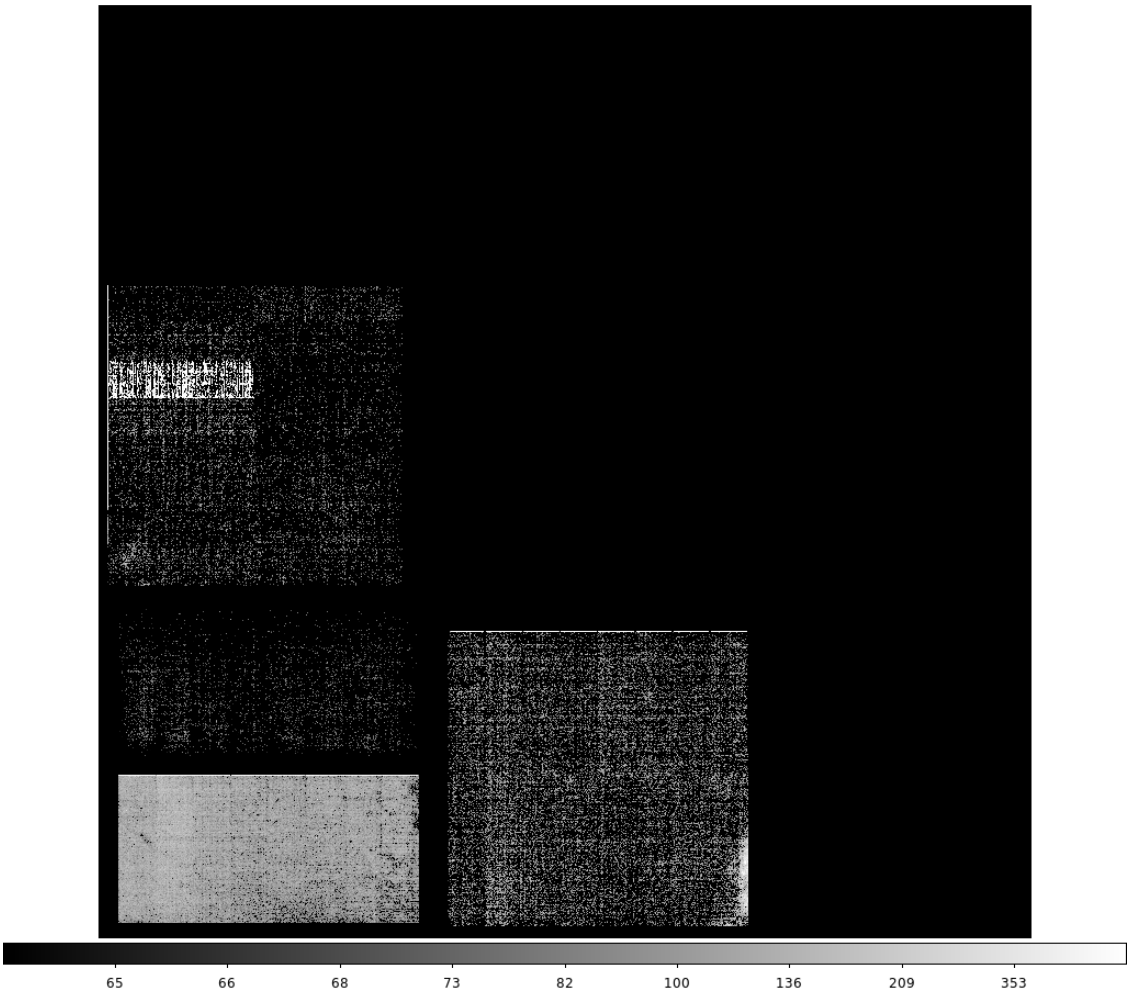

Figure 109: Phosphorescence transients for the R44 CRTM captured in the first 15 s following *red* CCOB LED at 400 ke$^-$/pix. With 8×8 blocking, the upper end of the color scale (640) corresponds to 10 e$^-$/pixel when averaged over 64 pixels contributing.

F Phosphorescence morphological comparisons with features seen in *blue* flat field response

Figures 110 through 115 are an incomplete selection of ITL sensors with phosphorescence. They compare expressed phosphorescence (transient term) with the *blue* CCOB LED flat response. Inspection of these images would lead one to conclude that in certain cases, the phosphorescence patterns resemble the coffee stain patterns' regions of lower QE at short wavelength (*cf.* Fig. 95, Fig. 114). In other cases, the opposite appears to be true (*cf.* Fig. 111, Fig. 112). In several cases, there appear to be no particular correlations.

In cases where variations in the blue flat-field response are due to *vampire pixels* (*cf.* Fig. 96) with a completely different wavelength dependence, presumably due to depth-dependence in the direction of the drift field lines), we see *high amplitude* and *long timescale* transient phosphorescence associated with these *vampire pixel* complexes. These tend to be the brightest phosphorescent features we see, and this fact may provide a strong hint regarding the origin of this phosphorescence phenomena. These quantitative differences are most easily seen in the kinetics discussion, Section **??**.

G Phosphorescence kinetics characterization

Figures 117 through 123 quantify the expressed phosphorescence distributions in ROIs on seven of the problematic ITL sensors. Previously, we had captured the phosphorescence *transient term* across the ITL sensors (*cf.* Figs. 98 thru 109); here we track ROI pixel distribution parameters of individual median images constructed from the selection of specific images acquired across the 20 B-protocol datasets available (listed in Table 12).

By fitting decay models to these persistence curves, it is immediately clear that there are multiple (>2) timescales at play for the pixels in each ROI. An example of such a fit is given in Figure 116 where a 3-population relaxation model is used to characterize evolution of the 99% quantile level of the distribution. In this case, there are three different exponential timescales determined: $(\tau_1, \tau_2, \tau_3) = (0.62, 2.5, 18.3)$ in image units (10.9, 43.8 & 320 seconds, respectively). The corresponding ratio of these populations works out to 4.5% (fast), 21.5% (medium) and 74% (slow), respectively. Inspection of the more detailed parameters plotted generally indicate skewed distributions from mismatches between medians and means; the choice of the

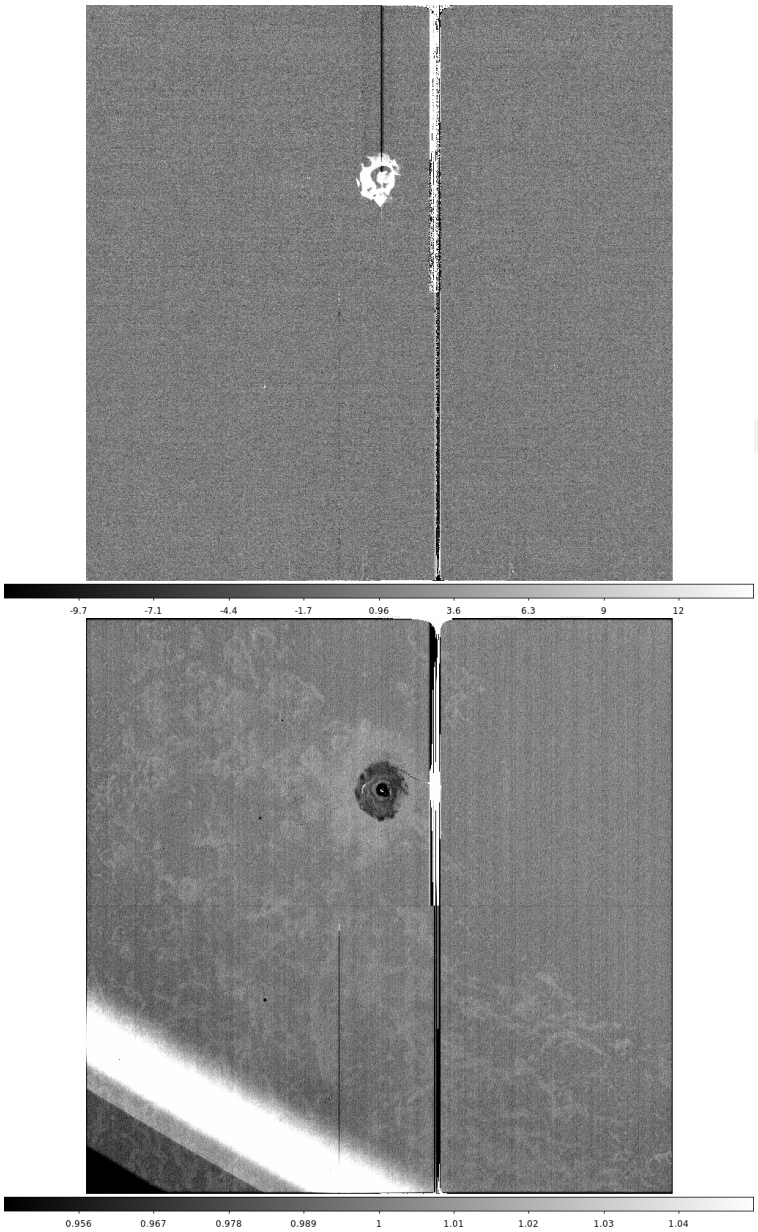

Figure 110: The ITL sensor R01_S00. Top: the transient phosphorescence term. Bottom: the *blue* flat response. The large, extended spot appears to be centered on a *vampire pixel*, which also expresses a large amplitude of phosphorescence, which emits enough current to contaminate the parallel overscan in at least the first 15 s exposure following trigger. The flat response feature has opposite polarity from the phosphorescence.

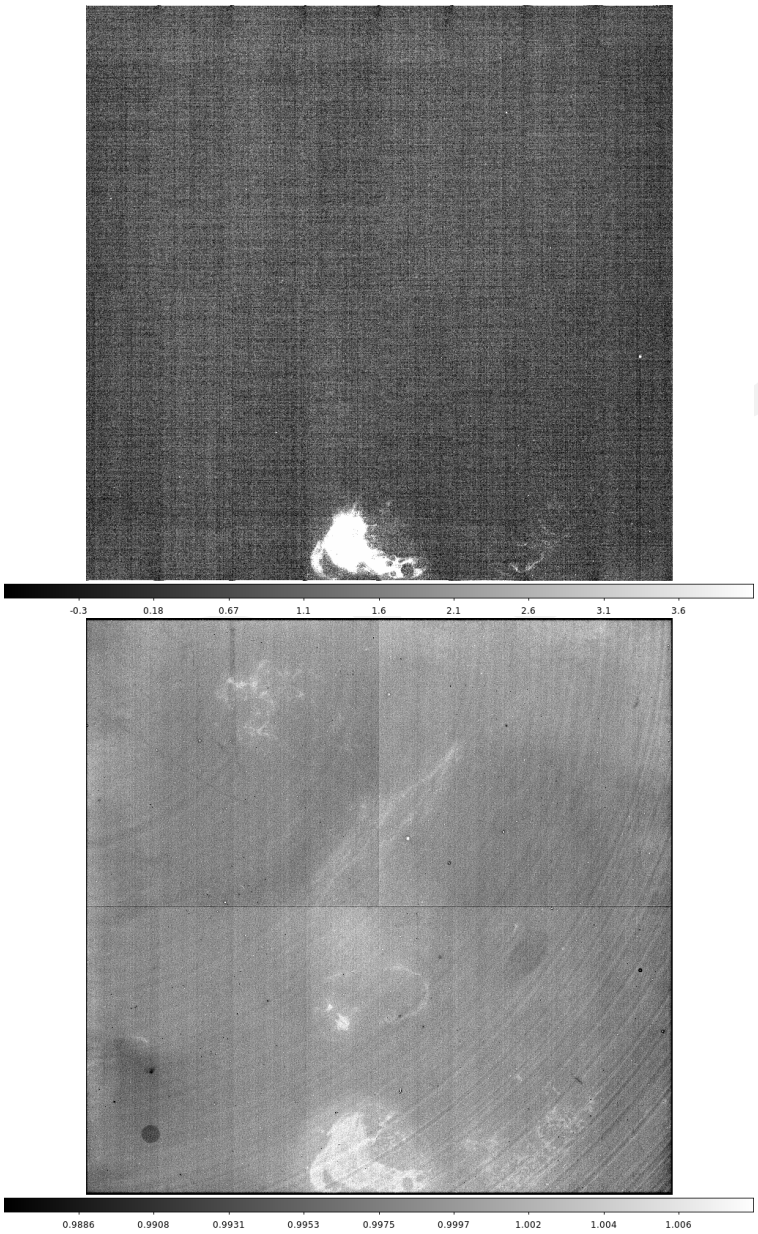

Figure 111: The ITL sensor R02_S02. Top: the transient phosphorescence term. Bottom: the *blue* flat response. The *coffee stain* feature in the flat response has the same polarity as the phosphorescence. A phosphorescent *vampire pixel* is seen in segment R02_S02_C07.

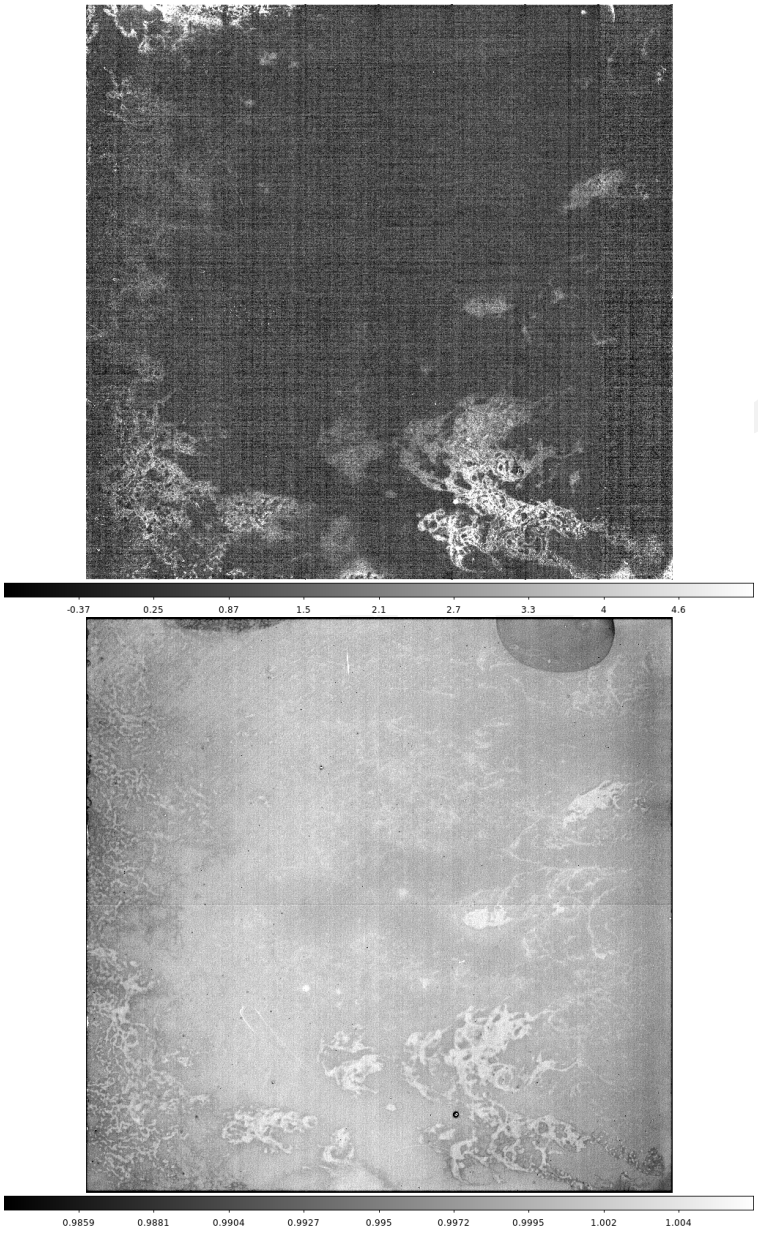

Figure 112: The ITL sensor R02_S12. Top: the transient phosphorescence term. Bottom: the *blue* flat response. Generally the polarity of the phosphorescence matches that of the *coffee stain* in the flat field response, but exceptions include the *vampire pixel* seen in segment R02_S12_C05.

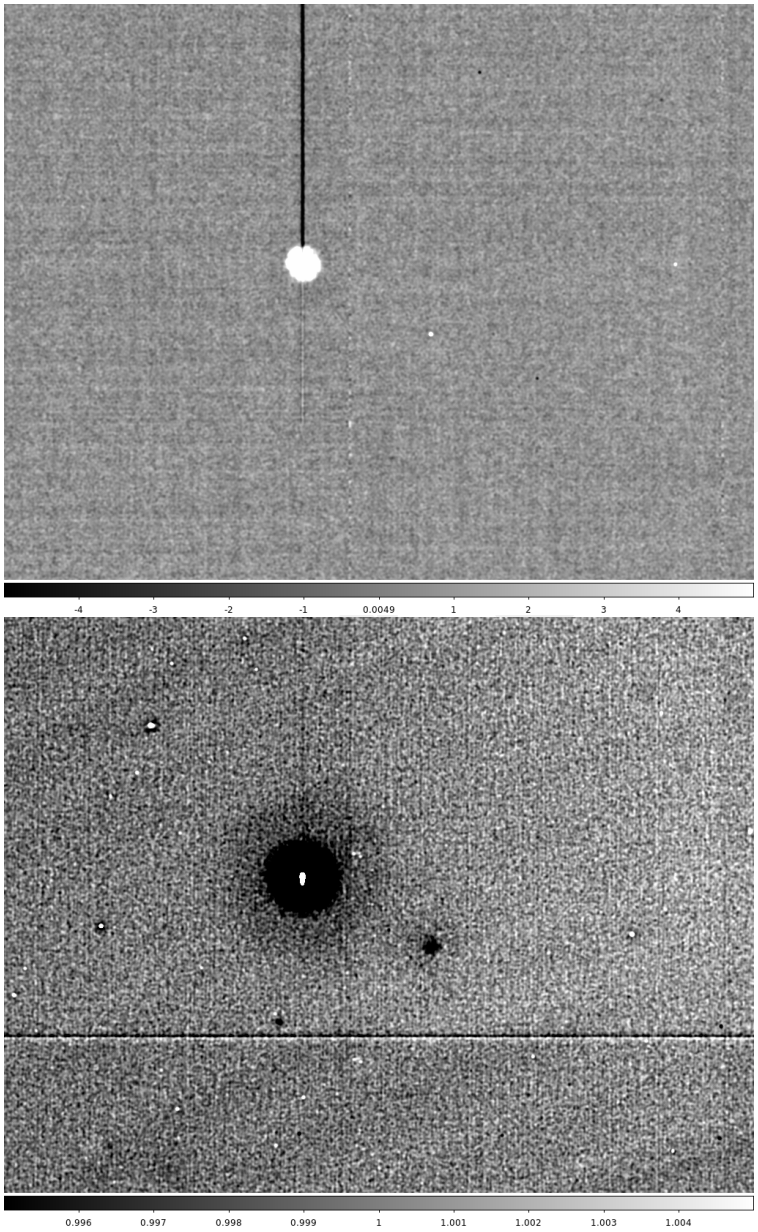

Figure 113: The ITL sensor R03_S10, detail of the *vampire pixel* of R03_S10_C15. Top: the transient phosphorescence term. Bottom: the *blue* flat response. As in previous examples, this *vampire pixel*'s transient term is large enough to contaminate the parallel overscan even after the first 15 s following trigger.

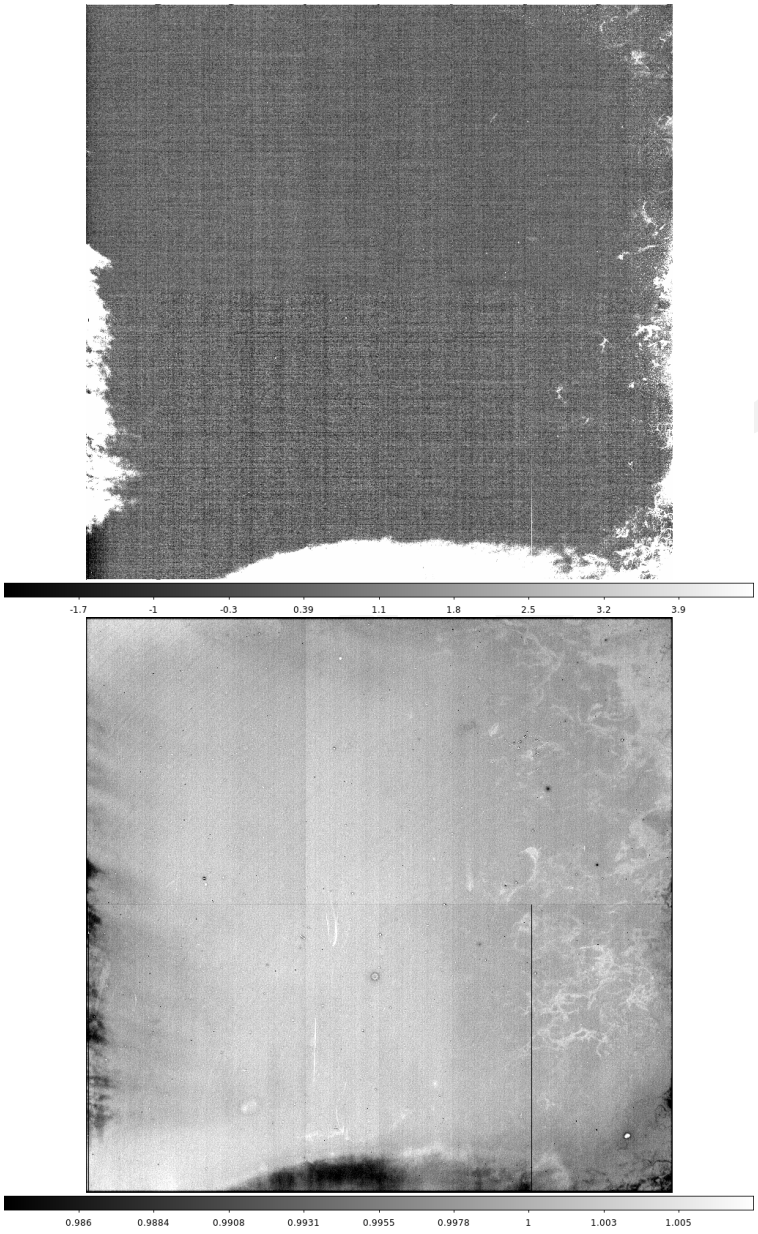

Figure 114: The ITL sensor R43_S11. Top: the transient phosphorescence term. Bottom: the *blue* flat response. This sensor appears to have the largest integrated phosphorescence among ITL sensors studied. The flat response feature has opposite polarity from the phosphorescence.

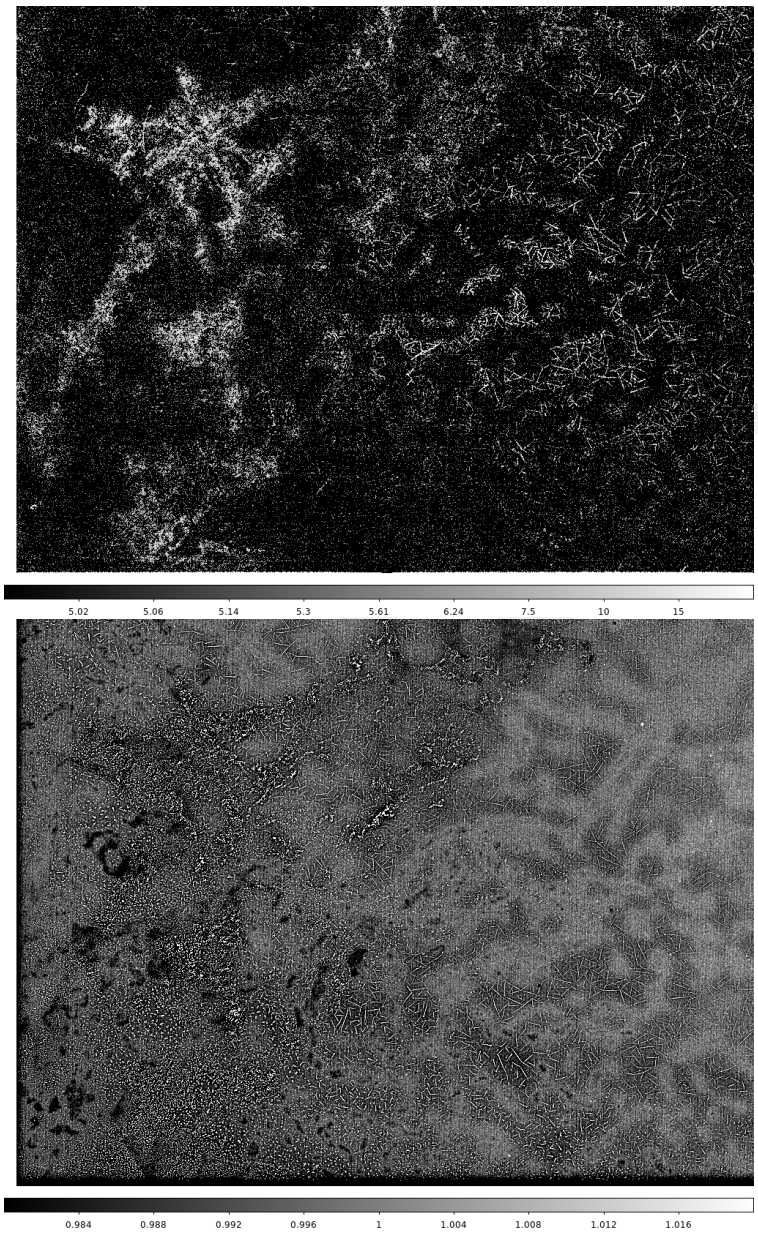

Figure 115: The ITL sensor R43_S20, segments C00 through C03. Top: the transient phosphorescence term. Bottom: the *blue* flat response. This sensor apparently exhibits peculiar radial crazing patterns seen in both phosphorescence as well as in flat field response, with polarities aligned.

99% quantile level to characterize was mainly to estimate the degree to which images would need to be phosphorescence-corrected (and/or the variance plane modified, given the asymmetric impact of the position specific, phosphorescence contribution in recorded images).

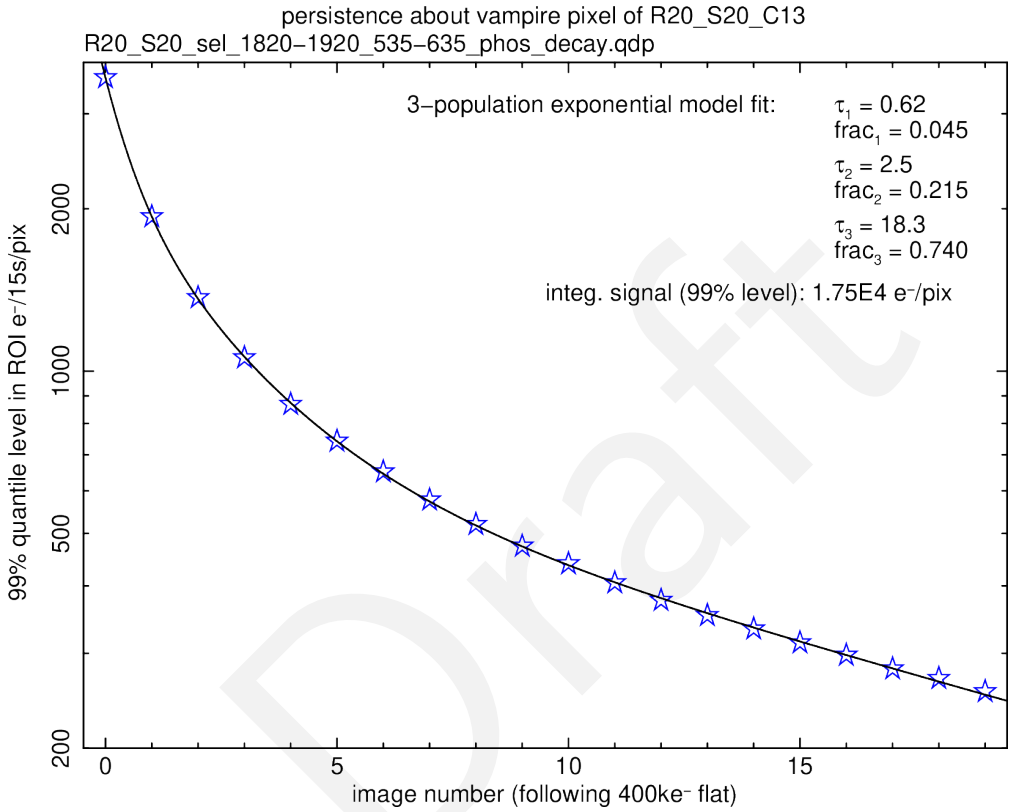

Figure 116: A three-population fit of the phosphorescence expressed by the vapire pixel region of R20_S20_C13. The fit was performed on the 99% quantile level where signal levels are well above the 3σ level of the noise distribution. Here, image numbers are parasitically used as time units, with roughly 17.5 seconds per image.

H Phosphorescence response characterization

Figures 124 through 130 attempt to quantify the expressed phosphorescence response in ROIs on seven of the problematic ITL sensors. Previously, we had captured the phosphorescence *transient term* across the ITL sensors (*cf.* Figs. 98 thru 109); we also tracked ROI pixel distribution parameters of individual median images constructed from the selection of specific images acquired across the 20 B-protocol datasets available (listed in Table 12). Here we analyze the signal level- and wavelength-dependences of the expressed phosphorescence captured in the first dark image following flat exposure. Table 27 provides the dataset IDs

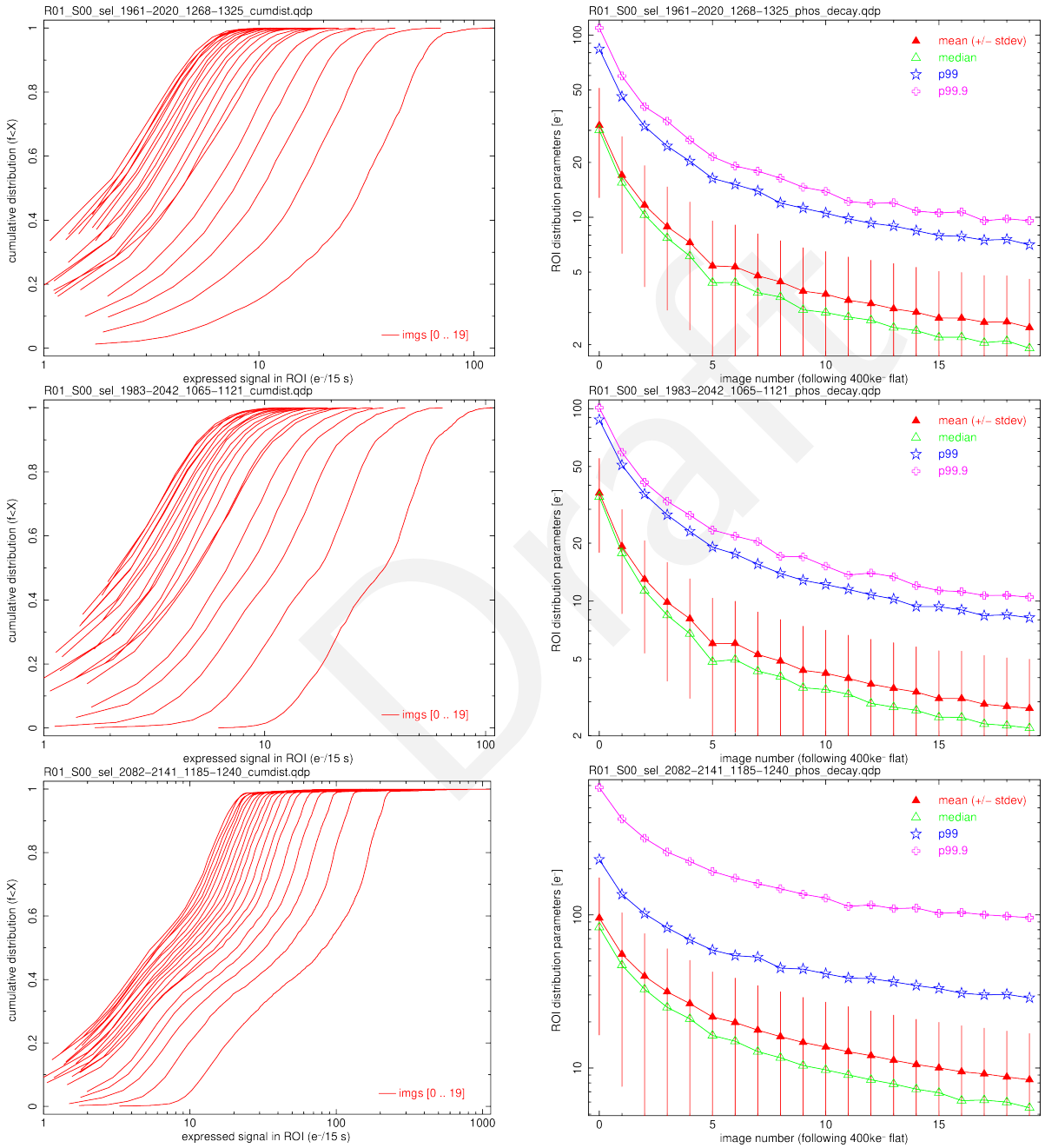

Figure 117: Kinetics for phosphorescence expression in ROIs of images for R01_S00. This is the prominent cosmetic seen in Fig. 110, which is apparently a *vampire* pixel.

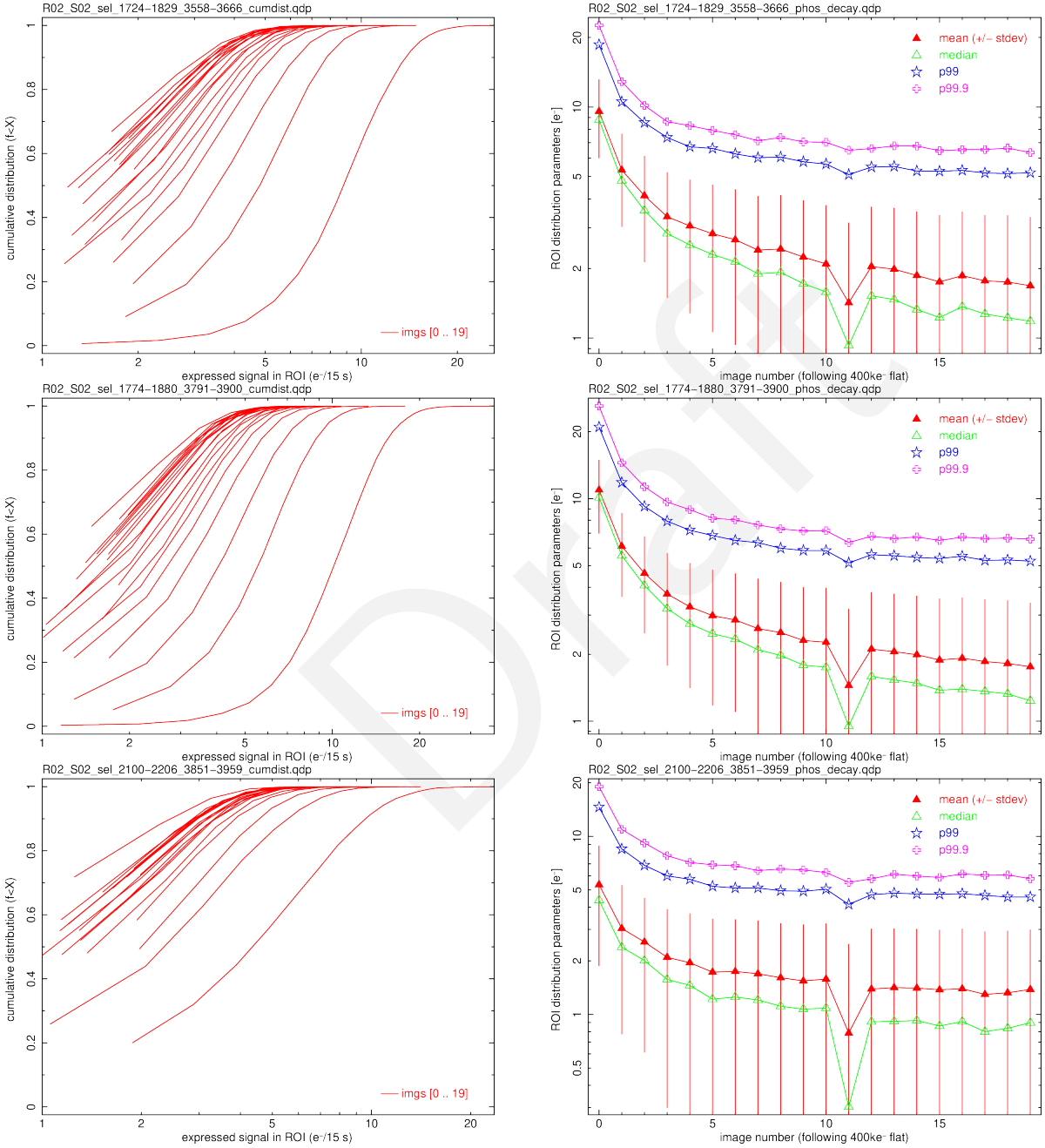

Figure 118: Kinetics for phosphorescence expression in ROIs of images for R02_S02. This is the diffuse phosphorescence that correlates with the coffee stains seen in Fig. 111. No extractions were performed on the *vampire pixels* found on the same sensor (R02_S02_C15 and R02_S02_C07).

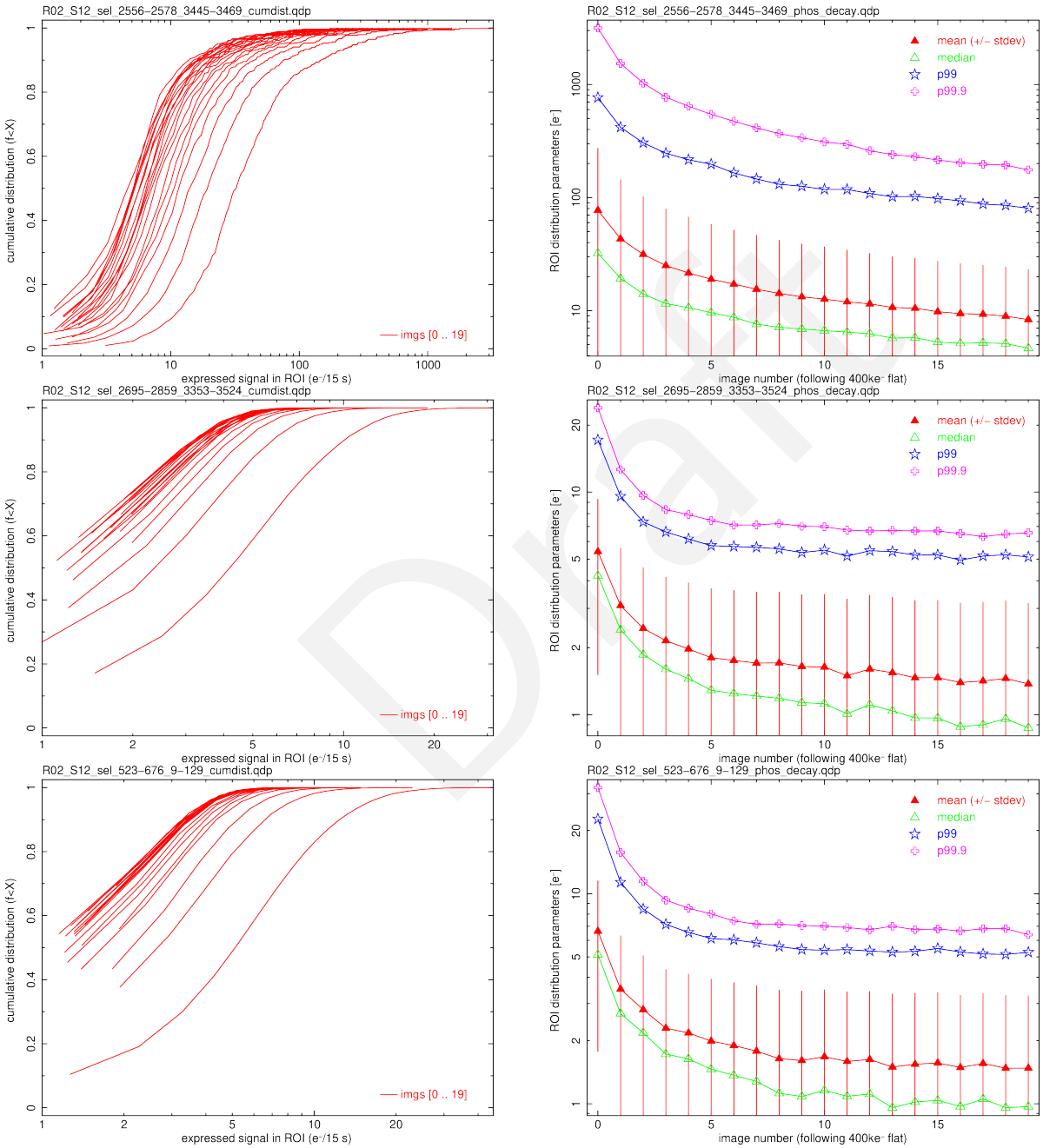

Figure 119: Kinetics for phosphorescence expression in ROIs of images for R02_S12. This is the structured phosphorescence that correlates with the coffee stains seen in Fig. 112.

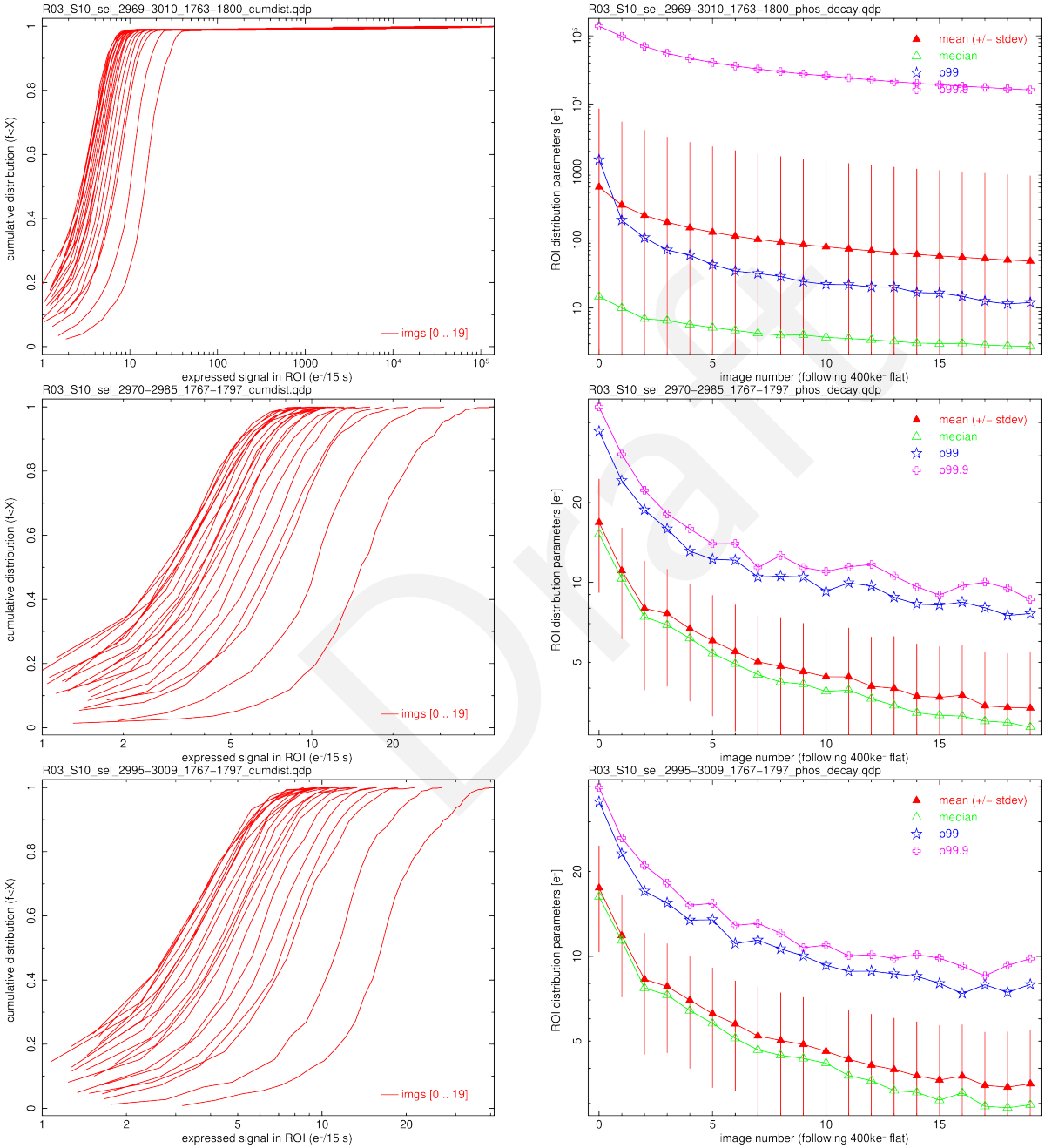

Figure 120: Kinetics for phosphorescence expression in ROIs of images for R03_S10. These describe regions including or near the bright/focusing *vampire pixel* seen in Figs. 113, 96b and 97b.

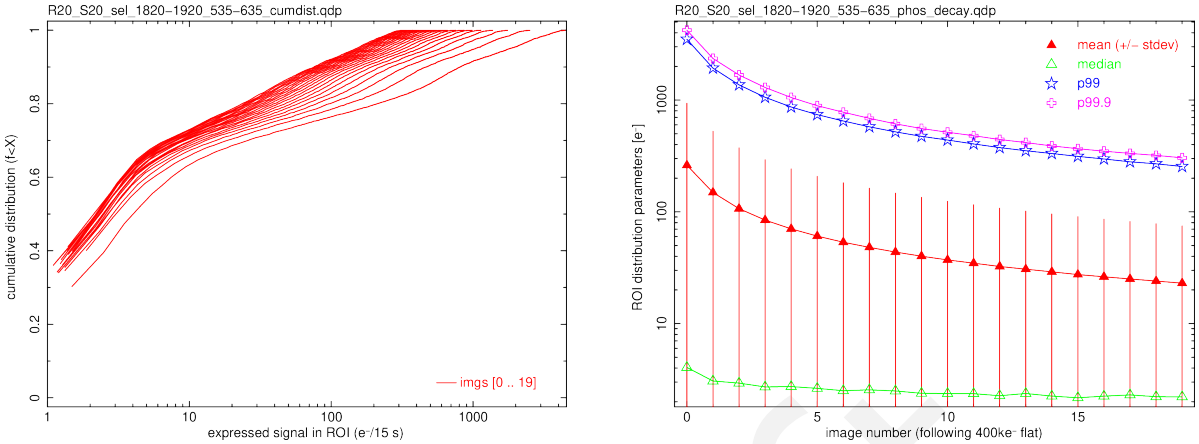

Figure 121: Kinetics for phosphorescence expression in ROIs of images for R20_S20. These describe the prominent non-focusing *vampire pixel* seen in Figs. 96d and 97d.

and SeqIDs used for this analysis.

Table 27: Zephyr Scale E-numbers and corresponding SeqIDs analyzed to estimate signal level and wavelength dependence of the phosphorescence response.

Run numbers and SeqIDs of first dark following trigger		
CCOB LED	trigger flat target signal	runID & SeqID
uv	500	E1770:20241028_000010
uv	1000	E1503:20241020_000489
uv	1500	E1771:20241028_000039
uv	3000	E1504:20241020_000533
uv	4500	E1772:20241028_000068
uv	5000	E1505:20241020_000577
uv	10000	E1506:20241020_000621
uv	13500	E1773:20241028_000097
uv	30000	E1507:20241020_000665
blue	500	E1774:20241028_000126
blue	1000	E1502:20241020_000445
blue	1500	E1775:20241028_000155
blue	3000	E1501:20241020_000401

Continued on next page

Table 27 – continued from previous page

Run numbers and SeqIDs of first dark following trigger		
blue	4500	E1776:20241028_000184
blue	5000	E1500:20241020_000357
blue	10000	E1499:20241020_000313
blue	13500	E1777:20241028_000213
blue	30000	E1498:20241020_000269
blue	50000	E1491:20241018_000989
blue	150000	E1485:20241018_000725
blue	400000	E1484:20241018_000678
red	50000	E1490:20241018_000945
red	150000	E1486:20241018_000769
red	400000	E1483:20241018_000634
nm750	50000	E1492:20241018_001033
nm750	150000	E1487:20241018_000813
nm750	400000	E1479:20241018_000543
nm850	50000	E1493:20241018_001077
nm850	150000	E1488:20241018_000857
nm850	400000	E1477:20241018_000455
nm960	50000	E1494:20241018_001121
nm960	150000	E1489:20241018_000901
nm960	400000	E1478:20241018_000499

These runs were performed to sample a two-dimensional, rectangular parameter space, and each measurement was executed only once. The resulting sampling was completed incrementally, over 3 separate days. Using only one image for each data point, we were not able to median multiple images acquired under identical conditions (as we had done for Sections E, F and G).

Because there is significant variation in morphological characteristics of the phosphorescence,

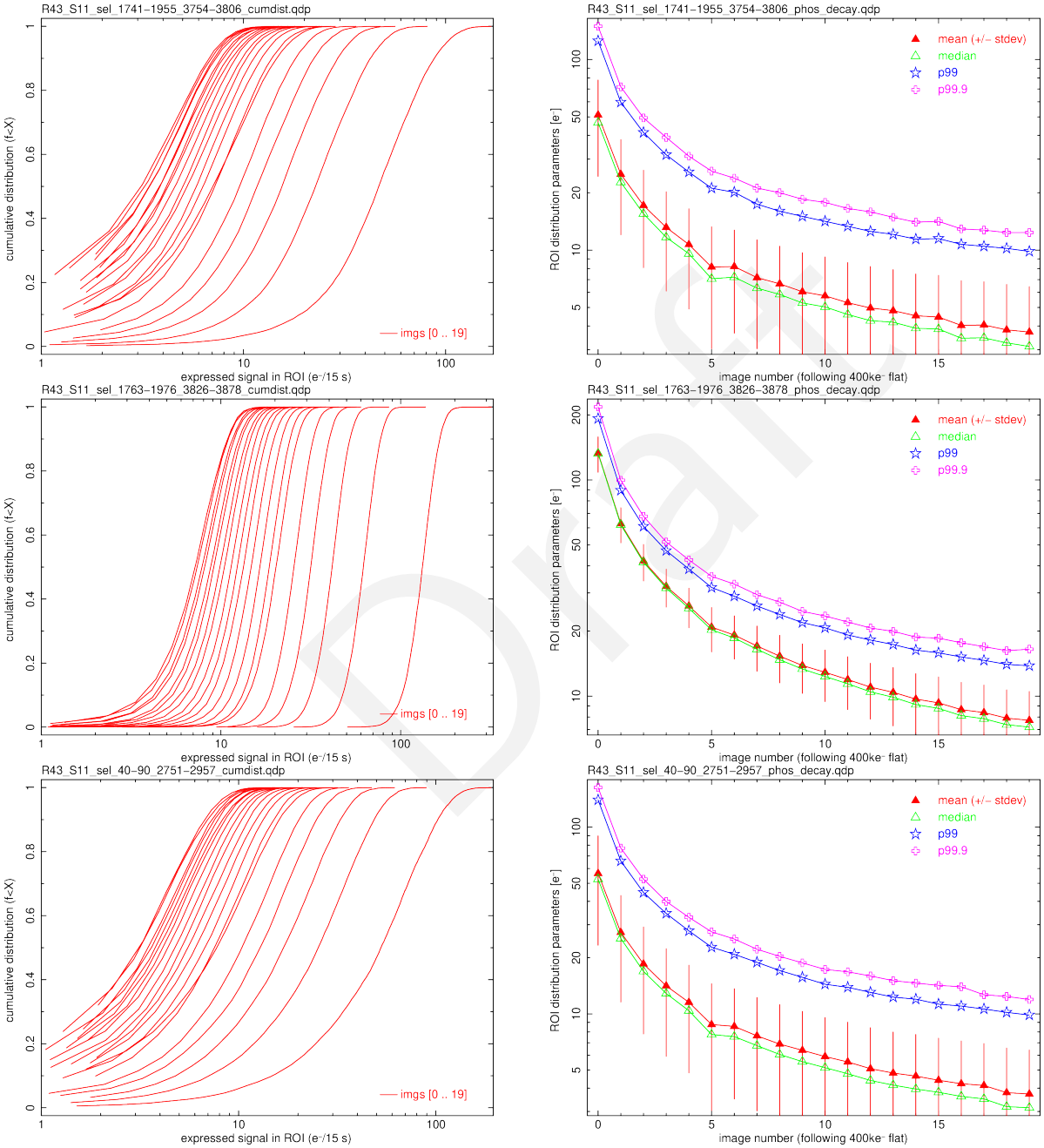

Figure 122: Kinetics for phosphorescence expression in ROIs of images for R43_S11. These describe bright, diffuse transient regions seen in Figs. 114 and 97f, which apparently turn off completely when the HV Bias is *off*.

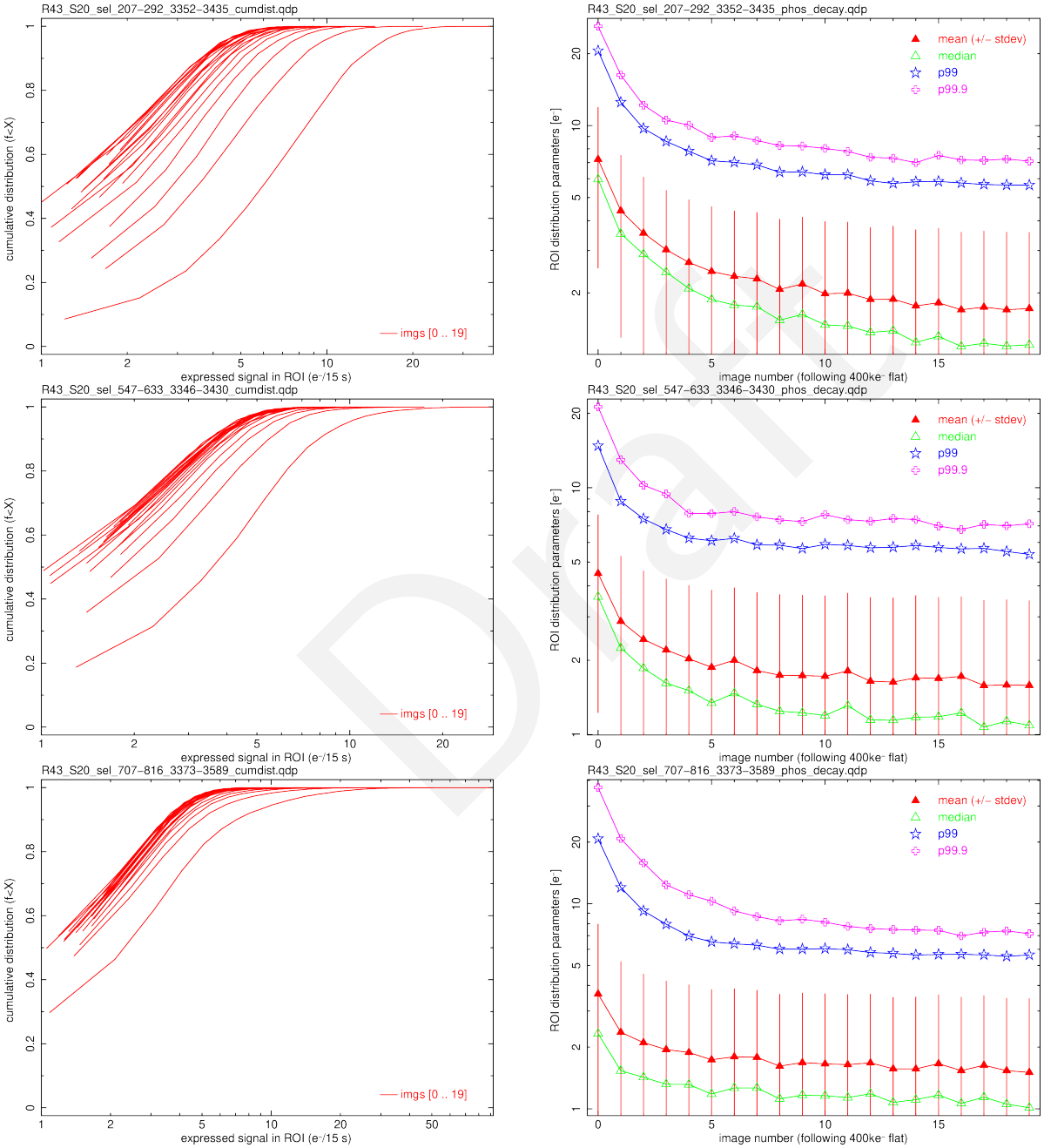

Figure 123: Kinetics for phosphorescence expression in ROIs of images for R43_S20. These include some of the the highly structured *snowflake-like* transient regions seen in Figs. 97h and 115.

we adopted the following strategy to quantify phosphorescence expression in each: Once the image is processed through ISR, each of the sensor specific ROIs are used to filter the pixels, and the signal distribution parameters are evaluated. The 99% quantile signal level was used as a bright end proxy for the expressed phosphorescence for each ROI. A consequence of this is that when there is insignificant or undetectable phosphorescence, this proxy choice would be artificially high, which would be pegged at about 4σ above the noise distribution mean.

The figures provide dashed lines that represent constant *phosphorescence efficiency ratios* to guide the eye (at 10%, 1% and 0.1%), while different color LED illumination are represented by different plotting symbols and line colors. The only CCOB LED used across the entire range of trigger flat signal levels is the *blue* one. The 400ke^- *blue* LED trigger flat induced phosphorescence levels are the only ones described thus far in Sections E, F and G.

Two of the sensors exhibiting distributed and structured phosphorescence expression (R02_S02 & R43_S20) appear to have phosphorescence yields below 3×10^{-3} for *uv* and *blue* LED illumination. Given the kinetics studied for these ROIs for *blue* LED illumination (*cf.* Figs 118 and 123), the worst case contribution may be 55 e^-/pix/15s (*uv* LED, $30\text{k}e^- \times e^{+0.62} \times 10^{-3}$). The $e^{+0.62}$ scaling factor comes from the fact that the LED flash occurs (and ends) at the beginning of the trigger flat illumination and typically lasts for just a fraction of the image time of ~ 17.5 seconds.

One other sensor with distributed, coffee stain-like phosphorescence (R02_S12) shows significantly more signal in one of the ROIs (*uv* and *blue* LEDs for 30ke^- and 400ke^-, respectively). Upon applying the $e^{+0.62}$ factor, the worst case phosphorescence here would scale to 560e^-/pix/15s and 1800e^-/pix/15s, respectively.

The remaining four sensors (R01_S00, R03_S10, R20_S20 & R43_S11) show even more phosphorescence. The first three of these are due to *vampire pixels* (with or without central hot spots), while the last one showed the diffuse glow along the edges which "shuts off" with HV Bias. The phosphorescent yield high-end proxy limits for these ROIs fall within the 10^{-2} to 10^{-1} range. There are even a few data points that approach or exceed 10^{-1} (R03_S10 & R20_S20) and such phosphorescence levels might be hard to believe, especially if the LED flash timing correction factor of $e^{+0.62}$ is also applied. One thing to keep in mind is that *vampire pixels* are known to bend drift field lines to produce regions with (apparently) $> 100\%$ QE. For example, the *vampire pixel* on R03_S10_C15 contains a group of pixels that can receive up to 15× the target level in a flat exposure, so such large yields as we've seen here are perhaps not so

mysterious after all.

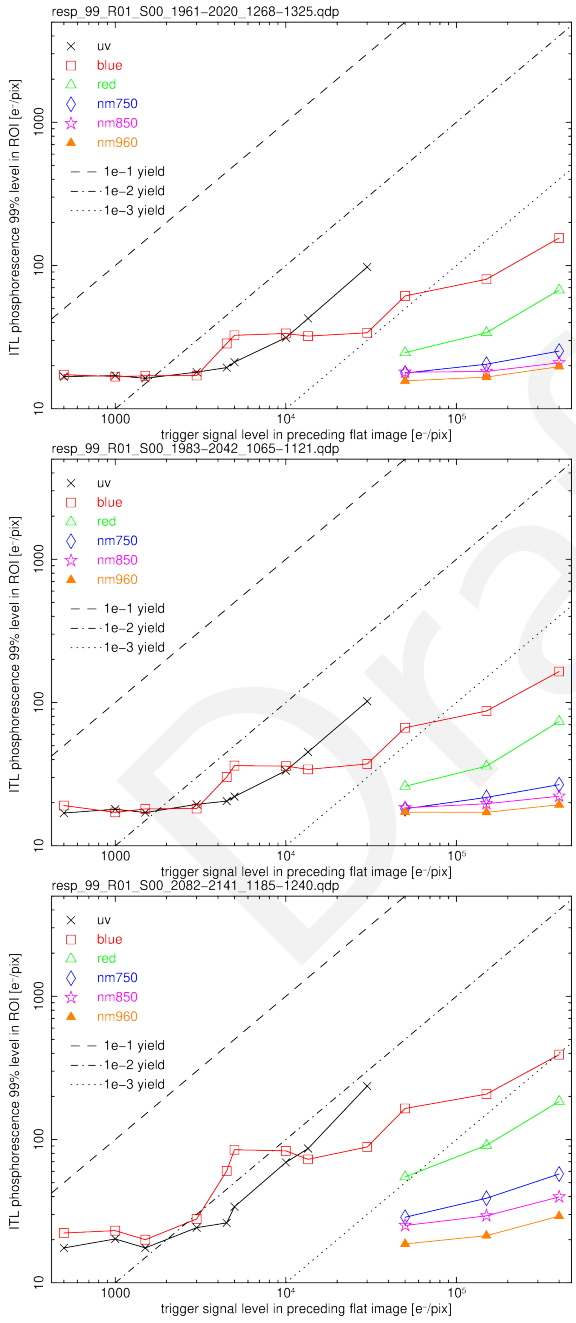

Figure 124: Signal and wavelength response for phosphorescence expression (99% level) in ROIs of images for R01_S00. This is the prominent cosmetic seen in Fig. 110, which is apparently a *vampire* pixel.

A References

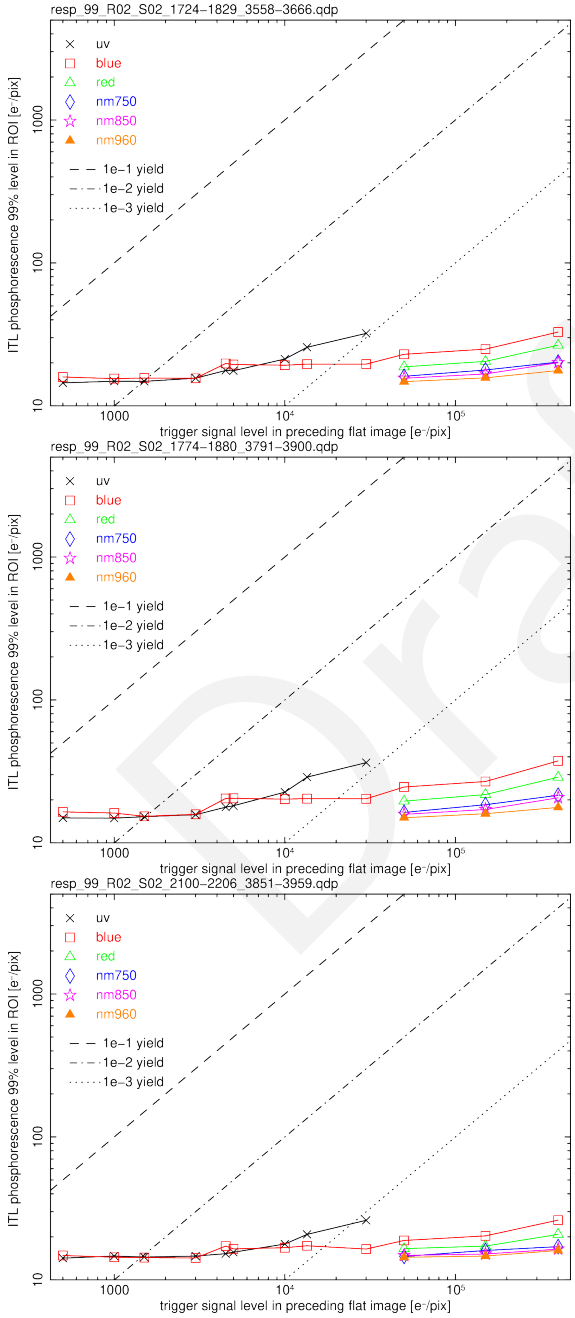

Figure 125: Signal and wavelength response for phosphorescence expression (99% level) in ROIs of images for R02_S02. This is the diffuse phosphorescence that correlates with the coffee stains seen in Fig. 111. No extractions were performed on the *vampire pixels* found on the same sensor (R02_S02_C15 and R02_S02_C07).

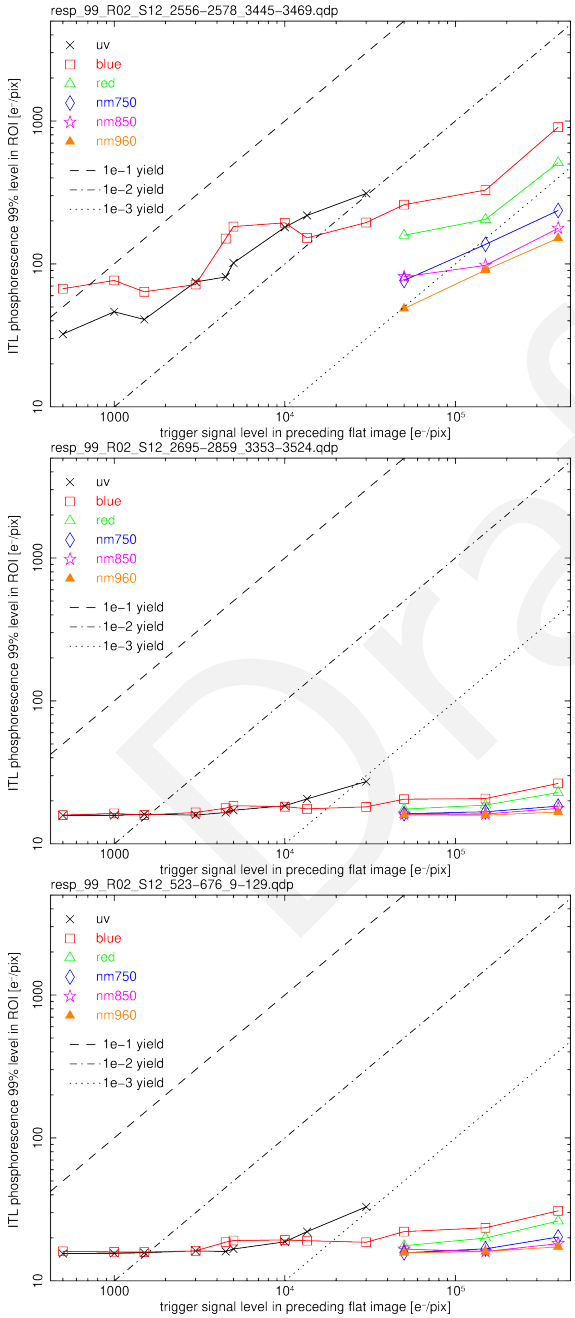

Figure 126: Signal and wavelength response for phosphorescence expression (99% level) in ROIs of images for R02_S12. This is the structured phosphorescence that correlates with the coffee stains seen in Fig. 112.

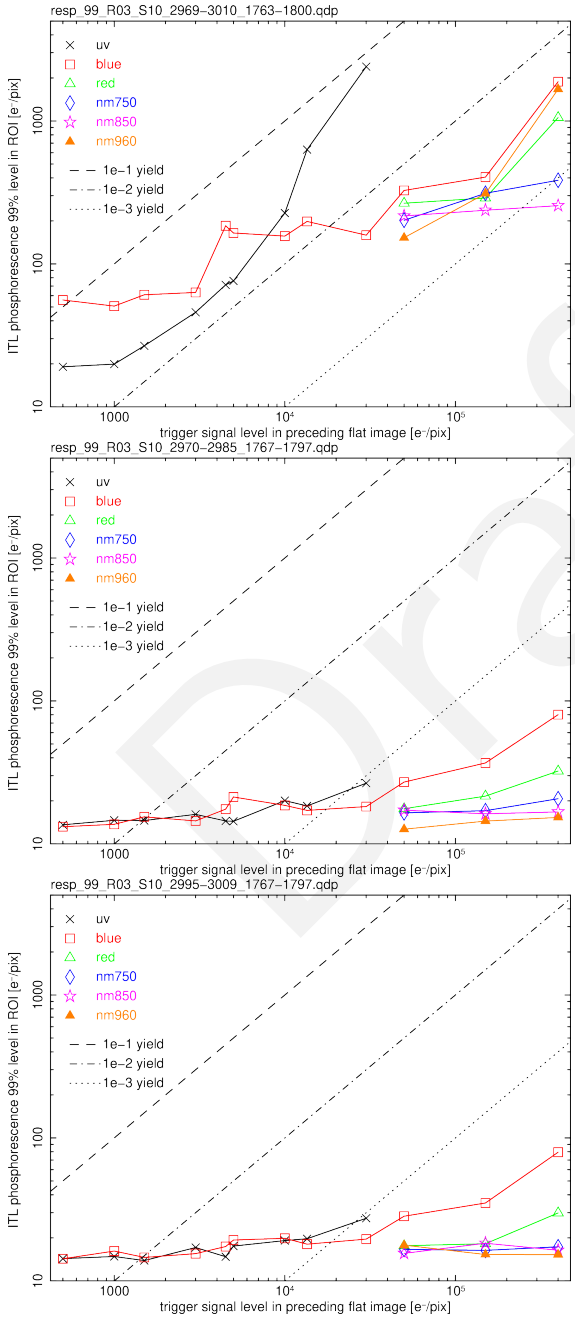

Figure 127: Signal and wavelength response for phosphorescence expression (99% level) in ROIs of images for R03_S10. These describe regions including or near the bright/focusing *vampire pixel* seen in Figs. 113, 96b and 97b.

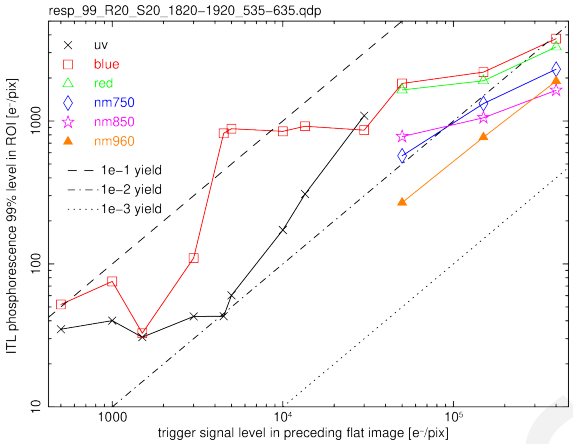

Figure 128: Signal and wavelength response for phosphorescence expression (99% level) in an ROI of images for R20_S20. These describe the prominent non-focusing *vampire pixel* seen in Figs. 96d and 97d.

References

Astier, P., Regnault, N., 2023, A&A, 670, A118 (arXiv:2301.03274), doi:10.1051/0004-6361/202245407, ADS Link

Astier, P., Antilogus, P., Juramy, C., et al., 2019, A&A, 629, A36 (arXiv:1905.08677), doi:10.1051/0004-6361/201935508, ADS Link

Banovetz, J., Utsumi, Y., Meyers, J., et al., 2024, arXiv e-prints, arXiv:2411.13386 (arXiv:2411.13386), doi:10.48550/arXiv.2411.13386, ADS Link

[DMTN-276], Banovetz, J., Utsumi, Y., Slater, C., 2024, Effects of Persistence on E2V Sensors and its Impacts on DC2 Data, URL https://dmtn-276.lsst.io/, Vera C. Rubin Observatory Data Management Technical Note DMTN-276

Doherty, P.E., Antilogus, P., Astier, P., et al., 2014, In: Holland, A.D., Beletic, J. (eds.) High Energy, Optical, and Infrared Detectors for Astronomy VI, vol. 9154 of Society of Photo-Optical Instrumentation Engineers (SPIE) Conference Series, 915418, doi:10.1117/12.2056733, ADS Link

Esteves, J.H., Utsumi, Y., Snyder, A., et al., 2023, PASP, 135, 115003 (arXiv:2308.00919), doi:10.1088/1538-3873/ad0a73, ADS Link

Janesick, J.R., 2001, *Scientific charge-coupled devices*, SPIE Optical Engineering Press, ADS Link

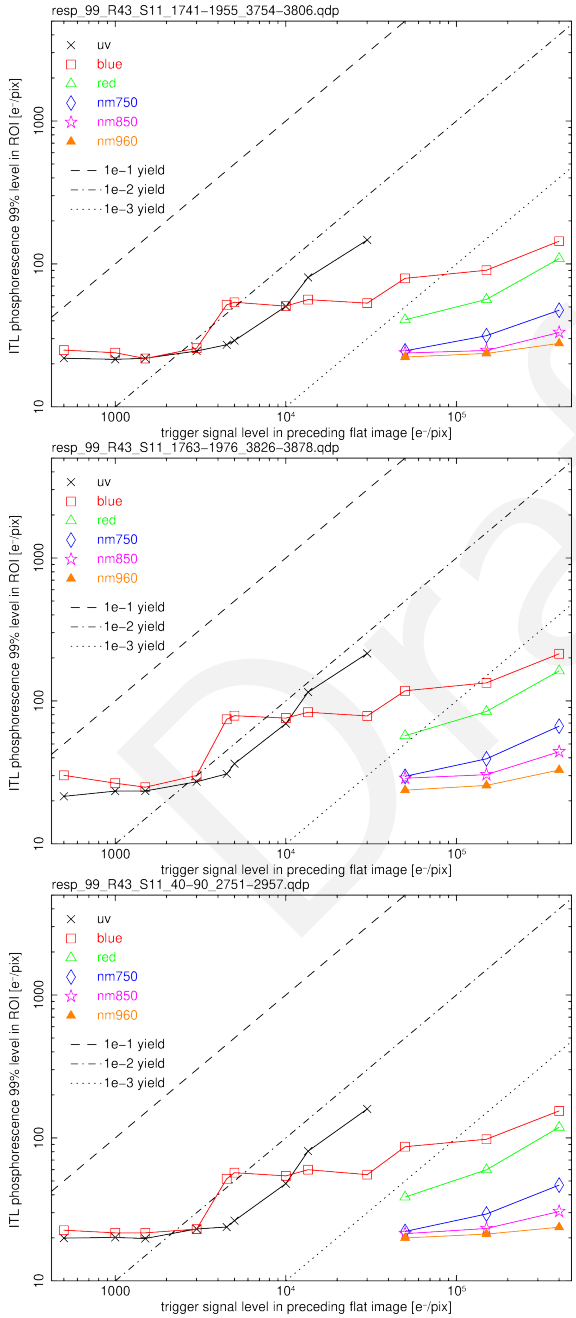

Figure 129: Signal and wavelength response for phosphorescence expression (99% level) in ROIs of images for R43_S11. These describe bright, diffuse transient regions seen in Figs. 114 and 97f, which apparently turn off completely when the HV Bias is *off*.

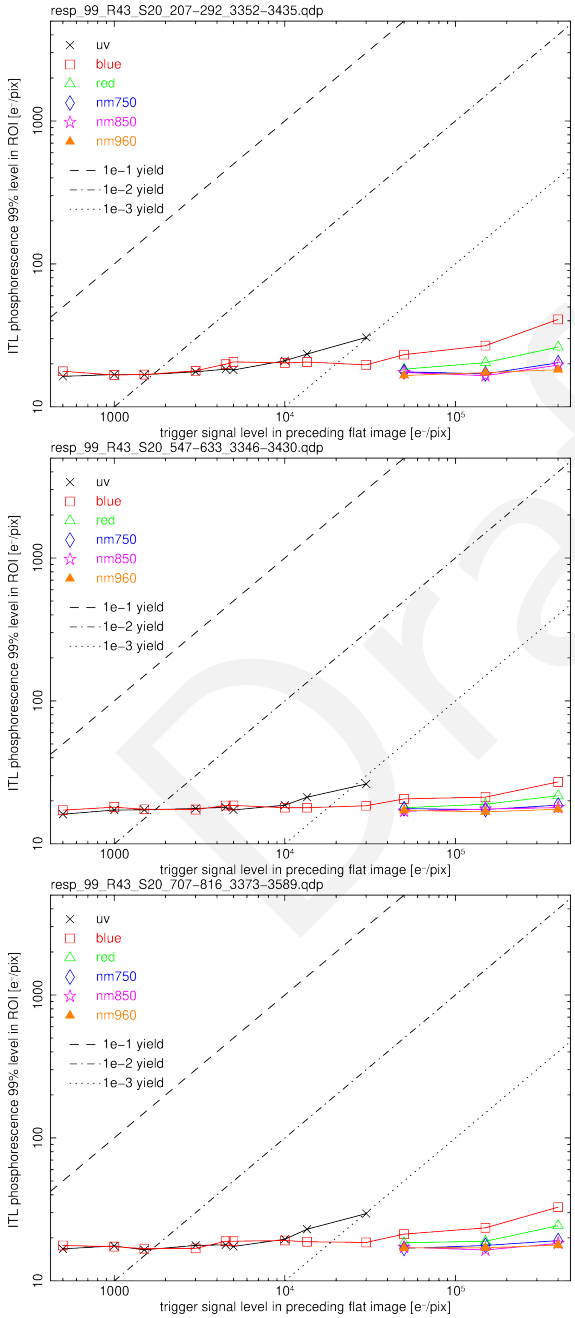

Figure 130: Signal and wavelength response for phosphorescence expression (99% level) in ROIs of images for R43_S20. These include some of the the highly structured *snowflake-like* transient regions seen in Figs. 97h and 115.

Juramy, C., Antilogus, P., Le Guillou, L., Sepulveda, E., 2020, arXiv e-prints, arXiv:2002.09439 (arXiv:2002.09439), doi:10.48550/arXiv.2002.09439, ADS Link

Snyder, A., Longley, E., Lage, C., et al., 2021, Journal of Astronomical Telescopes, Instruments, and Systems, 7, 048002, doi:10.1117/1.JATIS.7.4.048002, ADS Link

Snyder, A., Polin, D., Lage, C., Tyson, J.A., 2024, In: Holland, A.D., Minoglou, K. (eds.) X-Ray, Optical, and Infrared Detectors for Astronomy XI, vol. 13103 of Society of Photo-Optical Instrumentation Engineers (SPIE) Conference Series, 1310321, doi:10.1117/12.3020540, ADS Link

Utsumi, Y., Antilogus, P., Astier, P., et al., 2024, In: Holland, A.D., Minoglou, K. (eds.) X-Ray, Optical, and Infrared Detectors for Astronomy XI, vol. 13103 of Society of Photo-Optical Instrumentation Engineers (SPIE) Conference Series, 131030W, doi:10.1117/12.3019117, ADS Link

B Acronyms

Acronym	Description
2D	Two-dimensional
3D	Three-dimensional
AC	Access Control
ADC	atmospheric dispersion corrector
ADU	Analogue-to-Digital Unit
B	Byte (8 bit)
BOT	Bench for Optical Testing
CCD	Charge-Coupled Device
CCOB	Camera Calibration Optical Bench
CCS	Camera Control System
CMB	Cosmic Microwave Background
CMOS	complementary metal-oxide semiconductor
CTI	Charge Transfer Inefficiency
DC	Data Center
EO	Electro Optical
FES	Filter Exchange System
IR	infrared

ISR	Instrument Signal Removal
ITL	Imaging Technology Laboratory (UA)
L1	Lens 1
LCA	Document handle LSST camera subsystem controlled documents
LED	Light-Emitting Diode
LSST	Legacy Survey of Space and Time (formerly Large Synoptic Survey Telescope)
MC	Monte-Carlo (simulation/process)
OCS	Observatory Control System
OpSim	Operations Simulation
PCS	Pumped Coolant System
PCTI	Parallel Charge Transfer Inefficiency
PD	Program Development
PSF	Point Spread Function
PTC	Photon Transfer Curve
QE	quantum efficiency
REB	Readout Electronics Board
RTM	Raft Tower Module
S3	(Amazon) Simple Storage Service
SCTI	Serial Charge Transfer Inefficiency
SE	System Engineering
SLAC	SLAC National Accelerator Laboratory
TMA	Telescope Mount Assembly
UCD	Unified Content Descriptor (IVOA standard)
UT	Universal Time
UTC	Coordinated Universal Time